Phonon Spectroscopy
and
Low-Dimensional Electron Systems

– The Effect of Acoustic Anisotropy and Carrier Confinement –

Habilitationsschrift
zur Erlangung des Akademischen Grades
Dr. rer. nat. habil.

vorgelegt von

Dr. rer. nat. Dietmar Lehmann

geboren in Glauchau/Sa.

Institut für Theoretische Physik
Fakultät Mathematik und Naturwissenschaften
Technische Universität Dresden

2004

Contents

1 Introduction 1
1.1 Prologue . . . 1
1.2 Central themes of this work . . . 4

2 Phonon Spectroscopy and Phonon Imaging 9
2.1 The basis of phonon spectroscopy . . . 9
2.2 Typical experiments and their application . . . 11
2.2.1 Time-of-flight spectroscopy . . . 11
2.2.2 Phonon imaging . . . 13
2.3 Phonon spectroscopy and low-dimensional electron systems . . . 18

3 Phonon Pulse Propagation and Phonon Images 21
3.1 Acoustic phonons in anisotropic solids . . . 21
3.2 Phonon focusing . . . 26
3.3 Kinetic description of phonon pulses . . . 29
3.3.1 Kinetic equation for phonon pulses . . . 29
3.3.2 Phonon energy and quasimomentum flux . . . 33
3.3.3 Phonon mode distribution in the detector . . . 36
3.4 Method and results of numerical calculation of phonon focusing . . . 39

4 Acoustic Phonon Scattering in Low-Dimensional Electron Systems 47
4.1 Basic properties of quasi low-dimensional electron systems . . . 47
4.1.1 Bulk electronic structure – A short resumé . . . 48
4.1.2 Electronic states of heterostructures – The envelope function concept . . . 50
4.1.3 Simple models of confinement . . . 53
4.2 The electron-acoustic phonon scattering . . . 66
4.2.1 Deformation potential scattering . . . 66
4.2.2 Piezoelectric coupling . . . 68
4.2.3 Macroscopic deformation coupling . . . 69
4.2.4 The influence of acoustic anisotropy . . . 71
4.2.5 Electron-phonon interaction and electron confinement . . . 73

5 Phonon Induced Electric Current 75
- 5.1 Basic features and experimental setup . . . 75
- 5.2 Theoretical model of phonon drag . . . 77
- 5.3 Phonon-drag images – The result of anisotropy and confinement . . 88
  - 5.3.1 Comparison to experimental results . . . 88
  - 5.3.2 The effect of acoustic anisotropy . . . 92
  - 5.3.3 The effect of carrier confinement . . . 94
- 5.4 Outlook . . . 97

6 Acoustic Phonon Emission by Hot Electrons 99
- 6.1 Energy relaxation in low-dimensional systems – Basic features . . . 99
- 6.2 Theory of angle-resolved acoustic phonon emission . . . 105
- 6.3 Angular and mode dependence of acoustic phonon emission . . . 114
  - 6.3.1 Results and comparison with experiment . . . 114
  - 6.3.2 The effect of acoustic anisotropy . . . 120
  - 6.3.3 The effect of carrier confinement . . . 123
- 6.4 Open problems and outlook . . . 128

7 Summary and Conclusions 131

A Generation and Detection of Nonequilibrium Phonons 135
- A.1 Sources of nonequilibrium phonons . . . 135
- A.2 Phonon detectors . . . 140
- A.3 Wavevector and frequency dependence of a phonon radiator . . . 142

B Dynamic Susceptibility of Quasi Low-Dimensional Electron Gases 147
- B.1 Quasi two-dimensional systems . . . 147
  - B.1.1 The magnetic field case . . . 147
  - B.1.2 The zero field case . . . 151
- B.2 Quasi one-dimensional systems . . . 153

C Overlap Integrals and Form Factors 155
- C.1 Quasi two-dimensional systems . . . 155
  - C.1.1 Modulation-doped heterojunctions . . . 155
  - C.1.2 Quantum wells . . . 157
- C.2 Quasi one-dimensional systems . . . 158

Bibliography 161

Chapter 1

Introduction

1.1 Prologue

The interaction of electrons with acoustic phonons has important consequences for the performance of all semiconductor devices. Acoustic phonon scattering controls the relaxation of carriers to their band bottom, which is necessary for efficient laser action, for optical properties and for transport phenomena. At very low temperatures, electron-impurity scattering is dominant. However, at slightly higher temperatures the interaction of electrons with acoustic phonons is the limiting factor of the electron mobility and thus fundamental for the application of electronic devices. Impurity scattering can often be controlled by improved fabrication but the electron-phonon scattering is an intrinsic effect. Therefore, the understanding of the carrier-phonon interaction has always been a key objective of semiconductor research.

In this work we focus our attention on the interaction of acoustic phonons with *low-dimensional electron systems*. We speak of low-dimensional electron systems "if the only states into which an electron can scatter are determined by no change in the quantum numbers in one or more dimensions, or at most changes of one or more" (Kelly, 1995). Or, expressed by a more descriptive definition, we are in a low-dimensional situation if the electrons are confined in one or more spatial directions to within a few atomic layers. Such systems form the basis of a large portion of today's semiconductor physics and have a great practical impact on a wide range of electronic, optical and acoustic solid state devices such as, e.g. high electron mobility transistors, microwave sources and detectors, quantum well lasers, infrared and solar devices and high frequency ultrasonic generators. There are large differences in both the electrical and optical properties of low-dimensional systems compared to the corresponding bulk systems. On the one hand, bulk properties may be modified to a greater or lesser extent, on the other hand also completely novel (quantum) effects may arise. The question is therefore how the interaction of the electrons with acoustic phonons is altered by the reduced carrier dimensionality.

Probably the simplest and most known experimental method to study the interaction of low-dimensional electrons with acoustic phonons is to measure the electron mobility. But, firstly, it is not always easy to separate the contributions of the acoustic phonons from other scattering mechanisms and secondly, only information averaged over the contribution of all acoustic modes is available. This is also the case for the phonon-drag term of thermoelectric power. At low temperatures, the so called phonon drag contributes significantly to the total thermoelectric power, but here as well only averaged information about the coupling process can be obtained. A real alternative to transport measurements and also to optical methods is *phonon spectroscopy* which has been applied with increasing success to the study of low-dimensional electron systems and devices in the past twenty years. The value of phonon spectroscopy rests upon the *direct observation of nonequilibrium acoustic phonon pulses* that are either emitted or absorbed by the carriers in the low-dimensional structure. The ability to isolate phonons of particular mode and propagation direction is the decisive advantage of the phonon spectroscopy technique over other methods. This provides direct insight into the fundamental carrier-phonon coupling processes. It makes, for example, the distinction between different interaction mechanisms possible. However, the importance of phonon spectroscopy in relation to low-dimensional electron systems is not restricted to having a direct way of studying the electron-phonon coupling. Acoustic phonon pulses are also a most useful and unique probe for analysing the structure and the fundamental electron properties of low-dimensional semiconductor systems. This is due to the fact that the wavelength of acoustic phonons is comparable to the important length scales in these systems (such as the electron confinement lengths or the Fermi wavelength) and that energy *and* quasimomentum of acoustic phonons are well matched to the low-energy collective excitations of the low-dimensional electrons allowing their simultaneous probing in energy and momentum space. For example, the magnetoroton excitations in the fractional quantum Hall regime of two-dimensional (2D) electron systems can be studied very efficiently by acoustic phonon pulses since in contrast to optical experiments phonons are able to probe excitations that have a meV energy and a *non*zero wavevector.

Compared to spectroscopy with photons, electrons or neutrons the spectroscopy with acoustic phonons is a relatively young method and less widely known. Although restricted to low temperatures, because only in this case a ballistic or at least quasi-ballistic phonon propagation over macroscopic distances is possible, the technique has a wide field of application, which is by far not limited to semiconductor nanostructures. Phonons in the energy range of 10–1000 GHz are generally of great interest as a spectroscopic tool for many reasons. Primarily, this is a region of the spectrum in which there are almost no other suitable techniques, lying at the upper limit of microwave capabilities and at the lower limit of far infrared spectroscopy. Secondly, because of the larger density of states for phonons many defects and excitations are much more strongly coupled to phonons than they are to photons. Thermal conductivity measurements, which were for a long time the only method to study phonons with frequencies above 10 GHz, sample the phonon transport averaged over all modes and propagation directions and thus do not allow any ‘spectroscopy’. By contrast, angle- and time-resolved phonon spectroscopy gives more direct and unambiguous information on how the phonons travel across a crystalline sample, since the phonon trajectories can be resolved in time and space. Phonon spectroscopy can provide information about lattice dispersion, particularly for directions of phonon wavevectors away from symmetry axes, which are complementary to inelastic neutron scattering. The reason is that the results of phonon spectroscopy are extremely sensitive to the curvature of the surfaces of constant phonon frequency. In addition, acoustic phonon beams are highly sensitive to all types of lattice disorder and represent, above all, a nondestructive measure allowing, for instance, a nondestructive evaluation of microstructures or wafer bonds. So far, the application of phonon spectroscopy techniques is limited due to the fact that the spectral resolution falls in general short of what is routinely achieved in conventional optical spectroscopy. However, current progress in generating monochromatic phonon beams of very narrow spectral linewidth gives rise to the hope that this handicap can be overcome and that, in the future, even such interesting new fields like ‘phonon optics’ may be possible.

What is characteristic for all methods of phonon spectroscopy? They are based on a local generation of nonequilibrium pulses of acoustic phonons and on the study of the (ballistic) propagation of these phonons and their interaction with defects, low-dimensional electron systems, etc. Due to the intrinsic elastic anisotropy of the crystalline matter the phonon flux is channelled (focused) along certain crystal directions leading to an extremely anisotropic phonon propagation. In addition, the scattering of the phonons caused by defects in the crystal or by electrons is known to be highly anisotropic, that is dependent among others on the directions of the phonon wavevectors and their polarization. As a result, a large impact of acoustic anisotropy on the experimental findings is to be expected. Consequently, to interpret experimental results quantitatively, they must be compared with theoretical models and numerical simulations that take into account not only the specific phonon scattering processes, but also the striking effects of acoustic anisotropy in all their bearings. Despite the progress that has been made in the theoretical interpretation of phonon spectroscopy measurements over the years, a number of questions has been outstanding, particularly in connection with the study of low-dimensional electron systems. Problems remaining have included those of the correct angle dependence of phonon emission by 2D electrons, the magnitude of electron-phonon coupling constants or the detailed description of screening in a reduced dimensional situation. Therefore the aim of the present work and of the underlying papers published during the last years is to give an answer to some of these open questions and to achieve a better understanding of phonon spectroscopy experiments and of electron-phonon coupling in low-dimensional electron systems.

1.2 Central themes of this work

The particular objective of this work on phonon spectroscopy and low-dimensional electron systems is characterized by the subtitle '*The effect of acoustic anisotropy and carrier confinement*'. The choice of this subtitle stands consciously for two different aspects. One is that it emphasizes the significance of acoustic anisotropy and confinement in a general sense. They represent something like the foundation pillars of phonon spectroscopy and low-dimensional systems. Without the quantum confinement of the carriers no low-dimensional electron system would exist and phonon spectroscopy measurements, particularly the phonon imaging, would be very poor without the focusing due to acoustic anisotropy. This general aspect will have a large influence on the theoretical modelling of phonon spectroscopy and low-dimensional electron systems as explained in the first part of the work. However, giving a general view and presenting a universally applicable theoretical approach for the computer-modelled simulation of phonon spectroscopy on low-dimensional systems are only part of the intention. The aim is as well to show the influence of acoustic anisotropy and carrier confinement in detail and to prove that an understanding of the experimental findings is almost exclusively possible by a proper and exhaustive consideration of both factors in the theoretical modelling. This aspect is the topic of the second part of the work. Therefore the subtitle accounts for the specific goal of this study as well.

This work is organized as follows. In Chapter 2 a survey of phonon spectroscopy is given. Different techniques like phonon imaging or time-of-flight measurement (heat pulse method) as well as possible applications are discussed. Special attention is focused on the link between phonon spectroscopy and the study of low-dimensional semiconductor structures. This relation is particularly interesting because phonon spectroscopy is not only an experimental tool to study low-dimensional systems but low-dimensional electron systems also serve as useful phonon sources or phonon detectors in phonon spectroscopy experiments.

Chapter 3 deals with theoretical aspects of phonon spectroscopy. The propagation of ballistic phonon pulses through a nonmetallic crystalline medium at liquid helium temperatures is outlined and the effect of phonon focusing is explained. A theoretical model to describe the phonon energy and quasimomentum flux is discussed in detail. It allows us to calculate the nonequilibrium phonon distribution at a phonon detector as a function of time and of detector position for a wide range of phonon sources including the exact geometrical arrangement and the finite spatial extension of phonon source and detector as well as the phonon scattering by isotopes. The presented kinetic model and the accompanying numerical program package are something like a condition precedent for the theoretical interpretation of angle- and time-resolved phonon spectroscopy. The corresponding numerical results represent the phonon input to the computer simulation of phonon spectroscopy studies on low-dimensional electron systems. The chapter concludes with examples of our results showing the images of phonon energy and quasimomentum focusing for typical substrate materials of low-dimensional semiconductor structures. These images demonstrate the highly anisotropic phonon propagation due to the acoustic anisotropy of the crystalline substrates.

The electronic structure of low-dimensional semiconductor systems and the interaction of low-dimensional electrons with acoustic phonons are in the center of interest of Chapter 4. It starts with a collection of some basic facts about the bulk electronic structure of III-V semiconductors like gallium arsenide, followed by the so called envelope function concept for the theoretical description of the electronic structure of low-dimensional semiconductor systems. Since the electron envelope wavefunctions have a fundamental influence on the properties of electron-phonon coupling, the modelling of electron and hole confinement in modulation-doped heterojunctions as well as in quantum wells and quantum wires is explained explicitly. The second part of Chapter 4 is devoted to the theory of electron-phonon coupling. The different coupling mechanisms in gallium arsenide structures are discussed where we concentrate on the interaction of the low-dimensional carriers with bulk acoustic phonons. For a detailed study of phonon confinement in semiconductor nanostructures the reader is referred to reviews by Leburton *et al.* (1993), Ridley (1997) or Stroscio and Dutta (2001). We demonstrate the large angle dependence of the matrix elements both for deformation potential and piezoelectric electron-phonon coupling and prove how isotropic phonon models simplify, but also falsify the results. The most prominent example of the latter statement is the deformation potential coupling of transverse acoustic (TA) phonons, which is forbidden within the isotropic approximation, but may give relevant contributions for phonon wavevector directions away from the symmetry axes of the crystal. Furthermore it is shown how the carrier confinement affects the electron-phonon interaction via the overlap integrals of the envelope functions.

By means of two very characteristic practical examples, we will verify in Chapters 5 and 6 our theoretical studies about the influence of acoustic anisotropy and carrier confinement on the results of phonon spectroscopy of low-dimensional electron systems. In the first case, the phonon induced electric current is considered and the low-dimensional electron system serves as phonon detector recording the quasimomentum focusing of ballistic phonons. In the second case, the energy relaxation of hot 2D electrons is studied and the low-dimensional electron system acts as the phonon source. Therefore the phonon-drag images of Chapter 5 and the time- and angle-resolved intensities of acoustic phonon emission in Chapter 6 are not only an ideal test of our theoretical models for phonon pulse propagation and carrier confinement, they also allow a deep insight in the fundamental process of electron-phonon coupling of low-dimensional electron systems.

A central topic of Chapter 5 is the development of a theoretical model for the drag current induced in low-dimensional electron systems by pulses of nonequilibrium acoustic phonons. Our model is based on a many-body approach and involves screening of the electron-phonon coupling by electron-electron interaction and the influence of carrier confinement in a consistent and natural way. We have also included the case of a magnetic field applied to the electrons. In a typical phonon-drag experiment the induced electric current is measured as a function of the phonon source position. The resulting phonon-drag patterns are therefore a convolution of the images of phonon quasimomentum focusing as discussed in Chapter 3 and the probability that a current is induced by the phonon modes hitting the detector. Based on our theory of phonon pulse propagation and the phonon-drag model we calculate the induced current in 2D electron and hole gases as a function of the source-detector geometry including the characteristic features of the phonon source term and the acoustic properties of the substrate material and compare it with corresponding experimental results, both at zero and finite magnetic field. The deformation potential and the piezoelectric electron-phonon interaction make contributions to the phonon-drag signal which depend in different manner on the phonon source position. This allows the separation of the coupling mechanisms and the determination of the relative strength of the coupling constants. We show how much the primary focusing images determined by the acoustic anisotropy of the substrate material are destroyed by cutoff conditions due to conservation rules for the electron-phonon scattering process and to carrier confinement as well as by the acoustic anisotropy of the electron-phonon matrix elements. The influence of the carrier confinement on the drag patterns plays an important role in the whole chapter and the sensitivity to the parameters of confinement potential is demonstrated explicitly for 2D and one-dimensional (1D) electron systems.

Chapter 6 is devoted to the important question of the energy relaxation by hot electrons in low-dimensional systems and what we can learn about this process by direct phonon emission experiments. A theory for the angle- and mode-resolved acoustic phonon emission by hot 2D electrons is presented which includes the effect of acoustic anisotropy, not only on phonon propagation, but also on electron-phonon coupling, as well as a full dynamic screening of the electron-phonon interaction within the finite-temperature random-phase approximation. This is in contrast to earlier calculations using isotropic phonon models for the coupling and often insufficient screening. Our approach also encloses realistic models for the carrier confinement allowing for finite potential walls. The results of acoustic phonon emission depend very strongly on the detector position and on the phonon polarization. This makes, by angle- and time-resolved measurements, direct information concerning the phonon wavevector and mode dependence of the emission process possible. By comparing the experimental results with the calculations one can identify the contributions of the different coupling mechanisms. It is also possible to observe the effects by energy and in-plane momentum conservation as well as by confinement, which cut off the phonon emission at certain frequencies and in certain directions. One of the surprising experimental results was “the mystery of the missing longitudinal mode” (Kent *et al.*, 1997a) for acoustic phonon emission close to the normal to the 2D electrons. This phenomenon was observed in experiments on gallium arsenide heterojunctions and could not be explained by all existing theories. We demonstrate that acoustic anisotropy and screening of deformation potential coupling account for this effect and check our theoretical results by comparing them with experimental results for various 2D systems and different emission angles. We also prove that commonly used approximations for the envelope wavefunctions or the electron-phonon matrix elements, which work quite well in theories of total electron relaxation or electron transport, fail in the theoretical analysis of direct phonon emission experiments. All this will underline the central message of this work: to show the vital importance of acoustic anisotropy and carrier confinement for the interpretation of phonon spectroscopy measurements on low-dimensional semiconductor structures.

At the end of this introductory part, two comments should be made concerning the terminology used in the present work. In a narrow sense, phonon spectroscopy encompasses the experimental methods that resolve the frequency of nonequilibrium phonon pulses, whereas phonon imaging is involved with continuous scanning over the propagation directions of the phonons and the time-of-flight technique deals with the time resolution of phonon pulses. All these methods are founded on the generation and detection of nonequilibrium phonon pulses and their analysis depending on frequency and/or wavevector direction and/or polarization. Therefore the term *phonon spectroscopy* will be used in a more general sense for the whole family of methods cited above. This is also supported by the fact, that the mentioned methods are often combined. The second comment affects the correct characterization of the dimensionality of our low-dimensional systems. Carrier confinement plays a large role. Therefore it is important to emphasize that if speaking about 2D or 1D electron systems throughout this work we always have in mind (as long as not explicitly excluded) quasi-2D or quasi-1D systems.

Finally, the question of the concretely considered low-dimensional semiconductor systems has to be commented on. Apart from few exceptions in Chapters 2 and 3 all calculations and discussions in this work refer to gallium arsenide/aluminium arsenide structures. Due to their high electron mobility these structures are very interesting and are nowadays commonly used in the manufacture of advanced electronic and optoelectronic devices for wireless communication or satellite receivers. But of course it is possible to extend theory and experiment also to other low-dimensional semiconductor structures based for example on silicon or gallium nitride devices and to other substrate materials than gallium arsenide (see, e.g. Lehmann *et al.*, 2002b; Stanton *et al.*, 2003a).

Chapter 2

Phonon Spectroscopy and Phonon Imaging

In this chapter an introduction in the field of phonon spectroscopy is given. We explain the typical experimental methods like time-of-flight measurement or phonon imaging and their applications. In addition, we refer readers to Appendix A, where we have collected some information about the generation and detection of nonequilibrium phonons. The chapter concludes with a special section showing the impact of phonon spectroscopy on the study of low-dimensional electron systems.

2.1 The basis of phonon spectroscopy

Due to the direction-dependent elasticity of a crystalline solid the propagation of phonons is characterized by anisotropic phonon velocities. Even in a highly symmetric crystal like the zinc-blende cubic GaAs the angular variation in phase velocity, governed by the fourth-rank stiffness tensor, is nearly 30% (see e.g. Table 3.1 on page 24). A remarkable consequence of this (yet moderate) anisotropy is that the phonon group velocity, and with it the phonon energy propagation, are not collinear to the phonon wavevector. An anisotropic channelling of phonons with immense variations in ballistic heat flux is the result. By contrast, the thermal conductivity is usually governed by a second rank tensor which for cubic crystals implies isotropic propagation of heat. The different behaviour occurs due to the diffusive nature of phonon propagation in the case of ordinary heat conductivity. At room temperatures, phonons scatter frequently and the mean free path of the phonons is much shorter than the crystal dimensions. Therefore heat flow is diffusive or quasi-diffusive[1] instead of ballistic. However, when the temperature is decreased, the mean free path of the phonons increases rapidly. At temperatures of only a few degrees Kelvin, much lower than the Debye temperature, the density of thermal (equilibrium) phonons is low and the probability of interaction of them with the (few) nonequilibrium phonons in the pulse is negligible. The resulting mean free path is in the millimeter range and therefore comparable to crystal dimensions. Supposing now that the mean free path of the phonons is longer than the distance between phonon source and detector and that the duration of the heat pulse is much shorter than the phonon transit time, the phonon propagation is ballistic and it is possible to resolve the phonon flux both temporally and spatially. This is caused by the different propagation velocities for different phonon polarizations and by the different propagation directions. Thus, other than establishing a steady-state heat current, as done in thermal conductivity experiments, phonon spectroscopy is based on the generation and detection of short nonequilibrium phonon pulses and their highly anisotropic (nearly) ballistic propagation.

---

[1] Quasi-diffusive phonon propagation is realized if additionally to elastic scattering phonon decay through anharmonic interaction is present (Kazakovtsev and Levinson, 1978; Bron *et al.*, 1982).

The first heat pulse experiment was performed by von Gutfeld and Nethercot (1964) on single-crystalline quartz and sapphire rods, respectively. A short duration (100 ns) electrical current pulse was applied to a small metallic strip evaporated on one face of the crystal. The current burst generated a heat pulse and thereby a nonequilibrium distribution of phonons in the sample. On the opposite face of the crystal a phonon detector in form of a thin alloyed superconducting film was evaporated, whose resistance was sensitive to temperature changes. Fig. 2.1 shows a typical setup for such a heat pulse experiment. At low temperatures a large part of the generated phonons travelled ballistically and so it was possible to observe several sharp pulses in the detector signal at times corresponding to the travel times of the unscattered longitudinal and two transverse modes. The technique in the experiment of von Gutfeld and Nethercot was somewhat similar to the known pulse measurements of the attenuation of microwaves except that the phonons in the heat pulse experiment had a much higher frequency, were incoherent and not monochromatic. In the following decades the idea of a heat pulse experiment was modified and extended to several new kinds of solid state spectroscopy. Nevertheless the experiments may be classified into two main types of techniques, the time-of-flight and the phonon imaging technique, which often are also combined. A precondition for all types of experiments of phonon spectroscopy is the ability

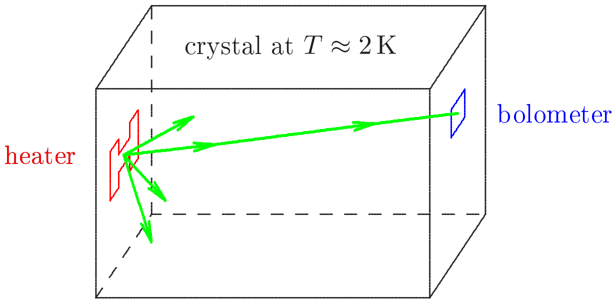

Figure 2.1: Typical setup for a heat pulse experiment.

to generate and detect nonequilibrium phonons. Therefore, a short review of existing and prospective phonon sources and detectors is given in Appendix A. Unlike in other spectroscopic methods (e.g. with photons), phonons must be generated inside the solid.

2.2 Typical experiments and their application

2.2.1 Time-of-flight spectroscopy

In time-of-flight spectroscopy short pulses of nonequilibrium phonons generated on one side of a sample are detected as a function of time on the opposite side. The 'time of flight' for a phonon to traverse the sample and with it the phonon group velocity can be directly measured by this technique. Typical results of time-of-flight experiments are plotted in the Figs. 2.2 and 2.3. Sharp ballistic signals corresponding to different polarized acoustic phonon modes (LA - longitudinal acoustic, FTA - fast transverse acoustic and STA - slow transverse acoustic) are followed by long tails due to scattered phonons. The signal onset occurs at the time given by the thickness of the crystal divided by the group velocity for the phonons of the highest velocity. The amplitude of the signal is a measure for the energy carried by the phonons incident on the detector. The relative magnitudes of the peaks depend strongly on the crystallographic arrangement of the phonon source and the detector as illustrated for the FTA phonon pulse in Fig. 2.3. Phonon focusing, extensively discussed in Chapter 3, and polarization-dependent scattering processes (Shields *et al.*, 1989; Ramsbey *et al.*, 1992) are the reason for this behaviour.

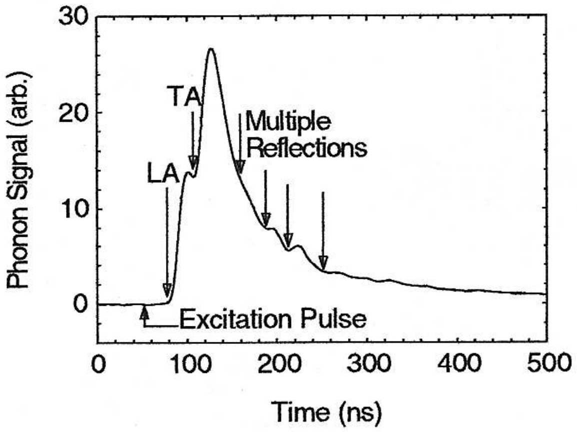

Figure 2.2: Heat pulse signal in 6H-SiC at a crystal temperature of $\simeq 2\,\mathrm{K}$. The bolometer is directly opposite the phonon source along the $c-$axis, the distance is 0.4 mm. The arrival of LA and TA phonons is marked. The fast and slow TA branches here are degenerate. Also marked are the signals arising from multiple reflections across the substrate. (From Stanton, Kent, and Lehmann, 2003a.)

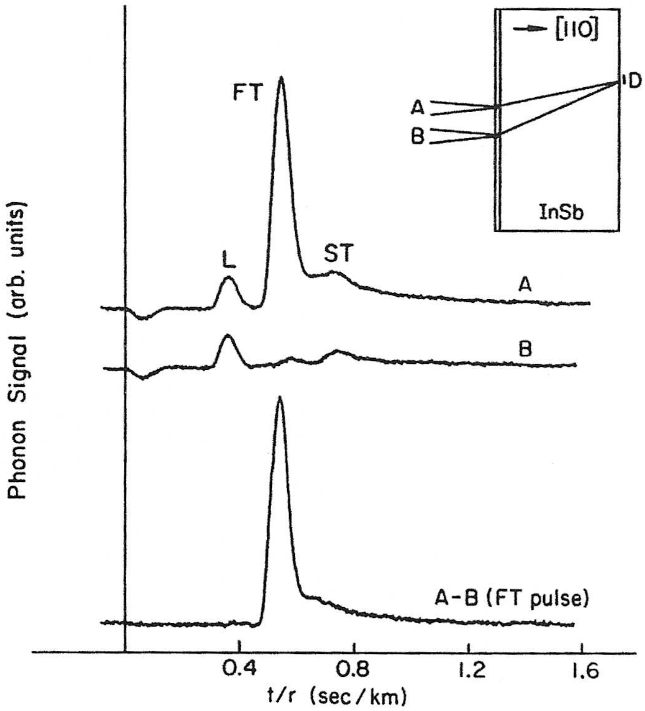

Figure 2.3: Heat pulse signal in InSb detected by a PbTl tunnel junction (430 GHz onset) for two different phonon source positions. As the phonon beam is slightly translated, dramatic changes in the FTA signal (here marked by FT) are seen, due to phonon focusing. A subtraction of the two traces shows only the FTA pulse with a long tail attributed to phonons scattered in the bulk. (From Hebboul and Wolfe, 1989.)

The time-of-flight technique allows one to distinguish ballistic and diffusive heat propagation. Furthermore, the times of flight of the arriving heat pulses permit identification of phonons of different modes and wavevector directions due to their different group velocities. This is in contrast to ordinary thermal conductivity experiments where the phonon information is averaged over all modes and wavevector directions.

For a given detector direction the ratios of intensities of the different modes can be accurately determined. Such measurements have a large field of application. They are used to research the phonon-defect and phonon-electron scattering or to probe the electronic states of impurity ions (for a review see Wybourne and Wigmore, 1988). Important contributions have been made by the time-of-flight technique to the study of the electronic states and the confinement potential in semiconductor nanostructures or to the understanding of the electron-phonon interaction in low-dimensional electron systems (see the recent book by Challis, 2003, and the examples given in Section 2.3 and Chapter 6).

In addition to the time-dependent response of detectors sensitive to phonon energy, one can also study the time dependence of 'phonon anemometers', i.e. the time-dependence of phonon quasimomentum flux (Jasiukiewicz, Lehmann, and Paszkiewicz, 1991; Danilchenko *et al.*, 1999). Such a time-of-flight spectrography for phonon quasimomentum has become possible by measuring the temporal dependence of the phonon induced electric current (Stanton *et al.*, 2000) or of the phonon induced drag of excitons (Akimov *et al.*, 1994, and references therein).

2.2.2 Phonon imaging

The phonon imaging technique as implemented by Northrop and Wolfe (1979, 1980) has revolutionized phonon spectroscopy. It is based on the work of Hensel and Dynes (1977) and visualizes directly the dramatic anisotropy in the ballistic propagation of acoustic phonons mentioned at the beginning of this chapter. Hensel and Dynes have introduced angular scanning to heat pulse experiments by using a special shaped hemicylindrical Ge crystal. Heat pulses were generated by optical excitation of a metal film on the cylindrical surface. By rotation of the sample while the detector was fixed the angular distribution of phonon propagation could be measured. This technique was essentially modified by Northrop and Wolfe holding the sample in place and using a two-axis mirror deflection system for precise scanning of a laser beam across the surface of the crystal. Combined with a (small) fixed phonon detector on the opposite side of the crystal a two-dimensional map of the phonon intensity with high angular resolution (ca. 0.5° of arc) and wide angular coverage could be obtained. A similar technique, but applying a conventional scanning electron microscope for phonon generation was used by Eichele *et al.* (1982).

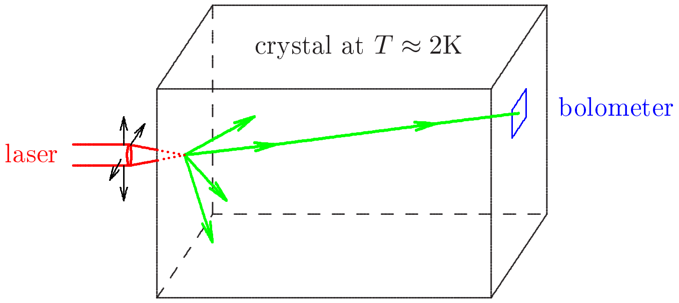

Figure 2.4: Typical setup for phonon imaging.

The common method to produce a phonon image (see Fig. 2.4) is therefore to raster scan the phonon source over the front face of the chosen sample and to record (the boxcar integrated) detector signal as a grey-tone image, where brightness is proportional to the heat flux. Fig. 2.5(a) shows such a typical experimental image for a germanium crystal as obtained in the early experiments of Northrop and Wolfe, whereas in Fig. 2.5(b) the corresponding pseudo three-dimensional (3D) representation of the image is depicted. The peaks identify maxima in the ballistic

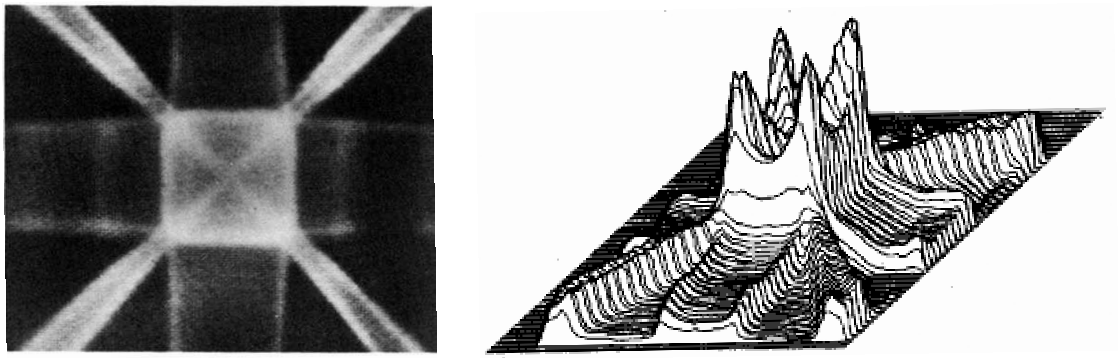
(a) (b)

Figure 2.5: (**a**) Image of the ballistic phonon intensities for Ge. Bright regions indicate a high phonon flux impinging on the (001) face of the crystal. From left to right the picture spans 50° in propagation direction with the [001] direction at the center of the pattern. The phonon source is at the center of the pattern on the opposing face of the crystal. (From Northrop and Wolfe, 1979.) (**b**) Pseudo-3D hidden-line representation of the image (a). (From Northrop and Wolfe, 1980.)

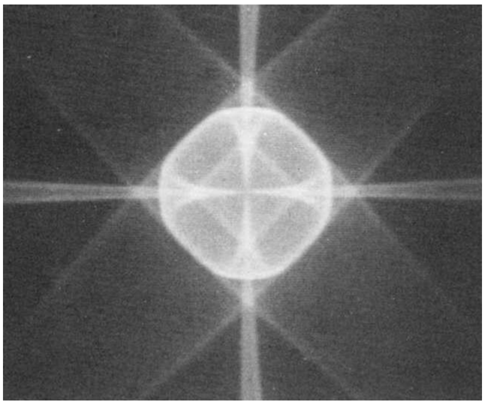

Figure 2.6: High-resolution phonon image of silicon. The center of the image corresponds to the [001] propagation direction. The width of the image is about 40° left to right. (From Shields *et al.*, 1993.)

phonon flux, but the absolute peak height depends, of course, also upon the solid angle subtended by the detector. Worth mentioning is also the good agreement with our numerical result on page 43, Fig. 3.8(a), for a cubic crystal with the same crystal orientation. The progress in angular resolution of experimental phonon images is demonstrated by Fig. 2.6, here for the example of ballistic phonon propagation in silicon.

Variations of the phonon imaging technique have been developed by employing a fixed phonon source and imaging the arriving flux. This has been done by using, for example, spatially selective large area tunnel junction detectors (Schreyer *et al.*, 1984), spatially resolving CdS detectors (Kent *et al.*, 1990) or superconducting strip bolometers (Kent *et al.*, 1995) or by utilizing excitonic photoluminescence for a time- and space-resolved optical detection of nonequilibrium phonons (Akimov *et al.*, 1977; Ramsbey *et al.*, 1994). The problem is that in most of the methods with spatially scannable detectors the resolution of the phonon images is rather limited. An impressive technique was applied by Eisenmenger (1980) who produced direct visual phonon images of Ge and Si crystals. In this technique the propagating nonequilibrium phonons are absorbed in a superfluid ^{4}He film covering the crystal surface. Along the directions of high phonon flux the local rise in temperature leads due to the fountain effect to an increase in the He film thickness which is imaged by a camera (Fig. 2.7).

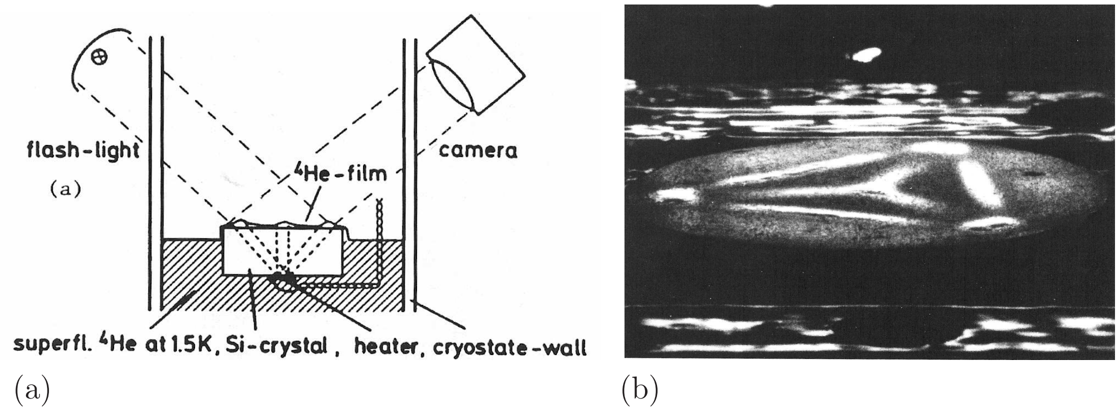

(a) (b)

Figure 2.7: (**a**) Experimental setup to observe the ballistic phonon propagation in crystals by the fountain effect of superfluid ^{4}He. (**b**) Phonon image obtained by a photograph of a Si surface covered with a superfluid ^{4}He film. The center of the image corresponds to the [111] propagation direction. The He film is thickest where the heat flux is greatest. (From Eisenmenger, 1980.)

A new field has been opened in the area of phonon imaging by using 2D semiconductor structures as phonon sources and phonon detectors (Karl *et al.*, 1988; Kent *et al.*, 1990; see also the review of Challis and Kent, 1994, and the references therein). An example is shown in Fig. 2.8(a), where an image of the phonon energy flux emitted by a 2D electron gas in a Si MOSFET is depicted (Challis *et al.*, 1990). A qualitative extension of phonon imaging was achieved with the imaging of the phonon-drag effect in low-dimensional electron systems first demonstrated by Karl *et al.* (1988) in GaAs/Al$_x$Ga$_{1-x}$As heterostructures (Fig. 2.8b).

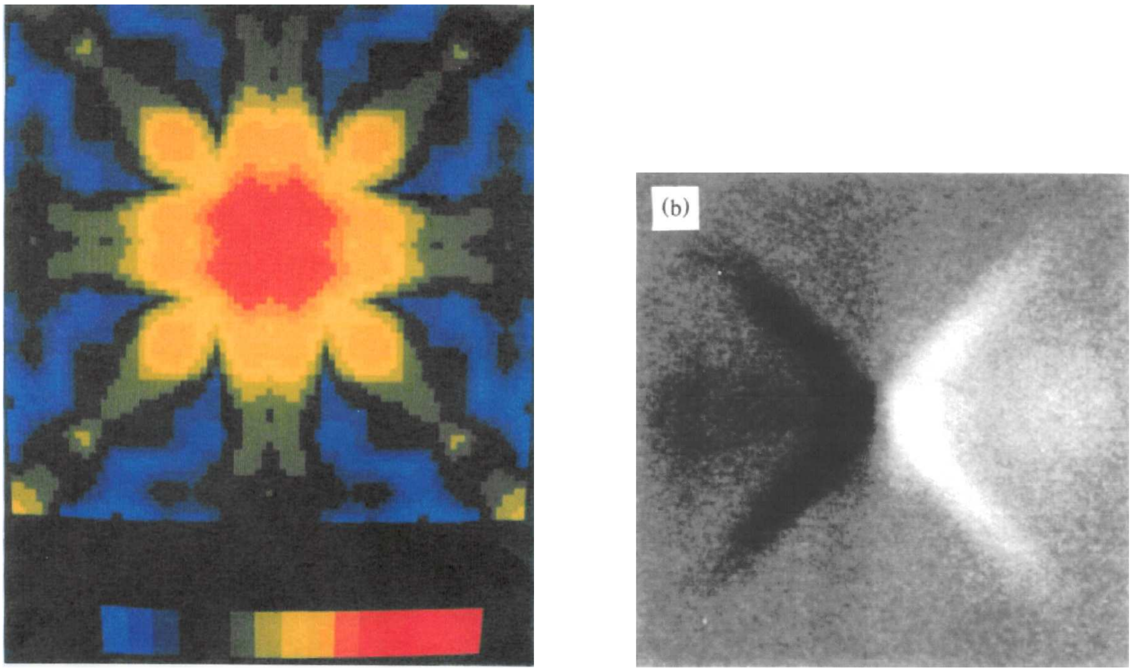

(a) (b)

Figure 2.8: Phonon images using 2D electron gases as phonon source and detector, respectively. (**a**) Image of the phonon energy flux emitted from a 2D electron gas in a Si MOSFET and obtained with an extended CdS bolometer. The phonon intensity is largely confined to a cone around the normal to the 2D electrons. (From Challis *et al.*, 1990.) (**b**) Phonon-drag pattern, where the voltage caused in a 2D electron gas by an incident ballistic phonon flux is measured as a function of phonon source position. Bright and dark areas correspond to positive and negative voltages, respectively. (From Karl *et al.*, 1988.)

With this technique not only the imaging of the phonon energy flux but also the imaging of phonon quasimomentum flux became possible (Jasiukiewicz, Lehmann, and Paszkiewicz, 1991). A detailed explanation of the images in Fig. 2.8 including a comparison with corresponding theoretical results will be given in Chapter 6 and Chapter 5, respectively.

If one considers the application of the phonon imaging technique, then at the beginning the study of phonon focusing and lattice dynamics in homogeneous materials was dominant. It was used as a sensitive experimental probe of the fundamental surfaces of constant energy for elastic waves in crystals and as a good testing ground for lattice dynamic models since a phonon image provides information on the dispersion relation for a broad range of directions, which is difficult to obtain by other methods, e.g. by inelastic neutron scattering (see the review by Wolfe, 1989). However, quite soon the experiments were also extended to investigate the coupling of phonons with impurities and defects, to image defect structures or to study the interaction of phonons with surfaces and interfaces. For example, by using several phonon detectors at different locations simultaneously stereoscopical imaging of defects became possible and with it 3D reconstructions of the defect distribution (Held *et al.*, 1989b). Phonon imaging has proved to be an effective method for the examination of phonon refraction at solid/solid interfaces (Höss *et al.*, 1990) and of reflection including mode conversion at surfaces (Every *et al.*, 1984; Northrop and Wolfe, 1984; Wichard and Dietsche, 1992). It is used to determine the frequency distribution of optically generated nonequilibrium acoustic phonons as well as to gauge the size and lifetime of phonon sources (Shields *et al.*, 1993; Msall and Wolfe, 2002). Other applications are the investigation of ferroelectric domain walls (Weilert *et al.*, 1993) and of superlattices (Hurley *et al.*, 1987, 1988; Tamura *et al.*, 1988; Tanaka *et al.*, 1998). An important field is the study of low-dimensional electron systems by phonon imaging, which will be subject of the subsequent sections and chapters.

Recently ballistic phonon images have been presented for superconducting niobium and lead, i.e. for single crystals of metal (Hauser *et al.*, 1999; Short and Wolfe, 2000). To overcome the strong electron-phonon interaction, the principal difficulty in observing the nonequilibrium phonon propagation in metals, phonons with energies less than twice the superconducting gap Δ have been used, because such phonons cannot break Cooper pairs. The experiments have demonstrated the capacity of ballistic phonon imaging as an angle-sensitive probe of the superconducting state.

A relatively new application of phonon imaging with high practical relevance is also the study of twist-bonded crystals (Msall *et al.*, 1999, 2000; Obata *et al.*, 2001). This has become possible by the technique of 'wafer direct bonding' (for a review see Gösele *et al.*, 1999), which creates an interface essentially free of phonon-scattering defects. For nonzero twist angles the resulting focusing patterns show structures which are not simply the bulk images weighted by the relative thickness of the bonded crystals. Since acoustic phonons due to their short wavelength ($\approx 10\,\mathrm{nm}$) are an extremely sensitive probe of the bond, unique information about the quality of the bonded interfaces seems to be possible. In addition, phonon measurements are a nondestructive method for testing the bond quality, in contrast to, for example, electron microscopy.

When discussing the use of phonon imaging, one should also mention the extension of the phonon imaging technique to the domain of ultrasonic frequencies (for a review see Every *et al.*, 1994; and Wolfe, 1998) and to surface acoustic waves (Kolomenskii and Maznev, 1993; Vines *et al.*, 1995a,b) including real-time imaging of coherent surface phonons (Wright *et al.*, 2002; Sugawara *et al.*, 2002).

2.3 Phonon spectroscopy and low-dimensional electron systems

Acoustic waves have an extremely low speed, about 10^{-5} of that of electromagnetic waves. Therefore their wavelength is much smaller than the wavelength of electromagnetic waves of the same frequency and is comparable to the important length scales in low-dimensional electron systems such as confinement lengths or the Fermi wavelength. Furthermore, acoustic bulk phonons couple very effectively to low-dimensional electron systems via deformation potential interaction and (for crystals without a center of inversion symmetry) via piezoelectric interaction (see Section 4.2). This effective coupling, together with the fact that *both* energy and wavevector of acoustic phonons are of the same order of magnitude as the typical electronic excitations, causes the situation that, on the one hand, low-dimensional electron systems are very useful devices for the generation and detection of ballistic phonons, and that, on the other hand, phonon spectroscopy is a powerful tool for the study of low-dimensional carrier systems. Reducing the dimensionality of electron systems, the available phase space for electron scattering is restricted and makes the electron-phonon interaction more sensitive to effects like the broadening of the phonon dispersion relation (Senna and Das Sarma, 1993) or the acoustic anisotropy (Lehmann *et al.*, 2000, 2002a, and references therein). The latter effect will be illustrated in detail in the following chapters. Phonon spectroscopy can provide details about the process and the type of the electron-phonon interaction including the angle and mode dependence. This is, as already mentioned in the introduction, of high interest for the performance of nanostructure semiconductor devices. However, ballistic phonons are also applied to spectroscopically probe the electronic states in low-dimensional electron systems and to obtain information about the electron density or the confinement potential.

The first direct experimental phonon studies on low-dimensional electron systems were carried out by Hensel *et al.* (1981, 1983a). Ballistic phonons generated by a short laser pulse propagate through a 2D electron gas and are detected by a superconducting bolometer after reflection from the Si-SiO$_2$ interface of a Si MOSFET (and from the 2D electron gas, see Hensel *et al.*, 1983b). The aim of the experiment was to observe the absorption of the ballistic phonons by the 2D electron gas, but the result was modulated by an interference between phonon amplitudes backscattered from the inversion layer and phonons reflected from the Si-SiO$_2$ interface. Restricted also by the limited spectral resolution, particularities provoked by the reduced dimensionality of the electron system could not be seen clearly. Later Chin *et al.* (1984) used the 2D electron gas of a GaAs single heterojunction as a heater and observed an unusual temporal spectrum, which differed from those obtained by 3D electrons. Qualitatively similar effects were also noted in the phonon emission from a 2D hole gas (Chin *et al.*, 1985).

The first experiment with a spectral analysis of the phonons emitted by a 2D electron gas was reported by Rothenfusser *et al.* (1986). Using superconducting tunnel junctions as phonon detectors, the $2k_{\mathrm{F}}$ cutoff in the frequency spectrum of the emitted phonons could be observed. As a consequence of the lower dimensionality of the electrons Rothenfusser *et al.* also demonstrated the dependence of the emitted phonon spectra on the emission angle.

A new step was taken with the study of 2D electron systems in high magnetic fields by methods of phonon spectroscopy. It was commenced with the phonon absorption experiment of Eisenstein *et al.* (1986), who measured the effect of the phonon pulses on the conductivity of the electrons in the integral quantum Hall regime. Besides the expected dependence of the absorption probability on the magnetic field and the Landau level index also the drop in absorption could be observed if the phonon wavevector (more precisely its component parallel to the 2D system) was larger than the inverse of the magnetic length (for an explanation see also Section 5.2, page 85). Over the years the investigation of the dissipative processes in the quantum Hall effect (QHE) regime has proved to be a very useful application of phonon spectroscopy (Challis *et al.*, 1990; Cooper *et al.*, 1995; Roshko *et al.*, 1998, 1999). In the QHE state, the power is dissipated at low temperatures as photons (far infrared radiation) but, primarily, as acoustic phonons. As the infrared contribution is less than 10^{-4} (for GaAs heterostructures) and 10^{-6} (for Si MOSFETs) of the total emission (Roshko *et al.*, 1998, and references therein) the study of the acoustic phonon emission is a very preferable approach. Phonon imaging based on the phonoconductivity technique has been applied in the integer QHE regime to analyse the edge states and to probe the local electron concentration in the 2D devices (McKitterick *et al.*, 1994). With much success phonon spectroscopy has also been used to investigate 2D systems in the incompressible fractional QHE state (Mellor *et al.*, 1995, 1999; Zeitler *et al.*, 1999; Devitt *et al.*, 2000, 2002). In combination with theoretical studies concerning the absorption of nonequilibrium phonon pulses by a 2D incompressible electron liquid (Benedict *et al.*, 1999; Benedict and Hills, 2001; Apalkov and Portnoi, 2002), valuable information about the gap and the dispersion curve of the low-lying collective excitations (magnetorotons) and the process of magnetoroton-phonon scattering could be extracted. Similar angle-resolved (Mellor *et al.*, 1999) and time-resolved (Zeitler *et al.*, 1999; Schulze-Wischeler *et al.*, 2001) ballistic phonon studies have been performed for systems with even denominator filling factors such as $\nu = 1/2$ and $\nu = 3/2$ where the 2D electron system can be regarded as a Fermi sea of composite fermions. There is a hope that phonon spectroscopy can provide information about phonon scattering of composite fermions, in particular about the unsolved question of the magnitude of the phonon wavevector cutoff (see Zelakiewicz *et al.*, 2000; Zelakiewicz and Gramila, 2002).

In 1D or better quasi-1D electron systems the angular and frequency dependence of the emission and absorption of (bulklike) acoustic phonons is expected to be much different from the 3D or 2D case and should depend quite sensitively on the parameters of the confinement potential (Shik and Challis, 1993; Totland *et al.*, 1999; Lehmann *et al.*, 2000). Phonon spectroscopy measurements using the phonoconductivity technique have therefore been applied to nonballistic and short ballistic quantum wires in GaAs to investigate directly the electron-phonon interaction (Naylor *et al.*, 1996; Kent *et al.*, 1997b, 2000). In all measurements, large oscillations of the phonon induced changes in conductivity have been observed if the wire width was varied (shifting of the position of Fermi energy relative to the bottom of the subbands). This is in agreement with corresponding theoretical studies (Blencowe and Shik, 1996, 1999; Lehmann *et al.*, 2000) and shows the ability of the method to probe the electronic states of 1D systems.

Chapter 3

Phonon Pulse Propagation and Phonon Images

After the introduction to the field of phonon spectroscopy we now focus our attention on the theoretical basis of the discussed experiments and phenomena. We explain the theoretical background of phonon focusing and develop a mathematical description of the phonon pulse propagation in anisotropic media. The presented formalism allows us to calculate focusing images of phonon energy and phonon quasimomentum for different types of phonon sources including the realistic geometrical arrangement of phonon source and detector. The resulting formulae for the nonequilibrium phonon distribution as a function of time and of detector position, derived in this chapter, are the phonon input to theory and interpretation of phonon spectroscopy studies on low-dimensional electron systems (as presented in Chapters 5 and 6). The chapter concludes with a short description of the used numerical methods and with examples of the results of focusing images for different crystal symmetries.

3.1 Acoustic phonons in anisotropic solids

In a semi-classical picture within the harmonic approximation the crystal dynamics is analysed in terms of a linear combination of $3pN$ normal modes of vibration, where N is the number of primitive cells and p the number of atoms per primitive cell. In doing so a normal mode is described in the form of a travelling wave $\mathbf{u_q} e^{i(\mathbf{qr}-\omega t)}$, where $\mathbf{q}$ is the wavevector, $\omega_\mathbf{q}$ is the (angular) frequency of the wave and $\mathbf{u_q}$ is the amplitude of vibration. There exist $3p$ normal mode frequencies for each wavevector $\mathbf{q}$. Three branches, the acoustic modes, have frequencies that tend to zero for $q \to 0$, whilst $3(p-1)$ branches, the optical modes, have a nonzero value of frequency for $q \to 0$. The energies of a normal mode are quantized. The quantum of energy $\hbar\omega_\mathbf{q}$ of a normal mode is associated with an elementary excitation called phonon.

At low temperatures, and this is the regime we are interested in, most of the phonons excited in a solid are confined to acoustic modes with small wavevectors far away from the Brillouin zone edge. Their wavelength $2\pi/q$ is much larger than the atomic spacing. Therefore details of the crystal structure can be ignored and the propagation of such long-wavelength acoustic phonons is very successfully described by the standard elasticity theory of continuum.

Within the framework of the linear theory of elasticity the equations of motion for a small volume element are

$$\varrho \frac{\partial^2}{\partial t^2} u_i = \sum_j \frac{\partial \sigma_{ij}}{\partial x_j} \ , \tag{3.1}$$

where ϱ is the mass density of the medium and u_i is the i-Cartesian component of the displacement $\mathbf{u}(\mathbf{r}, \mathbf{t})$ of the volume element at point $\mathbf{r}$ and time t. The right hand side of (3.1) describes the i-component of the forces applied to the surfaces of this volume element divided by its volume. It is expressed by the elements σ_{ij} of the stress tensor. The latter is related by Hooke's law to the strain tensor S_{kl} via a set of elastic constants C_{ijkl}

$$\sigma_{ij} = \sum_{kl} C_{ijkl} S_{kl} \ . \tag{3.2}$$

The fourth-rank tensor C is also called the stiffness tensor.[1] The component S_{kl} of the strain tensor is defined by the change of the displacement component u_k with change of position $\mathbf{r}$ in l-direction and inversely

$$S_{kl} = \frac{1}{2} \left(\frac{\partial u_k}{\partial x_l} + \frac{\partial u_l}{\partial x_k} \right) \ . \tag{3.3}$$

Because both σ_{ij} (due to vanishing torques) and S_{ij} (by definition) are symmetric, C_{ijkl} is invariant to interchange of i and j or k and l. In addition, $C_{ijkl} = C_{klij}$ holds. The number of independent elastic constants C_{ijkl} is further reduced by the crystal symmetry. For a cubic crystal there are only three independent components of C_{ijkl}, namely

$$C_{3333} = C_{2222} = C_{1111} \ , \ C_{2233} = C_{1133} = C_{1122} \ , \ C_{1212} = C_{1313} = C_{2323} \tag{3.4}$$

or in Voigt's notation C_{11}, C_{12} and C_{44}, respectively. They are required to satisfy the thermodynamic constraints $C_{44} > 0$, $C_{11} + 2C_{12} > 0$ and $C_{11} > |C_{12}|$. Using Hooke's law we obtain from (3.1) the elastic wave equation

$$\varrho \frac{\partial^2}{\partial t^2} u_i = \sum_{j,k,l} C_{ijkl} \frac{\partial^2 u_l}{\partial x_j \partial x_k} \ . \tag{3.5}$$

---

[1] In piezoelectric media, such as GaAs, Hooke's law has to be modified by the stiffening of the lattice due to the piezoelectric effect. However, in GaAs the influence of this piezoelectric stiffening can be neglected (Every and McCurdy, 1987).

Further we assume plane-wave solutions of the form

$$\mathbf{u}(\mathbf{r},t) = u_{\mathbf{q}}\,\mathbf{e}_{\mathbf{q}}\,e^{i(\mathbf{q}\mathbf{r}-\omega_{\mathbf{q}}t)}\ , \tag{3.6}$$

where the wavevector $\mathbf{q}$ is given and the frequency $\omega_{\mathbf{q}}$ and the polarization vector $\mathbf{e}_{\mathbf{q}}$ are to be determined. Setting $\omega = cq$ with c as the phase velocity yields the Christoffel equation

$$\sum_l \left(c^2\,\delta_{il} - \frac{1}{\varrho}\sum_{jk} C_{ijkl}\,\hat{q}_j\,\hat{q}_k \right) (\mathbf{e}_{\mathbf{q}})_l = 0\,. \tag{3.7}$$

This is a set of three equations to determine the eigenvalues of the matrix $D_{il} = \frac{1}{\varrho}\sum_{jk} C_{ijkl}\,\hat{q}_j\,\hat{q}_k$, where $\hat{q}_i = q_i/q$, i.e. $\hat{q}_i$ denotes the direction cosines of the wavevector $\mathbf{q}$.[2] The corresponding eigenvectors of the matrix D_{il} are the polarization vectors $\mathbf{e}$. Because D_{il} depends only on the direction of $\mathbf{q}$, the phase velocity is independent of the magnitude of the $\mathbf{q}$-vector and the dispersion relation $\omega = c_{\hat{\mathbf{q}}}\,q$ is linear. The secular determinant of Eq. (3.7) is a polynomial of third degree in c^2. Therefore, for a given direction $\hat{\mathbf{q}}$ three solutions exist which are associated with three modes with mutually orthogonal polarizations $\mathbf{e}_{\hat{\mathbf{q}},\lambda}$. Here the index λ identifies the modes. One of these modes is usually quasi-longitudinal in character and the other two are quasi-transverse. However, only under the condition $C_{11} - C_{12} = C_{44}$, i.e. for an elastically isotropic medium, it is always possible to choose the eigenvectors $\mathbf{e}_{\hat{\mathbf{q}},\lambda}$ such that one solution is purely polarized in the direction of $\hat{\mathbf{q}}$ and the other two are polarized perpendicular to $\hat{\mathbf{q}}$. For an anisotropic crystalline solid the polarization vector is only strictly parallel or perpendicular to the wavevector when $\hat{\mathbf{q}}$ is directed along a symmetry axis of the crystal. In general, for these directions the secular equation factors into a term linear in c^2 and into a term quadratic in c^2. For all other directions this is normally not the case. Therefore, it is more practical to label the modes according to their phase velocity as slow (quasi) transverse (STA), fast (quasi) transverse (FTA), and (quasi) longitudinal acoustic mode (LA), where $c_{\hat{\mathbf{q}},\lambda=\mathrm{STA}} \leq c_{\hat{\mathbf{q}},\lambda=\mathrm{FTA}} < c_{\hat{\mathbf{q}},\lambda=\mathrm{LA}}$.[3] For compactness the adjunct *quasi* is usually omitted, even though the polarization vectors are not purely longitudinal or transverse. Nevertheless, the existence of *quasi* transverse and *quasi* longitudinal modes has large consequences for the character and the angle dependence of electron-acoustic phonon coupling as it will be illustrated in Section 4.2.4.

Table 3.1 shows the phase velocities of GaAs for wavevectors along the symmetry directions, i.e. for the pure longitudinal and transverse modes. It is still clear

---

[2] Apart from a factor q^2, the matrix D_{il} is for the continuum limit identical to the dynamical matrix used in the microscopic theory of lattice dynamics.

[3] We will omit here a slightly *exotic*, but thermodynamically allowed domain of the elastic parameter space in which the transverse phase velocities may exceed the longitudinal phase velocity in some direction. Examples are certain Sm-Y-S intermediate valence compounds and Mn-Ni-C alloys. For details see Every and Stoddart (1985); Paszkiewicz and Pruchnik (2001).

Table 3.1: Phase velocities for a cubic lattice of GaAs. (From Blakemore, 1982.)

Direction of $\hat{\mathbf{q}}$	Polarization	Phase velocity	c in $10^3\ \frac{\mathrm{m}}{\mathrm{s}}$
[100]	[100]	$c_{\mathrm{LA}} = \sqrt{\frac{C_{11}}{\varrho}}$	4.7
	in (100) plane	$c_{\mathrm{STA}} = c_{\mathrm{FTA}} = \sqrt{\frac{C_{44}}{\varrho}}$	3.3
[110]	[110]	$c_{\mathrm{LA}} = \sqrt{\frac{C_{11}+C_{12}+2C_{44}}{2\varrho}}$	5.3
	[001]	$c_{\mathrm{FTA}} = \sqrt{\frac{C_{44}}{\varrho}}$	3.3
	$[1\bar{1}0]$	$c_{\mathrm{STA}} = \sqrt{\frac{C_{11}-C_{12}}{2\varrho}}$	2.5
[111]	[111]	$c_{\mathrm{LA}} = \sqrt{\frac{C_{11}+2C_{12}+4C_{44}}{3\varrho}}$	5.4
	in (111) plane	$c_{\mathrm{STA}} = c_{\mathrm{FTA}} = \sqrt{\frac{C_{11}-C_{12}+C_{44}}{3\varrho}}$	2.8

from the quoted speeds that the acoustic properties of GaAs are highly anisotropic. For an isotropic solid there should be only one constant velocity for the longitudinal modes and one for all transverse modes, independent of the direction of the wavevector. For arbitrary $\hat{\mathbf{q}}$ it is common to present the results of the secular equation of (3.7) in form of a *slowness surface*, i.e. as a polar plot of the magnitude $c_{\hat{\mathbf{q}},\lambda}^{-1}$ of the slowness vector

$$\mathbf{s}_{\hat{\mathbf{q}},\lambda} = c_{\hat{\mathbf{q}},\lambda}^{-1}\hat{\mathbf{q}}\,. \tag{3.8}$$

Similarly to the Fermi surface for electron transport in metals, the slowness surface plays a central role in phonon transport phenomena like phonon focusing or surface reflection and transmission. It contains all information about the solutions $c_{\hat{\mathbf{q}},\lambda}$ for all directions $\hat{\mathbf{q}}$ and thereby the information about the energy spectrum. Since the dispersion relation is linear, for long-wavelength acoustic modes the slowness surface has the same shape like the surfaces of constant energy or frequency in $\mathbf{q}$-space (for a chosen polarization λ) and differs only in a scaling factor.

For a given crystal the slowness surface is a centrosymmetric surface of three sheets corresponding to the three different polarization modes.[4] In case of an elastically isotropic medium all three sheets are concentric spheres. The innermost corresponds to the longitudinal mode and the outer two being degenerate are connected with the two transverse modes. For cubic symmetry all three sheets remain separated except along the fourfold $\langle 100\rangle$ axes where the transverse sheets make smooth contact (touch tangentially), and except along the threefold $\langle 111\rangle$ axes where the transverse sheets meet canonically at a point (Every, 1981). As the characteristic equation for the slowness surface is of the 6-th order in s, the inner sheet of the slowness surface must be completely convex. Fig. 3.1 shows the intersection of the three sheets of the GaAs slowness surface with the (010) and $(\bar{1}10)$ plane, respectively, demonstrating the tangential (a) and canonical (b) contact of the TA surfaces. A 3D plot of the slowness surface for the STA phonons in GaAs is presented in Fig. 3.2. Regions of the surface with convex, concave and saddle topology are apparent. The boundaries of these regions are parabolic lines, i.e. lines of vanishing Gaussian curvature. They are the reason for caustics in the phonon images as will be discussed in the next section. As already mentioned,

---

[4] The symmetry of the slowness surface can be higher than that of the crystal itself. For example, all slowness surfaces are centrosymmetric, even for crystals lacking a center of inversion.

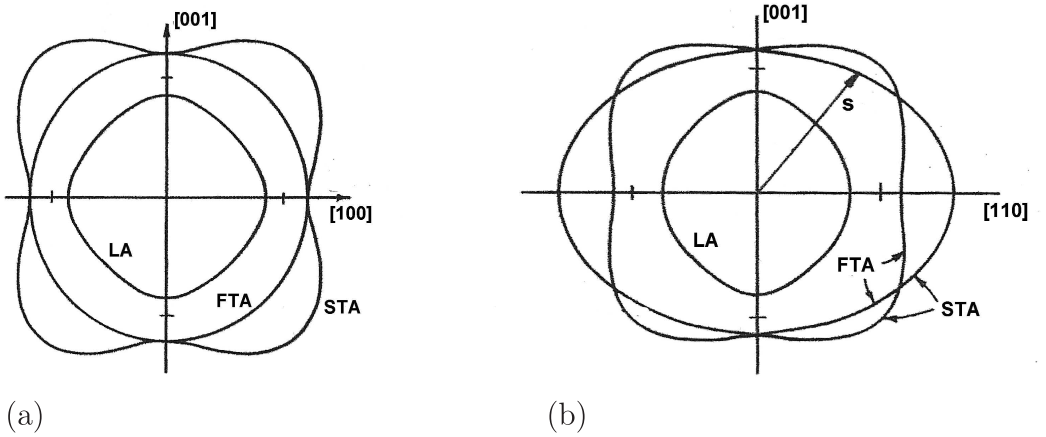

Figure 3.1: (**a**) Intersection of the slowness surface for GaAs with the (010) plane. (**b**) Intersection with the $(\bar{1}10)$ plane. The marks on the axes correspond to a slowness of $s = 2.5 \cdot 10^{-4}\,\mathrm{s/m}$. (From Auld, 1973.)

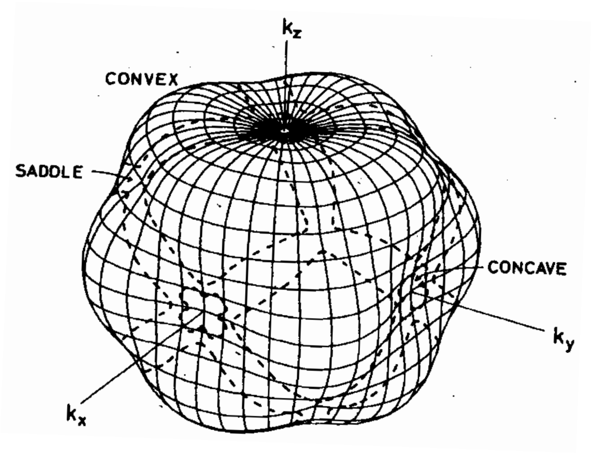

Figure 3.2: 3D plot of the STA sheet of the GaAs slowness surface showing the convex, concave and saddle topology. (From Tamura and Harada, 1985.)

the LA slowness surface is convex, however for GaAs it bulges out in the $\langle 100 \rangle$ directions and is flattest in the $\langle 111 \rangle$ directions.

An important consequence of the elastic anisotropy is that the group velocity $\mathbf{v}_{\mathbf{q},\lambda}$, which is normal to the surfaces of constant frequency (and therefore for long-wavelength acoustic modes also to the slowness surface), is generally not parallel to the wavevector $\mathbf{q}$. It follows from the definition of the group velocity

$$\mathbf{v}_{\mathbf{q},\lambda} = \nabla_{\mathbf{q}}\, \omega_{\mathbf{q},\lambda} \tag{3.9}$$

that for long-wavelength acoustic modes the group velocity $\mathbf{v}_{\mathbf{q},\lambda}$ depends just like the phase velocity only on $\hat{\mathbf{q}}$. Thus the group velocity and the slowness vector are related by means of

$$\mathbf{s}_{\hat{\mathbf{q}},\lambda} \cdot \mathbf{v}_{\hat{\mathbf{q}},\lambda} = 1 \; . \tag{3.10}$$

The direction of the group velocity indicates the direction of the vibrational energy propagation. Thus, the fact that nonspherical slowness surfaces are flatter in some directions than in others leads to concentrated energy flux along those directions. A measure for the energy flux in a particular direction is the *phonon enhancement* or *focusing factor* $\mathcal{A}$. It is depicted as the ratio of energy flux propagating in a given direction of an elastically anisotropic medium compared to the corresponding energy flux in an elastically isotropic medium. The phenomena of phonon focusing play a central role in the phonon spectroscopy. Therefore we will discuss this feature in a separate section.

By standard theory of field quantization, the normal mode displacement $\mathbf{u}_{\mathbf{q},\lambda}$ can be expressed in terms of the phonon annihilation and creation operators, $b_{\mathbf{q},\lambda}$ and $b^{+}_{\mathbf{q},\lambda}$, respectively. The general solution for the displacement field $\mathbf{u}(\mathbf{r})$ follows from (3.6) by a sum over all wavevectors $\mathbf{q}$ and all polarizations λ

$$\mathbf{u}(\mathbf{r}) = \sum_{\mathbf{q},\lambda} \left(\frac{\hbar}{2\varrho\, \omega_{\mathbf{q},\lambda} V_{\mathrm{c}}} \right)^{\frac{1}{2}} \left(\mathbf{e}_{\hat{\mathbf{q}},\lambda} b_{\mathbf{q},\lambda} e^{i\mathbf{qr}} + \mathbf{e}^{*}_{\hat{\mathbf{q}},\lambda} b^{+}_{\mathbf{q},\lambda} e^{-i\mathbf{qr}} \right) \;, \tag{3.11}$$

where V_{c} is the volume of the crystal. Later, this form will be used when calculating the electron-phonon coupling (cf. Section 4.2).

3.2 Phonon focusing

The study of phonon focusing in crystals dates back to 1969, when Taylor *et al.* (1969) noted in their heat pulse experiments that the relative intensities of longitudinal and transverse phonon pulses in crystals depend very strongly on the phonon propagation direction. They proposed that acoustic anisotropy accounts for the observed differences in the phonon propagation behaviour. The simplest way of illustrating the basic idea of phonon focusing is by means of a hypothetical slowness surface as presented in Fig. 3.3. The phonon energy flux is directed along the group velocity perpendicular to the slowness surface. Thus it is evident that

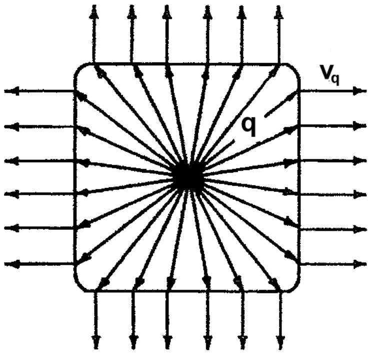

Figure 3.3: Intersection of a hypothetical slowness surface. An isotropic distribution of wavevectors results in a highly anisotropic distribution of phonon energy flux. (Adapted from Wolfe, 1998.)

where the curvature of the slowness surface is small or even zero (like in the figure), the group velocity vectors are most strongly concentrated in that direction, and consequently the vibrational energy flux in that direction is greatest. The conclusion is that an isotropic distribution of wavevectors in $\mathbf{q}$-space results in a strongly anisotropic distribution of energy flux in real space. To determine the energy flux in a given direction it is therefore necessary to calculate the phonon enhancement in that direction, i.e. the appropriate focusing factor. In a seminal paper Maris (1971) pointed out that the focusing factor $\mathcal{A}$ can be quantified by the ratio of the solid angles in wavevector space and group velocity space

$$\mathcal{A}_{\hat{\mathbf{q}},\lambda} = \frac{\mathrm{d}\Omega_{\mathbf{q}}}{\mathrm{d}\Omega_{\mathbf{v}}} \,. \tag{3.12}$$

Here $\mathrm{d}\Omega_{\mathbf{q}}$ is the solid angle subtended by an infinitesimal cone of wavevectors (or equivalent slowness vectors) about the direction $\hat{\mathbf{q}}$ and $\mathrm{d}\Omega_{\mathbf{v}}$ is the solid angle by their associated group velocity vectors. An intersection of a real slowness surface for STA modes and the intersection of the corresponding group velocity surface are shown in Figs. 3.4(a) and 3.4(b), respectively. Inflection points (parabolic lines) on the slowness surface, e.g. the point corresponding to the vector labelled 1 in Fig. 3.4(a), are the reason for the folds in the group velocity surface of Fig. 3.4(b). A constant real space solid angle $\Delta\Omega_{\mathbf{v}}$ in Fig. 3.4(b) (as subtended for example by a phonon detector) correlates to one or more $\mathbf{q}$-space solid angles of different magnitude and direction. The real space direction represented by the hatched area involves a defocusing of the phonon flux ($\mathcal{A}_{\hat{\mathbf{q}},\lambda} < 1$), while the $\Delta\Omega_{\mathbf{v}}$ indicated by the

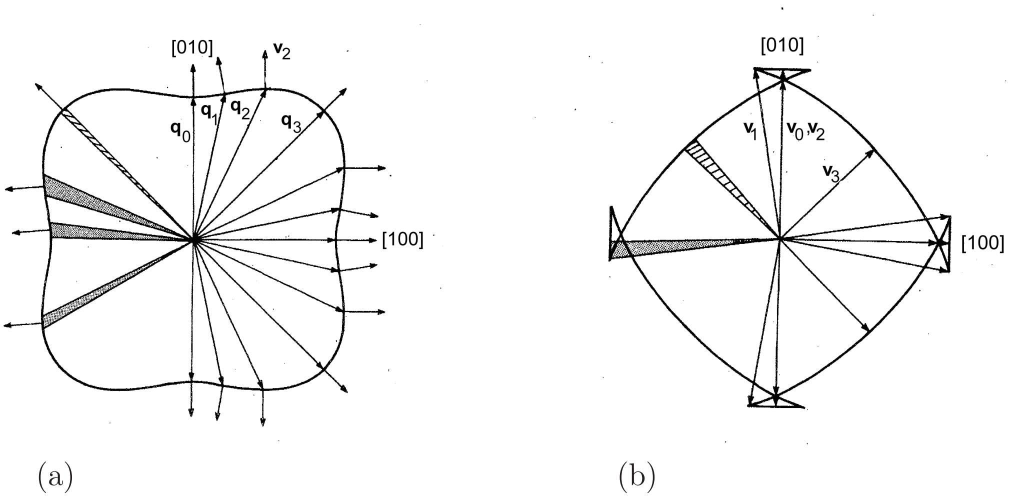

Figure 3.4: (**a**) Intersection of the slowness surface for the STA modes of a cubic crystal. The group velocity $\mathbf{v}_{\hat{\mathbf{q}}}$ for a given $\hat{\mathbf{q}}$ is normal to this curve. (**b**) Corresponding group velocity surface constructed by connecting the tails of all possible group velocity vectors. The numbered vectors $\mathbf{v}$ correlate to the numbered vectors $\mathbf{q}$ of figure (a). We note the cuspidal edges along the $\langle 100 \rangle$ directions in (b) where several wavevectors $\mathbf{q}$ correspond to the same group velocity and the mathematical functions involved are many valued. (Curves from Northrop and Wolfe, 1980.)

filled area in the $\mathbf{v}$-space maps into three different $\hat{\mathbf{q}}$-directions leading to strong phonon focusing ($\mathcal{A}_{\hat{\mathbf{q}},\lambda} > 1$).

The direct relation of $\mathcal{A}_{\hat{\mathbf{q}},\lambda}$ to the local geometric characteristics of the slowness surface (Lax and Narayanamurti, 1980) is an elegant way to calculate the focusing factor. For this purpose a small area element $\mathrm{d}A = \mathrm{d}u_1 \mathrm{d}u_2$ on the slowness surface is treated, where the two length elements $\mathrm{d}u_1$ and $\mathrm{d}u_2$ are chosen along two (perpendicular) directions of principal curvature of the slowness surface. Since the group velocity $\mathbf{v}$ is normal to the slowness surface, $\mathrm{d}A$ subtends a solid angle in the $\mathbf{v}$-space

$$\mathrm{d}\Omega_{\mathbf{v}} = \frac{\mathrm{d}A}{\rho_{u_1}\rho_{u_2}} \, , \tag{3.13}$$

where ρ_{u_1} and ρ_{u_2} are the principal radii of curvature associated with the curved segments $\mathrm{d}u_1$ and $\mathrm{d}u_2$ of the slowness surface. On the other hand $\mathrm{d}A$ subtends a solid angle in the $\mathbf{q}$-space

$$\mathrm{d}\Omega_{\mathbf{q}} = \frac{\mathrm{d}A \; (\hat{\mathbf{v}} \cdot \hat{\mathbf{q}})}{s^2} \, , \tag{3.14}$$

where $(\hat{\mathbf{v}} \cdot \hat{\mathbf{q}})$ takes the projection of $\mathrm{d}A$ (which is directed along $\mathbf{v}$) along $\mathbf{q}$. The ratio of Eq. (3.14) to Eq. (3.13) yields the focusing factor (3.12)

$$\mathcal{A}_{\hat{\mathbf{q}},\lambda} = \frac{(\hat{\mathbf{v}}_{\hat{\mathbf{q}},\lambda} \cdot \hat{\mathbf{q}})}{s^2_{\hat{\mathbf{q}},\lambda} \, |\Gamma^{(1)}_{\hat{\mathbf{q}},\lambda} \Gamma^{(2)}_{\hat{\mathbf{q}},\lambda}|} = \frac{c^3_{\hat{\mathbf{q}},\lambda}}{v_{\hat{\mathbf{q}},\lambda} \, |\Gamma_{\hat{\mathbf{q}},\lambda}|} \; , \tag{3.15}$$

where $\Gamma^{(1)}_{\hat{\mathbf{q}},\lambda}$ and $\Gamma^{(2)}_{\hat{\mathbf{q}},\lambda}$ are the principal curvatures (inverse radii) of the slowness surface, which can be positive or negative, and $\Gamma_{\hat{\mathbf{q}},\lambda} = \Gamma^{(1)}_{\hat{\mathbf{q}},\lambda} \Gamma^{(2)}_{\hat{\mathbf{q}},\lambda}$ is the corresponding Gaussian curvature. This Gaussian curvature can be directly determined from the second-order derivatives of the phase velocity (Every and McCurdy, 1987).

If we consider once more the STA slowness of Fig. 3.2 then a closed line l_{c} obtained by a central section of this surface has a fourfold geometry. The line l_{c} contains several inflection points (points on parabolic lines). At these points the Gaussian curvature of the slowness surface vanishes, thus it follows from (3.15) that the focusing factor $\mathcal{A}_{\hat{\mathbf{q}},\lambda}$ is mathematically infinitive (yet integrable) and corollary sharp singularities in phonon flux (caustics) occur along these directions. Therefore, parabolic lines on the slowness surface produce folds in the group velocity surface and the projection of these folds onto the experimental plane causes the caustics in the phonon images. A systematic study of slowness surface topology of cubic crystals, the associated caustic patterns and its impact on heat pulse images is given by Paszkiewicz and Pruchnik (1996) and Wolfe (1998) and references therein.

The determination of the phonon flux intensity for all real space directions is not trivial. The reason is that there is no one to one mapping from the directions in the slowness surface to the directions in real space. All points on the slowness surface which contribute to the flux in a particular direction have to be found numerically and the respective focusing factor has to be calculated for each of them. And this procedure has to be repeated for each individual real space direction. Our method of calculation and the resultant energy and quasimomentum focusing patterns will be illustrated in the next sections.

3.3 Kinetic description of phonon pulses

3.3.1 Kinetic equation for phonon pulses

In the typical experiments of phonon spectroscopy pulsed beams of nonequilibrium phonons are used. The pulse is generated on one face of the crystal or as in the case of phonons emitted by low-dimensional electron systems in a small crystal region. The emanated phonons, which for spatially inhomogeneous states are represented by wave packets, move through the crystalline media with the group velocity $\mathbf{v}_{\mathbf{q},\lambda}$. They carry the energy $\hbar\omega_{\mathbf{q},\lambda}$ and the quasimomentum $\hbar\mathbf{q}$. The experiments are performed at ambient temperatures much below the Debye temperature Θ_{D} (for

GaAs: $\Theta_\mathrm{D} \approx 345\,\mathrm{K}$) and on massive perfect specimens. As thermal phonons are practically frozen out, the injected phonons propagate almost ballistically. Using the suitable boxcar time-gate one can eliminate the contributions of boundary scattering or separate the contribution of a given phonon polarization. For most experiments the relevant phonon frequencies, $f = \omega/2\pi$, are below 1 THz, i.e. in the nondispersive, long-wavelength acoustic regime.

Under the conditions described above one can assume that the phonons propagate in a half-space filled with an anisotropic medium. The nonequilibrium state of the phonon gas at time t may be described by the deviation $\delta n(\mathbf{q}, \lambda, \mathbf{r}, t)$ of the phonon density distribution function from the equilibrium (Planck) distribution function $n_0(\hbar\omega/k_\mathrm{B}T)$. This deviation function obeys the Boltzmann-Peierls kinetic equation with a source term $Z(\mathbf{q}, \lambda, \mathbf{r}, t)$ (cf. Jasiukiewicz, Lehmann, and Paszkiewicz, 1992; Jasiukiewicz, Paszkiewicz, and Lehmann, 1994)

$$\left[\frac{\partial}{\partial t} + \mathbf{v}_{\hat{\mathbf{q}},\lambda}\nabla + \tau^{-1}(\omega_{\mathbf{q},\lambda})\right] \delta n(\mathbf{q}, \lambda, \mathbf{r}, t) = Z(\mathbf{q}, \lambda, \mathbf{r}, t)\ . \tag{3.16}$$

The even in very pure crystals remaining low probability of phonon scattering events, e.g. by isotopes, we take (in lowest order) into account by the relaxation time $\tau(\omega)$. Paszkiewicz and Wilczynski (1995) have studied the influence of isotopic disorder on the phonon pulse propagation in detail. For isotope scattering in GaAs the relaxation time is given in the low frequency limit by $\tau^{-1}(\omega) = 7.38\cdot 10^{-42}(\omega/2\pi)^4\,\mathrm{s}^{-1}$ (Tamura, 1984). The source term Z can be generally written in the form

$$Z(\mathbf{q}, \lambda, \mathbf{r}, t) = \frac{\Theta(t)\Theta(\Delta t - t)}{\Delta t} \int \mathrm{d}^3 r_\mathrm{s}\, g_\mathrm{s}(\mathbf{r}_\mathrm{s})\, \delta(\mathbf{r} - \mathbf{r}_\mathrm{s})\, \gimel_\mathrm{s}(\hat{\mathbf{q}}, \omega_{\mathbf{q},\lambda}, \mathbf{e}_{\hat{\mathbf{q}},\lambda})\ . \tag{3.17}$$

Here we assume that at time $t = 0$ a short phonon pulse of duration Δt will be generated at point $\mathbf{r}_\mathrm{s}$. The geometrical arrangement and the extension of the phonon source are described by the function $g_\mathrm{s}(\mathbf{r}_\mathrm{s})$. The phonon distribution $\gimel_\mathrm{s}(\hat{\mathbf{q}}, \omega_{\mathbf{q},\lambda}, \mathbf{e}_{\hat{\mathbf{q}},\lambda})$ of the source term may depend on the wavevector direction, the frequency (or equivalently the phase velocity) and the polarization vector. This is for example the case with a hot 2D electron gas as phonon source (as described in Chapter 6) where the emitted phonon flux depends not only on phonon wavevector and frequency but by the electron-phonon matrix elements also on the polarization vector.

For a *point source* at point $\mathbf{r}_0$ emitting in the upper half-space ($z \geq 0$) with *uniform angular distribution* of phonon wavevectors it holds

$$g_\mathrm{s}(\mathbf{r}_\mathrm{s}) = \delta(\mathbf{r}_\mathrm{s} - \mathbf{r}_0) \quad \text{and} \quad \gimel_\mathrm{s}(\hat{\mathbf{q}}, \omega_{\mathbf{q},\lambda}, \mathbf{e}_{\hat{\mathbf{q}},\lambda}) = \tilde{\gimel}_\mathrm{s}(\omega_{\mathbf{q},\lambda}, \mathbf{e}_{\hat{\mathbf{q}},\lambda})\, \Theta\big((\mathbf{v}_{\hat{\mathbf{q}},\lambda})_z\big)\ . \tag{3.18}$$

For a *monochromatic point source* the function $\tilde{\gimel}_\mathrm{s}$ reduces further to

$$\tilde{\gimel}_\mathrm{s}(\omega_{\mathbf{q},\lambda}, \mathbf{e}_{\hat{\mathbf{q}},\lambda}) \sim \frac{4\pi^2 c^3_{\hat{\mathbf{q}},\lambda}}{3V_\mathrm{c}\omega^2_{\mathbf{q},\lambda}}\, \delta(\omega_{\mathbf{q},\lambda} - \omega_0)\ , \tag{3.19}$$

while for a *Planckian source*

$$\tilde{\gimel}_{\mathrm{s}}(\omega_{\mathbf{q},\lambda}, \mathbf{e}_{\hat{\mathbf{q}},\lambda}) \sim \frac{1}{e^{\hbar\omega_{\mathbf{q},\lambda}/k_{\mathrm{B}}T_{\mathrm{s}}} - 1} \; , \tag{3.20}$$

where T_{s} is the source temperature. The choice of the functions (3.18) and (3.20) is equivalent to assuming a point heat source which has been used in most of the published calculations of focusing images, drag patterns etc. However, in reality the phonon sources are for example a locally heated planar metal film, a superconducting tunnel junction or a hot 2D electron gas. Therefore we have to take into account the finite dimensions of the phonon source by an appropriate choice of the function $g_{\mathrm{s}}(\mathbf{r}_{\mathrm{s}})$.

A more realistic model of a phonon source in form of a locally heated metal overlayer is discussed in Appendix A.3. For a heater of temperature T_{s} located at $z = 0$ with surface area A_{s} and pulse duration Δt the phonon distribution of the source term is (cf. Eq. (A.13))

$$\gimel_{\mathrm{s}}(\hat{\mathbf{q}}, \omega_{\mathbf{q},\lambda}, \mathbf{e}_{\hat{\mathbf{q}},\lambda}) = \Delta t \, \frac{A_{\mathrm{s}}}{V_{\mathrm{c}}} \, \frac{(\mathbf{v}_{\hat{\mathbf{q}},\lambda})_z}{e^{\hbar\omega_{\mathbf{q},\lambda}/k_{\mathrm{B}}T_{\mathrm{s}}} - 1} \, \Theta\Big(\frac{c_{\hat{\mathbf{q}},\lambda}}{c^{\mathrm{s}}_{\lambda}} - \sin\vartheta_{\mathbf{q}}\Big) \, \Theta\big((\mathbf{v}_{\hat{\mathbf{q}},\lambda})_z\big) \; , \tag{3.21}$$

where c^{s}_{λ} is the phonon phase velocity in the (polycristalline) heater film and $\vartheta_{\mathbf{q}}$ is the phonon wavevector angle in the crystal measured from the normal of the interface. Eq. (3.21) shows clearly that even in the case of an isotropic crystal, the *incident* phonon wavevector distribution in the crystal has by the z-component of the group velocity a cosine-dependence. In other words, not the phonon wavevectors are uniformly distributed, but rather their components parallel to the interface have a uniform distribution in the plane of the interface.

Furthermore we see from Appendix A.3, Eq. (A.11), that for a metal film radiator as phonon source the ratio of emitted LA to emitted TA phonons into the same crystal solid angle depends on the phonon phase velocities in the crystal (for the limiting case of an isotropic solid inversely proportional to the square of the corresponding velocities). This is caused by the fact that the size of the contributing solid angles in the heater is different for different modes. In contrast, the ratio of the total number of LA to TA phonons emitted into the crystal depends on the phonon phase velocities in the heater material because the critical angles for phonon transmission into the crystal, equal to $\arcsin(c_{\hat{\mathbf{q}},\lambda}/c^{\mathrm{s}}_{\lambda})$, are mode dependent.

The kinetic equation (3.16) can be readily solved using Green's function technique. For the universal source term (3.17) the solution which satisfies the boundary conditions is

$$\begin{aligned}\delta n(\mathbf{q},\lambda,\mathbf{r},t) &= \gimel_{\mathrm{s}}(\hat{\mathbf{q}},\omega_{\mathbf{q},\lambda},\mathbf{e}_{\hat{\mathbf{q}},\lambda})\int\limits_0^{\Delta t}\frac{\mathrm{d}t'\Theta(t-t')}{\Delta t}\,e^{-\frac{t-t'}{\tau(\omega_{\mathbf{q},\lambda})}} \\ &\quad\times\int\mathrm{d}^3r_{\mathrm{s}}\,g_{\mathrm{s}}(\mathbf{r}_{\mathrm{s}})\,\delta\big(\mathbf{r}-\mathbf{r}_{\mathrm{s}}-\mathbf{v}_{\hat{\mathbf{q}},\lambda}(t-t')\big) \qquad (3.22)\\ &= \gimel_{\mathrm{s}}(\hat{\mathbf{q}},\omega_{\mathbf{q},\lambda},\mathbf{e}_{\mathbf{q},\lambda})\int\mathrm{d}^3r_{\mathrm{s}}\,g_{\mathrm{s}}(\mathbf{r}_{\mathrm{s}})\,\frac{\Theta\Big(t-\frac{|\mathbf{r}-\mathbf{r}_{\mathrm{s}}|}{v_{\hat{\mathbf{q}},\lambda}}\Big)\,\Theta\Big(\frac{|\mathbf{r}-\mathbf{r}_{\mathrm{s}}|}{v_{\hat{\mathbf{q}},\lambda}}+\Delta t-t\Big)}{\Delta t} \\ &\quad\times\frac{e^{-\frac{|\mathbf{r}-\mathbf{r}_{\mathrm{s}}|}{\tau(\omega_{\mathbf{q},\lambda})\,v_{\hat{\mathbf{q}},\lambda}}}}{|\mathbf{r}-\mathbf{r}_{\mathrm{s}}|^2\,v_{\hat{\mathbf{q}},\lambda}\sin\vartheta_{\mathbf{v}_{\hat{\mathbf{q}},\lambda}}}\,\delta\big(\vartheta_{\mathbf{v}_{\hat{\mathbf{q}},\lambda}}-\vartheta_{\mathbf{r}-\mathbf{r}_{\mathrm{s}}}\big)\,\delta\big(\varphi_{\mathbf{v}_{\hat{\mathbf{q}},\lambda}}-\varphi_{\mathbf{r}-\mathbf{r}_{\mathrm{s}}}\big)\ . \qquad (3.23)\end{aligned}$$

In the last step we have expressed the vectors $\mathbf{v}_{\hat{\mathbf{q}},\lambda}$ and $(\mathbf{r}-\mathbf{r}_{\mathrm{s}})$ by their polar coordinates. Finally, we have to replace the polar angles $\vartheta_{\mathbf{v}_{\hat{\mathbf{q}},\lambda}}$ and $\varphi_{\mathbf{v}_{\hat{\mathbf{q}},\lambda}}$ of the group velocity by the corresponding angles of the wavevector $\mathbf{q}$

$$\delta\big(\vartheta_{\mathbf{v}_{\hat{\mathbf{q}},\lambda}}-\vartheta_{\mathbf{r}-\mathbf{r}_{\mathrm{s}}}\big)\,\delta\big(\varphi_{\mathbf{v}_{\hat{\mathbf{q}},\lambda}}-\varphi_{\mathbf{r}-\mathbf{r}_{\mathrm{s}}}\big)=\frac{\sin\vartheta_{\mathbf{v}_{\hat{\mathbf{q}},\lambda}}}{\sin\vartheta_{\mathbf{q}}}\,\mathcal{A}_{\hat{\mathbf{q}},\lambda}\sum_i\delta\big(\vartheta_{\mathbf{q}}-\vartheta_i^{\lambda}\big)\,\delta\big(\varphi_{\mathbf{q}}-\varphi_i^{\lambda}\big)\ , \tag{3.24}$$

where we have made use of the definition of the phonon focusing factor $\mathcal{A}_{\hat{\mathbf{q}},\lambda}$ (cf. Eq. (3.12)). Here $\vartheta_i^{\lambda},\varphi_i^{\lambda}$ are the polar angles of the solutions $\hat{\mathbf{q}}_i^{\lambda}$ of the equation $\hat{\mathbf{v}}_{\hat{\mathbf{q}},\lambda}=(\mathbf{r}-\mathbf{r}_{\mathrm{s}})/|\mathbf{r}-\mathbf{r}_{\mathrm{s}}|$. That is, all phonon wavevectors $\mathbf{q}_i^{\lambda}$ possessing a phonon group velocity $\mathbf{v}_{\hat{\mathbf{q}}_i^{\lambda},\lambda}$ directed along $(\mathbf{r}-\mathbf{r}_{\mathrm{s}})$ contribute to the sum over i. In general the solutions $\mathbf{q}_i^{\lambda}$ and their number will be different for each polarization λ.

The nature of solution (3.23) is obvious. It describes the collimated propagation of a phonon pulse in which the initial pulse shape remains unchanged. Kwok (1968) was the first who introduced a heating source (prescribing a phonon production rate) in the Boltzmann equation for heat pulse propagation and studied the phonon propagation far from thermal equilibrium and before the distribution relaxes to one which can be characterized by local thermodynamic variables like temperature and phonon drift velocity and their derivatives. In a series of papers we have extended this theory to finite linear dimensions and different types of phonon source and, most notably, have included the effects of acoustic anisotropy (Jasiukiewicz, Paszkiewicz, and Lehmann, 1994 and references therein). The phonon density distribution function in the form of (3.23) together with (3.24) allows a very global discussion of phonon pulse propagation for arbitrary phonon sources including the study of energy and quasimomentum focusing, phonon absorption, phonon drag etc.

3.3.2 Phonon energy and quasimomentum flux

From the phonon density distribution function we obtain the density of phonon energy flux

$$\mathbf{j}^{\lambda}(\mathbf{r},t) = \sum_{\mathbf{q}} \hbar\omega_{\mathbf{q},\lambda}\,\mathbf{v}_{\hat{\mathbf{q}},\lambda}\,\delta n(\mathbf{q},\lambda,\mathbf{r},t) \tag{3.25}$$

and the tensorial components of quasimomentum current density

$$\pi^{\lambda}_{\alpha\beta}(\mathbf{r},t) = \sum_{\mathbf{q}} \hbar q_{\alpha}(\mathbf{v}_{\hat{\mathbf{q}},\lambda})_{\beta}\,\delta n(\mathbf{q},\lambda,\mathbf{r},t)\ . \tag{3.26}$$

For a small detector surface at point $\mathbf{r}$ with surface area ΔA_{d} and normal $\hat{\mathbf{n}}_{\mathrm{d}}$ the energy per unit time of phonons with polarization λ falling onto it is

$$P^{\lambda}(\mathbf{r},t) = \Delta A_{\mathrm{d}} \sum_{\mathbf{q}} \hbar\omega_{\mathbf{q},\lambda}\,\mathbf{v}_{\hat{\mathbf{q}},\lambda}\cdot\hat{\mathbf{n}}_{\mathrm{d}}\,\delta n(\mathbf{q},\lambda,\mathbf{r},t)\ . \tag{3.27}$$

For a small strip of area ΔA_{d} and normal $\hat{\mathbf{n}}_{\mathrm{d}}$ directed along $\hat{\mathbf{e}}_{\eta}$ (see Fig. 3.5), the η-component of quasimomentum of all phonons with polarization λ falling onto the strip is

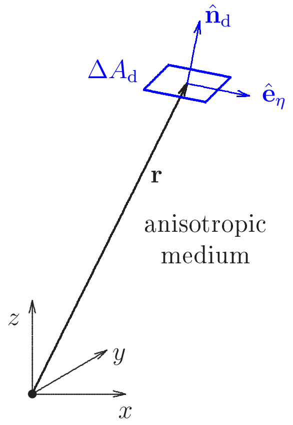

Figure 3.5: Geometrical arrangement of the detector surface for the phonon quasimomentum flux.

$$\Pi^{\lambda}_{\eta}(\mathbf{r},t) = \Delta A_{\mathrm{d}} \sum_{\mathbf{q}} \hbar q_{\eta}\,\mathbf{v}_{\hat{\mathbf{q}},\lambda}\cdot\hat{\mathbf{n}}_{\mathrm{d}}\,\delta n(\mathbf{q},\lambda,\mathbf{r},t)\ . \tag{3.28}$$

In the phonon imaging experiments one is often interested in the time-integrated projections of the density currents measuring the total energy $E(\mathbf{r})$ and the total quasimomentum component $Q_{\eta}(\mathbf{r})$ falling onto the surface of a suitable detector at position $\mathbf{r}$

$$E(\mathbf{r}) = \sum_\lambda \int_0^\infty \mathrm{d}t\, P^\lambda(\mathbf{r},t)\,, \tag{3.29}$$

$$Q_\eta(\mathbf{r}) = \sum_\lambda \int_0^\infty \mathrm{d}t\, \Pi_\eta^\lambda(\mathbf{r},t)\,. \tag{3.30}$$

For a monochromatic point source at $\mathbf{r} = 0$ it follows directly from the above equations that

$$E(\mathbf{r}) = \hbar\omega_0 \, \frac{\Delta A_\mathrm{d}\, \hat{\mathbf{n}}_\mathrm{d}\cdot\hat{\mathbf{r}}}{2\pi r^2}\, \frac{1}{3} \sum_\lambda \sum_i \mathcal{A}_{\hat{\mathbf{q}}_i^\lambda,\lambda}\, e^{-r/v_{\hat{\mathbf{q}}_i^\lambda,\lambda}\tau(\omega_0)}\,, \tag{3.31}$$

$$Q_\eta(\mathbf{r}) = \hbar\omega_0 \, \frac{\Delta A_\mathrm{d}\, \hat{\mathbf{n}}_\mathrm{d}\cdot\hat{\mathbf{r}}}{2\pi r^2}\, \frac{1}{3} \sum_\lambda \sum_i (\hat{\mathbf{e}}_\eta \cdot \mathbf{s}_{\hat{\mathbf{q}}_i^\lambda,\lambda})\, \mathcal{A}_{\hat{\mathbf{q}}_i^\lambda,\lambda}\, e^{-r/v_{\hat{\mathbf{q}}_i^\lambda,\lambda}\tau(\omega_0)} \tag{3.32}$$

(Jasiukiewicz, Lehmann, and Paszkiewicz, 1992), where the $\hat{\mathbf{q}}_i^\lambda$ are the solutions of the equation $\hat{\mathbf{v}}_{\hat{\mathbf{q}},\lambda} = \hat{\mathbf{r}} \equiv \mathbf{r}/r$. Both functions, $E(\mathbf{r})$ and $Q_\eta(\mathbf{r})$, contain the information about the local Gaussian curvature of the slowness surface via the focusing factor $\mathcal{A}_{\hat{\mathbf{q}},\lambda}$. Additionally, the function $Q_\eta(\mathbf{r})$ measures, by its dependence on s_η, the linear dimensions of the slowness surface. To illustrate the sensitivity of $E(\mathbf{r})$ and $Q_\eta(\mathbf{r})$ on the detector position $\mathbf{r}$ and to show the strong anisotropy of the phonon fluxes, the numerical results of Eqs. (3.31) and (3.32), the so called energy and quasimomentum focusing images, will be presented at the end of this chapter (Figs. 3.8–3.11). Energy focusing patterns can be directly measured by detectors sensitive to energy, i.e. bolometers, but also by low-dimensional electron systems as detector. Quasimomentum focusing patterns play the key role in the interpretation of the phonon-drag patterns of low-dimensional electron systems (Jasiukiewicz, Lehmann, and Paszkiewicz, 1991, 1992). The latter will be discussed in detail in Chapter 5. It is also very interesting that there exist crystalline directions for which the quasimomentum flux on the surface $\Pi_\eta^\lambda(\mathbf{r},t)$ changes its sign with time (Danilchenko *et al.*, 1999).

For a quantitative comparison with experimental results, the assumptions of an isotropic point-like monochromatic phonon source and a point detector used in the derivation of (3.31) and (3.32) are insufficient. Therefore, we have included in our theory and in the numerical programs the effects of finite source and detector size as well as different frequency and wavevector dependencies of the phonon emitter. In the case of a locally heated metal film as the phonon source, see Eq. (3.21), we obtain for the power incident on a detector surface in a plane at distance d from the crystal/source interface and with x-coordinates (y-coordinates) between

x_1 and x_2 (y_1 and y_2)

$$\begin{aligned} P_{\mathrm{d}}^{\lambda}(t) &= \iint\limits_{\mathrm{A_d}} \mathrm{d}x\mathrm{d}y \int \mathrm{d}z\, \delta(z-d)\ \mathbf{j}^{\lambda}(\mathbf{r},t)\cdot\mathbf{e}_z \\ &= \frac{\pi(k_{\mathrm{B}}T_{\mathrm{s}})^4}{120\hbar^3} \iint\limits_{A_{\mathrm{s}}} \mathrm{d}x_{\mathrm{s}}\mathrm{d}y_{\mathrm{s}} \int\limits_{x_1-x_{\mathrm{s}}}^{x_2-x_{\mathrm{s}}} \int\limits_{y_1-y_{\mathrm{s}}}^{y_2-y_{\mathrm{s}}} \frac{\mathrm{d}x'\mathrm{d}y'}{{r'}^2} \frac{d^2}{{r'}^2} \sum_i \mathcal{A}_{\hat{\mathbf{q}}_i^{\lambda},\lambda} \frac{v_{\hat{\mathbf{q}}_i^{\lambda},\lambda}}{(c_{\hat{\mathbf{q}}_i^{\lambda},\lambda})^3} \\ &\quad \times\ \Theta\Big(\frac{c_{\hat{\mathbf{q}}_i^{\lambda},\lambda}}{c_{\lambda}^{\mathrm{s}}} - \sin\vartheta_{\mathbf{q}_i^{\lambda}}\Big)\, \Theta\Big(\frac{r'}{v_{\hat{\mathbf{q}}_i^{\lambda},\lambda}} + \Delta t - t\Big)\, \Theta\Big(t - \frac{r'}{v_{\hat{\mathbf{q}}_i^{\lambda},\lambda}}\Big)\ , \end{aligned} \tag{3.33}$$

where $\mathbf{r}' = \mathbf{r} - \mathbf{r}_{\mathrm{s}}$ (see Fig. 3.6). For simplicity we have neglected the isotope scattering in the above expression. From (3.33) it follows for the normalized total energy of phonons with polarization λ falling onto the detector surface

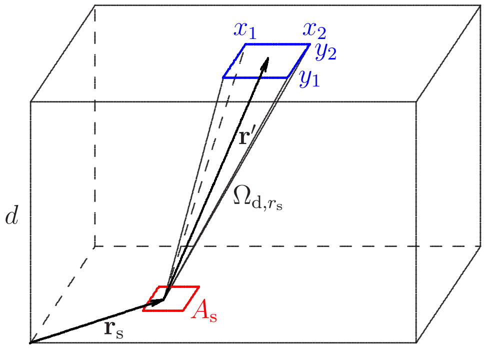
x_1
x_2
y_2
y_1
$\mathbf{r}'$
$\Omega_{\mathrm{d},r_{\mathrm{s}}}$
d
A_{s}
$\mathbf{r}_{\mathrm{s}}$

Figure 3.6: Phonons are generated at a point $\mathbf{r}_{\mathrm{s}}$ inside the source area A_{s}. They propagate ballistically and are detected at a point $\mathbf{r} = \mathbf{r}' + \mathbf{r}_{\mathrm{s}}$ with x between x_1 and x_2, y between y_1 and y_2 and $z = d$. The solid angle $\Omega_{\mathrm{d},r_{\mathrm{s}}}$ is subtended by the vectors of the corners of the detector surface.

$$\begin{aligned} \frac{E_{\mathrm{d}}^{\lambda}}{P_{\mathrm{s}}\,\Delta t} =& \frac{1}{\frac{1}{(c_{\mathrm{LA}}^{\mathrm{s}})^2} + \frac{2}{(c_{\mathrm{TA}}^{\mathrm{s}})^2}} \iint\limits_{A_{\mathrm{s}}} \frac{\mathrm{d}x_{\mathrm{s}}\mathrm{d}y_{\mathrm{s}}}{A_{\mathrm{s}}} \frac{1}{\pi} \int\limits_{\Omega_{\mathrm{d},r_{\mathrm{s}}}} \mathrm{d}\Omega_{\mathbf{r}'} \cos\vartheta_{\mathbf{r}'} \\ &\times \sum_i \mathcal{A}_{\hat{\mathbf{q}}_i^{\lambda},\lambda} \frac{v_{\hat{\mathbf{q}}_i^{\lambda},\lambda}}{(c_{\hat{\mathbf{q}}_i^{\lambda},\lambda})^3}\ \Theta\Big(\frac{c_{\hat{\mathbf{q}}_i^{\lambda},\lambda}}{c_{\lambda}^{\mathrm{s}}} - \sin\vartheta_{\mathbf{q}_i^{\lambda}}\Big)\ . \end{aligned} \tag{3.34}$$

As normalization constant we have used here the whole phonon energy coming from inside the heater and falling onto the source/crystal interface. Deriving (3.34) we have applied the identity

$$\int\limits_{x_1-x_{\mathrm{s}}}^{x_2-x_{\mathrm{s}}} \int\limits_{y_1-y_{\mathrm{s}}}^{y_2-y_{\mathrm{s}}} \frac{\mathrm{d}x'\mathrm{d}y'}{{r'}^2} \cos\vartheta_{\mathbf{r}'} = \int\limits_{\Omega_{\mathrm{d},r_{\mathrm{s}}}} \mathrm{d}\Omega_{\mathbf{r}'}\ , \tag{3.35}$$

where $\Omega_{\mathrm{d},r_\mathrm{s}}$ is the solid angle corresponding to the detector surface seen from a point $\mathbf{r}_\mathrm{s} = (x_\mathrm{s}, y_\mathrm{s}, 0)$ of the source/substrate interface. The result for the η-component of quasimomentum per unit time $\Pi_\mathrm{d}^\lambda(t)$ of all phonons with polarization λ falling at time t onto the detector surface follows from (3.33) by multiplying each term in the sum over i by the appropriate value of the η-component of the slowness vector $\mathbf{s}_{\hat{\mathbf{q}}_i^\lambda,\lambda}$.

3.3.3 Phonon mode distribution in the detector

For calculating such quantities like phonon induced drag or phonon absorption in a detector of finite volume V_d, we need the density or the number of nonequilibrium phonons with a particular wavevector $\mathbf{q}$ and polarization λ inside the detector at time t as input data. We assume that the acoustic properties of the detector material are identical to the substrate, as it is the case for the imbedded low-dimensional electron systems used as phonon detector. This also means that phonon scattering at the substrate/detector interface can be neglected. For a detector in shape of a layer of finite thickness Δz and with surface area A_d located at a distance d from the crystal/source interface (see Fig. 3.7) the number of nonequilibrium phonons at time t can be directly expressed by the solution $\delta n(\mathbf{q}, \lambda, \mathbf{r}, t)$ of the kinetic equation (3.16)

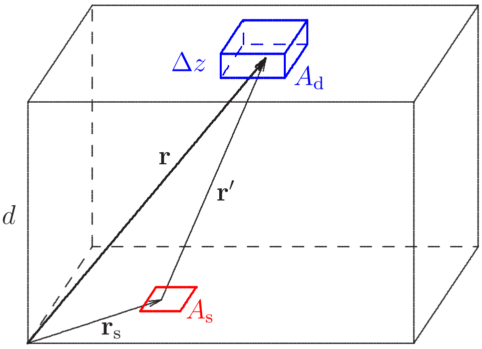

Figure 3.7: Phonon detector of finite volume V_d (surface area A_d, thickness Δz) in a plane at distance d from the crystal/source interface.

$$N^{\mathrm{d}}_{\mathbf{q},\lambda}(t) = \iint\limits_{A_\mathrm{d}} \mathrm{d}x\mathrm{d}y \int\limits_{d}^{d+\Delta z} \mathrm{d}z\, \delta n(\mathbf{q}, \lambda, \mathbf{r}, t) \tag{3.36}$$

or by the phonon density current falling onto the detector plane. Therefore for a planar phonon source and a emitted phonon pulse of duration Δt the number of phonons $N^{\mathrm{d}}_{\mathbf{q},\lambda}(t)$ inside V_{d} at time t is by means of Eq.(3.23)

$$
\begin{aligned}
N^{\mathrm{d}}_{\mathbf{q},\lambda}(t) = {} & \frac{\beth_{\mathrm{s}}(\hat{\mathbf{q}},\omega_{\mathbf{q},\lambda},\mathbf{e}_{\hat{\mathbf{q}},\lambda})}{\Delta t}\, e^{-d/\tau(\omega_{\mathbf{q},\lambda})\,(v_{\hat{\mathbf{q}},\lambda})_z} \\
& \times \int\limits_{d}^{d+\Delta z} \frac{\mathrm{d}z}{(v_{\hat{\mathbf{q}},\lambda})_z}\, e^{-(z-d)/\tau(\omega_{\mathbf{q},\lambda})(v_{\hat{\mathbf{q}},\lambda})_z}\, \Theta\Big(t-\frac{z}{(v_{\hat{\mathbf{q}},\lambda})_z}\Big)\Theta\Big(\frac{z}{(v_{\hat{\mathbf{q}},\lambda})_z}-(t-\Delta t)\Big) \\
& \times \iint\limits_{A_{\mathrm{s}}} \frac{\mathrm{d}x_{\mathrm{s}}\mathrm{d}y_{\mathrm{s}}}{A_{\mathrm{s}}} \int\limits_{x_1-x_{\mathrm{s}}}^{x_2-x_{\mathrm{s}}}\int\limits_{y_1-y_{\mathrm{s}}}^{y_2-y_{\mathrm{s}}} \frac{\mathrm{d}x'\mathrm{d}y'}{r'^{\,2}}\frac{\cos\vartheta_{\mathbf{r}'}}{\sin\vartheta_{\mathbf{q}}}\, \mathcal{A}_{\hat{\mathbf{q}},\lambda} \sum_i \delta(\vartheta_{\mathbf{q}}-\vartheta_i^{\lambda})\delta(\varphi_{\mathbf{q}}-\varphi_i^{\lambda})\,,
\end{aligned}
\tag{3.37}
$$

where the allowed ϑ_i^{λ} and φ_i^{λ} are again determined by the equation $\hat{\mathbf{v}}_{\hat{\mathbf{q}},\lambda}=\hat{\mathbf{r}}'$ with $\mathbf{r}'=\mathbf{r}-\mathbf{r}_{\mathrm{s}}$. The right hand side of Eq. (3.37) is the product of three terms. The first factor is the number of phonons of mode $(\mathbf{q},\lambda)$ emitted per unit time and reduced by isotope scattering en route to the detector. The second term is a measure for the transit time of the phonon through the detector. It is only nonzero, if t is equal to the time necessary for the phonon to pass the distance between source and detector. Lastly the third term describes the probability, that a phonon $(\mathbf{q},\lambda)$ emitted by the source will hit the detector. Using identity (3.35) the above expression for $N^{\mathrm{d}}_{\mathbf{q},\lambda}(t)$ simplifies under the conditions $d\gg\Delta z$ and $\Delta z/v^{\mathrm{c}}_{\hat{\mathbf{q}},\lambda}\ll\tau(\omega_{\mathbf{q},\lambda})$ (which are usually fulfilled)

$$
\begin{aligned}
N^{\mathrm{d}}_{\mathbf{q},\lambda}(t) = {} & \frac{\beth_{\mathrm{s}}(\hat{\mathbf{q}},\omega_{\mathbf{q},\lambda},\mathbf{e}_{\hat{\mathbf{q}},\lambda})}{\Delta t}\, e^{-d/\tau(\omega_{\mathbf{q},\lambda})\,(v_{\hat{\mathbf{q}},\lambda})_z} \int\limits_{d/(v_{\hat{\mathbf{q}},\lambda})_z}^{(d+\Delta z)/(v_{\hat{\mathbf{q}},\lambda})_z} \mathrm{d}\tilde{t}\;\Theta(t-\tilde{t})\Theta\big(\tilde{t}-(t-\Delta t)\big) \\
& \times \iint\limits_{A_{\mathrm{s}}} \frac{\mathrm{d}x_{\mathrm{s}}\mathrm{d}y_{\mathrm{s}}}{A_{\mathrm{s}}} \int\limits_{\Omega_{\mathrm{d},r_{\mathrm{s}}}} \mathrm{d}\Omega_{\mathbf{r}'}\frac{\mathcal{A}_{\hat{\mathbf{q}},\lambda}}{\sin\vartheta_{\mathbf{q}}} \sum_i \delta(\vartheta_{\mathbf{q}}-\vartheta_i^{\lambda})\;\delta(\varphi_{\mathbf{q}}-\varphi_i^{\lambda})\,.
\end{aligned}
\tag{3.38}
$$

To calculate the time-integrated phonon drag in Chapter 5 we still need another phonon quantity as input data, namely the time-integrated phonon number in a detector of volume V_{d} or, equivalently, the Fourier transform of $N^{\mathrm{d}}_{\mathbf{q},\lambda}(t)$ with $\omega=0$

$$
\begin{aligned}
\mathcal{N}_{\mathbf{q},\lambda}(0) &= \int\limits_{-\infty}^{\infty}\mathrm{d}t\,N^{\mathrm{d}}_{\mathbf{q},\lambda}(t) \\
&= V_{\mathrm{d}}\frac{\beth_{\mathrm{s}}(\hat{\mathbf{q}},\omega_{\mathbf{q},\lambda},\mathbf{e}_{\hat{\mathbf{q}},\lambda})}{(v_{\hat{\mathbf{q}},\lambda})_z\sin\vartheta_{\mathbf{q}}}\, e^{-d/\tau(\omega_{\mathbf{q},\lambda})\,(v_{\hat{\mathbf{q}},\lambda})_z} \iint\limits_{A_{\mathrm{s}}}\frac{\mathrm{d}x_{\mathrm{s}}\mathrm{d}y_{\mathrm{s}}}{A_{\mathrm{s}}} \\
&\qquad \times \int\limits_{\Omega_{\mathrm{d},r_{\mathrm{s}}}} \frac{\mathrm{d}\Omega_{\mathbf{r}'}}{A_{\mathrm{d}}}\,\mathcal{A}_{\hat{\mathbf{q}},\lambda}\sum_i \delta(\vartheta_{\mathbf{q}}-\vartheta_i^{\lambda})\;\delta(\varphi_{\mathbf{q}}-\varphi_i^{\lambda})\,.
\end{aligned}
\tag{3.39}
$$

Expression (3.39) is a quite powerful tool for obtaining the phonon input for the calculation of the time-integrated phonon drag or the time-integrated phonon absorption as a function of the detector position. It contains the focusing effects and isotope scattering as well as the full dependence from source and detector geometry and by an appropriate choice of $\mathfrak{J}_{\mathrm{s}}(\hat{\mathbf{q}}, \omega_{\mathbf{q},\lambda}, \mathbf{e}_{\hat{\mathbf{q}},\lambda})$, see Eqs. (3.18–3.21), the right frequency and wavevector distribution of the phonon source. Because of the fact that in the considered experiments the duration of the phonon heater pulse is much larger than the transit time of a phonon through the detector, the above equation allows as well a reasonable approximation of the amplitudes of absorption and drag. This is done by dividing the final results by the pulse duration Δt.

We now consider the limits for the implementation of the above derived phonon quantities in our calculations of phonon induced current or phonon absorption by electrons. The theoretical methods used for the description of the response of the electron gas to pulses of nonequilibrium phonons are based on the assumption of a homogeneous phonon distribution inside the detector. The consequential restriction for the detector size can be avoided for the detector area by splitting the whole detector area A_{d} into smaller segments ΔA_{d}, but it remains a limitation for the detector thickness.

Another question is the restriction to nondispersive phonons. Focusing of dispersive phonons was first observed by Dietsche *et al.* (1981). Constant-energy surfaces in the limit of high phonon frequencies have been constructed by Tamura and Harada (1985). For dispersive phonons the phase and group velocity do not depend only on the direction of the wavevector and we cannot use Eq. (3.10). However, the expressions (3.31) and (3.32) can be easily generalized (Jasiukiewicz, Paszkiewicz, and Lehmann, 1994). Similar formulae have also been derived by Northrop (1982) and Paszkiewicz and Wilczynski (1995) and there exist a number of theoretical and experimental papers on the ballistic propagation of large-wavevector acoustic phonons (see Wolfe, 1998 and references therein). However, the group velocities of dispersive phonons are small in comparison to the group velocities of long-wavelength acoustic phonons. So the detector of phonons placed at a macroscopic distance from the source registers mostly dispersionless acoustic phonons. Additionally, the high probability for scattering and decay processes will further reduce the number of dispersive phonons.

3.4 Method and results of numerical calculation of phonon focusing

With the help of the solutions for the incidence of phonon energy and quasimomentum onto a detector surface given by the Eqs. (3.31–3.34), including the modifications for quasimomentum of the latter two, we are able to calculate the phonon energy and quasimomentum focusing. Together with the expressions (3.38) and (3.39) for the phonon mode distribution inside a detector these solutions also serve as the essential input for the study of other quantities dominated by the acoustic anisotropy of phonon pulse propagation like angle-resolved phonon drag or phonon emission. In each case one needs the phase and group velocities for all long-wavelength acoustic phonon modes, i.e. for all values of $(\hat{\mathbf{q}}, \lambda)$. Additionally, in the cases where the interaction with electrons plays a role the phonon polarization vector has to be obtained for each phonon mode as well. For this purpose we have used the general closed-form expressions for the phase and group velocities and the polarization vector in elastically anisotropic solids derived by Every (1980, 1981). The focusing coefficient $\mathcal{A}_{\hat{\mathbf{q}},\lambda}$ has been calculated in conformity with the expressions obtained by Lax and Narayanamurti (1980). The advantage in doing so is that all mentioned quantities can be written in algebraic form. As input parameters for all our calculations concerning GaAs we have used the low-temperature values of density and elastic constants[5] given in Table 3.2.

Table 3.2: Values of crystal density and elastic constants for GaAs. (From Cottam and Saunders, 1973.)

Material	Density $[\mathrm{g/cm^3}]$	C_{11}	C_{12} $[10^{11}\,\mathrm{N/m^2}]$	C_{44}
GaAs	5.3169	1.2107	0.5477	0.6036

Having determined the phonon velocities the further procedure would be the following. For a given detector position $\mathbf{r}$, one has to find all phonon modes $(\hat{\mathbf{q}}, \lambda)$ with a group velocity $\mathbf{v}_{\hat{\mathbf{q}},\lambda}$ in direction of $\mathbf{r}$. Then for these modes one has to calculate the corresponding focusing factor $\mathcal{A}_{\hat{\mathbf{q}},\lambda}$ and the contributions to energy or quasimomentum and finally one has to sum over all involved phonon modes. However, there are at least two major problems. First, for focusing images or drag patterns we need the phonon signal as a function of (x, y), i.e. we have to rerun the procedure for a large number of different detector positions. And more important, for all points corresponding to parabolic points of the phonon slowness surface the

---

[5] We should mention here that the shape of the slowness surface depends only on the ratio of its elastic constants, e.g. for cubic crystals on $\frac{C_{11}-C_{44}}{C_{11}+2C_{44}}$ and $\frac{C_{11}-C_{12}-2C_{44}}{C_{11}+2C_{44}}$.

Gaussian curvature vanishes and the focusing factor $\mathcal{A}_{\hat{\mathbf{q}},\lambda}$ is singular. Therefore, for numerical calculations one has to modify the expressions derived in the previous section. A detailed description of the method used in our calculations is published in the paper by Jasiukiewicz, Paszkiewicz, and Lehmann (1994). Thus only the basic idea will be outlined here. As a case in point, an expression for anisotropic phonon pulse propagation as given in Eq. (3.34) will be used

$$\begin{aligned} &\iint\limits_{A_\mathrm{s}} \frac{\mathrm{d}x_\mathrm{s}\mathrm{d}y_\mathrm{s}}{A_\mathrm{s}} \int\limits_{\Delta\Omega_{\mathrm{d},r_\mathrm{s}}} \mathrm{d}\Omega_{\mathbf{r}'} \sum_i h(\hat{\mathbf{q}}_i^\lambda, \lambda, \mathbf{r}')\, \mathcal{A}_{\hat{\mathbf{q}}_i^\lambda,\lambda} \\ &= \iint\limits_{A_\mathrm{s}} \frac{\mathrm{d}x_\mathrm{s}\mathrm{d}y_\mathrm{s}}{A_\mathrm{s}} \int\limits_{4\pi} \mathrm{d}\Omega_{\mathbf{q}} \int\limits_{\Delta\Omega_{\mathrm{d},r_\mathrm{s}}} \mathrm{d}\Omega_{\mathbf{r}'}\, h(\hat{\mathbf{q}}, \lambda, \mathbf{r}')\, \mathcal{A}_{\hat{\mathbf{q}},\lambda} \sum_i \delta(\vartheta_{\mathbf{q}} - \vartheta_i^\lambda)\delta(\varphi_{\mathbf{q}} - \varphi_i^\lambda)\ , \end{aligned} \tag{3.40}$$

where $h(\hat{\mathbf{q}}_i^\lambda, \lambda, \mathbf{r}')$ is an arbitrary smooth function and the ϑ_i^λ and φ_i^λ are again the polar angles of the solutions $\hat{\mathbf{q}}_i^\lambda$ of the equation $\hat{\mathbf{v}}_{\hat{\mathbf{q}},\lambda} = \hat{\mathbf{r}}'$. This expression describes the realistic situation of a phonon source with finite surface area A_s and of a small phonon detector seen under a solid angle $\Delta\Omega_{\mathrm{d},r_\mathrm{s}}$ from a point $\mathbf{r}_\mathrm{s}$ of the phonon source. Now the total solid angle of the $\mathbf{q}$-space on the right hand side of (3.40) is divided into a finite set of n_q non-overlapping solid angles $\Delta\Omega_{\mathbf{q}}^{(j)}$

$$\sum_j^{n_q} \Delta\Omega_{\mathbf{q}}^{(j)} = 4\pi \quad , \quad \Delta\Omega_{\mathbf{q}}^{(j)} \cap \Delta\Omega_{\mathbf{q}}^{(l)} = 0 \text{ for } j \neq l\ . \tag{3.41}$$

The sufficiently small solid angle $\mathrm{d}\Omega_{\mathbf{q}}^{(j)}$ is spanned by three noncoplanar unit vectors $\hat{\mathbf{q}}_1^{(j)}$, $\hat{\mathbf{q}}_2^{(j)}$, $\hat{\mathbf{q}}_3^{(j)}$. There exists a triple of directions of group velocity vectors $\hat{\mathbf{v}}_{\hat{\mathbf{q}}_1,\lambda}^{(j)}$, $\hat{\mathbf{v}}_{\hat{\mathbf{q}}_2,\lambda}^{(j)}$, $\hat{\mathbf{v}}_{\hat{\mathbf{q}}_3,\lambda}^{(j)}$ to each triple of $\hat{\mathbf{q}}$-vectors (for each polarization λ). The solid angle corresponding to the triple of $\hat{\mathbf{v}}_{\hat{\mathbf{q}},\lambda}^{(j)}$-vectors in the real space ($\mathbf{v}$-space) is $\Delta\Omega_{\mathbf{v}\lambda}^{(j)}$. Changing the variables of integration in (3.40) and applying the definition (3.12) of the focusing factor yield

$$\begin{aligned} &\iint\limits_{A_\mathrm{s}} \frac{\mathrm{d}x_\mathrm{s}\mathrm{d}y_\mathrm{s}}{A_\mathrm{s}} \int\limits_{\Delta\Omega_{\mathrm{d},r_\mathrm{s}}} \mathrm{d}\Omega_{\mathbf{r}'} \sum_i h(\hat{\mathbf{q}}_i^\lambda, \lambda, \mathbf{r}')\, \mathcal{A}_{\hat{\mathbf{q}}_i^\lambda,\lambda} \\ &= \iint\limits_{A_\mathrm{s}} \frac{\mathrm{d}x_\mathrm{s}\mathrm{d}y_\mathrm{s}}{A_\mathrm{s}} \sum_j^{n_q} \int\limits_{\Delta\Omega_{\mathbf{v}\lambda}^{(j)}} \mathrm{d}\Omega_{\mathbf{v}} \left|\frac{\mathrm{d}\Omega_{\mathbf{q}}}{\mathrm{d}\Omega_{\mathbf{v}}}\right| \int\limits_{\Delta\Omega_{\mathrm{d},r_\mathrm{s}}} \mathrm{d}\Omega_{\mathbf{r}'}\, \tilde{h}(\hat{\mathbf{v}}, \lambda, \mathbf{r}')\, \delta(\hat{\mathbf{v}} - \hat{\mathbf{r}}') \end{aligned} \tag{3.42}$$

$$\approx \iint\limits_{A_\mathrm{s}} \frac{\mathrm{d}x_\mathrm{s}\mathrm{d}y_\mathrm{s}}{A_\mathrm{s}} \sum_j^{n_q} \left|\frac{\Delta\Omega_{\mathbf{q}}^{(j)}}{\Delta\Omega_{\mathbf{v}\lambda}^{(j)}}\right| \tilde{h}^{(j)}(\lambda, \mathbf{r}_\mathrm{s}) \int\limits_{\Delta\Omega_{\mathbf{v}\lambda}^{(j)}} \mathrm{d}\Omega_{\mathbf{v}} \int\limits_{\Delta\Omega_{\mathrm{d},r_\mathrm{s}}} \mathrm{d}\Omega_{\mathbf{r}'}\, \delta(\hat{\mathbf{v}} - \hat{\mathbf{r}}') \tag{3.43}$$

$$\approx \iint\limits_{A_\mathrm{s}} \frac{\mathrm{d}x_\mathrm{s}\mathrm{d}y_\mathrm{s}}{A_\mathrm{s}} \sum_j^{n_q} \tilde{h}^{(j)}(\lambda, \mathbf{r}_\mathrm{s})\, |\Delta\Omega_{\mathbf{q}}^{(j)}| \left|\frac{\Delta\Omega_{\mathbf{v}\lambda}^{(j)} \cap \Delta\Omega_{\mathrm{d},r_\mathrm{s}}}{\Delta\Omega_{\mathbf{v}\lambda}^{(j)}}\right|\ . \tag{3.44}$$

In (3.43) the function $\tilde{h}(\hat{\mathbf{v}}, \lambda, \mathbf{r}')$ is replaced by its average value $\tilde{h}^{(j)}(\lambda, \mathbf{r}_\mathrm{s})$ for the corresponding solid angles. For sufficiently large n_q this is always possible. In the last step we have made use of the fact that the two-fold integral over the two solid angles in (3.43) is equal to the magnitude of the common part of $\Delta\Omega^{(j)}_{\mathbf{v}\lambda}$ and $\Delta\Omega_{\mathrm{d},r_\mathrm{s}}$. For each chosen solid angle $\Delta\Omega^{(j)}_{\mathbf{q}}$ one simultaneously calculates the contribution to different detector positions (different $\Omega_{\mathrm{d},r_\mathrm{s}}$). Therefore the phonon signal as a function of detector position can be obtained after a single scan over a complete set of $\{\Delta\Omega^{(j)}_{\mathbf{q}}\}$. Moreover, it is usually enough to calculate only a subset of the set $\{\Delta\Omega^{(j)}_{\mathbf{q}}\}$ due to symmetry properties of the crystal and of the detector plane. Thus the described method is a very effective approach for any type of calculations where the anisotropic propagation of phonon beams or pulses plays a dominant role and it is faster than corresponding Monte Carlo simulations (see, e.g. Danilchenko *et al.*, 1994a; Gańcza and Paszkiewicz, 1995).[6]

To illustrate the theoretical approach discussed so far we will now present some of our numerical results for phonon energy and quasimomentum focusing. In all images we keep the source fixed and move the detector to obtain a phonon signal as a function of the detector position $\mathbf{r} = (x, y, d)$, where d is constant. This is opposite but equivalent to the situation in most experiments (cf. Chapter 2) where the phonon source is movable and the detector remains fixed.

Fig. 3.8(a) shows the relative intensity of the total ballistic phonon flux from a point source impinging on the (001) face of a GaAs crystal as a function of detector position. In Fig. 3.8(b) the same is displayed for the (311) face of GaAs. These plots are obtained on the basis of Eq. (3.31). They reveal all anisotropic features originating from the local symmetry of the slowness surface. The plot of Fig. 3.8(a) has the fourfold symmetry of the [001] axis. Both the ramps formed by the STA mode caustics and the diagonal ridges formed by the FTA mode caustics are clearly apparent. The four peaks represent the corners near the outer square of the box originating from the high STA phonon flux close to the ⟨100⟩ direction (cf. also Fig. 3.11(b)). Due to the cubic symmetry this 3D representation of energy focusing is similar to the relief in Fig. 2.5(b) obtained experimentally by Northrop and Wolfe for germanium. For comparison in Fig. 3.9 the anisotropy of the ballistic phonon flux for a trigonal sapphire crystal (a) and a hexagonal 6H-silicon carbide crystal (b) is presented. Both materials are currently very interesting for phonon imaging due to their application as substrate material for gallium nitride epilayers (Lehmann *et al.*, 2002b; Stanton *et al.*, 2003a).

The plot in Fig. 3.10 for the quasimomentum focusing is the visualization of the result of Eq. (3.32). The geometrical arrangement is for this computer experiment identical to the one for Fig. 3.8(a). Compared to the image of phonon intensity of Fig. 3.8(a) the lower symmetry in the observed features is evident. The quasimomentum flux vanishes along the mirror line in $[\bar{1}10]$ direction. Nevertheless, the caustics are also clearly visible in the quasimomentum image. Due to the increased sensitivity on scattering events the analysis of focusing images for the quasimomentum should be ideal for the study of phonon scattering.

---

[6] The advantage of Monte Carlo simulation programs for phonon propagation is the possibility to include in detail phonon scattering and phonon decay processes (Maris, 1990; Tamura, 1993; Msall and Wolfe, 1997; Gańcza *et al.*, 2001).

Fig. 3.11 demonstrates the influence of the detector size on the phonon images for GaAs. In (a) and (b) the time-integrated phonon intensity for the sum over all three polarization modes is calculated for a point phonon source and a point detector. Similar as in Fig. 3.8(a) the detector is moved in the plane perpendicular to the [001] direction of the crystal. The crystal thickness is 1.35 mm and with exception of pattern (b) the selected image section is $3.2\,\text{mm} \times 3.2\,\text{mm}$. Bright regions in the patterns indicate detector positions with high phonon energy flux. Figure (b) shows the enlarged box structure of (a) with the two squares formed by the STA modes. Compared to (a) the pattern in Fig. 3.11(c) is obtained for a phonon source and a detector of finite size. It is rather close to the experimental findings of Hübener and coworkers (Held *et al.*, 1989a) displayed in Fig. 3.11(d). The calculation for (c) is based on the source term given by Eq. (3.21) and the used parameters correspond to the ones of the experimental pattern.

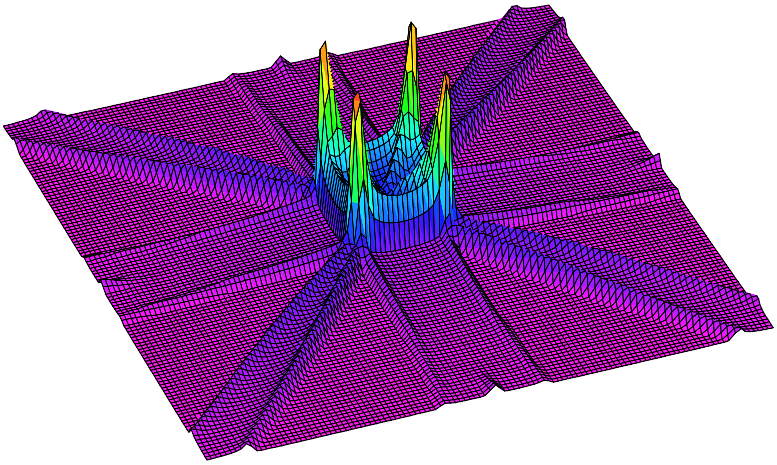

(a)

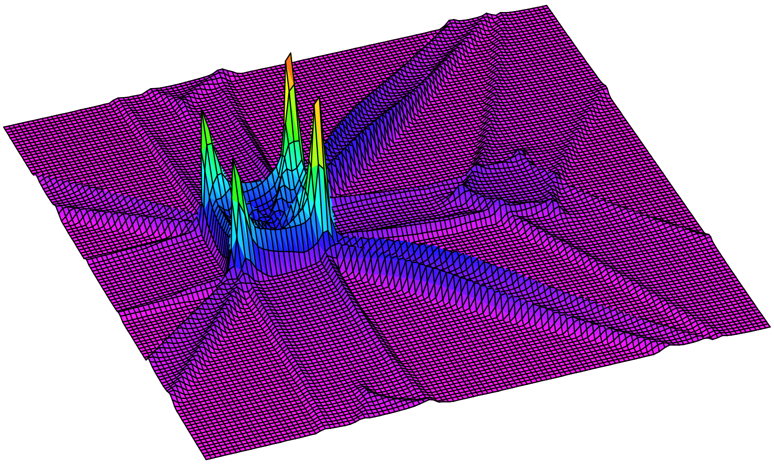

(b)

Figure 3.8: Pseudo-3D representation of phonon focusing for a GaAs crystal. The intensity of phonon flux is plotted as a function of detector position. (**a**) The detector is moved in the (001) face of the crystal and the scan from left to right (in [110] direction) corresponds to an angular range in phonon propagation direction of $-45° \ldots + 45°$. (**b**) The detector is moved in the (311) face and the angular range from left to right (in $[\bar{2}33]$ direction) is $-51° \ldots + 51°$. In both cases the (point) phonon source is located in the center on the opposing face of the crystal.

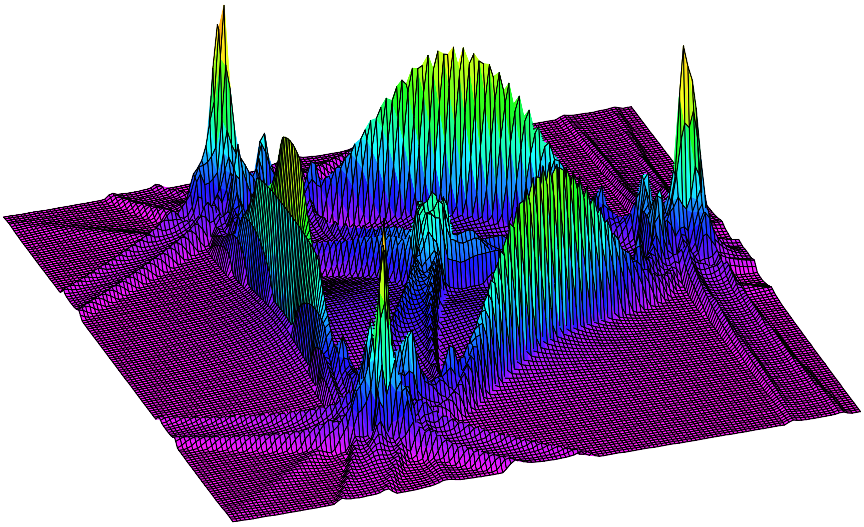

(a)

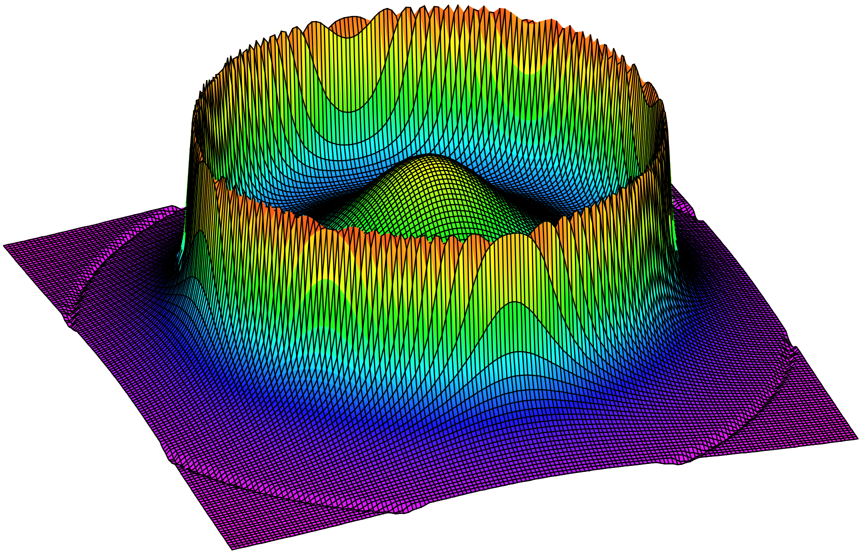

(b)

Figure 3.9: Pseudo-3D representation of phonon focusing for (**a**) sapphire and (**b**) 6H-SiC. The intensity of phonon flux is plotted as a function of detector position parallel to the (0001) plane. In (a) the image represents a ±60° horizontal scan, where the center point of the xy-surface corresponds to a phonon propagation in [0001] direction (along the c-axis). In (b) the image is a ±56° horizontal scan. The circular symmetry in the phonon image (b) arises because of the requirement that focusing should be independent of direction in the xy-plane due to the six-fold screw axis being parallel to the c-axis. Sharp focusing occurs for TA phonons at an angle of $\vartheta \approx 45°$.

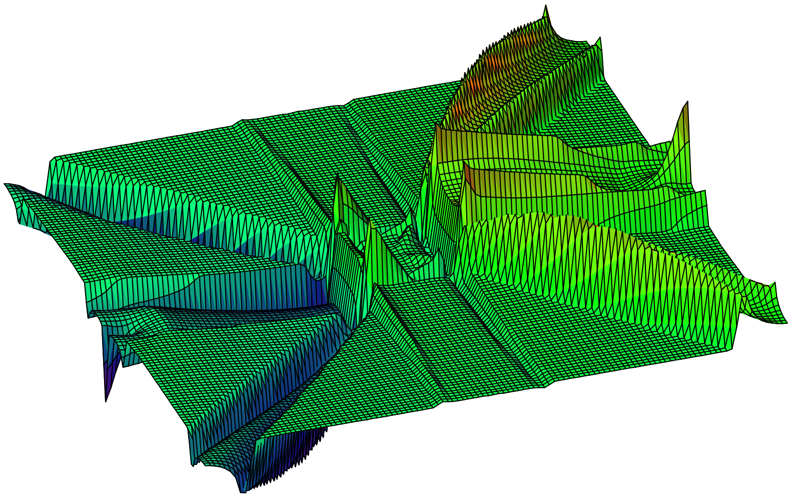

Figure 3.10: Pseudo-3D plot of quasimomentum focusing for a GaAs crystal. The detector measuring the [110] component of phonon quasimomentum is moved parallel to the (001) plane. The geometrical arrangement of phonon source and detector is identical to Fig. 3.8(a).

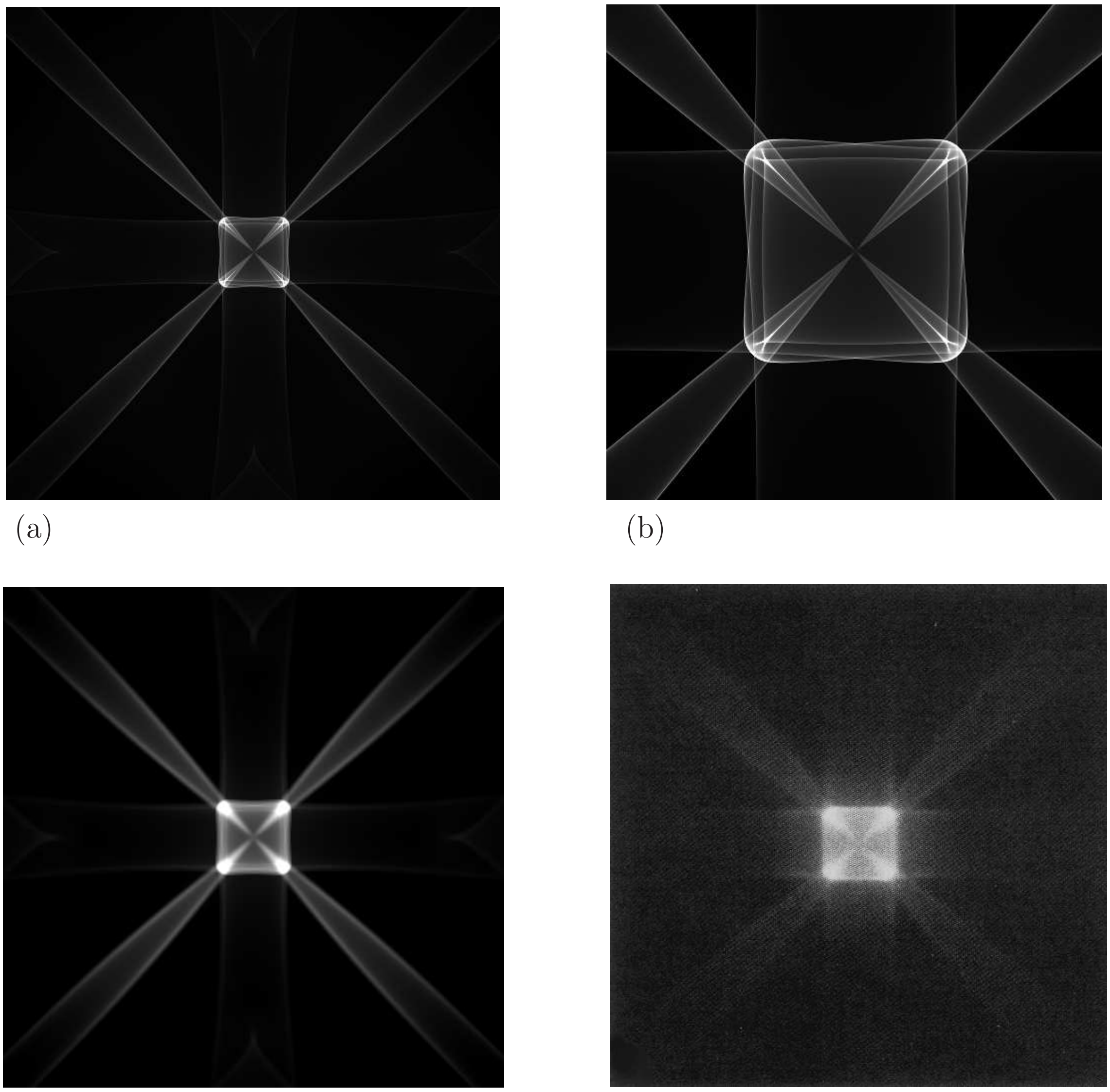

(a) (b)

(c) (d)

Figure 3.11: (**a**)–(**c**) Calculated phonon intensities for a phonon detector moved parallel to the (001) plane. Pattern (a) and (b) are for point source and detector, in pattern (c) the source diameter (28 μm) and the size of the detector (10 μm $\times$ 10 μm) correspond to the parameters of image (d). (**d**) Measured intensity of ballistic phonon flux using low-temperature scanning electron microscopy for imaging. (Experimental image from Held *et al.*, 1989a.)

Chapter 4

Acoustic Phonon Scattering in Low-Dimensional Electron Systems

Having treated of the phonon pulse propagation and the resulting nonequilibrium phonon distribution in the foregoing chapter, we now analyse the interaction of the phonon pulses with low-dimensional electron systems formed in semiconductor nanostructures. We start with a description of the electronic states of GaAs/AlGaAs heterostructures on the basis of the so called envelope function concept and discuss several models for the electron confinement. Then we examine the different mechanisms for the coupling of the low-dimensional electrons with the acoustic phonons and survey the influence of electron confinement and acoustic anisotropy on the interaction process.

4.1 Basic properties of quasi low-dimensional electron systems

Two main systems have driven research into low-dimensional systems over the last decades. The metal-oxide-semiconductor field-effect-transistor (MOSFET) was patented in 1930 but was first successfully demonstrated and perfected in the 1960s. The modulated semiconductor structures, namely modulation-doped heterojunctions, quantum wells and superlattices, were proposed later (Esaki and Tsu, 1970), but their study has developed very rapidly, from the point of view of basic physics as well as applications. In both the Si MOSFET and the modulation-doped heterostructure a 2D electron gas is formed.

To discuss the interaction of acoustic phonons with such systems we have to know the electronic properties and in particular the electron eigenfunctions. Therefore, in the following we will recapitulate the basic properties, starting with the characteristics of the corresponding bulk system, and describe the theoretical models we use. In accordance to the scope of this paper we will restrict ourselves on modulation-doped GaAs/$\mathrm{Al_xGa_{1-x}As}$ heterostructures.

4.1.1 Bulk electronic structure – A short resumé

A III-V semiconductor like GaAs crystallizes in the zinc-blende structure and each atom is tetrahedrally coordinated. The orbitals of one kind of atoms (s- or p-like) hybridize with the orbitals of its four nearest neighbours forming bonding and antibonding orbitals which broaden into bands in a solid. Because there are 8 outer electrons per unit cell (3 from Ga and 5 from As) the 4 binding orbitals are fully occupied and become the valence bands, while the antibonding orbitals are all empty and become the conduction bands. The gap between the filled valence band states and the lowest conduction band is of the order of a few eV (1.42 eV for GaAs; 2.23 eV for AlAs at room temperature). The top of the valence bands occurs at the center of the Brillouin zone (Γ-point) and, neglecting spin-orbit coupling, the upper three valence bands (originating from the bonding p orbitals) are degenerate at Γ. The lowest conduction band is singly degenerate and is a result of the antibonding s orbitals.

To simplify the many-ion many-electron problem the Schrödinger equation is considered in the mean field approximation. In this case the electron experiences a potential formed by the rigidly fixed ions and by an average over all the other electrons. The resulting effective one-electron potential $V(\mathbf{r})$ is periodic with the periodicity of the underlying lattice. Therefore the eigenfunctions of the one-electron Schrödinger equation including spin-orbit coupling (σ is the vector of electron spin)

$$\left\{ \frac{\mathbf{p}^2}{2m_{\mathrm{el}}} + V(\mathbf{r}) + \frac{\hbar}{4m_{\mathrm{el}}^2 c^2}[\sigma \times \nabla V(\mathbf{r})] \cdot \mathbf{p} \right\} \psi(\mathbf{r}) = E\psi(\mathbf{r}) \tag{4.1}$$

are Bloch functions

$$\psi_{\nu\mathbf{k}}(\mathbf{r}) = e^{i\mathbf{k}\mathbf{r}} u_{\nu\mathbf{k}}(\mathbf{r}) \ , \tag{4.2}$$

where m_{el} is the free electron mass and the function $u_{\nu\mathbf{k}}(\mathbf{r})$ shares the same periodicity as the underlying lattice. The Bloch state is labelled by the band index ν and the wavevector $\mathbf{k}$, which can be restricted to the first Brillouin zone.

It should be mentioned that in the case of solid solutions between III-V binary compounds, like $\mathrm{Al_xGa_{1-x}As}$, the potential felt by the electrons has in the strict sense no translational invariance. This is due to the random distribution of the Al and Ga atoms at the sites of one of the two fcc lattices forming the zinc-blende structure. However, in the virtual crystal approximation the random potential created by the Al and Ga atoms in the alloy is replaced by a periodic one whose strength is the weighted average.

When $\psi_{\nu\mathbf{k}}$ is inserted into Eq. (4.1) we obtain an equation for the periodic part of the Bloch function

$$\begin{aligned} \Bigg\{ & \frac{\mathbf{p}^2}{2m_{\mathrm{el}}} + V(\mathbf{r}) + \frac{\hbar}{4m_{\mathrm{el}}^2 c^2}[\sigma \times \nabla V(\mathbf{r})] \cdot \mathbf{p} + \\ & + \frac{\hbar^2 k^2}{2m_{\mathrm{el}}} + \frac{\hbar\mathbf{k}}{m_{\mathrm{el}}}\big(\mathbf{p} + \frac{\hbar}{4m_{\mathrm{el}} c^2}[\sigma \times \nabla V(\mathbf{r})]\big) \Bigg\} u_{\nu\mathbf{k}}(\mathbf{r}) = E_{\nu\mathbf{k}} u_{\nu\mathbf{k}}(\mathbf{r}) \ . \end{aligned} \tag{4.3}$$

In most of the common situations only the knowledge of the states close to the zone center is needed. Therefore a global description of the dispersion relation over the whole Brillouin zone is unnecessary and a local description of the band structure can be applied, the $\mathbf{k} \cdot \mathbf{p}$ method (Luttinger and Kohn, 1955). Here, the terms $\frac{\hbar^2 k^2}{2m_{\mathrm{el}}}$ and $\frac{\hbar \mathbf{k}}{m_{\mathrm{el}}}\big(\mathbf{p} + \frac{\hbar}{4m_{\mathrm{el}}c^2}[\sigma \times \nabla V(\mathbf{r})]\big)$ are treated as perturbations of the $\mathbf{k} = 0$ solutions $u_{\nu 0}$ and $E_{\nu 0}$ using either degenerate or nondegenerate perturbation theory. By the $\mathbf{k}{\cdot}\mathbf{p}$ method one can obtain analytic expressions for band dispersion, wavefunctions and effective masses around high symmetry points. For small k the dispersion relation of a nondegenerate band is (see e.g. Bastard, 1992)

$$E_{\nu\mathbf{k}} = E_{\nu 0} + \frac{\hbar^2}{2} \sum_{\alpha,\beta} k_\alpha \frac{1}{m^*_{\nu,\alpha\beta}} k_\beta \,, \tag{4.4}$$

where $m^*_{\nu,\alpha\beta}$ is the effective mass tensor

$$\frac{1}{m^*_{\nu,\alpha\beta}} = \frac{1}{m_{\mathrm{el}}} \delta_{\alpha\beta} + \frac{2}{m_{\mathrm{el}}^2} \sum_{\nu' \neq \nu} \frac{\pi^\alpha_{\nu\nu'} \pi^\beta_{\nu'\nu}}{E_{\nu 0} - E_{\nu' 0}} \tag{4.5}$$

and the vector $\pi_{\nu\nu'}$ is defined as

$$\pi_{\nu\nu'} = \int\limits_{\text{unit cell}} \mathrm{d}^3\mathbf{r}\, u^*_{\nu 0}(\mathbf{r}) \Big(\mathbf{p} + \frac{\hbar}{4m_{\mathrm{el}}c^2}[\sigma \times \nabla V]\Big)\, u_{\nu' 0}(\mathbf{r}) \,. \tag{4.6}$$

The corresponding wavefunctions are to first order in $\mathbf{k} \cdot \mathbf{p}$ theory

$$u_{\nu\mathbf{k}}(\mathbf{r}) = u_{\nu 0}(\mathbf{r}) + \frac{\hbar}{m_{\mathrm{el}}} \sum_{\nu' \neq \nu} \frac{\mathbf{k} \cdot \pi_{\nu'\nu}}{E_{\nu 0} - E_{\nu' 0}}\, u_{\nu' 0}(\mathbf{r}) \,. \tag{4.7}$$

Eq. (4.5) demonstrates the difference of the effective electron mass from the free electron mass because of the coupling between electronic states in different bands. It exhibits the fact that the electron experiences in reality a periodic crystal potential instead of moving in a constant potential. For the conduction band edge $m^*_{\nu,\alpha\beta}$ simplifies and is approximately a scalar. For larger k one has to go beyond the isotropic parabolic approximation as described e.g. by Mayer and Rössler (1991). Much different is the situation for the upper valence bands. The spin-orbit coupling lifts the sixfold (including spin) degeneracy at $\mathbf{k} = 0$ and gives rise to a quadruplet corresponding to total angular momentum $j = \frac{3}{2}$, and to a twofold degenerate level with $j = \frac{1}{2}$ (see Fig. 4.1). These latter are the so called spin split-off (so) states while the former ones are associated with light hole (lh, $m_j = \pm\frac{1}{2}$) and heavy hole states (hh, $m_j = \pm\frac{3}{2}$). Away from the zone center the bands couple via $\mathbf{k} \cdot \mathbf{p}$ interaction resulting in band warping, i.e. in anisotropic surfaces of constant energy, for the light and heavy hole bands as depicted in Fig. 4.2.

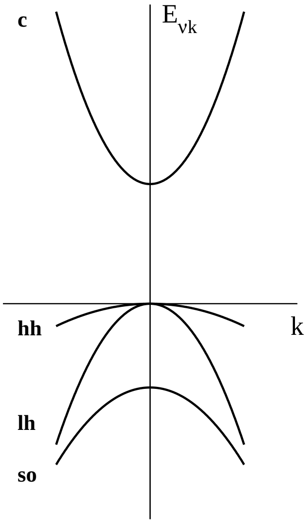

Figure 4.1: Schematic band structure of a direct gap III-V compound in the vicinity of the zone center. Only the states near the Fermi energy are presented.

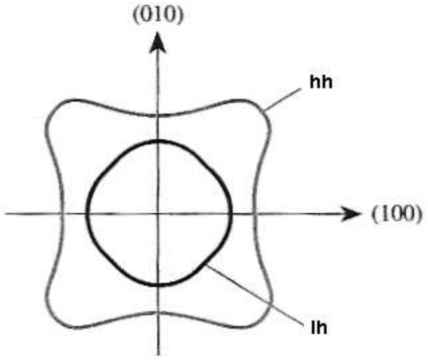

Figure 4.2: Surfaces of constant energy for the $j = \frac{3}{2}$ bands.

4.1.2 Electronic states of heterostructures – The envelope function concept

The complexity of the band structure is increased once the symmetry of the bulk lattice is reduced and we are interested in the electronic properties of a heterojunction or a quantum well. A heterojunction is formed between two lattice matched semiconductors with different band gaps while a quantum well is like a sandwich structure consisting of a thin layer of a semiconductor material between two layers of another semiconductor. The fabrication of such interfaces which are flat up to one atomic monolayer became possible with the development of advanced epitaxial techniques like molecular beam epitaxy or metal-organic chemical vapour deposition. In a layered structure that is lattice matched there is still the periodicity of the lattice but with discontinuities in the electron potential, which is set up by the conduction and valence band discontinuities between the different materials. The approximation of perfect lattice matching is relatively well justified for GaAs/$\mathrm{Al_xGa_{1-x}As}$ heterostructures where the relative lattice mismatch between the two host materials is smaller than 0.1%.

There exists a wide range of theoretical methods to calculate the electronic structure of heterostructures which can be divided into two main classes, the supercell approaches and the boundary-condition approaches. While in the supercell approaches the heterostructure is treated as a bulk material with a very large unit cell and the eigenfunctions of the hamiltonian are found by conventional band-structure methods, in the boundary-condition approach the eigenfunctions of the heterostructure hamiltonian are found by matching the wavefunctions in each of the constituent materials at the interfaces. We will consider here only a particularly simple and effective method where the boundary-condition approach is combined with the $\mathbf{k} \cdot \mathbf{p}$ theory, usually called the *envelope function model.* First BenDaniel and Duke (1966) applied this method in a simple one-band model to the case of a heterojunction. Later on it was extended by Bastard (1981), White and Sham (1981) and Ekenberg and Altarelli (1984) to the two-band envelope function model (mixing between the conduction and light hole bands or between the upper spin-orbit-split valence bands, respectively) and to the more general multi-band case (Altarelli, 1983). The envelope function method allows a comprehensive description of electron and hole states. It masters different geometries of quantum structures as well as perturbations by external or built-in potentials or strain. Like all boundary-condition approaches the envelope function method is restricted to the vicinity of the high symmetry points in the host Brillouin zone, but this is an adequate assumption for our applications. The method can be obtained by expanding the heterostructure wavefunction ψ into a complete set of periodic functions with a period equal to the lattice periodicity or, more precise, by writing ψ as a sum of products of rapidly varying zone center Bloch functions $u_{\nu 0}(\mathbf{r})$ and slowly varying envelope functions $\xi_\nu(\mathbf{r})$

$$\psi(\mathbf{r}) = \sum_\nu \xi_\nu(\mathbf{r})\, u_{\nu 0}(\mathbf{r}) \, . \tag{4.8}$$

In a good approximation the periodic zone center eigenfunctions $u_{\nu 0}$ are similar for all materials of which the heterostructure is composed. The latter is true because the constituent crystals are assumed to have a similar electronic structure. If one considers only states near the zone center, the envelope functions $\xi_\nu(\mathbf{r})$ will be slowly varying on an atomic scale and will fulfill the following equation (Burt, 1988a,b)

$$-\frac{\hbar^2}{2m_{\mathrm{el}}}\nabla^2 \xi_\nu(\mathbf{r}) - \frac{i\hbar}{m_{\mathrm{el}}} \sum_{\nu'} \mathbf{p}_{\nu\nu'} \cdot \nabla \xi_{\nu'}(\mathbf{r}) = \big(E - E_{\nu 0}(z)\big)\, \xi_\nu(\mathbf{r}) \, . \tag{4.9}$$

Here we have chosen the interfaces between the different materials normal to the z-direction. The $\mathbf{p}_{\nu\nu'}$ are the matrix elements of momentum with respect to the zone center Bloch functions (see Eq. (4.6), but neglecting spin-orbit coupling) and $E_{\nu 0}(z)$ is the energy of the ν-th zone center state of the material occupying the point z. Thus $E_{\nu 0}(z)$ changes discontinuously at abrupt interfaces. If we are interested in eigenstates with energy E much closer to the zone center energy $E_{\mu 0}$ of the μ-th band than to any other zone center energy then for $\nu \neq \mu$

$$\xi_\nu(\mathbf{r}) = -\frac{i\hbar}{m_{\mathrm{el}}} \, \frac{\mathbf{p}_{\nu\mu}}{E_{\mu 0}(z) - E_{\nu 0}(z)} \cdot \nabla \xi_\mu(\mathbf{r}) \tag{4.10}$$

holds to leading order. Substitution of (4.10) in (4.9) gives an effective mass equation for the envelope function $\xi_\mu(\mathbf{r})$

$$-\frac{\hbar^2}{2}\sum_{\alpha,\beta}\frac{\partial}{\partial x_\alpha}\Big[\frac{1}{m^*_{\mu,\alpha\beta}(z)}\frac{\partial}{\partial x_\beta}\,\xi_\mu(\mathbf{r})\Big]+E_{\mu 0}(z)\,\xi_\mu(\mathbf{r})=E\,\xi_\mu(\mathbf{r})\ . \tag{4.11}$$

According to the definition in (4.5) the factor

$$\frac{1}{m^*_{\mu,\alpha\beta}(z)}=\frac{1}{m_{\mathrm{el}}}\delta_{\alpha\beta}+\frac{2}{m^2_{\mathrm{el}}}\sum_{\nu\neq\mu}\frac{p^\alpha_{\mu\nu}p^\beta_{\nu\mu}}{E_{\mu 0}(z)-E_{\nu 0}(z)} \tag{4.12}$$

approximates a position dependent effective mass tensor. Since the lattice constants of the host layers are assumed to be the same, the heterostructure becomes translational invariant in the xy-plane (parallel to the interfaces). Thus the functions $\xi_\mu(\mathbf{r})$ can be factorized

$$\xi_\mu(\mathbf{r})\sim e^{i\,\mathbf{k}_\parallel\mathbf{r}_\parallel}\varphi_\mu(z)\ . \tag{4.13}$$

Substituting (4.13) into Eq. (4.11) and assuming an isotropic band we obtain a Schrödinger-like equation for the z-component of the envelope function

$$\Big(-\frac{\hbar^2}{2}\frac{\mathrm{d}}{\mathrm{d}z}\frac{1}{m^*_\mu(z)}\frac{\mathrm{d}}{\mathrm{d}z}+\frac{\hbar^2\mathbf{k}^2_\parallel}{2m^*_\mu(z)}+E_{\mu 0}(z)\Big)\varphi_\mu(z)=E\varphi_\mu(z)\ . \tag{4.14}$$

Integration across the interfaces leads to the necessity for $\varphi_\mu(z)$ and $\frac{1}{m^*_\mu(z)}\frac{\mathrm{d}\varphi_\mu}{\mathrm{d}z}$ to be continuous. The latter condition ensures that the particle flux is continuous across the interface. In the case where an external potential $V(z)$, e.g. a band bending potential arising from charges, slowly varying at the scale of the host unit cell is superimposed on the heterostructure potential, Eq. (4.14) is modified by the adjunction of the potential term

$$\Big(-\frac{\hbar^2}{2}\frac{\mathrm{d}}{\mathrm{d}z}\frac{1}{m^*_\mu(z)}\frac{\mathrm{d}}{\mathrm{d}z}+\frac{\hbar^2\mathbf{k}^2_\parallel}{2m^*_\mu(z)}+V(z)+E_{\mu 0}(z)\Big)\varphi_\mu(z)=E\varphi_\mu(z)\ . \tag{4.15}$$

Considering the assumptions made, the envelope function for a conduction band can be calculated from (4.14) or (4.15) provided that all the other host bands are remote for the conduction edge under consideration. This condition works quite well for the lowest conduction band we are interested in, but usually fails for hole bands. In the hole case coupling between the conduction and valence bands occurs and the envelope functions are the solutions of a differential equation system following with (4.13) from (4.9)

$$\sum_{\nu'}\Big\{\Big(\frac{-\hbar^2}{2m_{\mathrm{el}}}\frac{\partial^2}{\partial z^2}+\frac{\hbar^2\mathbf{k}^2_\parallel}{2m_{\mathrm{el}}}+E_{\nu 0}(z)-E\Big)\delta_{\nu\nu'}+\frac{\hbar}{m_{\mathrm{el}}}\mathbf{p}_{\nu\nu'}\cdot\Big(\mathbf{k}_\parallel-i\mathbf{e}_z\frac{\mathrm{d}}{\mathrm{d}z}\Big)\Big\}\varphi_{\nu'}(z)=0\ . \tag{4.16}$$

In practice the summation over ν' has to be restricted. In the two-band envelope function model usually only the lowest conduction and the light hole bands are considered. In the multi-band envelope function models the heavy hole bands, partly also the split-off bands or further valence band and conduction band states are additionally included in the summation over ν'. To the extent that the other host states are far from the edges of the explicitly included bands their effect on the related envelope functions is neglected or taken into account by a perturbation mixing to first order in the wavefunctions (for an overview see Smith and Mailhiot, 1990; Bastard, 1992).

In the next subsection we will apply the general formalism derived so far to typical models of low-dimensional electron systems.

4.1.3 Simple models of confinement

Confinement in modulation-doped heterojunctions

Thanks to the modulation doping technique, which was first applied by Dingle *et al.* (1978) to GaAs heterostructures, high mobility 2D electron gases can be realized. When a selectively n-doped wide gap material 'B' ($\mathrm{Al_xGa_{1-x}As}$ with x typically between 0.2 and 0.3) and a narrow gap material 'A' (GaAs) are brought together, electrons from the donor levels of $\mathrm{Al_xGa_{1-x}As}$ are transferred to the GaAs layer to create a uniform Fermi energy throughout the sample. Thus a spontaneous and irreversible charge transfer occurs and a band bending takes place due to the dipole formed between the positive charges (ionized donors) and the negative charges (electrons). Averaging the donor distribution in the layer plane, the band bending depends only on the growth direction (z-axis). The resulting self-consistent potential felt by the electrons has therefore a quasi triangular shape near the interface and is limited by the conduction band discontinuity at the interface $z = 0$ and the z-dependent conduction band edge at $z > 0$ as schematically displayed in Fig. 4.3. The consequence is that the electrons in the GaAs layer are confined close to the

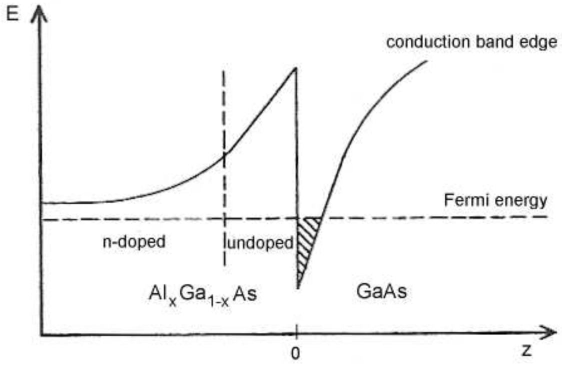

Figure 4.3: Schematic band diagram for a GaAs/$\mathrm{Al_xGa_{1-x}As}$ heterojunction.

interface and bound states E_l with $l = 1, 2, \dots$ are formed for the z motion. To distinguish these electron energy levels from the electron energy levels of the corresponding bulk crystal, the energy bands of the confined electrons are known as subbands. If the energy spacings between the levels $E_2 - E_1,\ E_3 - E_2, \dots$ are much larger than the thermal or collisional broadenings, the electron motion becomes effectively two-dimensional. For an electron density of $5 \cdot 10^{15}\,\mathrm{m}^{-2}$ the first excited state E_2 of the confining potential is about 50 meV above the bottom of the ground subband (Stern and Das Sarma, 1984) and the Fermi energy ($E_\mathrm{F} \approx 18\,\mathrm{meV}$) locates well below E_2. By separating the ionized donors in the $\mathrm{Al_xGa_{1-x}As}$ from the interface with a spacer layer as shown in Fig. 4.3, the electron scattering can be dramatically reduced and very high mobilities of the electron gas are achieved.

Within the framework of the effective mass approximation the envelope wavefunctions for the electrons and the energy levels of the corresponding subbands can be easily obtained. Starting with Eq. (4.15) for the lowest conduction band ($\mu = (\mathrm{c})$) we only have to substitute $E_{\mu 0}(z)$ by $E^\mathrm{A}_{(\mathrm{c})0} + V_{(\mathrm{c})}\,\Theta(-z)$

$$\left(-\frac{\hbar^2}{2}\frac{\mathrm{d}}{\mathrm{d}z}\frac{1}{m^*_{(\mathrm{c})}(z)}\frac{\mathrm{d}}{\mathrm{d}z} + \frac{\hbar^2 \mathbf{k}_\parallel^2}{2m^*_{(\mathrm{c})}(z)} + E^\mathrm{A}_{(\mathrm{c})0} + V_{(\mathrm{c})}\,\Theta(-z) + V(z) \right)\varphi_{(\mathrm{c})}(z) = E\varphi_{(\mathrm{c})}(z) \tag{4.17}$$

with $V_{(\mathrm{c})}$ as the conduction band discontinuity at the interface. The position dependent effective mass is now

$$m^*_{(\mathrm{c})}(z) = \begin{cases} m^*_\mathrm{A} & \text{if} \quad z > 0 \\ m^*_\mathrm{B} & \text{if} \quad z < 0 \end{cases} , \tag{4.18}$$

where $m^*_\mathrm{A} = m^*_\mathrm{GaAs} = 0.067 m_\mathrm{el}$ and $m^*_\mathrm{B} = m^*_{\mathrm{Al_xGa_{1-x}As}} = (0.067 + 0.083x) m_\mathrm{el}$ (Zachau *et al.*, 1986). To decouple the electron motion perpendicular and parallel to the z-axis the factor $m^{*-1}_{(\mathrm{c})}(z)$ in the $\mathbf{k}_\parallel^2$-term of (4.17) can be approximated by a new (parallel) effective mass m^*_l defined by

$$\frac{1}{m^*_l} = \int\limits_0^\infty \mathrm{d}z |\varphi_{(\mathrm{c})l}(z)|^2 \frac{1}{m^*_\mathrm{A}} + \int\limits_{-\infty}^0 \mathrm{d}z |\varphi_{(\mathrm{c})l}(z)|^2 \frac{1}{m^*_\mathrm{B}} \, . \tag{4.19}$$

The error made by this substitution is of the fourth order in $k_\parallel$, i.e. of the same order like the nonparabolic corrections to the host conduction bands, and is negligible for small $k_\parallel$.

The shape of the electrostatic potential $V(z)$ in (4.17) depends on the presence of free carriers and ionized impurities. It has to be self-consistently determined from the Poisson equation

$$\frac{\mathrm{d}^2 V}{\mathrm{d}z^2} = -\frac{e^2}{\varepsilon_0 \varepsilon_r}\Big(\sum_l^{\mathrm{occ.}} |\varphi_{(\mathrm{c})l}(z)|^2 n_l - N_\mathrm{D}(z) + N_\mathrm{A}(z) \Big) \, , \tag{4.20}$$

where n_l is the areal concentration of the (transferred) electrons in the l-th subband, $N_{\mathrm{D}}(z)$ and $N_{\mathrm{A}}(z)$ are the concentrations of the ionized donors in the barrier-acting material B and the ionized (residual) acceptors in the well-acting material A, respectively. The z-dependence of N_{D} and N_{A} occurs due to the selective doping and the presence of the heterojunction (charge transfer). Charge balance causes the condition

$$\sum_{l}^{\mathrm{occ.}} n_l \int\limits_{-\infty}^{\infty} \mathrm{d}z \, |\varphi_{(\mathrm{c})_l}(z)|^2 = \int\limits_{-\infty}^{0} \mathrm{d}z \, N_{\mathrm{D}}(z) - \int\limits_{0}^{\infty} \mathrm{d}z \, N_{\mathrm{A}}(z) \; . \tag{4.21}$$

The self-consistency requirement for the electrostatic potential is a special feature of energy level and wavefunction calculation in doped heterostructures, which is absent in undoped ones, where the confining potentials are fixed.

In the region of interest ($z \gtrapprox 0$) and for not too high doping the solution of the Poisson equation (4.20) can be approximated by an expression linear in z

$$V(z) = \gamma \, z \; , \tag{4.22}$$

where

$$\gamma = \frac{e^2}{\varepsilon_0 \varepsilon_r} \Big\{ N_{\mathrm{depl}} + \sum_{l}^{\mathrm{occ.}} n_l \Big(1 - \int\limits_{-\infty}^{0} \mathrm{d}z \; |\varphi_{(\mathrm{c})_l}(z)|^2 \Big) \Big\} \tag{4.23}$$

(Takada and Uemura, 1977). Here $N_{\mathrm{depl}} = \int_0^\infty \mathrm{d}z \, N_{\mathrm{A}}(z)$ is the (2D) density of charges in the GaAs depletion layer and $\sum_l^{\mathrm{occ.}} n_l = n_{2\mathrm{D}}$ is the total electron density in the 2D channel. As already qualitatively discussed a triangular-like confinement potential for the electrons (see Fig. 4.3) is the consequence of the result for $V(z)$ (Eq. 4.22) and the band discontinuity at $z = 0$. The situation is quite similar to inversion layers in Si MOSFETs reviewed by Ando *et al.* (1982), but with the exception of the barrier height. For the Si/SiO$_2$ interface the SiO$_2$ barrier is usually assumed to be infinite which implicates vanishing electron wavefunctions inside the barrier. However, the discontinuity in the conduction band edges at GaAs/Al$_{\mathrm{x}}$Ga$_{1-\mathrm{x}}$As interfaces (with $x < 0.45$) is less than 360 meV (Adachi, 1994) in contrast to approximately 3 eV for a Si/SiO$_2$ interface (Williams, 1977). Therefore one has to consider the finite barrier height in the calculations, particularly for applications, where the confinement length of the (quasi-)2D electrons plays an important role (as in the case of angle-resolved phonon emission described in Chapter 6).

With the implementations made above, the equation for the envelope function (4.17) becomes

$$\left(E_l - E^{\mathrm{A}}_{(\mathrm{c})0} - \frac{\hbar^2 \mathbf{k}_\parallel^2}{2 m_l^*} \right) \varphi_{(\mathrm{c})_l}(z) = \left\{ \begin{array}{ll} \big(-\frac{\hbar^2}{2m_{\mathrm{B}}^*} \frac{\mathrm{d}^2}{\mathrm{d}z^2} + V_{(\mathrm{c})} \big) \varphi_{(\mathrm{c})_l}(z) & \text{for} \quad z < 0 \\ \big(-\frac{\hbar^2}{2m_{\mathrm{A}}^*} \frac{\mathrm{d}^2}{\mathrm{d}z^2} + \gamma z \big) \varphi_{(\mathrm{c})_l}(z) & \text{for} \quad z > 0 \end{array} \right. , \tag{4.24}$$

valid in the vicinity of $z = 0$. Its solutions are Airy functions $\mathrm{Ai}(x)$ (see, e.g. Abramowitz and Stegun, 1972) and particularly for the ground substate ($l = 1$) we end up with

$$\varphi^{\mathrm{Ai}}_{(\mathrm{c})_1}(z) = \begin{cases} B_{\mathrm{h}} \exp\left(\sqrt{\frac{2m^*_{\mathrm{B}}V_{(\mathrm{c})}}{\hbar^2} - \frac{m^*_{\mathrm{B}}\tilde{k}^2}{m^*_{\mathrm{A}}}}\, z\right) & \text{for } z < 0 \\ A_{\mathrm{h}}\, \mathrm{Ai}(z/\bar{\gamma} - \tilde{k}^2\bar{\gamma}^2) & \text{for } z > 0 \end{cases} \tag{4.25}$$

$$E_1 \equiv E_{1\mathbf{k}_\parallel} = E^{\mathrm{A}}_{(\mathrm{c})0} + \frac{\hbar^2\tilde{k}^2}{2m^*_{\mathrm{A}}} + \frac{\hbar^2\mathbf{k}^2_\parallel}{2m^*_1}\,, \tag{4.26}$$

where $\bar{\gamma} = (\hbar^2/2m^*_{\mathrm{A}}\gamma)^{1/3}$. The constants A_{h}, B_{h} and $\tilde{k}$ have to be calculated from the continuity conditions at $z = 0$ and the normalization condition. At low temperatures, in almost all practical cases only the lowest electron subband is occupied in $\mathrm{GaAs/Al_xGa_{1-x}As}$ heterojunctions. Therefore our restriction on the ground subband is totally adequate. For $V_{(\mathrm{c})} \to \infty$ the above solution reduces to the result obtained by Stern (1972) for an n-type Si inversion layer with infinite barrier.

It is more convenient and therefore widely used to approximate the ground state solution by a trial function introduced by Fang and Howard (1966) for Si inversion layers with infinite barrier

$$\varphi^{\mathrm{FH}}_{(\mathrm{c})_1}(z) = \begin{cases} 0 & \text{for } z < 0 \\ (2b^3)^{-1/2} z \exp(-z/2b) & \text{for } z \geq 0 \end{cases} \tag{4.27}$$

or by a so called modified Fang-Howard function (Ando *et al.*, 1982)

$$\varphi^{\mathrm{FH}}_{(\mathrm{c})_1}(z) = \begin{cases} B'_{\mathrm{h}} \exp\left(\sqrt{\frac{2m^*_{\mathrm{B}}V_{(\mathrm{c})}}{\hbar^2}}\, z\right) & \text{for } z < 0 \\ A'_{\mathrm{h}} \cdot (z - z_0) \exp(-z/2b) & \text{for } z \geq 0 \end{cases} \tag{4.28}$$

in the case of finite $V_{(\mathrm{c})}$. The constants z_0, A'_{h} and B'_{h} follow again from normalization and boundary conditions. In (4.27) and (4.28) b is a trial parameter chosen to minimize the energy and thus only determined by the electron density $n_{2\mathrm{D}}$ in the 2D electron channel and the depletion charge density N_{depl}. However, b is also a measure of the spatial extent of $|\varphi^{\mathrm{FH}}_{(\mathrm{c})_1}(z)|^2$ and with it of the characteristic 'thickness' ($2\Delta z$) of the quasi-2D system. It results from (4.27) that $\Delta z = \sqrt{\langle z^2\rangle - \langle z\rangle^2} = \sqrt{3}\, b$.

For energy levels calculation and many applications the approximation by the trial functions (4.27) or (4.28) is sufficient, but we have shown (Lehmann and Jasiukiewicz, 2002, see also Section 6.3.3) that using envelope functions of Fang-Howard type there are large discrepancies in the results of angle-resolved acoustic phonon emission calculations. The reason is the much slower decline for large z

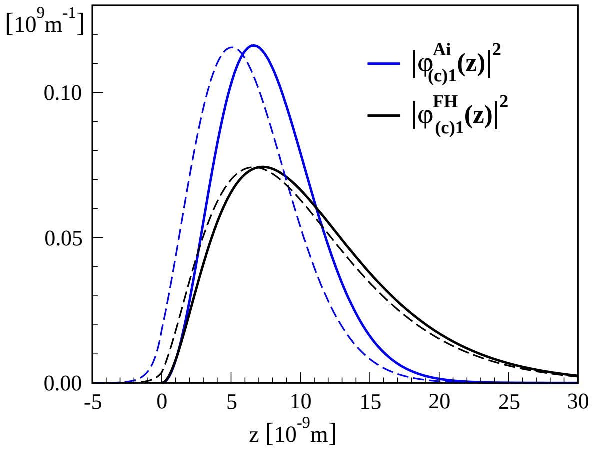

Figure 4.4: Spatial dependence of the squared wavefunction for the Airy and the Fang-Howard solution. Solid lines for $V_{(\mathrm{c})} = \infty$, dashed lines for $V_{(\mathrm{c})} = 300\,\mathrm{meV}$.

in the case of Fang-Howard type trial functions compared to the more exact Airy solution as shown in Fig. 4.4.

A better asymptotic behaviour is obtained by a more adjusted variational wavefunction proposed by Takada and Uemura (1977)

$$\varphi^{\mathrm{TU}}_{(\mathrm{c})_1}(z) = \begin{cases} 0 & \text{for } z < 0 \\ (\frac{3}{2b^3})^{1/2} z \exp(-\frac{1}{2}(\frac{z}{b})^{3/2}) & \text{for } z \geq 0 \end{cases} \quad . \tag{4.29}$$

However, this function does not allow simple analytic expressions of the overlap integral and the form factor (necessary for calculation of electron-phonon and electron-electron interaction in low-dimensional systems) and has therefore for our purpose hardly any practical advantages over the direct solution by Airy functions.

So far we have discussed the envelope functions for a quasi-2D system of electrons formed at the interface of a modulation-doped heterojunction. However, it is also possible to generate a quasi-2D hole gas if the narrow gap GaAs is joined with a p-doped $\mathrm{Al_xGa_{1-x}As}$. Now the discontinuity in the valence bands at the $\mathrm{GaAs/Al_xGa_{1-x}As}$ interface and the band bending near the interface cause a 2D channel for holes. Compared to the electron system important new features appear. The degeneracy of the valence bands and the electric field near the interface combine to couple strongly the parallel and perpendicular motion of the holes. As a consequence of the interaction between the valence bands one has to solve the coupled differential equations (4.16) with simultaneous addition of the electrostatic potential $V(z)$ describing the band bending. A possible approach is to approximate the z-dependent part of the envelope functions for the upper heavy and light hole levels by Fang-Howard trial functions

$$\begin{aligned} \varphi_{(\mathrm{hh})_1}(z) = & \ (2b_{\mathrm{hh}}^3)^{-1/2} z \exp(-z/2b_{\mathrm{hh}})\, \Theta(z) \\ \varphi_{(\mathrm{lh})_1}(z) = & \ (2b_{\mathrm{lh}}^3)^{-1/2} z \exp(-z/2b_{\mathrm{lh}})\, \Theta(z) \end{aligned} \quad , \tag{4.30}$$

as it was used, e.g. by Broido and Sham (1985) in a model where only the upper four bulk valence bands (light and heavy holes) were taken into account. Due to the interplay of the spin-orbit coupling and the lack of inversion symmetry at the interface the resulting subbands exhibit a lifting of the twofold spin degeneracy for $\mathbf{k}_\parallel \neq 0$. This feature was first demonstrated by Eisenstein *et al.* (1984) in magnetotransport measurements. The smaller barrier height of the hole potential at the interface is a further characteristic in determining the hole envelope functions in modulation-doped heterojunctions. Only about 35% of the band gap discontinuity at a GaAs/Al$_\mathrm{x}$Ga$_{1-\mathrm{x}}$As interface is in the valence band (Adachi, 1994).

Figs. 4.5 and 4.6 show the result of self-consistent calculations based on the envelope function approach of Winkler and Rössler (1993) for two different geometries of p-type GaAs/Al$_\mathrm{x}$Ga$_{1-\mathrm{x}}$As heterojunctions. As already discussed, in both cases the hole sublevels consist of two distinct subbands ('spin subbands') with different effective masses. It is noticeable that both for the (001) and (311) 2D hole system at least one subband of the second pair (the original light hole bands) bends up as $k_\parallel$ is increased from zero, i.e. these hole bands have electron-like effective masses. However, it is also apparent, that for the considered (typical) hole densities only

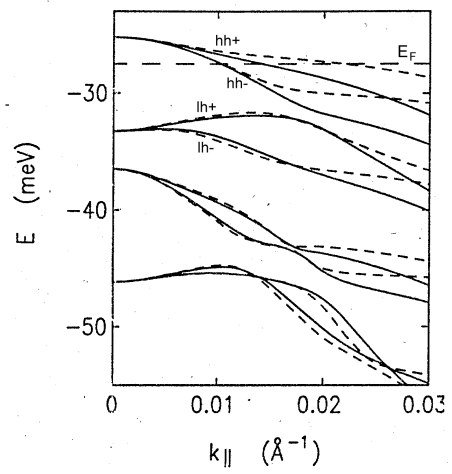

Figure 4.5: Hole subbands for a (001) GaAs/AlGaAs heterojunction with 2D hole density $n_{2\mathrm{D}} = 3.3 \cdot 10^{15}\,\mathrm{m}^{-2}$. Solid lines are for wavevectors in [100] direction, dashed lines for wavevectors in [110] direction. Different spin subbands are denoted by '+' and '−'. (From Rössler and Winkler, 1997.)

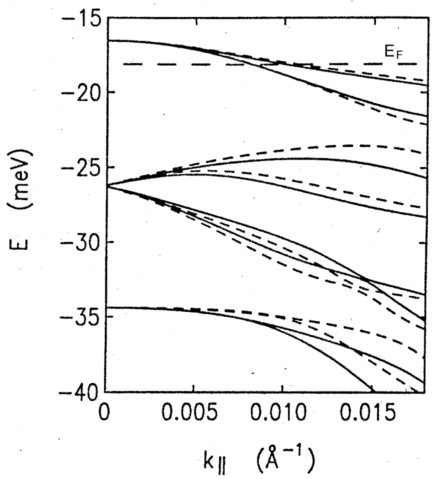

Figure 4.6: Hole subbands for a (311)A GaAs/AlGaAs heterojunction with 2D hole density $n_{2\mathrm{D}} = 1.3 \cdot 10^{15}\,\mathrm{m}^{-2}$. Solid lines are for wavevectors in $[\bar{2}33]$ direction, dashed lines for wavevectors in $[01\bar{1}]$ direction. (From Rössler and Winkler, 1997.)

the top subband pair has filled levels. It has been found that for a (001) 2D hole system with a total hole density of $n_{2\mathrm{D}} = 3.8 \cdot 10^{15}\,\mathrm{m}^{-2}$ more than 73% of the holes are in the uppermost spin subband (Mendez, 1986).

Compared to the (001) hole system the absolute values of the effective masses are smaller for the (311) heterojunction and, as depicted in Fig. 4.7, the anisotropy of the subband dispersion is less. All in all, the results of Figs. 4.5–4.7 document that for not too high carrier densities and for wavevectors $k < k_\mathrm{F}$ the use of an isotropic and parabolic approximation for the occupied hole bands seems to be an acceptable starting point for phonon-drag calculations (as performed in Chapter 5).

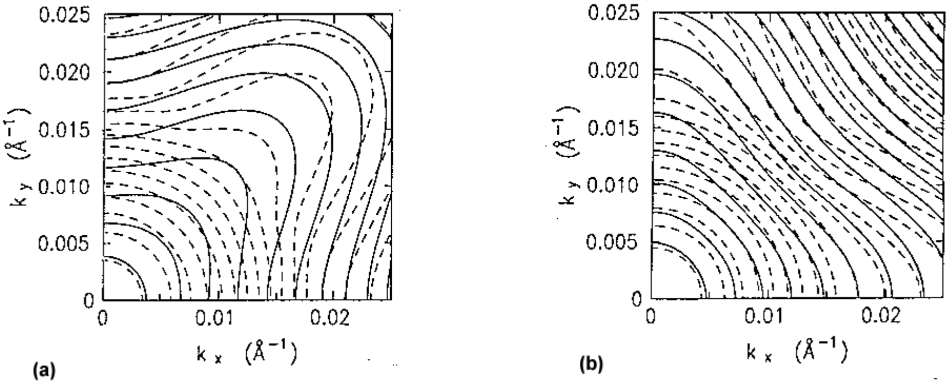

Figure 4.7: Constant energy contours for the upper two hole subbands (solid and dashed lines, respectively). The difference between two solid (dashed) lines corresponds to 0.5 meV. Figure (**a**) is for the (001) GaAs/Al$_\mathrm{x}$Ga$_{1-\mathrm{x}}$As heterojunction described in Fig. 4.5, figure (**b**) for the (311)A GaAs/Al$_\mathrm{x}$Ga$_{1-\mathrm{x}}$As heterojunction of Fig. 4.6. (From Rössler and Winkler, 1997.)

Confinement in quantum wells

Now we consider a heterostructure consisting of two heterojunctions. An undoped GaAs layer 'A' of thickness L_A is imbedded between two n-doped Al$_\mathrm{x}$Ga$_{1-\mathrm{x}}$As layers 'B' as shown in Fig. 4.8. For large L_A we have the situation of two separated single heterojunctions. However, below some critical value of L_A the neutral barrier in the center disappears and the free space charges spread over the whole width of the GaAs layer. Assuming a homogenous distribution of the transferred electrons the band bending caused by the transferred electrons can be qualitatively estimated. The corresponding electrostatic potential $V(z)$ follows from the Poisson equation with $n_{2\mathrm{D}}/L_\mathrm{A}$ as the averaged electron density in layer A

$$V(z) - V(0) = -\frac{e^2}{2\varepsilon_0\varepsilon_r}\frac{n_{2\mathrm{D}}}{L_\mathrm{A}}z^2 \,. \tag{4.31}$$

Therefore the amplitude of the bending potential $|V(0) - V(\frac{L_\mathrm{A}}{2})|$ is proportional to the width L_A of the A layer. For small enough L_A the amplitude decreases and

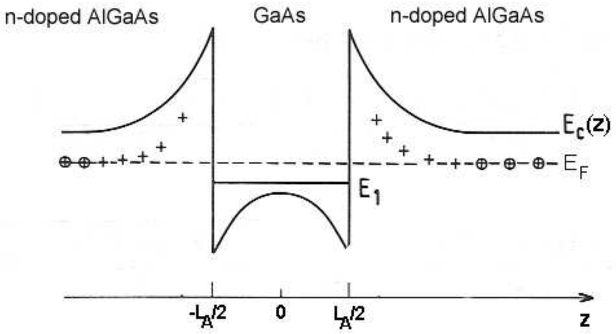

Figure 4.8: Schematic band diagram of a modulation-doped quantum well.

the band bending can be neglected or treated only as a small perturbation of the undoped quantum well. As a consequence a nearly perpendicular potential well exists for the conduction band with a depth corresponding to the conduction band discontinuity $V_{(c)}$ at the interface. A similar well but with different (smaller) band discontinuity exists for the valence band.

Thus Eq. (4.15) for the envelope function of the conduction band (i.e. $\mu = (c)$) takes the form

$$\left(-\frac{\hbar^2}{2}\frac{\mathrm{d}}{\mathrm{d}z}\frac{1}{m^*_{(c)}(z)}\frac{\mathrm{d}}{\mathrm{d}z} + \frac{\hbar^2 \mathbf{k}_\parallel^2}{2m^*_{(c)}(z)} + E^{\mathrm{A}}_{(c)0} + V_{(c)}\,\Theta\Big(|z| - \frac{L_{\mathrm{A}}}{2}\Big)\right)\varphi_{(c)}(z) = E\varphi_{(c)}(z) \tag{4.32}$$

with

$$m^*_{(c)}(z) = \begin{cases} m^*_{\mathrm{A}} & \text{if} \quad |z| \le \frac{L_{\mathrm{A}}}{2} \\ m^*_{\mathrm{B}} & \text{if} \quad |z| \ge \frac{L_{\mathrm{A}}}{2} \end{cases} . \tag{4.33}$$

Except for the fact that the effective masses m^*_{A} and m^*_{B} may be different or negative, Eq. (4.32) at $\mathbf{k}_\parallel = 0$ is identical to the quantum mechanics textbook case of a particle confined in a 1D square well with finite barrier height. In our case $m^*_{\mathrm{A}} = m^*_{\mathrm{GaAs}}$ and $m^*_{\mathrm{B}} = m^*_{\mathrm{Al_xGa_{1-x}As}}$ are positive, but slightly different. Because of the inversion symmetry around the midplane of the well, the wave functions have either even or odd parity, and so the bound state solutions are given by

$$\varphi_{(c)}(z) = \begin{cases} A\cos(k_{\mathrm{A}} z) & \text{if} \quad |z| < L_{\mathrm{A}}/2 \\ Be^{-\kappa_{(c)}(|z| - L_{\mathrm{A}}/2)} & \text{if} \quad |z| \ge L_{\mathrm{A}}/2 \end{cases} \tag{4.34}$$

or

$$\varphi_{(c)}(z) = \begin{cases} A\sin(k_{\mathrm{A}} z) & \text{if} \quad |z| < L_{\mathrm{A}}/2 \\ Be^{-\kappa_{(c)}(|z| - L_{\mathrm{A}}/2)} & \text{if} \quad |z| \ge L_{\mathrm{A}}/2 \end{cases} \tag{4.35}$$

with

$$E - E^{\mathrm{A}}_{(c)0} = \frac{\hbar^2 k_{\mathrm{A}}^2}{2m^*_{\mathrm{A}}} + \frac{\hbar^2 \mathbf{k}_\parallel^2}{2m^*_{\mathrm{A}}} = V_{(c)} - \frac{\hbar^2 \kappa_{(c)}^2}{2m^*_{\mathrm{B}}} + \frac{\hbar^2 \mathbf{k}_\parallel^2}{2m^*_{\mathrm{B}}} . \tag{4.36}$$

The continuity conditions at the interfaces yield

$$\tan\left(\frac{k_{\mathrm{A}} L_{\mathrm{A}}}{2}\right) = \frac{\kappa_{(c)}}{k_{\mathrm{A}}}\frac{m^*_{\mathrm{A}}}{m^*_{\mathrm{B}}} \quad \text{and} \quad \tan\left(\frac{k_{\mathrm{A}} L_{\mathrm{A}}}{2}\right) = -\frac{k_{\mathrm{A}}}{\kappa_{(c)}}\frac{m^*_{\mathrm{B}}}{m^*_{\mathrm{A}}} , \tag{4.37}$$

respectively, whose roots are the bound state solutions of the quantum well problem. In general, there is no analytical solution for the problem except of the limiting case where $V_{(\mathrm{c})}$ is infinite and hence m^*_{B} becomes irrelevant. In this case the carriers are completely confined inside the well and

$$\varphi_{(\mathrm{c})}(z) \equiv \varphi^{\infty}_{(\mathrm{c})_l}(z) = \sqrt{\frac{2}{L_{\mathrm{A}}}} \begin{cases} \cos(l\pi z/L_{\mathrm{A}}) & l = 1, 3, 5, \ldots \\ \sin(l\pi z/L_{\mathrm{A}}) & l = 2, 4, 6, \ldots \end{cases}, \tag{4.38}$$

where l denotes again the subband levels. The corresponding energy eigenvalues are

$$E^{\infty}_{l\mathbf{k}_{\|}} = E^{\mathrm{A}}_{(\mathrm{c})0} + \frac{\hbar^2}{2m^*_{\mathrm{A}}} \frac{l^2\pi^2}{L^2_{\mathrm{A}}} + \frac{\hbar^2 \mathbf{k}^2_{\|}}{2m^*_{\mathrm{A}}}\,. \tag{4.39}$$

These subband energies are usually considerably different from those of a finitely deep well. However, in many applications the solutions for the envelope function (4.38) describing the confinement of the electrons in an infinitely deep well are sufficiently accurate for the finite barrier case as well. For higher precision one has to solve numerically the equation

$$\sqrt{\frac{m^*_{\mathrm{A}}}{m^*_{\mathrm{B}}} \frac{2m^*_{\mathrm{A}}}{\hbar^2 k^2_{\mathrm{A}}} \Big(V_{(\mathrm{c})} - \frac{\hbar^2 \mathbf{k}^2_{\|}}{2m^*_{\mathrm{A}}} (1 - \frac{m^*_{\mathrm{A}}}{m^*_{\mathrm{B}}}) - \frac{\hbar^2 k^2_{\mathrm{A}}}{2m^*_{\mathrm{A}}} \Big)} = \begin{cases} \tan\left(\frac{k_{\mathrm{A}} L_{\mathrm{A}}}{2}\right) \\ -\cot\left(\frac{k_{\mathrm{A}} L_{\mathrm{A}}}{2}\right) \end{cases} \text{for } \begin{matrix} \text{even} \\ \text{odd} \end{matrix}\ \varphi_{(\mathrm{c})} \tag{4.40}$$

in order to obtain $k_{\mathrm{A}l}$ (l numerates the different solutions) and with it via (4.34–4.37) also the envelope functions $\varphi_{(\mathrm{c})_l}(z)$ and the energy eigenvalues $E_{l\mathbf{k}_{\|}}$. Note, that the confining potential $V_{(\mathrm{c})}$ of the well is reduced in Eq. (4.40) by the effective mass mismatch by an amount of $\frac{\hbar^2 \mathbf{k}^2_{\|}}{2}(\frac{1}{m^*_{\mathrm{A}}} - \frac{1}{m^*_{\mathrm{B}}})$, which depends on the electron motion perpendicular to the well growth direction. Therefore, the solutions of (4.40) are $k_{\|}$-dependent and with them the envelope functions $\varphi_{(\mathrm{c})_l}$ as well. A similar approximation as for the heterojunction, see Eq. (4.19), can be made to decouple parallel and perpendicular electron motion in the quantum well. For small quantization energies and small kinetic energies of the electrons (compared to the fundamental gap) the position dependent effective mass $m^*_{(\mathrm{c})}(z)$ in the in-plane dispersion term $\frac{\hbar^2 \mathbf{k}^2_{\|}}{2m^*_{(\mathrm{c})}(z)}$ of (4.32) can be replaced by an averaged effective in-plane mass m^*_l with

$$\frac{1}{m^*_l} = \frac{1}{m^*_{\mathrm{A}}} \left[1 - 2 \int\limits_{L_{\mathrm{A}}/2}^{\infty} \mathrm{d}z\, |\varphi_{(\mathrm{c})_l}(z)|^2 \right] + \frac{2}{m^*_{\mathrm{B}}} \int\limits_{L_{\mathrm{A}}/2}^{\infty} \mathrm{d}z\, |\varphi_{(\mathrm{c})_l}(z)|^2\,. \tag{4.41}$$

Then Eq. (4.32) simplifies to

$$\Big(-\frac{\hbar^2}{2} \frac{\mathrm{d}}{\mathrm{d}z} \frac{1}{m^*_{(\mathrm{c})}(z)} \frac{\mathrm{d}}{\mathrm{d}z} + V_{(\mathrm{c})}\, \Theta\Big(|z| - \frac{L_{\mathrm{A}}}{2}\Big)\Big) \varphi_{(\mathrm{c})_l}(z) = \Big(E_l - E^{\mathrm{A}}_{(\mathrm{c})0} - \frac{\hbar^2 \mathbf{k}^2_{\|}}{2m^*_l} \Big) \varphi_{(\mathrm{c})_l}(z) \tag{4.42}$$

and the resulting equation corresponding to (4.40) becomes independent of $k_\parallel$. In this way $k_{\mathrm{A}l}$ and the envelope functions $\varphi_{(\mathrm{c})_l}(z)$ will be equivalent to the $\mathbf{k}_\parallel = 0$ solutions of Eq. (4.32) and the energy eigenstates are

$$E_l \equiv E_{l\mathbf{k}_\parallel} = E^{\mathrm{A}}_{(\mathrm{c})0} + \frac{\hbar^2 k^2_{\mathrm{A}l}}{2m^*_{\mathrm{A}}} + \frac{\hbar^2 \mathbf{k}^2_\parallel}{2m^*_l} \,. \tag{4.43}$$

Zheng Yisong *et al.* (1997) have discussed in detail the influence of the finite barrier height and the effective mass mismatch on the electron-acoustic phonon scattering rate for GaAs/$\mathrm{Al_{0.3}Ga_{0.7}As}$ quantum wells. Particularly for narrow well widths below 10 nm the scattering rate calculated within the model of an infinitely high potential well is highly overestimated. On the other hand the effective mass mismatch has a significant effect only for higher electron energies. For narrow quantum wells additional corrections due to the conduction band nonparabolicity are important (Ekenberg, 1989).

Just like in the case of modulation-doped heterojunctions, the states for holes in quantum wells are much more complex than in the electron case. The set of functions which diagonalize the bulk $\mathbf{k}\cdot\mathbf{p}$ Hamiltonian is not a basis set for the quantum well potential symmetry. Strong mixing of the $j = \frac{3}{2}$ states with $m_j = \pm\frac{3}{2}$ and $m_j = \pm\frac{1}{2}$ is required to satisfy the boundary conditions at the interfaces. Thus, to deduce the valence band structure in a quantum well, one has once again to solve the differential equation system (4.16) numerically. In Fig. 4.9 the result of such a calculation is displayed for a GaAs/$\mathrm{Al_{0.3}Ga_{0.7}As}$ quantum well. The reduced symmetry lifts the degeneracy between the light and heavy hole bulk states for $\mathbf{k} = 0$.

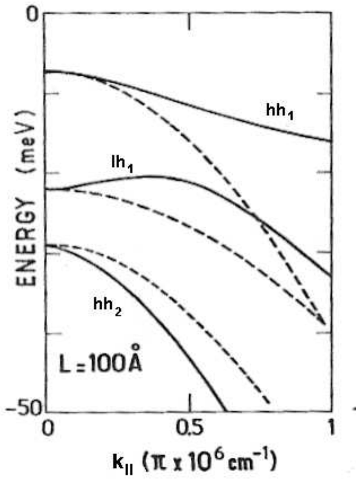

Figure 4.9: In-plane dispersion relations of valence subbands for a (100) GaAs/$\mathrm{Al_{0.3}Ga_{0.7}As}$ quantum well of 100 Å width (solid lines). Dashed lines correspond to a diagonal approximation, when coupling is neglected. (From Bastard, 1992.)

Then the $\mathbf{k}\cdot\mathbf{p}$ interaction term causes even in a simple-minded successive perturbation theory (considering only the diagonal terms) a mass reversal of the $m_j = \pm\frac{3}{2}$ and $m_j = \pm\frac{1}{2}$ states as exposed by the dashed lines in Fig. 4.9. The bulk heavy hole band ($m_j = \pm\frac{3}{2}$) has now a light in-plane mass (and a heavy mass along the z-direction), whereas the light hole band ($m_j = \pm\frac{1}{2}$) now has a heavy in-plane mass (and a light mass in z-direction). Therefore the labelling arising from the original light hole (lh_n) and heavy hole bulk bands (hh_n) is only symbolic. The mass reversal effect causes hh_1 to cross lh_1, as the $\mathbf{k}_\| = 0$ lh_1 state is below the $\mathbf{k}_\| = 0$ hh_1 state. The coupling via the $\mathbf{k}_\|$-dependent off-diagonal terms replaces this crossing by anticrossing. The mixing between the $\mathbf{k} = 0$ levels is very strong, resulting in highly nonparabolic subband dispersions (solid lines in Fig. 4.9). Due to the coupling between lh_1 and hh_2 (and other states of lower energies) this fact becomes most apparent in the electron-like behaviour of the lh_1 subband near $\mathbf{k}_\| = 0$. Figure 4.10 shows the considerable differences in the hole band structure of quantum wells with different orientations (growth directions) as obtained by Houng *et al.* (1988). For the (001) and (111) quantum wells the in-plane dispersions are nearly spherically symmetric (in contrast to the (110) quantum well). We see that the effective hole masses and the spacing between the subbands strongly depend on the orientation of the quantum well as it was also verified by the calculations of Meney (1992). For a (311) $\mathrm{GaAs/Al_xGa_{1-x}As}$ quantum well the uppermost hole state is again nearly isotropic, but lower hole subbands exhibit significant anisotropy (Valadares, 1992; Hayden *et al.*, 1994).

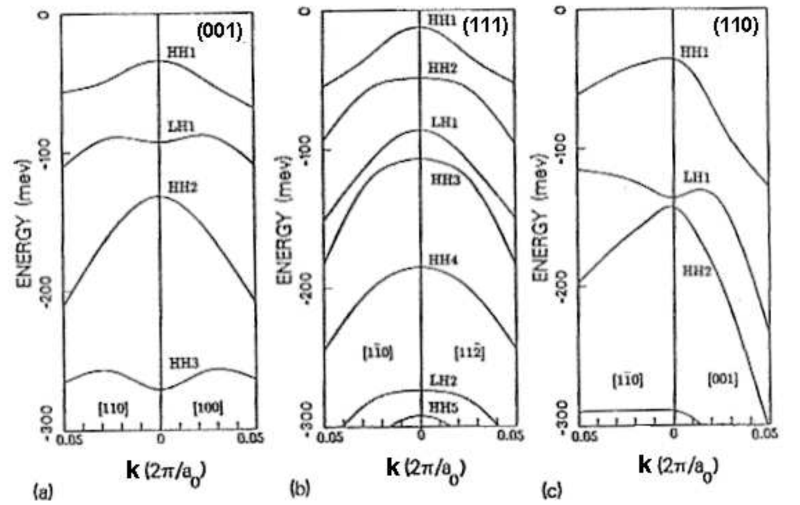

Figure 4.10: Calculated valence subbands for a $\mathrm{GaAs/Al_{0.3}Ga_{0.7}As}$ quantum well of width $L_\mathrm{A} = 85\,\mathrm{\AA}$ for three different growth directions. (From Houng *et al.*, 1988.)

Confinement in quantum wires

If a lateral confinement is added to a 2D electron system, the electronic states are quantized in two directions and the carrier transport is one-dimensional. Following a suggestion of Sakaki (1980) such (quasi-)1D carrier systems in GaAs heterostructures were first studied by Petroff *et al.* (1982). In practice, the 1D systems are realized with the help of electron beam lithography forming patterned gates on the top of a sample with a 2D electron gas. If one puts a negative voltage on parallel gates, the electrons are repelled from the regions directly under the gates to the regions between them. And, if the potential is large enough, the 2D electron gas breaks up into independent strips with quasi-1D behaviour. A self-consistent modelling of the electrostatic fields in these so called quantum wires is complicated and the exact shape is hardly known. Therefore simpler analytic models have been invoked to explain the experimental data. Because the electrons move freely (in the effective mass sense) only in one direction (here in the y-direction) and are confined in the other two, the following ansatz for the electron envelope function is made

$$\xi(\mathbf{r}) \sim e^{iky}\varphi(z)\,\phi(x)\ . \tag{4.44}$$

This particular choice results in a complete separation of the electron motion in the three spatial directions and seems to be a fairly good approximation (Lai and Das Sarma, 1986; Bastard *et al.*, 1991) for the systems of interest to us.[1] For the z-direction, solutions of the modulation-doped heterojunction (4.25,4.27) or of the quantum well (4.38) are used, depending on the system which serves as the 2D basis. The potential confining the electrons in x-direction can be approximated either by a 'particle-in-a-box' rectangular well (Wheeler *et al.*, 1982) or by a 'harmonic-oscillator-like' parabolic well. Detailed self-consistent numerical results by Laux *et al.* (1988), as displayed in Fig. 4.11, show that the actual confining potential is somewhat in between. In respect of uncertainties in the experimental geometry and in the diverse parameters entering the theory, both models are a reasonable approximation to real quasi-1D systems and offer the demanded analytical simplicity. Thus the function $\phi(x)$ is given in the first case by harmonic wave functions restricted to the confined region of $-w \le x \le w$

$$\phi(x) \equiv \phi_n(x) = \sqrt{\frac{1}{w}}\left\{\begin{array}{ll}\cos(n\pi x/2w) & n = 1,3,5,\ldots\\ \sin(n\pi x/2w) & n = 2,4,6,\ldots\end{array}\right. . \tag{4.45}$$

For the case of a parabolic confinement potential in x-direction, namely $V(x) = \frac{\hbar^2}{2m^*}\frac{x^2}{w^4}$, with a characteristic channel 'width' of the order of $2w$, the function $\phi(x)$

---

[1] Due to the usually narrower well width in the growth direction (z) than in the lateral direction (x), the energy spacing between different z-sublevels is large compared to the lateral confinement energies. In this case, the separation of the carrier motion in z-direction from the lateral motion should be a reasonable approximation.

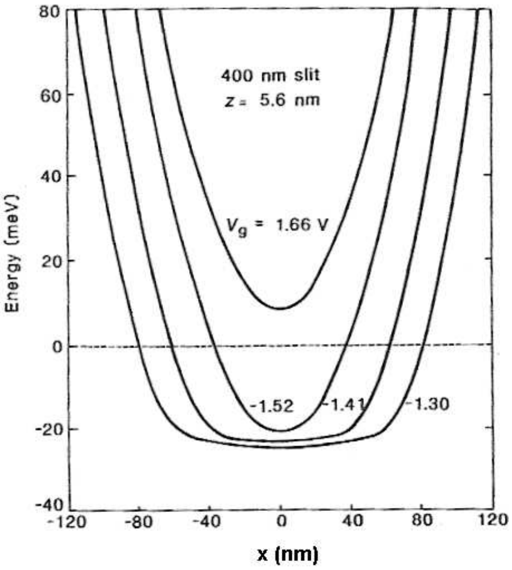

Figure 4.11: Self-consistent potential profile in a line at 5.6 nm below a GaAs/AlGaAs heterojunction across a quasi-1D channel defined in a 2D electron gas by a gate separation of 400 nm with different biases applied to the gates. (From Laux *et al.*, 1988.)

is equal to the oscillator eigenfunctions

$$\phi(x) \equiv \phi_n(x) = \sqrt{\frac{1}{\pi^{1/2}(n-1)!\,2^{n-1}\,w}}\; e^{-x^2/2w^2}\; \mathrm{H}_{n-1}(x/w) \quad n = 1, 2, 3, \ldots \; . \tag{4.46}$$

Here, $\mathrm{H}_n(x)$ denotes the Hermite polynomials

$$\mathrm{H}_n(x) = (-1)^n e^{x^2} \frac{\mathrm{d}^n}{\mathrm{d}x^n} e^{-x^2} \; . \tag{4.47}$$

The one-electron energy is

$$E_{lnk} = E_{(\mathrm{c})0} + E_l + E_n + \frac{\hbar^2 k^2}{2m^*} \; , \tag{4.48}$$

where E_l and E_n are the appropriate solutions for the bound state energy levels in the z- and x-direction, respectively. For the square well potential it is $E_n = \frac{\hbar^2}{2m^*}\frac{\pi^2 n^2}{(2w)^2}$ and for the parabolic well $E_n = \frac{\hbar^2}{2m^*}\frac{2n-1}{w^2}$. Due to the fact that the well width in the growth direction (z) is typically narrower than in the lateral direction (x), the energy spacing ΔE_l between different z-sublevels is large compared to the lateral confinement energies E_n. Therefore, relating to the confinement in z-direction only the lowest substate is occupied, whereas due to the confinement in x-direction several subbands may be occupied simultaneously.

4.2 The electron-acoustic phonon scattering

In this section we discuss the scattering between low dimensionality confined electrons and acoustic bulk phonons. In using the bulk phonons we neglect all confinement effects on the phonons like the modification of the extended acoustic modes due to the presence of interfaces or the existence of confined and interface acoustic modes (Wendler and Grigoryan, 1988; Nishiguchi, 1994, 1995; Stroscio and Dutta, 2001). This approach is approved by the large ratio of electron and phonon confinement energies, which scales like the ratio of the ion and electron mass. The derived results are mostly not very different from that of calculations including confined acoustic and interface acoustic phonon modes (see, e.g. Das Sarma *et al.*, 1992, and references therein). Confined phonon modes play a quantitative role only for confinement lengths less than 5 nm. Interface phonon contributions are not significant unless the well width is below 3 nm. The reason for the latter fact is that the electron wavefunction is usually very small at the interface where the interface phonon amplitude peaks.

Two principal mechanisms account for electron-acoustic phonon interaction in GaAs: deformation potential scattering, and piezoelectric scattering. Both interaction mechanisms will be discussed in the following subsections. In addition we will shortly review the so called macroscopic deformation coupling or ripple mechanism, intrinsic for systems with interfaces but significant only for small-size nanostructures.

4.2.1 Deformation potential scattering

The *deformation potential* (DP) theorem of Bardeen and Shockley (1950) states for long-wavelength acoustic modes, that the electron-phonon interaction potential can be taken as

$$V_{\mathrm{el-ph}}^{(\mathrm{DP})} = \sum_{k,l} \Theta_{kl} S_{kl} \ , \tag{4.49}$$

where S_{kl} is the strain tensor defined in Eq. (3.3) and Θ_{kl} is the so called deformation potential tensor. The fundamentals of the deformation potential method are as follows: When an elastic wave propagates in a crystal the elementary cells change their volume or, more general, are deformed. Thus the position of the electron bands is shifted because of its dependence on the lattice constants. Since in semiconductors the electron states of interest are usually those near a band extremum this variation of electron band bottom is just the interaction energy between an electron and an acoustic phonon. Its value must be related to the local displacement $\mathbf{u}(\mathbf{r})$ in the crystal and/or its derivatives. Since for long-wave acoustic oscillations neighbouring atoms or unit cells move by almost the same amount, the interaction energy cannot be proportional to the displacement itself. Therefore, in lowest order only the differential displacement, namely the strain S, is of importance. In general, the deformation potential tensor Θ_{kl} has 6 independent components since S_{kl} is symmetrical and Θ_{kl} must have the same property. For cubic crystals this number reduces to three independent components. If the extremum of the band is in the Brillouin zone center (like for the lowest conduction band in GaAs), Θ_{kl} is simply a scalar

$$\Theta_{kl} = \delta_{kl}\Theta_{\mathrm{d}} \tag{4.50}$$

and relates to pure dilatation. Then

$$V_{\mathrm{el-ph}}^{(\mathrm{DP})} = \Theta_{\mathrm{d}} \nabla \cdot \mathbf{u}(\mathbf{r}) \tag{4.51}$$

and a shear deformation that does not alter the relative change in volume $(\nabla \cdot \mathbf{u})$ sets up no deformation potential. In spite of a large number of calculations and measurements there is no absolutely reliable numerical value for the parameter Θ_{d}. Its value for GaAs varies from -6 to $-18\,\mathrm{eV}$ (Adachi, 1994), but the most probable value should be between -7 and $-11\,\mathrm{eV}$.

When $\mathbf{u}(\mathbf{r})$ is expanded into terms of travelling plane waves, see Eq. (3.11), it is

$$\begin{aligned} V_{\mathrm{el-ph}}^{(\mathrm{DP})} &= i\,\Theta_{\mathrm{d}} \sum_{\mathbf{q},\lambda} \Big(\frac{\hbar}{2\varrho\omega_{\mathbf{q},\lambda}V_{\mathrm{c}}}\Big)^{\frac{1}{2}} \mathbf{e}_{\hat{\mathbf{q}},\lambda}\cdot\mathbf{q}\,\Big(b_{\mathbf{q},\lambda}e^{i\mathbf{qr}} - b^{+}_{\mathbf{q},\lambda}e^{-i\mathbf{qr}}\Big) \\ &= \sum_{\mathbf{q},\lambda} h^{(\mathrm{DP})}_{\mathbf{q},\lambda}\; e^{i\mathbf{qr}}\Big(b_{\mathbf{q},\lambda} + b^{+}_{-\mathbf{q},\lambda}\Big)\;, \end{aligned} \tag{4.52}$$

where we have introduced the notations

$$h^{(\mathrm{DP})}_{\mathbf{q},\lambda} = i\,\Theta_{\mathrm{d}}\Big(\frac{\hbar}{2\varrho V_{\mathrm{c}} c_{\hat{\mathbf{q}},\lambda}}\Big)^{\frac{1}{2}}\,\sqrt{q}\;(\mathbf{e}_{\hat{\mathbf{q}},\lambda}\cdot\hat{\mathbf{q}}) \tag{4.53}$$

and $\hat{\mathbf{q}} = \mathbf{q}/q$. Note, that the appearance of the scalar product between the polarization vector $\mathbf{e}_{\hat{\mathbf{q}},\lambda}$ and the direction of the phonon wavevector $\hat{\mathbf{q}}$ does not mean that only longitudinal acoustic phonons interact with electrons via deformation potential scattering. The opposite statement, found in many textbooks and papers about electron-phonon coupling in semiconductors, is true only for phonon wavevectors in direction of high crystal symmetry, where the polarization vector of the transverse phonon modes is really perpendicular to $\mathbf{q}$.

In the case of the degenerate valence bands, uniaxial strains tend to remove the degeneracy. According to Bir and Pikus (1960, 1972) the deformation potential scattering of holes with acoustic phonons is described by three deformation potentials a, b and d. The constant a is associated with pure dilatation produced by hydrostatic pressure and describes the shift of the band edge, whereas b and d give the splitting of the heavy and light hole bands at $\mathbf{k} = 0$ due to uniaxial shear strains in the $\langle 100\rangle$ and $\langle 111\rangle$ directions, respectively. Lawaetz (1968) has shown that within the scope of an isotropic phonon model (as discussed in Section 4.2.4) an approximate description by a single effective deformation potential Θ_{eff} can at least fit some details of the hole-acoustic phonon interaction with sufficient accuracy. For GaAs, this value of Θ_{eff} is reported as 6.7 eV (Adachi, 1994).

4.2.2 Piezoelectric coupling

In polar crystals the vibrations of oppositely charged ions induce long range macroscopic fields and the interaction of the electrons with these fields produces contributions to the electron-phonon scattering. First order polarization occurs in connection with the contrary displacement of two atoms in the primitive cell. This electron-optical phonon interaction is known as Fröhlich interaction (Fröhlich, 1937) and is the dominant scattering mechanism of pure III-V semiconductors at room temperature. In polar crystals with no inversion symmetry there exists still an additional, second order polarization proportional to acoustic strain. The resulting scattering mechanism, the *piezoelectric* (PE) electron-acoustic phonon interaction was first investigated by Meijer and Polder (1953) and is very important in the low temperature range, in which we are interested.

In the presence of the piezoelectric effect the components of the polarization vector $\mathbf{P}$ are given by

$$P_j = \sum_k \varepsilon_0 \kappa^0_{jk} E_k + \sum_{k,l} \beta_{j,\,kl} S_{kl} \ , \tag{4.54}$$

where $\mathbf{E}$ is the electric field, κ^0_{jk} is the polarizability tensor, and $\beta_{j,\,kl}$ is the piezoelectric tensor. Consequently the components of the electric displacement $\mathbf{D}$ are

$$D_j = \sum_k \varepsilon_0 \kappa_{jk} E_k + \sum_{k,l} \beta_{j,\,kl} S_{kl} \tag{4.55}$$

with $\kappa_{jk} = 1 + \kappa^0_{jk}$ as the dielectric permittivity tensor. On the other hand, $\nabla \cdot \mathbf{D} = \rho$ and $\mathbf{E} = -\nabla\varphi$, where ρ is the free charge density and φ the electrostatic potential. Thus we derive the equation

$$\sum_{j,k} \varepsilon_0 \kappa_{jk} \frac{\partial^2 \varphi}{\partial x_j \partial x_k} - \sum_{j,k,l} \beta_{j,\,kl} \frac{\partial S_{kl}}{\partial x_j} = -\rho \ , \tag{4.56}$$

from which we can find the electrostatic potential φ and finally the interaction potential $V^{(\text{PE})}_{\text{el-ph}} = -|e|\,\varphi$. Assuming bare lattice polarization ($\varrho = 0$) and inserting (3.11) into (3.3) we get from Eq. (4.56) the relation

$$\sum_{j,k} \varepsilon_0 \kappa_{jk} \frac{\partial^2 \varphi}{\partial x_j \partial x_k} = -\sum_{\mathbf{q},\lambda} \left(\frac{\hbar}{2\varrho\omega_{\mathbf{q},\lambda} V_{\text{c}}} \right)^{\frac{1}{2}} \left(b_{\mathbf{q},\lambda} e^{i\mathbf{qr}} + b^+_{\mathbf{q},\lambda} e^{-i\mathbf{qr}} \right) \sum_{j,k,l} \beta_{j,\,kl} (\mathbf{e}_{\hat{\mathbf{q}},\lambda})_l q_k q_j \ . \tag{4.57}$$

This equation can be solved by expanding φ into a Fourier series and we obtain

$$V_{\mathrm{el-ph}}^{(\mathrm{PE})} = -|e| \sum_{\mathbf{q},\lambda} \left(\frac{\hbar}{2\varrho\omega_{\mathbf{q},\lambda} V_{\mathrm{c}}} \right)^{\frac{1}{2}} \frac{\sum_{j,k,l} \beta_{j,\,kl} \, (\mathbf{e}_{\hat{\mathbf{q}},\lambda})_l \, q_j q_k}{\sum_{j,k} \varepsilon_0 \kappa_{jk} \; q_j q_k} \, e^{i\mathbf{qr}} \big(b_{\mathbf{q},\lambda} + b^{+}_{-\mathbf{q},\lambda} \big) \; . \tag{4.58}$$

For cubic crystals of zinc-blende type the dielectric permittivity tensor is a scalar $\kappa_{jk} = \varepsilon_{\mathrm{r}} \, \delta_{jk}$, while the piezoelectric tensor has only one independent constant: $\beta_{y,\,xz} = \beta_{z,\,xy} = \beta_{x,\,yz} (\equiv \beta_{14}$ in reduced notation) and $\beta_{j,\,kl} = 0$ if only two indices coincide. Thus the piezoelectric electron-phonon interaction potential can be written in the form

$$\begin{aligned} V_{\mathrm{el-ph}}^{(\mathrm{PE})} &= -\sum_{\mathbf{q},\lambda} \left(\frac{\hbar}{2\varrho\omega_{\mathbf{q},\lambda} V_{\mathrm{c}}} \right)^{\frac{1}{2}} \frac{2|e|\beta_{14}}{\varepsilon_0 \varepsilon_{\mathrm{r}}} \, e^{i\mathbf{qr}} \big(b_{\mathbf{q},\lambda} + b^{+}_{-\mathbf{q},\lambda} \big) \\ &\qquad \times \frac{q_x q_y (\mathbf{e}_{\hat{\mathbf{q}},\lambda})_z + q_y q_z (\mathbf{e}_{\hat{\mathbf{q}},\lambda})_x + q_x q_z (\mathbf{e}_{\hat{\mathbf{q}},\lambda})_y}{q^2} \\ &= \sum_{\mathbf{q},\lambda} h_{\mathbf{q},\lambda}^{(\mathrm{PE})} \, e^{i\mathbf{qr}} \Big(b_{\mathbf{q},\lambda} + b^{+}_{-\mathbf{q},\lambda} \Big) \end{aligned} \tag{4.59}$$

with

$$h_{\mathbf{q},\lambda}^{(\mathrm{PE})} = 2|e| h_{14} \left(\frac{\hbar}{2\varrho V_{\mathrm{c}} c_{\hat{\mathbf{q}},\lambda}} \right)^{\frac{1}{2}} \frac{\hat{q}_x \hat{q}_y (\mathbf{e}_{\hat{\mathbf{q}},\lambda})_z + \hat{q}_y \hat{q}_z (\mathbf{e}_{\hat{\mathbf{q}},\lambda})_x + \hat{q}_x \hat{q}_z (\mathbf{e}_{\hat{\mathbf{q}},\lambda})_y}{\sqrt{q}} \; . \tag{4.60}$$

The value of the constant $h_{14} = -\beta_{14}/\varepsilon_0 \varepsilon_{\mathrm{r}}$ ranges for GaAs between 1.4 and $1.6 \cdot 10^9\,\mathrm{V/m}$ taking $\beta_{14} = -0.16\,\mathrm{C/m^2}$ (Adachi, 1994).
The above equations show that even with the symmetry properties of the piezoelectric tensor the interaction potential remains highly anisotropic (for details see Section 4.2.4).

4.2.3 Macroscopic deformation coupling

Vasko and Mitin (1995) and Knipp and Reinecke (1995a,b) have shown that there is an additional coupling mechanism between electrons and acoustic phonons in semiconductor heterostructures. Contrary to the mechanisms discussed before, it is intrinsic to systems that have interfaces. Both longitudinal and transverse acoustic phonons induce vibrations of the heterointerfaces and thereby time variations of the confining potential of the electrons. Perturbations of the electron wavefunctions are the consequence. Therefore, the associated interaction between electrons and acoustic phonons is due to *macroscopic* deformations of the nanostructure and does not depend on the microscopic deformation potential tensor (as in the case of the ordinary deformation potential interaction described in Section 4.2.1). It is called macroscopic deformation acoustic coupling or following Knipp and Reinecke (1995b) also *ripple* (RI) mechanism. The latter is in analogy to the inelastic scattering of photons or electrons from a vibrating free surface (Marvin *et al.*, 1980, and

Martin *et al.*, 1988, respectively), but now we have to deal with buried interfaces.

Let $V(\mathbf{r})$ be the potential governing the envelope functions of the electronic state. Then the ripple potential is

$$V_{\mathrm{el-ph}}^{(\mathrm{RI})} = V(\mathbf{r}+\mathbf{u}(\mathbf{r})) - V(\mathbf{r}) \approx \mathbf{u}(\mathbf{r}) \cdot \nabla V(\mathbf{r}) \ . \tag{4.61}$$

If we assume a nanostructure of material 'A' embedded in material 'B' and take the potential in the conduction band to be higher in material 'B' and if we assume a piecewise uniform potential $V(\mathbf{r})$ (cf. Eq. (4.42) for the example of a quantum well), it holds

$$\nabla V(\mathbf{r}) = V_{(\mathrm{c})} \int\limits_S \mathrm{d}^2 r_{\mathrm{s}} \, \delta(\mathbf{r}-\mathbf{r}_{\mathrm{s}}) \, \hat{\mathbf{n}}_{\mathrm{s}} \ . \tag{4.62}$$

Here S is the interface between the inner and outer material, $\mathbf{r}_{\mathrm{s}}$ is a position on this interface, $\hat{\mathbf{n}}_{\mathrm{s}}$ is the outwardly pointing surface normal, and $V_{(\mathrm{c})}$ is the potential barrier between the inner and outside media for the conduction band. Using in a first approximation the bulklike expression for the displacement operator $\mathbf{u}(\mathbf{r})$ we obtain the operator of the ripple electron-phonon interaction in a form similar to (4.52) and (4.59)

$$V_{\mathrm{el-ph}}^{(\mathrm{RI})} = \sum_{\mathbf{q},\lambda} h_{\mathbf{q},\lambda}^{(\mathrm{RI})} \, e^{i\mathbf{q}\mathbf{r}} \left(b_{\mathbf{q},\lambda} + b_{-\mathbf{q},\lambda}^{+} \right) \tag{4.63}$$

with

$$h_{\mathbf{q},\lambda}^{(\mathrm{RI})} = V_{(\mathrm{c})} \left(\frac{\hbar}{2\varrho V_{\mathrm{c}} c_{\hat{\mathbf{q}},\lambda}} \right)^{\frac{1}{2}} \int\limits_S \mathrm{d}^2 r_{\mathrm{s}} \, \delta(\mathbf{r}-\mathbf{r}_{\mathrm{s}}) \, \frac{\hat{\mathbf{n}}_{\mathrm{s}} \cdot \mathbf{e}_{\hat{\mathbf{q}},\lambda}}{\sqrt{q}} \ . \tag{4.64}$$

The δ-function in (4.64) makes sure that, in the corresponding electron-phonon matrix elements, the integral over the electron wavefunctions is restricted to the interfaces.

Following Knipp and Reinecke (1995a), there exists still another term contributing to the ripple interaction which is connected with the spatial dependence of the effective mass. Variations of the effective mass caused by vibrations of the interfaces induce changes of the kinetic term in the envelope function equation (see, e.g. Eq. (4.42)) and therefore account for modulations of the electron quantization energy. The resulting electron-phonon interaction potential is proportional to the difference of the effective masses on both sides of the interface and leads to matrix elements which contain the derivatives of the electron envelope functions taken exclusively at the position of the interfaces.

Normally the ripple interaction is weak compared to ordinary deformation potential or piezoelectric coupling. A very rough estimation shows that for a quantum well of thickness L_{A} the relative strength of ripple and deformation potential is of the order of $V_{(\mathrm{c})}/\Theta_{\mathrm{d}} q L_{\mathrm{A}}$ and for ripple and piezoelectric potential of $V_{(\mathrm{c})}/|e| h_{14} L_{\mathrm{A}}$, respectively. Therefore, this additional mechanism gives relevant contributions only for very narrow quantum wells. The fact that it is significant for small size nanostructures can also be qualitatively understood in a way that, for narrow quantum wells, the position of the energy levels is more affected by the change in the well width than by a change in the band gap. Recent results of Alcalde *et al.* (2000) for quantum dots and of Nishiguchi (2002) for quantum wires, including also the effect of confinement on the phonon modes, have supported the qualitative predictions made by the assumption of pure bulk phonon modes. Both calculations demonstrate that the ripple mechanism should be considered for dot radii or lateral wire dimensions typically less than 3 nm.

4.2.4 The influence of acoustic anisotropy

As shown in Figs. 4.12(d–f) piezoelectric electron-phonon coupling has a complicated directional dependence. The interaction disappears both for longitudinal and transverse phonons travelling along a principal crystal axis. Only TA phonons interact when the phonon direction lies in a cube face (e.g.: $q_x \neq 0$, $q_y \neq 0$, $q_z = 0$) whereas only LA phonons couple for phonon wavevectors along a cube diagonal ($q_x = q_y = q_z$).

The exact determination of the wavevector and polarization dependence of the electron-phonon coupling coefficients for the piezoelectric interaction (4.60) is difficult and requires the knowledge of the polarization vector $\mathbf{e}_{\hat{\mathbf{q}},\lambda}$ for each phonon mode $\mathbf{q}, \lambda$ (the same also holds for the deformation potential interaction, see Eq. (4.53)). Therefore, most of the calculations have involved only averaging over direction. Meijer and Polder (1953) simply took an average of the phonons propagating in $\langle 100 \rangle$, $\langle 110 \rangle$ and $\langle 111 \rangle$ directions, whereas Hutson (1961) and, more general, Zook (1964) calculated a spherical average of $h^{(\mathrm{PE})}_{\mathbf{q},\lambda}$ over the longitudinal and the combined transverse (STA + FTA) phonon modes. To date, the most frequently applied method in calculation of the electron-acoustic phonon coupling is an approximation which disregards the acoustic anisotropy of the phonons. If the elastic anisotropy of the crystal is only small, the polarization vector of the three normal modes will lie approximately along the axes of the phonon coordinate system

$$\mathbf{e}^{\mathrm{is}}_{\mathbf{q},\lambda} = \begin{cases} \parallel \hat{\mathbf{q}} & \text{for LA} \\ \perp \hat{\mathbf{q}} & \text{for TA} \end{cases} . \tag{4.65}$$

In this case the (squared) coupling coefficients of Eq. (4.60) reduce to

$$\left[h^{(\mathrm{PE-is})}_{\mathbf{q},\lambda=\mathrm{LA}}\right]^2 = \frac{\hbar\,(2eh_{14})^2}{2\varrho V_{\mathrm{c}} c_{\hat{\mathbf{q}},\lambda}}\,\frac{9\,\hat{q}_x^2\hat{q}_y^2\hat{q}_z^2}{q} \tag{4.66}$$

for longitudinal phonons and to

$$\left[h^{(\mathrm{PE-is})}_{\mathbf{q},\lambda=\mathrm{STA}}\right]^2 + \left[h^{(\mathrm{PE-is})}_{\mathbf{q},\lambda=\mathrm{FTA}}\right]^2 = \frac{\hbar\,(2eh_{14})^2}{2\varrho V_{\mathrm{c}} c_{\hat{\mathbf{q}},\lambda}}\,\frac{\hat{q}_x^2\hat{q}_y^2 + \hat{q}_x^2\hat{q}_z^2 + \hat{q}_y^2\hat{q}_z^2 - 9\,\hat{q}_x^2\hat{q}_y^2\hat{q}_z^2}{q} \tag{4.67}$$

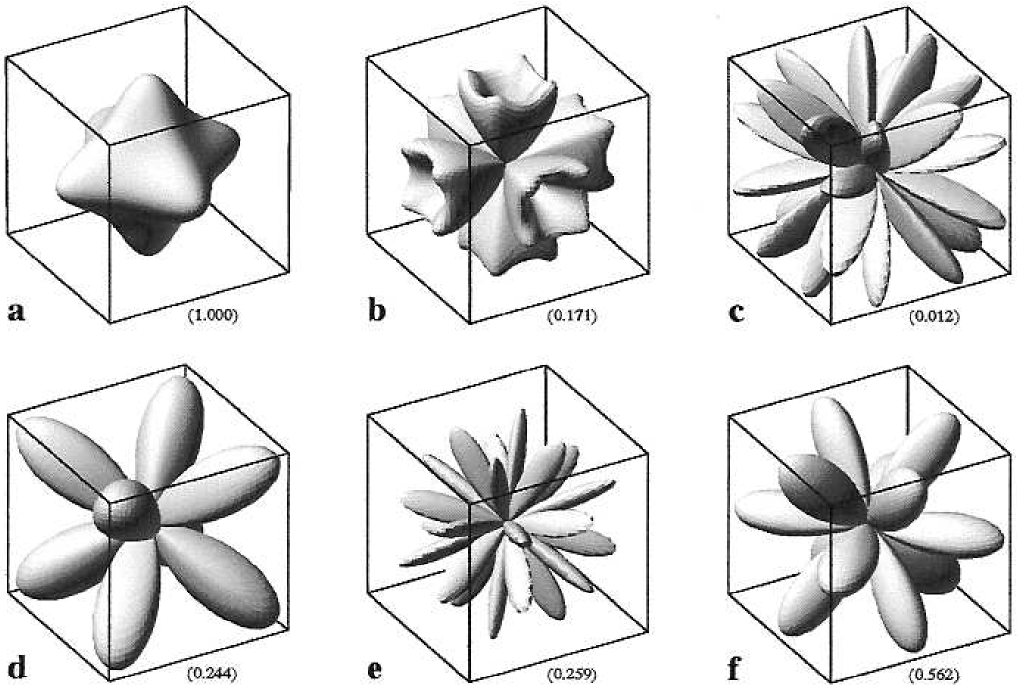

Figure 4.12: (**a**)–(**c**) Angular dependence of the function $\left[\frac{\mathbf{e}_{\hat{\mathbf{q}},\lambda}\cdot\hat{\mathbf{q}}}{c^2_{\mathbf{q},\lambda}}\right]^2$ for the deformation potential coupling in a zinc-blende type crystal. (**d**)–(**f**) Angular dependence of the function $\left[\frac{\hat{q}_x\hat{q}_y(\mathbf{e}_{\hat{\mathbf{q}},\lambda})_z+\hat{q}_y\hat{q}_z(\mathbf{e}_{\hat{\mathbf{q}},\lambda})_x+\hat{q}_x\hat{q}_z(\mathbf{e}_{\hat{\mathbf{q}},\lambda})_y}{c_{\mathbf{q},\lambda}}\right]^2$ for the piezoelectric coupling. The edges of each cube are parallel to the fourfold axes of the cubic symmetry. The numbers in brackets are the relative linear dimensions of the respective cube. Plots (a,d) are for LA, (b,e) for STA and (c,f) for FTA phonons. (From Jasiukiewicz, 1998.)

for transverse phonons (Zook, 1964). Also the (squared) coupling coefficients for the deformation potential coupling (Eq. (4.53)) simplify in this *isotropic approximation*

$$\left[h^{(\mathrm{DP-is})}_{\mathbf{q},\lambda}\right]^2 = \frac{\hbar\,(\Theta_\mathrm{d})^2}{2\varrho V_\mathrm{c} c_{\hat{\mathbf{q}},\lambda}}\; q \begin{cases} 1 & \text{for LA} \\ 0 & \text{for STA, FTA} \end{cases} . \tag{4.68}$$

It is quite obvious by (4.68) that no deformation potential coupling occurs for transverse phonons within the acoustic isotropic approximation.

The above isotropic approximation for the coupling coefficients (formulae (4.66)–(4.68)) is reasonable as long as we are interested in quantities containing a sum over phonons with many different propagation directions (as it is the case in transport measurements). Nevertheless, it is used in most of the calculations performed for phonon emission or drag. However, even a glance at Fig. 4.12 presenting the plot of the anisotropic coupling coefficients documents the shortcomings of the isotropic approximation. Not only the complete neglect of deformation potential coupled

TA phonons but also the smearing out of the characteristic angular dependence of the piezoelectric interaction lead to wrong results and interpretations. An extensive discussion of this fact is given for the case of acoustic phonon emission in Section 6.3.2.

4.2.5 Electron-phonon interaction and electron confinement

Having determined the coupling coefficients it is now advisable to write the electron-phonon interaction of the many-particle electron system in second quantized form. For this purpose we introduce electron field operators $\hat{\psi}(\mathbf{r})$ and obtain

$$\begin{aligned} H_{\mathrm{el-ph}} &= \int \mathrm{d}^3 r \; \hat{\psi}^{+}(\mathbf{r}) V_{\mathrm{el-ph}}(\mathbf{r}) \hat{\psi}(\mathbf{r}) \\ &= \sum_{\alpha,\alpha'} \int \mathrm{d}^3 r \; \psi_\alpha^*(\mathbf{r}) V_{\mathrm{el-ph}}(\mathbf{r}) \psi_{\alpha'}(\mathbf{r}) \; c_\alpha^+ c_{\alpha'} \; . \end{aligned} \tag{4.69}$$

In the second step of (4.69) the electron field operator has been expanded into terms of a single-electron basis $\psi_\alpha(\mathbf{r})$, i.e. $\hat{\psi}(\mathbf{r}) = \sum_\alpha \psi_\alpha(\mathbf{r})\, c_\alpha$, with c_α, c_α^+ as electron annihilation and creation operators. Following the arguments of Section 4.1.2 the wavefunction $\psi_\alpha(\mathbf{r})$ for a heterostructure is presented as a sum of products of slowly varying envelope functions $\xi_\nu^{(\alpha)}(\mathbf{r})$ and rapidly varying zone center Bloch functions $u_{\nu 0}^{(\alpha)}(\mathbf{r})$. For the interesting case of large phonon wavelengths the variation in the disturbance potential $V_{\mathrm{el-ph}}(\mathbf{r})$ is very small within one elementary cell and the integral over the volume V of the whole electron system can be written in the form (see, e.g. Askerov, 1994)

$$\begin{aligned} &\int_V \mathrm{d}^3 r \; \psi_\alpha^*(\mathbf{r}) V_{\mathrm{el-ph}}(\mathbf{r}) \psi_{\alpha'}(\mathbf{r}) \\ &\qquad \approx \sum_{\nu,\nu'} \int_V \mathrm{d}^3 r \; \left(\xi_\nu^{(\alpha)}(\mathbf{r})\right)^* V_{\mathrm{el-ph}}(\mathbf{r})\, \xi_{\nu'}^{(\alpha')}(\mathbf{r}) \; \frac{1}{\Omega_0} \int_{\Omega_0} \mathrm{d}^3 r' \; \left(u_{\nu 0}^{(\alpha)}(\mathbf{r}')\right)^* u_{\nu' 0}^{(\alpha')}(\mathbf{r}') \; , \end{aligned} \tag{4.70}$$

where Ω_0 is the elementary cell volume. Approximation (4.70) is based on the fact that when expanding $u_{\nu 0}^*(\mathbf{r}) u_{\nu' 0}(\mathbf{r})$ as a Fourier series over reciprocal lattice vectors $\mathbf{G}$, only the term with $\mathbf{G} = 0$ will give a significant contribution to the integral over V. All allowed nonzero values of $\mathbf{G}$ are much larger than the typical values of carrier and phonon wavevectors.

Thus in a one-band model valid mainly for electron-phonon scattering in the conduction band only the overlap integral over the envelope functions remains and

$$\begin{aligned} H_{\mathrm{el-ph}} &\approx \sum_{\alpha,\alpha'} \int_V \mathrm{d}^3 r \, \left(\xi^{(\alpha)}(\mathbf{r})\right)^* V_{\mathrm{el-ph}}(\mathbf{r}) \, \xi^{(\alpha')}(\mathbf{r}) \; c_\alpha^+ c_{\alpha'} \\ &= \sum_{\mathbf{q},\lambda} h_{\mathbf{q},\lambda}(b_{\mathbf{q},\lambda} + b^+_{-\mathbf{q},\lambda}) \sum_{\alpha,\alpha'} \int_V \mathrm{d}^3 r \, \left(\xi^{(\alpha)}(\mathbf{r})\right)^* e^{i\mathbf{qr}} \xi^{(\alpha')}(\mathbf{r}) \; c_\alpha^+ c_{\alpha'} \\ &\equiv \sum_{\mathbf{q},\lambda} h_{\mathbf{q},\lambda}(b_{\mathbf{q},\lambda} + b^+_{-\mathbf{q},\lambda}) \rho_{-\mathbf{q}} \; . \end{aligned} \tag{4.71}$$

As the envelope function $\xi^{(\alpha)}(\mathbf{r})$ is identical to the wavefunction of an (ideal) quasi low-dimensional electron gas, the operator

$$\rho_{\mathbf{q}} = \sum_{\alpha,\alpha'} \int_V \mathrm{d}^3 r \, \left(\xi^{(\alpha)}(\mathbf{r})\right)^* e^{-i\mathbf{qr}} \xi^{(\alpha')}(\mathbf{r}) \; c_\alpha^+ c_{\alpha'} \tag{4.72}$$

introduced in (4.71) is equal to the Fourier transform of the density operator of a *quasi* low-dimensional electron gas. For a quasi-2D electron system in a modulation-doped heterojunction or quantum well the envelope function is $\xi^{(\alpha)}(\mathbf{r}) \sim e^{i\mathbf{k}_\parallel \mathbf{r}_\parallel} \varphi_l(z)$ with $\alpha = \{l, \mathbf{k}_\parallel, \sigma\}$ and $\varphi_l(z)$ as the solution of the respective 1D Schrödinger equation for the given confinement potential (Eq. (4.24) and Eq. (4.42), respectively). Therefore it holds

$$\rho_{\mathbf{q}} = \sum_{ll'} G_{ll'}(q_z) \sum_{\mathbf{k}_\parallel,\sigma} c^+_{l\,\mathbf{k}_\parallel - \mathbf{q}_\parallel\,\sigma} c_{l'\mathbf{k}_\parallel \sigma} \; , \tag{4.73}$$

where

$$G_{ll'}(q_z) = \int \mathrm{d}z \, \varphi_l^*(z) e^{-iq_z z} \varphi_{l'}(z) \tag{4.74}$$

is the so called *overlap integral.* Thus the information about the influence of electron confinement on the electron interaction with bulk acoustic phonons is comprised in the electron density operator or, more precise, in the particular form of the corresponding overlap integral. For typical 1D and 2D confinement potentials in $\mathrm{GaAs/Al_xGa_{1-x}As}$ heterostructures the overlap integral is determined in Appendix C.

The electron-phonon interaction operator in the form of Eq. (4.71) was derived for the single-band case. For a confined hole system a mixing between different valence states usually occurs as it was described in the Sections 4.1.2 and 4.1.3. A detailed study of electron-hole coupling requires therefore the application of multiband models. Corresponding matrix elements have been calculated on the basis of a four-band $\mathbf{k} \cdot \mathbf{p}$ scheme by Kelsall *et al.* (1990) for the case of a GaAs/AlAs quantum well.

Chapter 5

Phonon Induced Electric Current

Now we apply our theoretical concepts of phonon pulse propagation and electron-phonon interaction in low-dimensional systems to a typical experiment of phonon spectroscopy: phonon-drag imaging. In this case, the low-dimensional electrons act as a detector of the phonon quasimomentum flux. We develop a many-body theory for the electric current induced by nonequilibrium phonons in quasi-2D and 1D electron systems, valid also in nonzero magnetic fields. On this basis and using explicitly the results of the phonon focusing calculations of Chapter 3 we then study the phonon induced current as a function of the detector position and the phonon source characteristics. The chapter concludes with detailed analyses of the influence of carrier confinement and acoustic anisotropy on the drag images. These give insights into the properties of low-dimensional electron systems and their coupling to acoustic phonons.

5.1 Basic features and experimental setup

In a system consisting of two subsystems of interacting (quasi-)particles, a directed flow of particles in one of the subsystems may excite by momentum transfer a directed flow in the other subsystem. This process, when it happens between phonons and electrons is called electron-phonon drag and was first predicted by Gurevich (1946). Since this time, various manifestations of the effect have been studied both theoretically and experimentally, but for many years the interest was concentrated on the influence on heat transfer (for a review, see Gurevich and Mashkevich, 1989). By the middle of the eighties it was even the common opinion that the electron-phonon drag, while playing an important part in heat transfer, is negligible in electron transport. Later this belief was vitiated both by new systematic theoretical studies of electron-phonon drag (Gurevich and Mashkevich, 1989) and new thermoelectric power measurements. Fletcher *et al.* (1988) and Ruf *et al.* (1988) showed the dominance of the phonon-drag contribution over the electron diffusion contribution to the thermopower in heterojunctions and MOSFETs at liquid helium temperatures. For a review of theoretical approaches to the phonon drag in the context of thermopower of low-dimensional semiconductor structures see Smith and Butcher (1990) and Butcher (1993). In contrast to the situation in thermopower measurements we are interested in the induction of a voltage or electric current by direct momentum transfer from ballistic phonon pulses. This is known as the phonon-drag effect and was for the case of low-dimensional electron systems first demonstrated in the experiments of Karl *et al.* (1988). Spatially and frequency resolved measurements of this effect allow in combination with numerical calculations a very detailed insight in the electronic properties of low-dimensional systems and their interaction with phonons (Jasiukiewicz *et al.*, 1992; Lehmann *et al.*, 1996). A typical experimental setup for making phonon-drag measurements

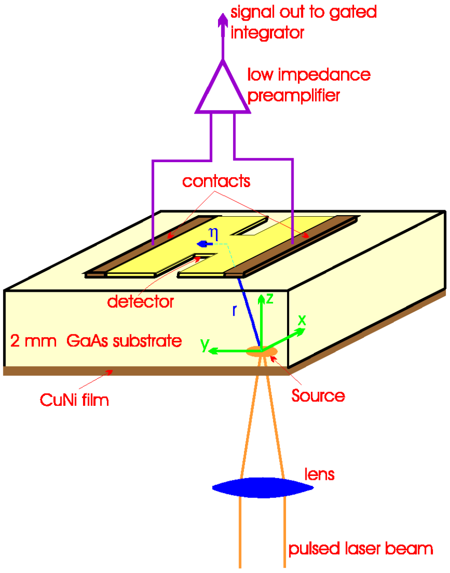

Figure 5.1: Schematic view of a phonon-drag experiment. Nonequilibrium acoustic phonons are generated on the bottom of the crystal, e.g. by thermalizing a laser pulse in a metal film deposited on the GaAs surface. The phonons absorbed by the narrow bridge in the center of the detector (2D electron or hole gas) cause a phonon-drag signal if they have a momentum component in direction of the bridge (here the η-direction). The induced phonon-drag current is mapped as a function of the laser spot position. (From Gańcza *et al.*, 1996.)

is shown in Fig. 5.1. A 2D electron or hole gas formed in a GaAs/$\mathrm{Al_xGa_{1-x}As}$ heterostructure is prepared on one side of a nominally undoped semi-insulating GaAs crystal. On the opposite side of the crystal pulses of nonequilibrium phonons with a typical pulse length of a few tens of nanoseconds are generated. This is realized by heating a small region of a deposited metal film with a focused pulsed laser beam. By scanning the laser over the surface of the film, the phonon-drag signal is detected as a function of the laser position and a two-dimensional map (image) of the phonon-drag effect can be built up. The experimental arrangement of this phonon-drag imaging method is quite similar to the phonon imaging technique described in Section 2.2.2. Karl *et al.* used in their pioneering experiment monochromatic phonon pulses (for the resulting drag image see Fig. 2.8(b) of Chapter 2). Instead of a metal film in the normal state, a superconducting Al film with T_c near 2 K was adopted. Therefore the spectrum of emitted phonons consisted mainly of frequencies around the gap frequency $2\Delta/h$ (see Appendix A.1). The application of tunable superconducting tunnel junctions as the phonon source is an other possibility (Lega *et al.*, 1990). In this case the phonon-drag effect is studied as a function of phonon frequency for a (finite) number of phonon propagation directions (depending on the position of the tunnel junctions). Common to all experiments is that they are carried out at liquid He temperatures, i.e. at temperatures much lower than the Debye temperature. In a very simplistic view the generated nonequilibrium phonons travel ballistically through the crystal and when they are incident on the area of the 2D electron system they are partially absorbed by the electrons. This electron-phonon interaction leads to a transfer of phonon energy and momentum to the electrons. In a next step the excited electrons transfer their gained momentum and energy due to electron-electron interaction within a time of a few hundred femtoseconds to all of the electrons of the low-dimensional system. As a consequence, the momentum distribution function is shifted in the direction of the incoming phonons and a current will flow until an opposing electric field is established. Both, the current or the corresponding electric field can be measured. Both methods produce qualitatively the same results.

Following our explanations made above, the phonon-drag images can be generally interpreted as a convolution of phonon focusing images (describing the magnitude of the incoming phonon signal) and the probability that a current will be induced by these phonons. The calculation of the incoming phonon flux was the main topic of Chapter 3. Therefore we turn our attention now to the question of phonon-drag calculation assuming that the phonon distribution is known.

5.2 Theoretical model of phonon drag

In the following we will present a theory, where the phonon-drag current will be naturally described by the motion of the center of mass of all electrons (Lehmann *et al.*, 1997a). The method is based on the quantum Langevin equation approach to the quantum transport of interacting systems of electrons, impurities and phonons as proposed by Ting and Nee (1986) and Hu and O'Connell (1987). However, we adopt this formalism to a different problem. First of all we apply it to *quasi* low-dimensional electron systems. The fundamental difference is, however, the fact that in our case, the nonfrictional part of the forces due to the phonons does *not* disappear after averaging. Furthermore we use a much more straightforward formulation based on the advantages of the technique of Mori products. In this way and contrary to former theoretical approaches to phonon drag at zero magnetic field (Jasiukiewicz *et al.*, 1992; Lehmann, 1994) and with magnetic field (Falko and Iordanskii, 1992; Dietzel *et al.*, 1993; Gańcza *et al.*, 1996) screening and confinement problems are easier to handle, the basic equations are independent of the dimension of the system and last but not least the underlying physics is more clear.

To describe the motion of the center of mass we consider an electron system of density n_{el}, containing N_{el} electrons with effective mass m^*, interacting with phonons and impurities in the presence of a homogeneous and constant magnetic field. The corresponding Hamiltonian in the center-of-mass and relative coordinates description

$$H = H_{\mathrm{CM}} + H_{\mathrm{el}} + H_{\mathrm{ph}} + H_{\mathrm{el-ph}} + H_{\mathrm{el-im}} \tag{5.1}$$

consists of terms of different nature

$$\begin{aligned}
H_{\mathrm{CM}} &= \tfrac{1}{2N_{\mathrm{el}}m^*}[\hat{\mathbf{P}} - N_{\mathrm{el}}\, e\mathbf{A}(\hat{\mathbf{R}})]^2 + V(\hat{\mathbf{R}}) \ , \\
H_{\mathrm{el}} &= \sum_n E_n c_n^+ c_n + H_{\mathrm{el-el}} \ , \\
H_{\mathrm{ph}} &= \sum_{\mathbf{q},\lambda} \hbar\omega_{\mathbf{q},\lambda} b^+_{\mathbf{q},\lambda} b_{\mathbf{q},\lambda} \ , \\
H_{\mathrm{el-ph}} &= \sum_{\mathbf{q},\lambda} h_{\mathbf{q},\lambda} e^{i\mathbf{q}\hat{\mathbf{R}}} (b_{\mathbf{q},\lambda} + b^+_{-\mathbf{q},\lambda})\rho_{-\mathbf{q}} \ , \\
H_{\mathrm{el-im}} &= \sum_{\mathbf{q}} d_{\mathbf{q}} e^{i\mathbf{q}\hat{\mathbf{R}}} \rho_{-\mathbf{q}} \ .
\end{aligned} \tag{5.2}$$

The term H_{CM} depends only on center-of-mass variables. $\hat{\mathbf{P}}$ and $\hat{\mathbf{R}}$ are the operator of the center-of-mass momentum and coordinate, respectively, $V(\hat{\mathbf{R}})$ is the confinement potential of the electrons depending on the dimension and the structure of the considered electron system. The electron charge is $e = -|e|$ and $\hat{\mathbf{A}}(\mathbf{R})$ is the vector potential, which we take in the Landau gauge. The terms H_{el} and H_{ph} represent the motion of the electrons and phonons relative to the center of mass including the electron-electron Coulomb interaction $H_{\mathrm{el-el}}$. The operators c_n^+ and c_n are related to the relative electron motion and create or annihilate a 'relative' electron in a state n with energy E_n. The concrete form of the operator $H_{\mathrm{el-el}}$ depends on the dimension of the electron system but always only the 'relative' electron operators contribute. The operators $b^+_{\mathbf{q},\lambda}$ and $b_{\mathbf{q},\lambda}$ create and annihilate a phonon with wavevector $\mathbf{q}$, polarization λ and frequency $\omega_{\mathbf{q},\lambda}$ in a three-dimensional crystal of volume V. The only coupling between the center of mass and the 'relative' electrons is due to the electron-phonon (el-ph) and electron-impurity (el-im) interaction. The function $d_{\mathbf{q}}$ is the Fourier transform of the electron-impurity potential and $h_{\mathbf{q},\lambda}$ is the electron-phonon matrix element (see Chapter 4.2). The operator $\rho_{\mathbf{q}}$ has been defined in Eq. 4.72 and corresponds to the Fourier transform of the electron density operator of a quasi low-dimensional electron gas. The influence by the finite confinement of the electrons on the interaction terms is here hidden in the respective representation of $\rho_{\mathbf{q}}$.

The character of the motion of the center of mass and of the 'relative' electrons is quite different. The former moves as a classical 'Brownian' particle with enormous mass $M = N_{\mathrm{el}} \cdot m^*$, and its motion is governed by a (stochastic) equation of the Langevin type. On the other hand, the motion of the huge number of interacting 'relative' electrons is described by a statistical density matrix $\hat{\rho}_{\mathrm{el}}(t)$. Since the induced drag current density of the electrons

$$\mathbf{j}(t) = e n_{\mathrm{el}}\, \dot{\mathbf{R}}(t) \tag{5.3}$$

is proportional to the center-of-mass velocity $\dot{\mathbf{R}}(t)$, we only need to study the equation of motion for the center of mass. It follows from (5.2) with $\omega_{\mathrm{C}} = |e|B/m^*$ and $\mathbf{e}_B = \mathbf{B}/B$ for all directions α perpendicular to the confinement

$$\begin{aligned} & M\ddot{R}_\alpha(t) + M\omega_{\mathrm{C}}(\dot{\mathbf{R}}(t) \times \mathbf{e}_B)_\alpha \qquad (5.4)\\ & \quad = \sum_{\mathbf{q}} q_\alpha \,\mathrm{Im}\Big\{ e^{i\mathbf{q}\mathbf{R}(t)} \Big(2 \sum_{\lambda} h_{\mathbf{q},\lambda} \left\langle b_{\mathbf{q},\lambda} \rho_{-\mathbf{q}} \right\rangle (t) + d_{\mathbf{q}} \left\langle \rho_{-\mathbf{q}} \right\rangle (t) \Big) \Big\} \,. \end{aligned}$$

In (5.4) we have replaced the center-of-mass operator $\hat{\mathbf{R}}$ with its expectation value $\mathbf{R}(t)$, i.e. with the time dependent coordinate of the center of mass. This can be approximately done due to the enormous mass leading to an almost classical equation of motion.

The terms on the right hand side of (5.4) are the forces exerted on the center of mass by the electron-phonon and electron-impurity interaction, respectively. In the following, we will split up these forces into drag forces and frictional forces ($\sim \dot{\mathbf{R}}$) neglecting all quadratic or higher order terms in $\mathbf{q}\dot{\mathbf{R}}$. For these purposes we have to analyse $\langle b_{\mathbf{q},\lambda}\rho_{-\mathbf{q}}\rangle$ and $\langle \rho_{-\mathbf{q}} \rangle$. In doing so we will consider the phonon and impurity interaction terms as perturbation turned on at $t = t_0$. Within linear response theory and by neglecting all two- and higher order phonon processes and all processes involving simultaneously phonons and impurities we obtain

$$\begin{aligned} \left\langle b_{\mathbf{q},\lambda}\rho_{-\mathbf{q}} \right\rangle (t) &= -\sum_{\mathbf{q}',\lambda'} h^*_{\mathbf{q}',\lambda'} \frac{i}{\hbar} \int_{t_0}^{t} \mathrm{d}t' e^{-i\mathbf{q}'\mathbf{R}(t')} e^{i\omega_{\mathbf{q},\lambda}(t'-t)} \Big\{ \delta_{\mathbf{q},\mathbf{q}'}\, \delta_{\lambda,\lambda'} \left\langle \rho^+_{\mathbf{q}} \rho_{\mathbf{q}}(t'-t) \right\rangle_{\hat{\rho}^\beta_{\mathrm{el}}} \\ & \qquad + \left\langle b^+_{\mathbf{q}',\lambda'}(t')\, b_{\mathbf{q},\lambda}(t') \right\rangle \left\langle [\rho^+_{\mathbf{q}}, \rho_{\mathbf{q}'}(t'-t)] \right\rangle_{\hat{\rho}^\beta_{\mathrm{el}}} \Big\} \,, \qquad (5.5) \\ \left\langle \rho_{-\mathbf{q}} \right\rangle (t) &= -\sum_{\mathbf{q}'} d^*_{\mathbf{q}'} \frac{i}{\hbar} \int_{t_0}^{t} \mathrm{d}t' e^{-i\mathbf{q}'\mathbf{R}(t')} \left\langle [\rho^+_{\mathbf{q}}, \rho_{\mathbf{q}'}(t'-t)] \right\rangle_{\hat{\rho}^\beta_{\mathrm{el}}} \,. \qquad (5.6) \end{aligned}$$

In (5.5) and (5.6), it has been assumed that the electron system was in a state of thermal equilibrium at time t_0, describable by using the canonical statistical operator $\hat{\rho}^\beta_{\mathrm{el}} = \exp(-\beta H_{\mathrm{el}})/\mathrm{Tr}\,(\exp(-\beta H_{\mathrm{el}}))$ with $k_{\mathrm{B}}\beta$ as inverse electron temperature.

The first term on the right hand side of (5.5) is connected with the emission of (equilibrium) phonons by the electron system. Since at typical experimental conditions the electron temperature is very low, this term can be dropped and only the second term caused by the (nonequilibrium) phonons will be left.
The exponential factor in the above equations $\exp(-i\mathbf{q}'\mathbf{R}(t'))$ can be expanded to linear order in $\dot{\mathbf{R}}$,

$$e^{-i\mathbf{q}'\mathbf{R}(t')} \approx e^{-i\mathbf{q}'\mathbf{R}(t)}\left(1 + i\mathbf{q}'\int_{t'}^{t}\mathrm{d}t''\,\dot{\mathbf{R}}(t'')\right) . \tag{5.7}$$

Substituting this result and interchanging the order-of-time integration we find

$$\begin{aligned}\langle b_{\mathbf{q},\lambda}\rho_{-\mathbf{q}}\rangle(t) \approx \sum_{\mathbf{q}',\lambda'} e^{-i\mathbf{q}'\mathbf{R}(t)} h^{*}_{\mathbf{q}',\lambda'} \Bigg\{ &\frac{-i}{\hbar}\int_{t_0}^{t}\mathrm{d}t'\,\left\langle b^{+}_{\mathbf{q}',\lambda'}(t')b_{\mathbf{q},\lambda}(t')\right\rangle \left\langle [\rho^{+}_{\mathbf{q}}, e^{i(L+\omega_{\mathbf{q},\lambda})(t'-t)}\rho_{\mathbf{q}'}]\right\rangle_{\hat{\rho}^{\beta}_{\mathrm{el}}} \\ &+ \frac{1}{\hbar}\int_{t_0}^{t}\mathrm{d}t'\mathbf{q}'\dot{\mathbf{R}}(t')\int_{t_0}^{t'}\mathrm{d}t''\,\left\langle b^{+}_{\mathbf{q}',\lambda'}(t'')b_{\mathbf{q},\lambda}(t'')\right\rangle \left\langle [\rho^{+}_{\mathbf{q}}, e^{i(L+\omega_{\mathbf{q},\lambda})(t''-t)}\rho_{\mathbf{q}'}]\right\rangle_{\hat{\rho}^{\beta}_{\mathrm{el}}} \Bigg\} ,\end{aligned} \tag{5.8}$$

$$\begin{aligned}\langle\rho_{-\mathbf{q}}\rangle(t) \approx \sum_{\mathbf{q}'} e^{-i\mathbf{q}'\mathbf{R}(t)} d^{*}_{\mathbf{q}'} \Bigg\{ &\frac{-i}{\hbar}\int_{t_0}^{t}\mathrm{d}t'\,\left\langle [\rho^{+}_{\mathbf{q}}, e^{iL(t'-t)}\rho_{\mathbf{q}'}]\right\rangle_{\hat{\rho}^{\beta}_{\mathrm{el}}} \\ &+ \frac{1}{\hbar}\int_{t_0}^{t}\mathrm{d}t'\mathbf{q}'\dot{\mathbf{R}}(t')\int_{t_0}^{t'}\mathrm{d}t''\,\left\langle [\rho^{+}_{\mathbf{q}}, e^{iL(t''-t)}\rho_{\mathbf{q}'}]\right\rangle_{\hat{\rho}^{\beta}_{\mathrm{el}}} \Bigg\} .\end{aligned} \tag{5.9}$$

Displaying (5.8) and (5.9), we have used the Liouville operator L corresponding to H_{el}. L is defined by $LA = \frac{1}{\hbar}[H_{\mathrm{el}}, A]$ and therefore $A(t) = e^{iLt}A(0)$. The above derived equations can be rewritten by introducing a Mori operator product in Liouville space as follows

$$(A|B) = \int_{0}^{\beta}\mathrm{d}\lambda\,\left\langle A^{+}e^{-\lambda H_{\mathrm{el}}}Be^{\lambda H_{\mathrm{el}}}\right\rangle_{\hat{\rho}^{\beta}_{\mathrm{el}}} . \tag{5.10}$$

With this definition and using the Kubo identity, $\langle[A^{+}, B]\rangle_{\hat{\rho}^{\beta}_{\mathrm{el}}} = \hbar\,(A|LB)$ (for details see, e.g. Fick and Sauermann, 1990), we may write

$$\begin{aligned}
\left\langle b_{\mathbf{q},\lambda}\rho_{-\mathbf{q}}\right\rangle(t) \; &= \\
&= -\sum_{\mathbf{q}',\lambda'} e^{-i\mathbf{q}'\mathbf{R}(t)} h^*_{\mathbf{q}',\lambda'} \Bigg\{ \int\limits_{t_0}^{t} \mathrm{d}t' \left\langle b^+_{\mathbf{q}',\lambda'}(t') b_{\mathbf{q},\lambda}(t')\right\rangle \left(\rho_{\mathbf{q}}|iLe^{i(L+\omega_{\mathbf{q},\lambda})(t'-t)}\rho_{\mathbf{q}'}\right) \\
&\quad + i\int\limits_{t_0}^{t} \mathrm{d}t'\mathbf{q}'\dot{\mathbf{R}}(t') \int\limits_{t_0}^{t'} \mathrm{d}t'' \left\langle b^+_{\mathbf{q}',\lambda'}(t'') b_{\mathbf{q},\lambda}(t'')\right\rangle \left(\rho_{\mathbf{q}}|iLe^{i(L+\omega_{\mathbf{q},\lambda})(t''-t)}\rho_{\mathbf{q}'}\right)\Bigg\} , \qquad (5.11)
\end{aligned}$$

$$\begin{aligned}
\left\langle \rho_{-\mathbf{q}}\right\rangle(t) = \; & -\sum_{\mathbf{q}'} e^{-i\mathbf{q}'\mathbf{R}(t)} d^*_{\mathbf{q}'} \Bigg\{ \int\limits_{t_0}^{t} \mathrm{d}t' \left(\rho^+_{\mathbf{q}}|iLe^{iL(t'-t)}\rho_{\mathbf{q}'}\right) \\
& + \; i\int\limits_{t_0}^{t} \mathrm{d}t'\mathbf{q}'\dot{\mathbf{R}}(t') \int\limits_{t_0}^{t'} \mathrm{d}t'' \left(\rho_{\mathbf{q}}|iLe^{iL(t''-t)}\rho_{\mathbf{q}'}\right)\Bigg\} . \qquad (5.12)
\end{aligned}$$

Inserting now (5.11) and (5.12) into (5.4), we obtain for $t > t_0$ the following result for the equation of motion of the center of mass in linear order of $\dot{\mathbf{R}}$

$$M\left(\ddot{\mathbf{R}}(t) + \omega_{\mathrm{C}}\,\dot{\mathbf{R}}(t)\times\mathbf{e}_B\right)_\alpha = F_\alpha(t) - \sum_\beta \int\limits_{t_0}^{t} \mathrm{d}t' M_{\alpha\beta}(t',t)\dot{R}_\beta(t') \, . \qquad (5.13)$$

Here the drag force is equal to

$$\begin{aligned}
\mathbf{F}(t) \;\; = \;\; & -\sum_{\mathbf{q}} \mathbf{q}\,\mathrm{Im}\Bigg\{ 2\sum_\lambda |h_{\mathbf{q},\lambda}|^2 \int\limits_{0}^{t-t_0} \mathrm{d}t'\, N_{\mathbf{q},\lambda}(t-t') \left(\rho_{\mathbf{q}}|iLe^{-i(L+\omega_{\mathbf{q},\lambda})t'}\rho_{\mathbf{q}}\right) \\
& + |d_{\mathbf{q}}|^2 \int\limits_{0}^{t-t_0} \mathrm{d}t' \left(\rho_{\mathbf{q}}|iLe^{-iLt'}\rho_{\mathbf{q}}\right)\Bigg\} \qquad (5.14)
\end{aligned}$$

and the so called memory matrix (since the integrand in the frictional forces depends on the past of the quantity $\dot{\mathbf{R}}$) is

$$\begin{aligned}
M_{\alpha\beta}(t',t) \;\; = \;\; & -\sum_{\mathbf{q}} q_\alpha q_\beta\,\mathrm{Im}\Bigg\{ |d_{\mathbf{q}}|^2 \int\limits_{t_0}^{t'} \mathrm{d}t'' \left(\rho_{\mathbf{q}}|Le^{iL(t''-t)}\rho_{\mathbf{q}}\right) \\
& + 2\sum_\lambda |h_{\mathbf{q},\lambda}|^2 \int\limits_{t_0}^{t'} \mathrm{d}t'' N_{\mathbf{q},\lambda}(t'') \left(\rho_{\mathbf{q}}|Le^{i(L+\omega_{\mathbf{q},\lambda})(t''-t)}\rho_{\mathbf{q}}\right)\Bigg\} . \qquad (5.15)
\end{aligned}$$

According to Section 3.3.3 we have used here the abbreviation $N_{\mathbf{q},\lambda}(t)$ for the number of phonons $\left\langle b^+_{\mathbf{q},\lambda}(t) b_{\mathbf{q},\lambda}(t)\right\rangle$ with quasimomentum $\hbar\mathbf{q}$ and polarization λ. In the expressions (5.14) and (5.15) we have restricted ourselves to the random-phase approximation (RPA). This means that we keep only the contributions with $\mathbf{q}' = \mathbf{q}$ and assume that the remaining terms cancel each other out.

The impurity part of the force $\mathbf{F}$ averaged over all impurity positions disappears due to fact that it is an odd function of $\mathbf{q}$ and vanishes after taking the sum over $\mathbf{q}$ (the total momentum carried by the impurity potential should be zero). Therefore only the nonequilibrium (ballistic) phonons will contribute to the drag force. On the other hand, at the considered low temperatures, the phonon part of the memory matrix will be small compared to the impurity part and can be neglected. Moreover, due to symmetry arguments only the diagonal part of $M_{\alpha\beta}$ will be nonzero.

With these simplifications and using adequate approximations for many-particle systems, the right hand side of the Eqs. (5.14) and (5.15) can be carried out and the system of equations (5.13) could be solved. However, instead of finding a direct solution for $\dot{\mathbf{R}}(t)$ it is easier to obtain the time integral $\int_{t_0}^{\infty} dt\, \dot{\mathbf{R}}(t)$. This makes sense, since in most phonon-drag experiments the time-integrated current rather than the instantaneous current is measured.[1] Therefore we consider the Laplace transformation of (5.13) multiplying the equation by $\exp(izt)$ ($z = \omega + i\eta$, $\mathrm{Im} z > 0$) and integrating from t_0 to ∞. After some algebra we get for the Laplace transform $\dot{\mathcal{R}}(\omega)$ of the center-of-mass velocity $\dot{\mathbf{R}}(t)$

$$-i\omega M\dot{\mathcal{R}}_\alpha(\omega) + M\omega_{\mathrm{C}}\left(\dot{\mathcal{R}}(\omega)\times\mathbf{e}_B\right)_\alpha = \mathcal{F}_\alpha(\omega) - \mathcal{M}_{\alpha\alpha}(\omega)\dot{\mathcal{R}}_\alpha(\omega) \tag{5.16}$$

with

$$\mathcal{F}_\alpha(\omega) = 2\sum_{\mathbf{q},\lambda} q_\alpha\, |h_{\mathbf{q},\lambda}|^2\, \mathcal{N}_{\mathbf{q},\lambda}(\omega)\left(\rho_{\mathbf{q}}|\frac{izL}{(L+\omega_{\mathbf{q},\lambda})^2 - z^2}\rho_{\mathbf{q}}\right)\Bigg|_{\eta\to 0} \tag{5.17}$$

and

$$\mathcal{M}_{\alpha\alpha}(\omega) = -\sum_{\mathbf{q}} q_\alpha^2 |d_{\mathbf{q}}|^2 \left(\rho_{\mathbf{q}}|\frac{iz}{L^2 - z^2}\rho_{\mathbf{q}}\right)\Bigg|_{\eta\to 0}, \tag{5.18}$$

where the calligraphic letters denote the Laplace transformed quantities, i.e. $\mathcal{A}(\omega) = \int_{t_0}^{\infty} \mathrm{d}t e^{izt} A(t)\big|_{\eta\to 0}$.

For the time-integrated current density $\int_{t_0}^{\infty}\mathrm{d}t\mathbf{j}(t) = -en_{\mathrm{el}}\dot{\mathcal{R}}(0)$ we have to set $\omega = 0$ in (5.16) and obtain

$$\begin{aligned} M\omega_{\mathrm{C}}\left(\dot{\mathcal{R}}(0)\times\mathbf{e}_B\right)_\alpha &+ \dot{\mathcal{R}}_\alpha(0)\sum_{\mathbf{q}} q_\alpha^2 |d_{\mathbf{q}}|^2\, \mathrm{Im}\left\{\left(\rho_{\mathbf{q}}|\frac{1}{L+i\eta}\rho_{\mathbf{q}}\right)\Bigg|_{\eta\to 0}\right\} \\ &= 2\sum_{\mathbf{q},\lambda} q_\alpha\, |h_{\mathbf{q},\lambda}|^2\, \mathcal{N}_{\mathbf{q},\lambda}(0)\, \mathrm{Im}\left\{\left(\rho_{\mathbf{q}}|\frac{L}{L+\omega_{\mathbf{q},\lambda}+i\eta}\rho_{\mathbf{q}}\right)\Bigg|_{\eta\to 0}\right\}. \end{aligned} \tag{5.19}$$

---

[1] In a subsequent paper Danilchenko *et al.* (1999) have analysed in detail the temporal structure of instantaneous phonon-drag images.

From (5.19) we can estimate the time-integrated phonon induced drag current for an electron system with and without applied magnetic field. As an input parameter we need the time integral over the (nonequilibrium) phonon distribution in the electron system, $\mathcal{N}_{\mathbf{q},\lambda}(\omega)$, which has to be determined by phonon focusing calculations as described in Section 3.3. The effects of electron confinement and screening are contained in the density-density response functions $\mathrm{Im}\left\{(\rho_{\mathbf{q}}|...\rho_{\mathbf{q}})\big|_{\eta\to 0}\right\}$. Their special form depends on the respective dimension of the electron system and on the corresponding overlap integrals and form factors (see Appendix B and C).

For a quasi-2D electron system (electron density $n_{\mathrm{el}} \equiv n_{\mathrm{2D}}$) in a magnetic field perpendicular to the 2D plane an explicit expression for the in-plane phonon-drag current follows from Eqs. (5.19) and (B.26)

$$\int_{t_0}^{\infty} \mathrm{d}t\, \mathbf{j}_{\parallel}(t) = -\frac{\mu}{1+(\mu B)^2}\,\frac{n_{\mathrm{2D}}}{N_{\mathrm{el}}}\left[\mathcal{F}_{\parallel}(0) - \mu B\,\left(\mathcal{F}_{\parallel}(0)\times \mathbf{e}_B\right)\right] \tag{5.20}$$

with the time-integrated drag force

$$\mathcal{F}_{\parallel}(0) = -2\sum_{\mathbf{q},\lambda} \mathbf{q}_{\parallel}\, |h_{\mathbf{q},\lambda}|^2\, \mathcal{N}_{\mathbf{q},\lambda}(0)\,\mathrm{Im}\left\{\frac{|G_{11}(q_\perp)|^2\,\chi_{11}^{(B)}(q_\parallel,\omega_{\mathbf{q},\lambda})}{1-v(q_\parallel)\,g_{11}^{11}(q_\parallel)\,\chi_{11}^{(B)}(q_\parallel,\omega_{\mathbf{q},\lambda})}\right\} \tag{5.21}$$

and the mobility

$$\mu = \left(\frac{-1}{2N_{\mathrm{el}}|e|}\sum_{\mathbf{q}} q_\parallel^2 |d_{\mathbf{q}}|^2\,\mathrm{Im}\left\{\frac{\mathrm{d}}{\mathrm{d}\omega}\left(\frac{|G_{11}(q_\perp)|^2\,\chi_{11}^{(B)}(q_\parallel,\omega)}{1-v(q_\parallel)\,g_{11}^{11}(q_\parallel)\,\chi_{11}^{(B)}(q_\parallel,\omega)}\right)\bigg|_{\omega=0}\right\}\right)^{-1} . \tag{5.22}$$

Here we have assumed that of the subbands associated with the confined motion along the direction perpendicular to the 2D electron system only the lowest one is occupied. Thus $\chi_{11}^{(B)}(q_\parallel,\omega_{\mathbf{q},\lambda})$ is the multi-subband susceptibility for a strictly 2D noninteracting electron gas in the presence of a perpendicular magnetic field. It takes into account all intra and inter Landau level transitions. The overlap integral $G_{11}(q_\perp)$, see (B.5), and the form factor $g_{11}^{11}(q_\parallel)$, see (B.11), are the corrections due to the *quasi* two-dimensionality of the system, i.e. the result of the finite electron localization in direction perpendicular to the 2D electron system. Using the explicit form of $\chi_{11}^{(B)}(q_\parallel,\omega_{\mathbf{q},\lambda})$ taken from (B.18) and (B.19) we obtain for the force term

$$\mathcal{F}_{\parallel}(0) = N_{\mathrm{el}}\frac{2m^*}{\hbar^2 k_{\mathrm{F}}}\sum_{\mathbf{q},\lambda}\frac{\mathbf{q}_\parallel}{q_\parallel}\,\mathcal{N}_{\mathbf{q},\lambda}(0)\left|\frac{h_{\mathbf{q},\lambda}}{\varepsilon_{11}(q_\parallel,\omega_{\mathbf{q},\lambda})}\right|^2 |G_{11}(q_\perp)|^2\,\Lambda_{\mathrm{2D}}^{(B)}(q_\parallel,\omega_{\mathbf{q},\lambda}) \tag{5.23}$$

with

$$\begin{aligned}\Lambda_{\mathrm{2D}}^{(B)}(q_\parallel,\omega) \;&=\; \frac{2\pi q_\parallel}{k_{\mathrm{F}}}e^{-\frac{(q_\parallel l_B)^2}{2}}\sum_{n=1}^{\infty}\sum_{\Delta n=1}^{\infty}\frac{(n-1)!}{(n+\Delta n-1)!}\left[L_{n-1}^{\Delta n}\Big(\frac{(q_\parallel l_B)^2}{2}\Big)\right]^2\\ &\times\;\left[\frac{(q_\parallel l_B)^2}{2}\right]^{\Delta n}(f_{1n}-f_{1n+\Delta n})\,\delta\Big(\Delta n-\frac{m^* l_B^2\omega}{\hbar}\Big)\,,\end{aligned} \tag{5.24}$$

where f_{1n} denotes the Fermi equilibrium distribution function, $l_B = \sqrt{\hbar/|e|B}$ is the magnetic length and $L_n^m(x)$ stands for the associated Laguerre function. The function $|\varepsilon_{11}(q_\parallel, \omega_{\mathbf{q},\lambda})|^2 = \left|1 - v(q_\parallel)\, g_{11}^{11}(q_\parallel)\, \chi_{11}^{(B)}(q_\parallel, \omega_{\mathbf{q},\lambda})\right|^2$ in the denominator of the term with the electron-phonon interaction potential $h_{\mathbf{q},\lambda}$ describes the dynamical screening of the electron-phonon coupling by the electron-electron interaction.

An important point is the influence of disorder on the drag force for $B \neq 0$. Even in the presence of weak disorder each δ-function peak in the density of states or the magnetic susceptibility broadens into a Landau level of finite width with the level broadening determined by the strength and the range of disorder in the system. This broadening allows intra Landau level transitions by phonon scattering. Otherwise the sharp Landau levels would prohibit such transitions. The simplest physically plausible approximation of this disorder broadening is the substitution of the sum of δ-functions by a sum of Gaussian functions with a level width proportional to $\sqrt{B}$ (Ando and Uemura, 1974) valid in the limit of strong magnetic fields. Tamura and Kitagawa (1989) have shown that this approximation works well for electron-phonon interaction problems calculating the thermal conductance of $\mathrm{GaAs/Al_xGa_{1-x}As}$ heterostructures at high magnetic fields.

Up to now no discussion was made concerning the role of the spin degree of freedom. To simplify the formulas, the spin of the electron has been disregarded so far. In the considered semiconductor structures the effective mass m^* occurring in the cyclotron frequency $\omega_\mathrm{C} = eB/m^*$ is much smaller than the bare electron mass occurring in the Bohr magneton $\mu_\mathrm{B} = e\hbar/2m_\mathrm{el}$. Therefore the spin Zeeman energy splitting $\mu_\mathrm{B}B$ is small in comparison to the Landau level broadening brought about by disorder. Thus, we will ignore the spin degree of freedom.

In zero magnetic field the equation for the time-integrated drag force simplifies and from Eqs. (5.21, B.33, B.37) we obtain in the limit of low temperatures directly

$$\mathcal{F}_\parallel(0) = N_\mathrm{el}\frac{2m^*}{\hbar^2 k_\mathrm{F}} \sum_{\mathbf{q},\lambda} \frac{\mathbf{q}_\parallel}{q_\parallel}\, \mathcal{N}_{\mathbf{q},\lambda}(0) \left|\frac{h_{\mathbf{q},\lambda}}{\varepsilon_{11}(q_\parallel, \omega_{\mathbf{q},\lambda})}\right|^2 |G_{11}(q_\perp)|^2 \Lambda_{2\mathrm{D}}^{(0)}(q_\parallel, \omega_{\mathbf{q},\lambda}) \ , \qquad (5.25)$$

where

$$\Lambda_{2\mathrm{D}}^{(0)}(q_\parallel, \omega) = 2\mathrm{Re}\left\{\sqrt{1 - (\frac{q_\parallel}{2k_\mathrm{F}} - \frac{m^*\omega}{\hbar q_\parallel k_\mathrm{F}})^2} - \sqrt{1 - (\frac{q_\parallel}{2k_\mathrm{F}} + \frac{m^*\omega}{\hbar q_\parallel k_\mathrm{F}})^2}\right\} . \qquad (5.26)$$

As visualized in Fig. 5.2 the function $\Lambda_{2\mathrm{D}}^{(0)}(q_\parallel, \omega)$ represents also the limiting case of Eq. (5.24) for low fields. For $B \to 0$ the magnetic length l_B will increase rapidly resulting in larger values of Δn. Therefore the difference between the distribution functions $(f_{1n} - f_{1n+\Delta n})$ in the double sum of Eq. (5.24) will not vanish for a larger number of different values of n. As a consequence, the number of contributing

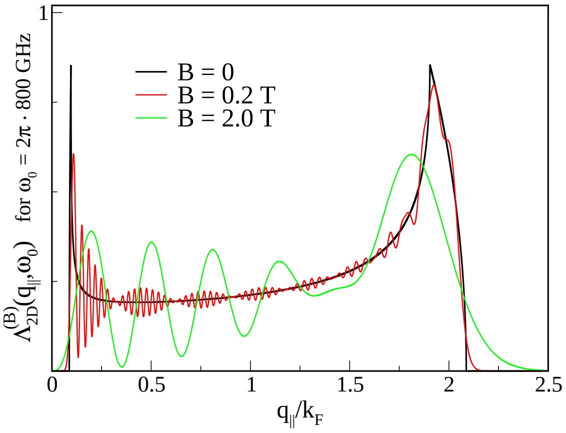

Figure 5.2: $\Lambda^{(B)}_{2\mathrm{D}}(q_{\|}, \omega_0)$ calculated for $\omega_0 = 2\pi \cdot 800\,\mathrm{GHz}$ as a function of $q_{\|}$ for $B = 2.0\,\mathrm{T}$, $B = 0.2\,\mathrm{T}$ and the zero-field case. The chosen frequency fulfills the condition $m^* l_B^2 \omega/\hbar$ = integer for both nonzero values of B. The effective mass is $m^* = 0.07 m_{\mathrm{el}}$, the electron density $n_{2\mathrm{D}} = 5.3 \cdot 10^{15}\,\mathrm{m}^{-2}$.

intersubband transitions increases causing more oscillations but with ever smaller amplitudes in $\Lambda^{(B)}_{2\mathrm{D}}(q_{\|}, \omega)$.

Another characteristic feature of $\Lambda^{(0)}_{2\mathrm{D}}(q_{\|}, \omega)$, the sharp dropoff for $q_{\|} > 2k_{\mathrm{F}}$, becomes also apparent in Fig. 5.2. This so called $2k_{\mathrm{F}}$ cutoff provides a direct measurement of the Fermi wavevector and is therefore very important for the application of phonon spectroscopy to low-dimensional electron systems. The physical origin is simple. At zero temperature an electron absorbing a phonon scatters from an occupied state $|\mathbf{k}| < k_{\mathrm{F}}$ to an unoccupied state $|\mathbf{k}'| > k_{\mathrm{F}}$. Since the phonon energy is small compared to the Fermi energy, the scattering is quasi-elastic and therefore due to energy and crystal momentum conservation (in the plane) the scattering is limited to phonons with $q_{\|}$ at maximum only slightly larger than twice the Fermi wavevector ($q_{\|} < 2k_{\mathrm{F}} + 2m^* c_{\mathbf{q},\lambda} q/q_{\|}$). It should be noted that in Fig. 5.2 the function $\Lambda^{(0)}_{2\mathrm{D}}(q_{\|}, \omega_0)$ is represented at constant frequency ω_0. This is different to the well known figure in the paper of Hensel *et al.* (1983a), where a similarly defined function $\Lambda^{(0)}_{2\mathrm{D}}(q_{\|}, \omega)$ is also plotted as a function of $q_{\|}$, but at a fixed angle, i.e. $\Lambda^{(0)}(q_{\|}) = \Lambda^{(0)}(q_{\|}, c_\lambda q_{\|} \sin\vartheta_0)$. This type of presentation makes sense if we are interested in the phonon absorption at a fixed detector point as a function of phonon frequency, but here we are more interested in phonon imaging studies. For $B \neq 0$ the decrease of $\Lambda^{(B)}$ to zero happens at wavevectors $q_{\|} > l_B^{-1}$ for high fields and at $q_{\|} > 2k_{\mathrm{F}}$ for low fields, respectively. $\Lambda^{(B)}$ is according to (B.19) and (B.7) proportional to the spatial overlap between the 2D electron wavefunctions $\phi_n(x + l_B^2 k)$ and $\phi_{n'}(x + l_B^2(k + q_y))$. If we take the spatial extent of a Landau state n as $\sqrt{2}$ times the expectation value for the broadening of the wavefunction (this corresponds to the classical amplitude of motion) then the integral will tend to zero when the displacement $l_B^2 q_y > l_B\sqrt{2n-1} + l_B\sqrt{2n'-1}$. For low fields follows $l_B q_y > 2\sqrt{2n^*}$, where n^* is the number of the highest occupied Landau state. The last relation will be better satisfied the higher the number of occupied states is, i.e the lower the B-field is. Substituting n^* by the electron density or further by the Fermi wavevector, $n^* = \pi l_B^2 n_{2\mathrm{D}} = l_B^2 k_\mathrm{F}^2/2$, we end up with a sharp decrease at $q_y > 2k_\mathrm{F}$ and therefore also at $q_\parallel > 2k_\mathrm{F}$. As displayed in Fig. 5.3, the $2k_\mathrm{F}$ cutoff depends on the value of the effective mass m^* and is in GaAs heterostructures both for $B \neq 0$ and $B = 0$ sharper for electrons than for hole gases with their typical much higher m^*.

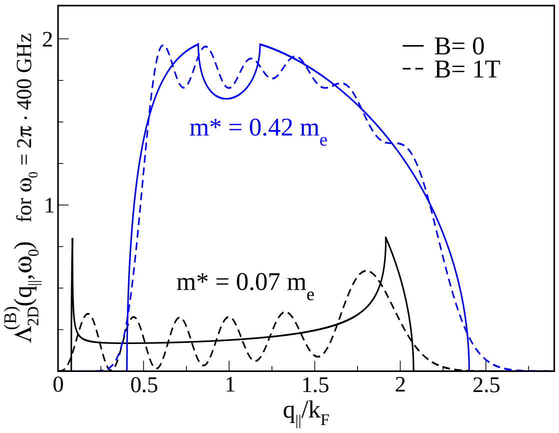

Figure 5.3: $\Lambda_{2\mathrm{D}}^{(B)}(q_\parallel, \omega_0)$ calculated for $\omega_0 = 2\pi \cdot 400\,\mathrm{GHz}$ as a function of $q_\parallel$ for 2 different effective masses each for $B = 1\,\mathrm{T}$ and $B = 0$. The chosen frequency fulfills the condition $m^* l_B^2 \omega/\hbar =$ integer for both m^*. The electron density is $n_{2\mathrm{D}} = 3.0 \cdot 10^{15}\,\mathrm{m}^{-2}$.

The cutoff of $\Lambda_{2\mathrm{D}}^{(B)}(q_\parallel, \omega_0)$ at low phonon wavevectors $q_\parallel$ (for zero or small B) has hitherto received little attention. Similar to the $2k_\mathrm{F}$ cutoff, it is due to momentum and energy conservation. Eq. (5.26) and Fig. 5.4 show that this effect disappears for small effective masses and low frequencies ω_0 (see also Jasiukiewicz, Lehmann, and Paszkiewicz, 1996). However, for hole gases and monochromatic phonon sources or hot Planckian phonon sources with only a small amount of low frequency phonons it should become important.

So far we have derived explicit formulas for the phonon-drag current of quasi-2D systems. Another interesting problem is the quasi-1D case. Using our dimension independent general expression (5.19) the drag force in a 1D system can now be easily determined. With (B.42–B.49) it follows for the time-integrated force in direction of the 1D channel (here we have chosen the y-direction)

$$\mathcal{F}_y(0) = N_\mathrm{el} \frac{2m^*}{\hbar^2 \bar{k}_\mathrm{F}} \sum_{\mathbf{q},\lambda} \frac{q_y}{|q_y|} \mathcal{N}_{\mathbf{q},\lambda}(0)\, |h_{\mathbf{q},\lambda}|^2 \sum_{n,n'} \frac{|G_{nn'}^{11}(q_z, q_x)|^2}{|\varepsilon_{nn'}(\mathbf{q}, \omega)|^2} \Lambda_{1\mathrm{D}}^{nn'}(q_y, \omega_{\mathbf{q},\lambda}) \;, \qquad (5.27)$$

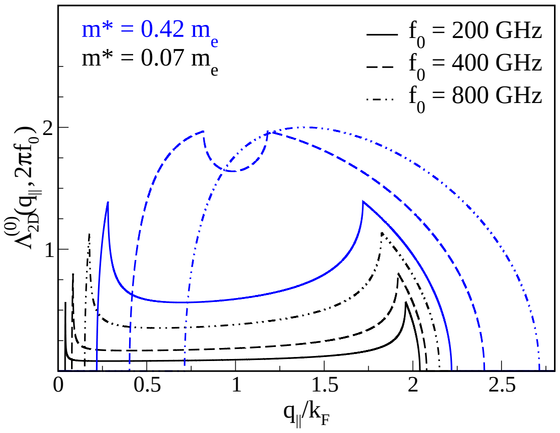

Figure 5.4: $\Lambda^{(0)}_{2\mathrm{D}}(q_{\|}, 2\pi f_0)$ calculated as a function of $q_{\|}$ for different frequencies f_0 and different effective masses m^*. The electron density is $n_{2\mathrm{D}} = 3.0 \cdot 10^{15}\,\mathrm{m}^{-2}$.

where

$$\Lambda^{nn'}_{1\mathrm{D}}(q,\omega) = \frac{\pi}{2}\left\{\Theta\big(k_{\mathrm{F}}^{(n)} - |\frac{q}{2} - \tilde{k}_{nn'}(q,\omega)|\big) - \Theta\big(k_{\mathrm{F}}^{(n')} - |\frac{q}{2} + \tilde{k}_{nn'}(q,\omega)|\big)\right\}\ . \tag{5.28}$$

In (5.27) and (5.28) we have used the abbreviations $\bar{k}_{\mathrm{F}} = \frac{\pi}{2} n_{1\mathrm{D}}$ (in case of a strictly 1D system $\bar{k}_{\mathrm{F}}$ would be identical to the Fermi wavevector), $\tilde{k}_{nn'}(q,\omega) = \frac{m^*}{\hbar^2 q}(\hbar\omega + E_{1n0} - E_{1n'0})$, and $k_{\mathrm{F}}^{(n)} = \sqrt{\frac{2m^*}{\hbar^2}\,(E_{\mathrm{F}} - E_{1n0})}$. The latter quantity describes the position of the Fermi energy E_{F} relative to the respective subband minima E_{1n0}. The overlap integral $G^{11}_{nn'}(q_z, q_x)$ and the dielectric matrix $\varepsilon_{nn'}(\mathbf{q},\omega)$ are defined in Appendix B.2 and are calculated for different confinement potentials in Appendix C.2. For quasi-1D systems the confinement length in the lateral direction (L_x) is typically larger than the confinement length in growth direction (z-direction) and consequentially, the energy spacing between different x-sublevels is small. Therefore, due to the localization in x-direction, more subbands are occupied or are accessible by acoustic phonon induced excitations. The result is that, in contrast to the previously discussed quasi-2D case, one has to consider in the calculations not only intraband but also the possible interband transitions.

5.3 Phonon-drag images – The result of anisotropy and confinement

5.3.1 Comparison to experimental results

In this section numerical results of our theory will be presented and compared with experimental phonon-drag images. Thereby the main interest will be focused on the influence of acoustic anisotropy and confinement. As already mentioned, phonon-drag patterns are extremely sensitive to the characteristics of the phonon source, to focusing effects, and to the dimension and the electronic properties of the low-dimensional electron system. Therefore, the final expression for the drag current is based on the results of the previous section in combination with the results of Chapter 3 for the phonon pulse propagation. For the realistic case of a locally heated metal film as the phonon source (see Appendix A.3) we obtain from (3.39,3.21) and (5.20,5.23) for the time-integrated phonon-drag current induced in a quasi-2D electron system under the influence of a perpendicular magnetic field

$$\begin{aligned}\int \mathrm{d}t\, j_x(t) \;&=\; -\frac{\mu}{1+(\mu B)^2}\frac{(\Delta t)(\Delta z)m^* k_\mathrm{F}}{8\pi^4\hbar^2}\iint\limits_{A_\mathrm{s}} \mathrm{d}x_\mathrm{s}\mathrm{d}y_\mathrm{s} \int\limits_{\Omega_{\mathrm{d},r_\mathrm{s}}} \mathrm{d}\Omega_{\mathbf{r}'} \\ &\times \int \frac{\mathrm{d}\omega\,\omega^2}{e^{\hbar\omega/k_\mathrm{B}T_\mathrm{s}}-1}\sum_\lambda\sum_i \Theta(\frac{c_{\hat{\mathbf{q}}_i^\lambda,\lambda}}{c_\lambda^\mathrm{S}}-\sin\vartheta_i^\lambda)\frac{1}{c^3_{\hat{\mathbf{q}}_i^\lambda,\lambda}}\mathcal{A}_{\hat{\mathbf{q}}_i^\lambda,\lambda}\, e^{-r'/\tau v_{\hat{\mathbf{q}}_i^\lambda,\lambda}} \\ &\times \Big[(\hat{\mathbf{q}}_i^\lambda)_x-\mu B\cdot(\hat{\mathbf{q}}_i^\lambda)_y\Big]\left|\frac{h_{\mathbf{q}_i^\lambda,\lambda}}{\varepsilon_{11}(\frac{\omega}{c_{\hat{\mathbf{q}}_i^\lambda,\lambda}}\sin\vartheta_i^\lambda\,,\omega)}\right|^2 \\ &\times \left|G_{11}(\frac{\omega}{c_{\hat{\mathbf{q}}_i^\lambda,\lambda}}\cos\vartheta_i^\lambda)\right|^2\frac{1}{\sin\vartheta_i^\lambda}\,\Lambda^{(B)}_\mathrm{2D}\Big(\frac{\omega}{c_{\hat{\mathbf{q}}_i^\lambda,\lambda}}\sin\vartheta_i^\lambda\,,\omega\Big)\,. \qquad (5.29)\end{aligned}$$

The 2D electron system is here chosen parallel to the source (xy-plane) at position $\mathbf{r}$, the location of the source is described by the vector $\mathbf{r}_\mathrm{s}$ (see Fig. 3.6 in Chapter 3). The angles ϑ_i^λ and φ_i^λ are solutions of the equation $\hat{\mathbf{v}}_{\hat{\mathbf{q}},\lambda}=\hat{\mathbf{r}}'$ for each individual phonon polarization λ with $\mathbf{r}'=\mathbf{r}-\mathbf{r}_\mathrm{s}$, $\hat{\mathbf{r}}'=\mathbf{r}'/r'$, $\vartheta_\mathbf{q}=\arccos\hat{q}_z$ and $\varphi_\mathbf{q}=\arccos(\hat{q}_x/\sin\vartheta_\mathbf{q})$.

Formula (5.29) acts as the starting point for the numerical calculations and discussions. The first line contains the topology and dimension of the phonon source and the detector described by the integrals over the source area A_s and over the solid angle $\Omega_{\mathrm{d},r_\mathrm{s}}$ (solid angle corresponding to the detector surface seen from a point $\mathbf{r}_\mathrm{s}$ of the phonon source). The second line comprises the characteristic phonon properties of the source term (phonon frequency distribution) and the critical angles for the heater-crystal interface (Θ-function) as well as the acoustic properties of the substrate (focusing factor $\mathcal{A}_{\hat{\mathbf{q}},\lambda}$ and damping by isotope scattering $e^{-r'/\tau v_{\hat{\mathbf{q}},\lambda}}$). The electron-phonon interaction (both deformation potential coupling and piezoelectric scattering) and its screening by the electrons (described by the dielectric

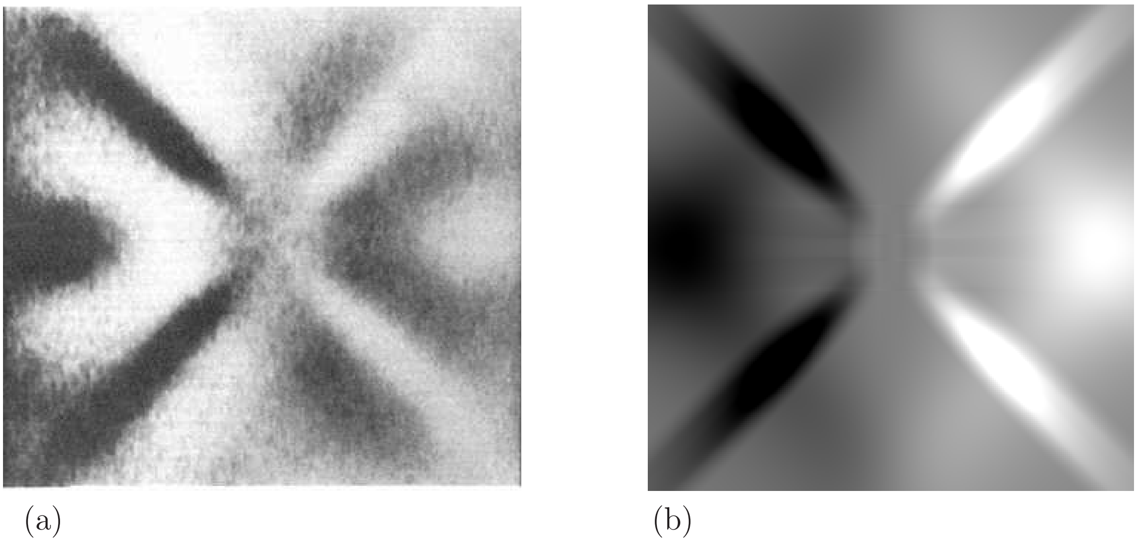
(a) (b)

Figure 5.5: Experimental (**a**) and calculated (**b**) image of phonon drag for a Planckian type phonon source. Each point of the two-dimensional map corresponds to a respective position of the phonon source. Drag current is measured in [110] direction. Positive and negative signals are represented as dark and bright shades, an average gray tone corresponds to zero signal. Scanning area 1 mm × 1 mm, sample thickness 0.35 mm, electron density $n_{2\mathrm{D}} = 3.8 \cdot 10^{15}\,\mathrm{m}^{-2}$. (Experimental image (a) from Dietzel *et al.*, 1993.)

function $\varepsilon_{11}(q_{\parallel}, \omega)$) are part of the third line. Lastly the fourth line includes the cutoff conditions for the electron-phonon coupling in form of the overlap integral $G_{11}(q_{\perp}, \omega)$ and the $\Lambda^{(B)}_{2\mathrm{D}}(q_{\parallel}, \omega)$ function. The effects of acoustic anisotropy are mainly included in the focusing factor and the electron-phonon matrix elements. The influence of the confinement is hidden in the overlap integral, in $\Lambda^{(B)}_{2\mathrm{D}}(q_{\parallel}, \omega)$, and in the dielectric function.

In Fig 5.5 experimental and theoretical results of phonon-drag images are compared for a quasi-2D electron system formed in a (001) GaAs/Al$_{\mathrm{x}}$Ga$_{1-\mathrm{x}}$As heterojunction. The experimental setup used by Dietzel *et al.* (1993) was similar to the one presented in Fig. 5.1. Acoustic phonons with an approximately Planckian spectrum were generated by thermalizing short laser pulses in a metal film (here aluminium) evaporated on the bottom of the substrate. The corresponding phonon source temperature was approximately 15 K and thus much higher than the sample temperature of about 1.5 K. The scanned laser beam was focused to a spot of about 10 μm across and the phonon induced signal was recorded as a function of phonon source (laser spot) position. The 'active' area of the 2D electrons was 50 μm × 50 μm. A detailed study concerning the question of why only this small part of the detector contributes to the signal was given by Kershaw *et al.* (1996). As verified by the numerical calculations the sharp ridges in the image are due to FTA phonons propagating near the {100} planes. The two larger round areas are due to LA phonons which are focused near the ⟨111⟩ directions. The theoretical pattern has been calculated on the basis of the program package for phonon focusing patterns in case of finite area detectors described in Sections 3.3 and 3.4. This program package provides apart from the phonon density also the other phonon input data (like phonon polarization vectors or the angle and mode dependence of the phonon velocities) necessary to calculate the drag current according to Eq. (5.29). Having regard to the fact that there have been no free parameters in the calculations, the agreement between the experimentally and the numerically obtained image is satisfactory. Only the ratio between the deformation potential and the piezoelectric coupling constant has been varied. However, the best agreement has been found for $eh_{14}/\Theta_{\mathrm{d}} = 1.7 \cdot 10^{8}\,\mathrm{m}^{-1}$, which is consistent with the conclusions from our calculations of the phonon frequency dependence of the drag current (Jasiukiewicz, Lehmann, and Paszkiewicz, 1992) and their comparison with experiments for certain phonon distribution directions (Lega *et al.*, 1990) as well as with the results of electron transport measurements (see Adachi, 1994).

Figs. 5.6 and 5.7 show experimental and theoretical drag current images of a quasi-2D system for different values of magnetic field applied perpendicular to the layer. Such phonon-drag experiments in magnetic fields were first performed by Dietzel *et al.* (1993, 1994) for 2D electrons and by Kent et al. (Gańcza *et al.*, 1996; Lehmann *et al.*, 1997b) for the corresponding 2D hole gas. Fig. 5.6 presents the experimental results for a 2D hole system at the interface of a p-type GaAs/$\mathrm{Al_xGa_{1-x}As}$ heterojunction grown on [001] oriented GaAs substrates for $B = 0\,\mathrm{T}$, $B = 0.25\,\mathrm{T}$ and $B = 4.71\,\mathrm{T}$. In contrast to the other numerical results in this section the patterns of Fig. 5.7 (Lehmann *et al.*, 1997a) are based on Monte-Carlo simulations for the phonon transport in the substrate. This allows a more detailed treatment of phonon isotope scattering effects. The characteristic result for high magnetic fields is the apparent anticlockwise 'rotation' of the axis about which the drag signal reverses its polarity (Lehmann *et al.*, 1997b). To see how this comes about one must remember that according to Eq. (5.29) the pattern obtained in a field is the superposition of two components. The parallel one is due to the phonon momentum along the line joining the contacts and the transverse one is due to the phonon momentum perpendicular to this line (with the note, that owing to the opposite charge of holes the term $-[(\hat{\mathbf{q}}_i)_x - \mu B \cdot (\hat{\mathbf{q}}_i)_y]$ changes to $+[(\hat{\mathbf{q}}_i)_x + \mu B \cdot (\hat{\mathbf{q}}_i)_y]$). The ratio between the two components is given by the factor μB. At $B = 0$ only the parallel component contributes. At $B = 4.71\,\mathrm{T}$ (i.e. $\mu B \gg 1$) the transverse component dominates giving a theoretical rotation of 90°. Strong evidence for this effect can also be seen in the experimental pattern for 4.71 T, however, it is severely affected by noise. This is the case because the drag signal is proportional to the prefactor $[1 + (\mu B)^2]^{-1}$. At $B = 0.25\,\mathrm{T}$ the ratio μB is approximately one (the mobility of the 2D holes was $5\,\mathrm{m^2V^{-1}s^{-1}}$ at $T = 4\,\mathrm{K}$) and both components contribute equally. The result is a pretended superposition and some of the characteristic zero-field features cancel out. The parameters used in the calculation correspond to the experimental conditions with the exception of the linear dimensions of the source. They were chosen larger to simulate scattering effects at the interfaces.

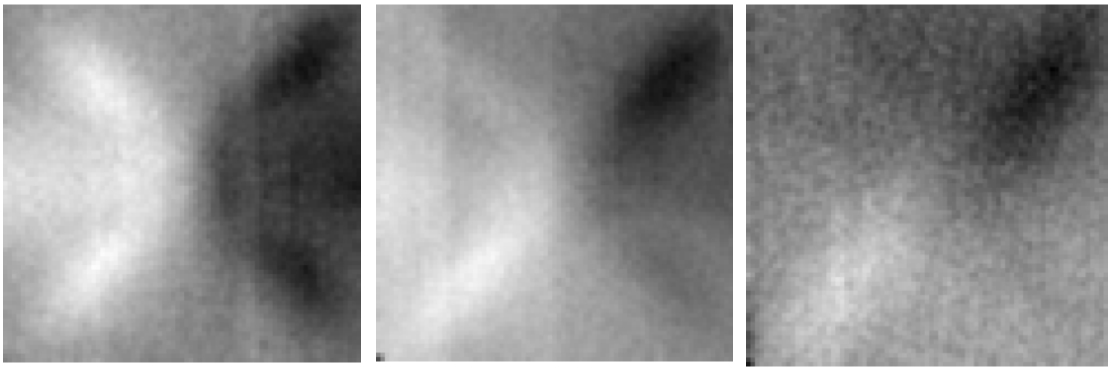

Figure 5.6: Experimental drag current images of a 2D hole gas for different values of the magnetic field: $B = 0\,\mathrm{T}$, $B = 0.25\,\mathrm{T}$, $B = 4.71\,\mathrm{T}$ (from left to the right). The dark and white areas correspond to regions with positive and negative drag current (measured in [110] direction). The scanning area was $4\,\mathrm{mm} \times 4\,\mathrm{mm}$, the sample thickness 2 mm and the hole density was $3.3 \cdot 10^{15}\,\mathrm{m}^{-2}$. (From Lehmann *et al.*, 1997b.)

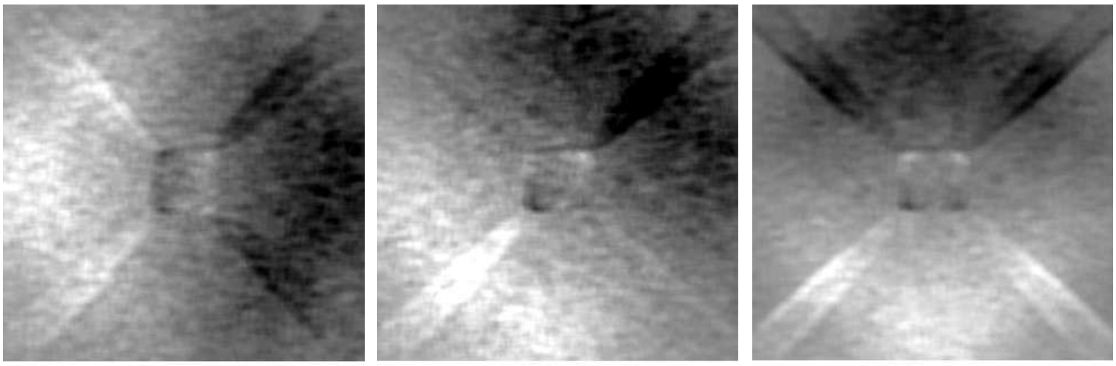

Figure 5.7: Calculated drag current images of a quasi-2D hole gas for different values of the magnetic field: $B = 0\,\mathrm{T}$, $B = 0.25\,\mathrm{T}$, $B = 4.71\,\mathrm{T}$ (from left to the right corresponding to Fig. 5.6). Scattering in the substrate is included, the phonon mean free path is about 1 mm (for $f_0 = 800\,\mathrm{GHz}$). Due to the low hole density only the lowest heavy hole subband is considered, anisotropic and nonparabolic effects of the hole dispersion are neglected (see discussion in Section 4.1.3).

5.3.2 The effect of acoustic anisotropy

The question is how acoustic anisotropy influences the phonon-drag results. To give an answer, we study the phonon-drag images for two typical geometrical arrangements of GaAs/Al$_{\mathrm{x}}$Ga$_{1-\mathrm{x}}$As heterojunctions, a 2D electron gas in the (001) plane (i.e. the direction of confinement is the [001] axis), and a 2D hole gas in the (311) plane. Figs. 5.8 and 5.9 compare the results of phonon-drag calculations (separately for the two main electron-phonon coupling mechanisms) with the corresponding quasimomentum focusing patterns.[2] Particularly for the piezoelectric coupling many details of the phonon-drag images are due to the acoustic anisotropy of the substrate which gives rise to a highly anisotropic and focused flux of TA phonons on the 2D carrier systems (as observable in the quasimomentum focusing images). However, the drag current patterns (b,c) also demonstrate that the pure focusing images (a) are manifestly destroyed by the cutoff conditions and the anisotropy of the electron-phonon coupling mechanism itself.

How much the phonon focusing of the substrate is recognizable in the drag images depends mainly on the characteristic frequency of the used nonequilibrium phonons. For phonons of frequency $f_0 = \omega_0/2\pi = 120\,\mathrm{GHz}$ most of the phonons interact with the 2D carriers. The focusing image (Fig. 5.10(a)) is superimposed by an additional signal of the nearly unfocused but, by deformation potential coupling, very effectively interacting LA phonons. This signal, see Fig. 5.10(b), becomes apparent for large in-plane components of the phonon wavevector $q_{\parallel}$. The situation is different in the case of 300 GHz phonons (Fig. 5.10(c)). Here we have a large influence of the cutoff conditions suppressing the absorption of phonons with large in-plane components of phonon wavevector ($2k_{\mathrm{F}}$ cutoff) and with large normal components (cutoff by the overlap integral). Figs. 5.8–5.10 also demonstrate that the destruction of the focusing image by the cutoffs is more severe for the TA modes (and there again for the STA modes) owing to their larger wavevectors at the same frequency.

Because the interest is concentrated on acoustic anisotropy we have neglected in our drag-current calculations possible effects of anisotropy in the electron (hole) dispersion relation. For 2D electron gases in (001) GaAs/Al$_{\mathrm{x}}$Ga$_{1-\mathrm{x}}$As heterojunctions the dispersion of the conduction band near the band minimum is almost isotropic and this type of anisotropy shouldn't play any role. More difficult is the situation for 2D hole gases owing to their complicated hole subband structure as explained in Section 4.1.3. The influence of the valence band anisotropy on the carrier-phonon interaction of a 2D hole gas was discussed by Oh and Singh (2001) but only within the approximation of an isotropic phonon model. On the other hand it has been asserted by Greipel and Rössler (1992) that the angular dependence of the microscopic hole-phonon scattering process is dominated by the

---

[2] The quasimomentum focusing pattern of Fig. 5.8(a) is the 2D analog of the pseudo-3D plot of quasimomentum focusing in Fig. 3.10 of Chapter 3.

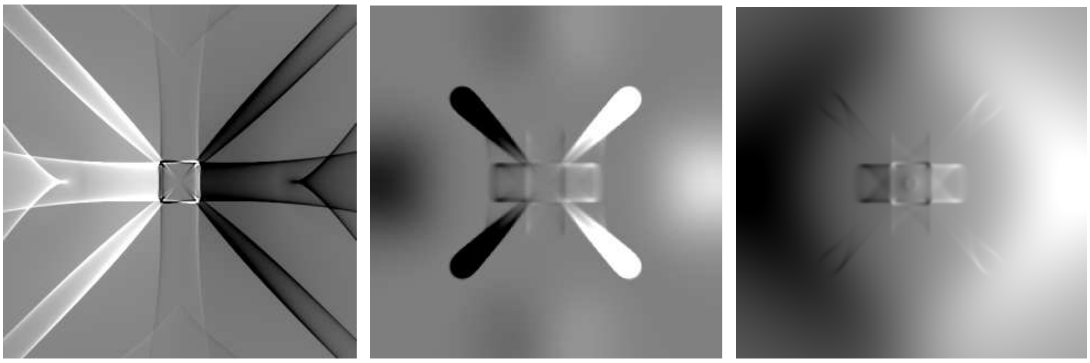
(a) (b) (c)

Figure 5.8: Calculated phonon quasimomentum focusing pattern (**a**) and calculated patterns of phonon-drag current (**b**,**c**) induced in a 2D electron gas of a (001) GaAs/$\mathrm{Al_xGa_{1-x}As}$ heterostructure by a monochromatic phonon source of frequency 200 GHz. Contributions of piezoelectric coupling (**b**) and deformation potential interaction (**c**) are separately presented. All patterns show the [110] component of phonon quasimomentum and drag current, respectively. The 2D electron density is $2.8 \cdot 10^{15}\,\mathrm{m}^2$.

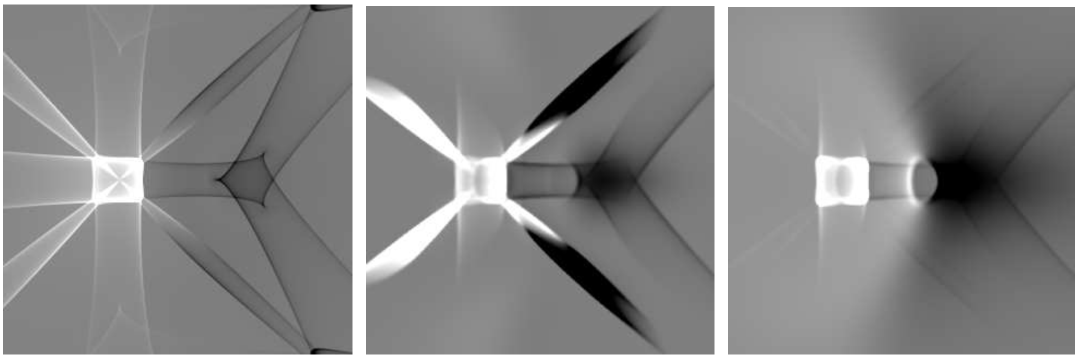
(a) (b) (c)

Figure 5.9: Calculated quasimomentum (**a**) and phonon-drag current (**b**,**c**) patterns like in Fig 5.8, but here for a 2D hole gas formed in a (311) GaAs/$\mathrm{Al_xGa_{1-x}As}$ heterostructure. Quasimomentum and current are measured in [$\bar{2}$33] direction, the 2D density of the holes is $3.3 \cdot 10^{15}\,\mathrm{m}^2$.

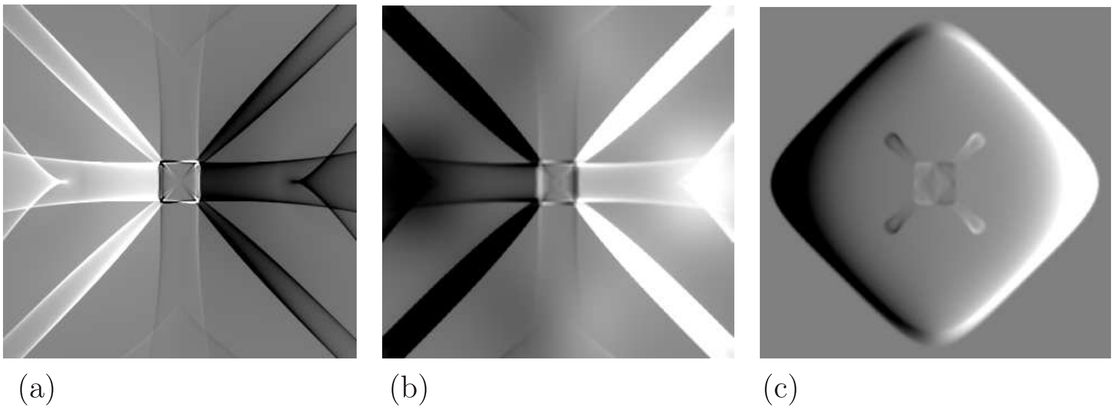
(a) (b) (c)

Figure 5.10: Images of the quasimomentum focusing (**a**) and of the phonon-drag current induced in a 2D electron gas of a (001) GaAs/Al$_x$Ga$_{1-x}$As heterostructure by monochromatic phonon sources of 120 GHz phonons (**b**) and 300 GHz phonons (**c**), respectively.

anisotropy of the coupling mechanism and of the phonon dispersion, whereas the anisotropy of the hole subband dispersion plays a negligible role. Phonon-drag calculations including the whole acoustic anisotropy of the sound waves as well as the anisotropy of the hole bands are still an open challenge.

5.3.3 The effect of carrier confinement

Fig. 5.11 shows how the width of a (quasi-)2D electron system affects the phonon-drag images. For a Planckian phonon source (heater temperature 15 K) we have

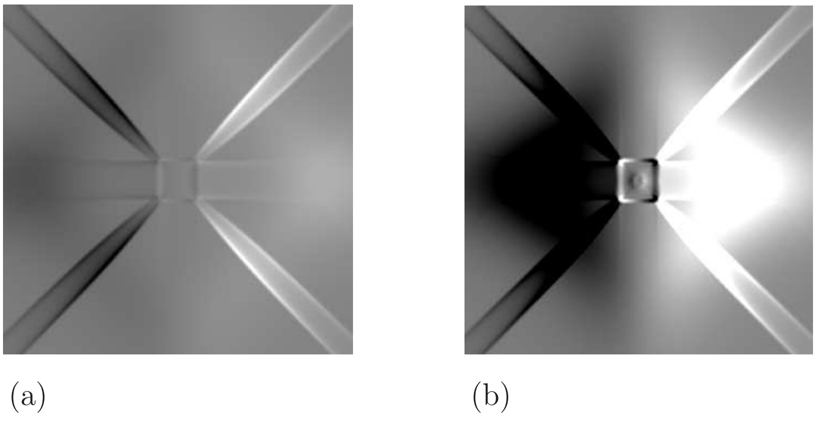
(a) (b)

Figure 5.11: Dependence of phonon-drag images on the confinement length of a (hypothetical) 2D electron system in a (001) GaAs/Al$_x$Ga$_{1-x}$As heterojunction. The images are calculated for a broadband (Planckian) phonon source. In (**a**) the Fang-Howard parameter is 3.6 nm, in (**b**) it is 1.6 nm. This corresponds to a 'width' of the 2D system of about 11 nm and 5 nm, respectively.

calculated the drag current induced in 2D electrons of a (001) GaAs/Al$_x$Ga$_{1-x}$As heterojunction. As an illustration two different values for the Fang-Howard parameter b (see Section 4.1.3, Eq. (4.27)) have been used, $b = 3.6\,\mathrm{nm}$ (Fig. 5.11(a)) and $b = 1.6\,\mathrm{nm}$ (Fig. 5.11(b)). For the 2D electron density we have assumed in both cases $2.8 \cdot 10^{15}\,\mathrm{m}^{-2}$ and the images cover an area of $1 \times 1\,\mathrm{mm}^2$ for a substrate thickness of 0.35 mm. The squared overlap integral, $|G_{11}(q_z)|^2 = \left(1 + (q_z b)^2\right)^{-3}$ (cf. Appendix C.1.1, Eq. (C.13)), causes a reduction of phonon drag for perpendicular components q_z of phonon wavevector larger than $1/b$. Contributions of high frequency phonons and/or phonons with small angles of incidence are ruled out for larger values of b, i.e. 'thicker' 2D systems. This effect becomes apparent in Fig. 5.11, where compared to figure (b) in figure (a) the signals of the high frequency LA phonons and the near-perpendicularly incident TA phonons are absent.

The study of the influence of confinement on phonon-drag images in the case of quasi-1D electron systems is naturally very interesting. Typical values of Fermi wavevector and sublevel spacing are comparable to phonon wavevectors and phonon energies used in drag imaging experiments. Due to the restriction in phase space the distortion of the phonon quasimomentum focusing image of Fig. 5.10(a) by the electron-phonon interaction is much stronger than in the case of phonon drag in 2D systems. Additionally, the presence of electrons in multi-subbands introduces peculiar behaviour for the acoustic phonon scattering. Fig. 5.12 shows theoretical drag patterns for a quasi-1D electron gas lying in the (001) plane of a $\mathrm{GaAs/Al_xGa_{1-x}As}$ heterojunction and aligned along the [110] direction. For all patterns the calculations have been performed for a pointlike monochromatic phonon source with isotropic phonon distribution in the source and a phonon frequency of 120 GHz. The results are presented separately for different coupling mechanisms (Figs. 5.12(a–d) for deformation potential interaction, Figs. 5.12(e–h) for piezoelectric coupling). Based on our discussion in Section 4.1.3 the confinement potential in $[\bar{1}10]$ direction (i.e. the additional lateral confinement in the 2D plane) is approximated by a parabolic well (images (d) and (h)) and a rectangular well (all the rest of images), respectively. Figs. 5.12(a,b) and (e,f) demonstrate the sensitivity of the phonon-drag images on changes of the Fermi wavevector. For Figs. 5.12(a,e) the electron density is chosen $n_{1\mathrm{D}} = 1 \cdot 10^7\,\mathrm{m}^{-1}$, only one subband is occupied and no phonon induced interband transitions are possible. For comparison, in Figs. 5.12 (b,f), the electron density $n_{1\mathrm{D}}$ is raised to $1 \cdot 10^8\,\mathrm{m}^{-1}$, two subbands are occupied. Now intra- and interband transitions are possible leading to larger angle ranges with nonzero drag signal. The images of the next column, i.e. Figs. 5.12(c,g), indicate directly the influence of the confinement potential. The channel width is here $2w = 150\,\mathrm{nm}$ instead of 100 nm. All other parameters are the same as in the second column. By the increase in the channel width not only the overlap integral reduces the drag signal for larger q_x (corresponding to Eq. (C.32)), but due to the smaller value of subband energy spacing one additional subband is occupied. Thus the relative Fermi wavevector $k_{\mathrm{F}}^{(n)}$ in each subband n is

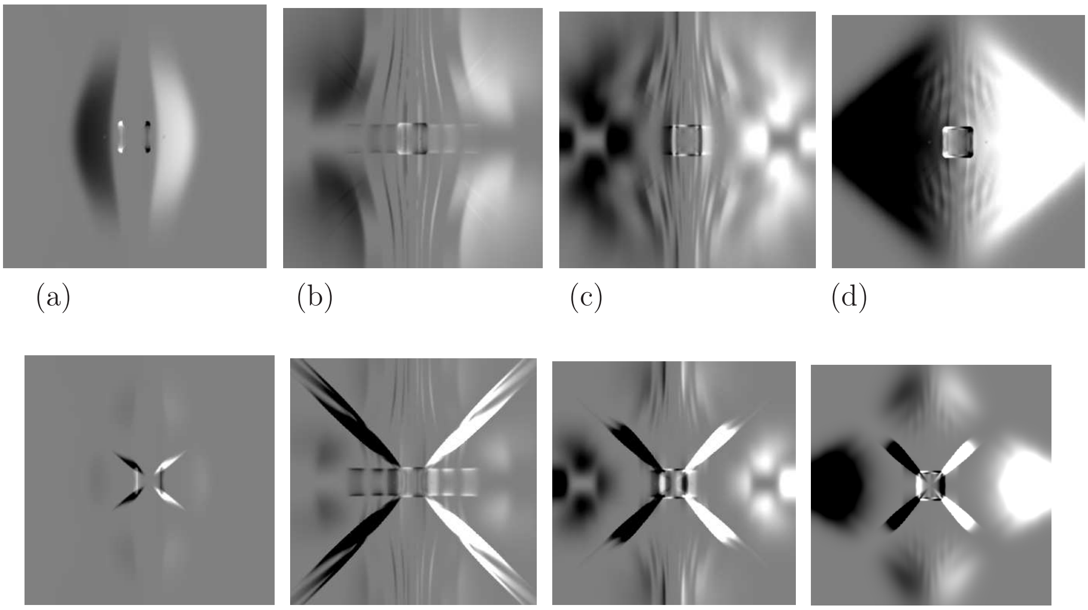

(a) (b) (c) (d)

(e) (f) (g) (h)

Figure 5.12: Theoretical patterns of the time-integrated drag current induced in a quasi-1D electron system by beams of monochromatic phonons of frequency $f_0 = 120\,\mathrm{GHz}$. The images are calculated as a function of phonon propagation direction for different electron densities and different parameters of confinement potential. The scanning area is $1.4\,\mathrm{mm} \times 1.4\,\mathrm{mm}$, the substrate thickness 0.5 mm. In the upper row only the contributions by deformation potential interaction are considered, in the bottom one only the piezoelectric coupling. Each point of an image corresponds to a respective position of the phonon source. The dark and bright areas represent regions with positive and negative drag current, respectively.

modified leading to changes of the function $\Lambda_{\mathrm{1D}}^{nn'}(q,\omega)$ (cf. Eq. (5.28)). The result is a remarkable variance of the drag patterns. A similar effect is seen in the outside right images (Figs. 5.12(d,h)). Here the characteristic channel width is again 100 nm, but a parabolic confinement potential is used instead of the box model of a rectangular well. The sublevel spacing is now equidistant and more subbands are occupied. This, together with the changes in the functional dependence of the overlap integral (Eq. (C.32) has to be replaced by (C.27)), causes a limitation of the in-plane components q_x and q_y of the phonon wavevectors contributing to the drag, particularly for the TA modes. However, on the other hand, it enhances the number of transition possibilities for smaller values of q_x and q_y. This is clearly seen by comparing Fig. 5.12(d) with Fig. 5.12(b).

For simplicity the screening of electron-phonon coupling has been neglected in the calculations performed for Fig. 5.12. Allowing for this effect one should expect an additional damping of the drag signal, particularly for phonons with small in-plane components of the phonon wavevector. More numerical results of phonon-drag images of 1D electron systems, including the influence of different phonon frequencies, have been published (Lehmann, 1994).

5.4 Outlook

Recently there has been an increasing interest in using phonon-drag imaging for the study of GaN epilayers (Stanton *et al.*, 2000; Lehmann *et al.*, 2002b). The wide band gap semiconductor GaN and its alloys are currently very interesting because of their potential applications in blue/near ultraviolet light emitting devices and high temperature, high frequency, high power transistors. However, compared to GaAs systems the electron-phonon interaction in GaN has been studied much less extensively and one expects significant differences. This is due to the much stronger piezoelectricity of GaN and also due to its different crystal structure (wurtzite for GaN films epitaxially grown on sapphire instead of zinc-blende for homoepitaxial GaAs). Although there is a good qualitative agreement between the calculated and the experimental drag images (Lehmann *et al.*, 2002b), two problems remain to be solved for still better understanding. The first is the trouble with the large lattice mismatch between GaN and the sapphire substrate leading to a strong diffuse phonon scattering at the interface. A possible experimental solution could be the use of 6H-silicon carbide as substrate material (Stanton *et al.*, 2003a). The second problem is more fundamental. It is still an open challenge of the theory to develop a model of phonon induced drag current for highly disordered materials.

Chapter 6

Acoustic Phonon Emission by Hot Electrons

The technologically important problem of energy relaxation by hot carriers is a second example for our theoretical analysis of phonon spectroscopy on low-dimensional systems. We develop a theoretical model for the angle- and mode-resolved acoustic phonon emission by hot quasi-2D electrons and calculate both the total emission rate and the emission rate as a function of detector position for different electron-phonon coupling mechanisms and for different models of electron confinement. Additionally we show how the screening of the electron-phonon coupling by the electron-electron interaction will influence the theoretical results. By comparison with corresponding experiments, we demonstrate that commonly applied isotropic phonon models as well as some approximations for the electron envelope functions (describing the carrier confinement) fail in the case of angle- and mode-resolved phonon emission. Particularly for phonon emission normal to the 2D electrons, acoustic anisotropy and screening lead to surprising results, as e.g. the relatively large contributions by deformation potential coupled TA phonons.

6.1 Energy relaxation in low-dimensional systems – Basic features

So called hot electrons dissipate their energy by emitting phonons and (rarely) photons or by exiting other electrons. We speak of hot carriers or, to be precise, of a hot carrier regime if the carrier distribution function can be described by a Fermi-Dirac distribution with a single carrier temperature higher than the lattice temperature. Such a heating of electrons is possible by optical or electrical excitations due to applied photon or electric fields. If e.g. a semiconductor is excited by a pulsed laser, the electrons or holes are initially in a nonthermal regime, but can be described by a hot carrier regime within less than one picosecond. This equilibration of the electrons takes place via elastic scattering with (immobile) impurities and other electrons. The following temporal drop of the carrier temperature due to inelastic scattering processes is described by the energy loss rate per carrier. The detailed mechanism of this energy dissipation depends, for a given material, mainly on the considered temperature range.

The study of electron energy loss rates provides fundamental insight into the electron-phonon interaction because they are directly related to inelastic collisions with phonons. In contrast, mobility measurements, while useful in many ways, provide only limited information about electron-phonon interactions because mobilities are also influenced by elastic collisions (e.g. by impurity scattering). In the following, a short overview over the process of energy relaxation by hot carriers is given, followed by a detailed discussion of acoustic phonon emission by hot (quasi) 2D electron systems. For further details on energy relaxation by hot carriers in semiconductor nanostructures the reader is referred to reviews by Ridley (1991), Shah (1992), Balkan (1998), and Kent and Wigmore (2003).

For the s-like electrons in the lowest conduction band of GaAs the polar optical scattering (Fröhlich interaction) with longitudinal optical (LO) phonons is the dominant relaxation mechanism at temperatures above 40-50 K [1], while at lower temperatures acoustic phonon scattering via deformation potential and piezoelectric interaction is dominating. The dominance of optical phonon emission at higher temperatures is due to the approximately exponential dependence of the corresponding average energy loss rate on the electron temperature T_{el}

$$\left\langle \frac{\mathrm{d}E}{\mathrm{d}t} \right\rangle = \frac{\hbar\omega_{\mathrm{LO}}}{\tau_{\mathrm{LO}}}\, e^{-\hbar\omega_{\mathrm{LO}}/k_{\mathrm{B}}T_{\mathrm{el}}} \tag{6.1}$$

(Conwell, 1967). Here $\hbar\omega_{\mathrm{LO}}$ is the energy of the LO phonons (about 36 meV for bulk GaAs) and $1/\tau_{\mathrm{LO}}$ presents a (dimension dependent) characteristic rate for the polar optical phonon scattering. In deriving (6.1) it was assumed that the electrons emitting an LO phonon have a classical Maxwell-Boltzmann distribution, that for the considered temperatures $k_{\mathrm{B}}T_{\mathrm{el}}/\hbar\omega_{\mathrm{LO}} \ll 1$ is valid and that the electron-phonon interaction is unscreened. Additionally, so called hot phonon effects were neglected, which are provoked by the presence of a nonequilibrium LO phonon population due to the emission process itself.[2] The result of such a nonequilibrium phonon population may be a reabsorption of phonons by the electrons and hence a reduction of the net energy loss rate of the electrons (Shah *et al.*, 1970, 1985; Cai *et al.*, 1987, see also a review by Shah, 1999).

In contrast to the exponential increase of optical phonon emission with temperature, the increase in acoustic phonon emission is, due to the restrictions by energy and momentum conservation, approximately linear (valid at not too low electron temperatures). Therefore the temperature at which the changeover from acoustic to optical phonon emission takes place depends mainly on the LO phonon energy.

---

[1] For holes also the nonpolar optical scattering (deformation potential electron–optical phonon interaction) has to be included.

[2] Due to the small group velocity and the finite lifetime (long compared to the typical time for generation), a large number of emitted optical phonons may be present in the photoexcited volume. In this case the phonon occupation number is not determined by the lattice temperature but rather by the phonon generation and absorption rate as well as by the anharmonic decay rate into acoustic phonons.

In the temperature range where usually acoustic phonon emission is assumed to be dominating two other channels of energy dissipation may still exist, giving rise to an enhancement of energy loss. This is caused by the many-body renormalization of the phonon spectral function due to the coupling with the electron gas. In polar materials LO phonons can couple via the Fröhlich interaction to plasmons and quasiparticle excitations resulting in three hybrid branches of the phonon density of states: the phonon-like branch near the LO phonon energy, the plasmon-like branch near the plasmon energy and a quasiparticle-like branch in the low energy quasiparticle excitation region (Das Sarma *et al.*, 1990). Coupled plasmon-LO phonon modes predicted by Yokota (1961) were first observed in the Raman spectrum of GaAs (Mooradian and Wright, 1966) and were used first by Das Sarma *et al.* (1988b) to explain the discrepancy in the power loss rates between the experiment and the numerical results calculated with conventional scattering mechanisms. Even though the phonon spectral weight of the plasmon-like modes is very small compared to the phonon spectral weight of the phonon-like modes—and that of quasiparticle-like modes is usually still much smaller—under certain conditions these modes may lead to modifications of the power loss by the acoustic and bare LO phonons. This can be the case for the plasmon-like modes at low electron densities (when the plasmon energy is much below the LO phonon energy) and in an intermediate temperature range between 30 and 50 K, since the exponential term $e^{-\hbar\omega/k_\mathrm{B}T}$ in the expression for the energy loss favours the lower energy modes at low temperatures (Das Sarma *et al.*, 1988a,c). At high carrier densities and low electron temperatures the quasiparticle-like modes also can give relevant contributions to the energy relaxation as it was shown in calculations by Kawamura *et al.* (1990) for GaAs/$\mathrm{Al_xGa_{1-x}As}$ heterojunctions. However, to give a final answer about the role of coupled phonon modes in the process of energy loss at low temperatures, more should be known about their behaviour after excitation. If the coupled modes themselves can lose their energy only by exciting single electrons (Landau damping), no net energy loss from the hot electrons would be the result. On the other hand there is convincing evidence that these modes predominantly decay into a pair of (bare) phonons (Kozorezov *et al.*, 1997), whose acoustic decay products are detected in phonon emission experiments (Giltrow *et al.*, 1995; Al Jawhari *et al.*, 1999; Wigmore *et al.*, 2001).

The process of energy relaxation of hot low-dimensional electrons can be directly observed using the heat pulse technique described in Chapter 2. More traditional techniques for determining electron energy relaxation rates include for example far infrared emission measurements (Höpfel and Weimann, 1985; Akimov *et al.*, 1991; Hirakawa *et al.*, 1993), luminescence measurements (see, e.g. Shah *et al.*, 1985; Yang *et al.*, 1985; Leo *et al.*, 1988) or transport (Payne *et al.*, 1983; Ouali *et al.*,

1999) and magnetotransport (Shubnikov-de Haas) measurements (Hirakawa and Sakaki, 1986; Ma *et al.*, 1991; Balkan *et al.*, 1995; Sugaya *et al.*, 2002; Çelik *et al.*, 2002). The advantage of the heat pulse technique over these traditional techniques is that direct phonon emission studies give not only integrated information about the strength of the electron-phonon interaction process and its dependence from the parameters of the considered electron system, but also detailed information about the polarization and the wavevector of the phonons involved. With the greater quantity of observable data, phonon emission experiments are a better test of theoretical models of the electron-phonon interaction in low-dimensional systems.

A typical setup of such a phonon emission experiment is shown in Fig. 6.1. A sample which consists of a small low-dimensional electron device fabricated on a semiconductor substrate is cooled to liquid helium temperatures. By passing a short current pulse through the device the carriers are heated above the substrate temperature. The emitted phonons are detected using a superconducting bolometer. By placing the detector at different positions the angular resolution of the acoustic phonon emission is possible. A resolution between different polarized acoustic phonons is possible if the excitation pulse is shorter than the difference between the flight times of the longitudinal and the two transverse modes. In the case of optical or coupled LO phonons the emitted modes cannot be detected directly by the bolometer, but the acoustic decay products via anharmonic down-conversion are observed. Due to isotope scattering and further down-conversion processes the propagation of the acoustic decay products will be quasi-diffusive instead of ballistic, leading to a delayed diffuse detector signal. Only a small part will arrive at close to the time expected of ballistic phonon propagation (Maris, 1990).

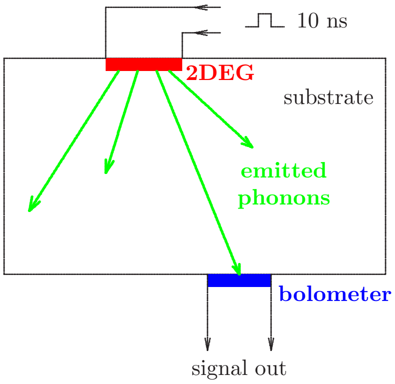

Figure 6.1: Experimental geometry for a typical phonon emission experiment.

Measurements of the strengths of the different acoustic phonon modes as a function of the electron temperature give direct information about the character of the electron-phonon scattering process and the confinement potential of the electrons. The experimental results have demonstrated the change from a predominant emission of acoustic phonons (and possibly coupled modes) to optical phonons with rising electrical input power (Chin *et al.*, 1984; Hawker *et al.*, 1992; Wigmore *et al.*, 1993; Danilchenko *et al.*, 1994c; Kent *et al.*, 1997c; Al Jawhari *et al.*, 1999; Cross *et al.*, 1999). The intensity of acoustic phonon signals from hot low-dimensional carrier systems depends strongly on the emission angle and on the phonon polarization (Rothenfusser *et al.*, 1986; Wigmore *et al.*, 1991; Danilchenko *et al.*, 1994b; Kent *et al.*, 1997c), it varies for different sample structures and different confinement potentials (George *et al.*, 1995; Hawker *et al.*, 1995; Asche *et al.*, 1995; Cross *et al.*, 1999; Lehmann *et al.*, 2002a).

However, to interpret the experimental results quantitatively they must be compared with theoretical models. Such theoretical studies of the angular dependence and the mode dependence of acoustic phonon emission have been performed by several authors both for low-dimensional electron and hole systems (Rothenfusser *et al.*, 1986; Vass, 1987; Challis *et al.*, 1987; Vasko *et al.*, 1993; Xu and Mahanty, 1994; Totland *et al.*, 1999; Oh and Singh, 2001). The case of an applied quantizing magnetic field has also been taken into account (Toombs *et al.*, 1987; Benedict, 1991; Shik and Challis, 1993; Xu and Zhang, 1996; Xu, 1996). However, in almost all practical calculations an isotropic model for the phonons has been used in the electron-phonon matrix elements. Acoustic anisotropy has been at most considered by including roughly the effect of focusing on the phonon propagation.[3] Moreover, screening of the electron-phonon coupling has often been treated inadequately.

As a consequence, a number of experimental findings could not be explained. For example, one of the surprising results for the 2D electron systems was the weakness of the LA mode emission. In the experiments on GaAs heterojunctions using a phonon detector directly opposite the 2D electrons, the LA mode was barely detectable while the TA was very strong (Chin *et al.*, 1984; Hawker *et al.*, 1992; Wigmore *et al.*, 1993). In measurements on 2D electrons in δ-doped GaAs (Danilchenko *et al.*, 1994b; Asche *et al.*, 1995) an LA signal was observed, but still much weaker than the TA one. These results were in strong contradiction to all theoretical studies. Theory had predicted that the deformation potential coupled LA phonons should be dominant. As shown in Section 4.2, Eqs. (4.53) and (4.60), the coupling coefficients for the deformation potential interaction $|h^{\mathrm{DP}}_{\mathbf{q},\lambda}|^2$ are proportional to the phonon wavevector q, whereas for piezoelectric coupling $|h^{\mathrm{PE}}_{\mathbf{q},\lambda}|^2 \sim q^{-1}$. In GaAs the two are about equal in strength at $q \approx 10^8\,\mathrm{m}^{-1}$ corresponding to $T_{\mathrm{el}} \approx \hbar q\bar{c}/3k_{\mathrm{B}} \approx 3\,\mathrm{K}$, where $\bar{c}$ is the average phase velocity of the phonons. Therefore, the LA mode should be strongest at the electron temperatures relevant to the above experiments with $T_{\mathrm{el}} = $ 10-50 K since the isotropic phonon model rules out the coupling of electrons with TA phonons via deformation potential interaction. Even allowing for phonon focusing, which gives a TA:LA ratio of about 20:1 for phonon propagation in a small cone around the [001] direction (the actual enhancement depends on the precise size and orientation of device and detector), a dominant LA signal is still predicted. The fact that the disagreement cannot be explained by phonon focusing as initially expected was also supported by experiments with (311) GaAs/AlGaAs heterojunctions (George *et al.*, 1995), where in normal direction no strong effect by focusing should appear, and by phonon emission from a bulk n-type GaAs epilayer. In case of the 3D electron system at about the same electron temperature as the heterojunction the LA emission is totally dominant over the TA emission (Kent *et al.*, 1997a).

---

[3] Only in theoretical studies for the acoustic phonon emission by 2D hole gases the effect of acoustic anisotropy on the angular dependence of the microscopic scattering process has been considered (Greipel and Rössler, 1992). However, these calculations have been restricted to transition probabilities for deformation potential coupling neglecting, among other things, screening. Nevertheless, they have demonstrated the strong influence on the scattering rates by the anisotropy of the phonon dispersion and of the coupling mechanism.

To explain this *mystery of the missing LA mode* for hot 2D electrons, systematic measurements of systems with different confinement potential were performed by Kent and coworkers (George *et al.*, 1995; Kent *et al.*, 1997a; Cross, 2001; Lehmann *et al.*, 2002a). It has been shown that for not too narrow wells larger confinement lengths involve a suppression of the LA phonon emission in directions normal to the 2D carrier systems. This led to the conclusion (George *et al.*, 1995; Kent *et al.*, 1997a) that the effect can be understood by a cutoff of the perpendicular phonon momentum due to the overlap integral (see Eqs. (C.13) and (C.17)). In GaAs heterostructures the perpendicular component of the phonon wavevector is typically restricted to less than about $10^8\,\mathrm{m}^{-1}$, which means that emission is cut off before the deformation potential interaction takes over from piezoelectric interaction as the dominant phonon-coupling mechanism. Nevertheless, the effect is too small to explain the almost complete absence of the LA mode in the heat pulse signals of 2D electrons in single heterojunctions. Time- and angle-resolved measurements also prove that the enhanced TA:LA ratio cannot be the result of the decay of coupled modes into TA phonons.

In a series of papers (Lehmann *et al.*, 1998; Lehmann and Jasiukiewicz, 1999; Jasiukiewicz *et al.*, 1999; Lehmann *et al.*, 2002a) we have shown that the main reason for the collapse of the conventional theories in the case of application to angle-resolved phonon emission is the non-consideration of the effects of acoustic anisotropy on the electron-phonon matrix elements. The total exclusion of deformation potential coupling to TA phonons, as explained in Section 4.2.4, is such a serious deficiency of the isotropic phonon model. Another grave problem of some of the earlier calculations is that they only allow for screening, normally in a static approximation, of the piezoelectric interaction. The argument commonly given for not screening the deformation potential interaction is that it is a short range interaction for which the in-plane component of phonon wavevector $q_\parallel$ is larger than the inverse screening length q_S. While this is usually a reasonable approximation at large wavevectors q where the deformation coupling is dominant, for emission in a direction nearly normal to the 2D layer $q_\parallel$ can also be very small for large q and screening is effective. Furthermore, for 2D electrons in a heterojunction or quantum well the electron-phonon interaction may be cut off for wavevectors comparable to q_{S}.

The aim of the following sections is to describe in detail the influence of acoustic anisotropy and screening on the results of angle- and time-resolved acoustic phonon emission from hot 2D electron systems and to explain the experimental results without artificially enhancing the coupling constants and additional relaxation channels. Furthermore, considering the example of quasi-2D electrons in GaAs/Al$_{\mathrm{x}}$Ga$_{1-\mathrm{x}}$As heterojunctions and quantum wells we will show how sensitively the results depend on the electron confinement. In doing so, we will demonstrate that approximations that are usually accepted and work relatively well for calculating the overall energy loss rates of hot electrons and the electrical transport quantities, fail to interpret angle-resolved emission experiments correctly.

6.2 Theory of angle-resolved acoustic phonon emission

Below we will present a theoretical model for the acoustic phonon emission by hot electrons in low-dimensional electron systems which serves to explain and predict the results of angle- and time-resolved heat pulse measurements. The model (Lehmann *et al.*, 1998, 2002a) includes the effects of acoustic anisotropy, not only on phonon propagation, but also on electron-phonon coupling, as well as a full dynamic screening of the electron-phonon interaction within the finite-temperature random-phase approximation (RPA). It uses realistic models for the confinement of the electrons, as described in Section 4.1.3, that also allow for the penetration of the electron wavefunctions into the barriers.

We consider a low-dimensional electron system with N_{el} electrons embedded in a bulk substrate. Then the general expression for the acoustic phonon emission rate per electron is

$$P(t) = \frac{1}{N_{\mathrm{el}}} \sum_{\mathbf{q},\lambda} \hbar\omega_{\mathbf{q},\lambda} \; \frac{\mathrm{d}}{\mathrm{d}t} \left\langle b^{+}_{\mathbf{q},\lambda} b_{\mathbf{q},\lambda} \right\rangle (t) \; . \tag{6.2}$$

The variables $\omega_{\mathbf{q},\lambda}$, $\mathbf{q}$ and λ denote the frequency, the wavevector and the polarization of the bulk acoustic phonons as introduced in Section 3.1. The time derivative of the phonon number operator $b^{+}_{\mathbf{q},\lambda} b_{\mathbf{q},\lambda}$ is calculated for the coupled electron-phonon system with the Hamiltonian

$$H = H_{\mathrm{el}} + \sum_{\mathbf{q},\lambda} \hbar\omega_{\mathbf{q},\lambda} b^{+}_{\mathbf{q},\lambda} b_{\mathbf{q},\lambda} \; , + \sum_{\mathbf{q},\lambda} h_{\mathbf{q},\lambda} (b_{\mathbf{q},\lambda} + b^{+}_{-\mathbf{q},\lambda}) \rho_{-\mathbf{q}} \; , \tag{6.3}$$

where the electron term H_{el} includes also the contribution of the electron-electron interaction $H_{\mathrm{el-el}}$. The last term in (6.3) accounts for the electron-phonon interaction which is specified by the electron-phonon matrix elements $h_{\mathbf{q},\lambda}$ discussed in

Section 4.2. The dimensionality of the electron system and the influence of the electron confinement potential that has been used are completely covered in $H_{\mathrm{el-el}}$ and the Fourier transform of the electron density operator $\rho_{\mathbf{q}}$.

At this point a comment concerning the form of our electron-phonon interaction term, which is restricted to one-phonon processes, should be made. Falko and Challis (1993) have pointed out that two-phonon emission may give significant contributions to the energy loss of hot 2D electrons if the one-phonon emission process is strongly suppressed by the constraints due to in-plane selections rules and electron confinement. In a recent paper Kubakaddi *et al.* (2002) have calculated the energy relaxation of 2D electrons in $\mathrm{GaAs/Al_xGa_{1-x}As}$ quantum wells and heterojunctions including the two-phonon coupling and have found an enhanced power loss in the temperature region above 20 K caused by electron interaction with two near zone boundary TA phonons. Despite the second order nature of two-phonon processes their significance is plausible since the emission of two phonons with approximately equal and oppositely directed phonon wavevectors avoids the constraints imposed by the momentum conservation and the overlap integral. In addition the phonon density of states is high for band edge TA phonons. Although a more detailed analysis is necessary, as a result of these studies two-phonon emission processes (as well as the emission of coupled LO modes) should be included in detailed calculations for the total power loss of hot 2D electrons close to the onset of the dominance of LO phonon emission. Nevertheless, the influence of two-phonon processes on the results of angle- and time-resolved phonon emission measurements should be negligible. Since the dispersion curve is flat at the zone boundary, the band edge TA phonons travel slowly and they are (in general) unable to decay easily into faster moving phonons due to the restrictions by energy and momentum conservation. Furthermore, due to the high frequency of the band edge phonons, a very high probability for isotope scattering is to be expected, which gives in consequence mainly contributions to the delayed diffusive phonon signal. Therefore in the following we will restrict ourselves to one-phonon emission processes.

Evaluating the commutator of the phonon number operator with the Hamiltonian of (6.3) we obtain for the emission rate

$$P(t) = -\frac{2}{N_{\mathrm{el}}} \sum_{\mathbf{q},\lambda} \omega_{\mathbf{q},\lambda} \,\mathrm{Im}\left\{ h_{\mathbf{q},\lambda} \left\langle b_{\mathbf{q},\lambda} \rho_{-\mathbf{q}} \right\rangle (t) \right\} . \tag{6.4}$$

Within linear response theory the expression $\left\langle b_{\mathbf{q},\lambda} \rho_{-\mathbf{q}} \right\rangle (t)$ can be calculated using adiabatic initial conditions and neglecting all two and higher order phonon processes

$$\begin{aligned} \left\langle b_{\mathbf{q},\lambda} \rho_{-\mathbf{q}} \right\rangle (t) = -\, h^*_{\mathbf{q},\lambda}(t) \int_0^\infty \mathrm{d}t' \Big\{ \left\langle b^+_{\mathbf{q},\lambda} b_{\mathbf{q},\lambda} \right\rangle \left(\rho_{\mathbf{q}} \middle| iL e^{-i(L+\omega_{\mathbf{q},\lambda}-i\eta)t'} \rho_{\mathbf{q}} \right) \\ + \frac{i}{\hbar} \left\langle \rho^+_{\mathbf{q}} e^{-i(L+\omega_{\mathbf{q},\lambda}-i\eta)t'} \rho_{\mathbf{q}} \right\rangle_{\hat{\rho}_{\mathrm{el}}^{\beta_{\mathrm{el}}}} \Big\} \Big|_{\eta\to 0} . \end{aligned} \tag{6.5}$$

In (6.5) we have made use of the Liouville operator L corresponding to H_{el} and the Mori operator product introduced in Section 5.2. Assuming that the electron system was in thermal equilibrium at $t \to -\infty$ the expectation values of the electron variables on the right hand side of (6.5) are determined by the statistical operator $\hat{\rho}_{\text{el}}^{\beta_{\text{el}}} = \exp(-\beta_{\text{el}} H_{\text{el}})/\text{Tr}\,(\exp(-\beta_{\text{el}} H_{\text{el}}))$ with $T_{\text{el}} = 1/k_{\text{B}}\beta_{\text{el}}$ as effective electron temperature. By means of the dissipation-fluctuation theorem for the density-density correlation function

$$\frac{1}{2\hbar}\int\limits_{-\infty}^{\infty} \mathrm{d}t\, \left\langle \rho_{\mathbf{q}}^{+} e^{-i(L+\omega)t} \rho_{\mathbf{q}} \right\rangle_{\hat{\rho}_{\text{el}}^{\beta_{\text{el}}}} e^{-\eta|t|} \bigg|_{\eta\to 0} = \frac{1}{1-e^{\beta_{\text{el}}\hbar\omega}}\, \text{Im}\Big(\rho_{\mathbf{q}}\Big|\frac{L}{L+\omega-i\eta}\rho_{\mathbf{q}}\Big)\Big|_{\eta\to 0} \tag{6.6}$$

and the symmetry relation

$$\text{Im}\Big(\rho_{\mathbf{q}}\Big|\frac{L}{L+\omega-i\eta}\rho_{\mathbf{q}}\Big) = \text{Im}\Big(\rho_{\mathbf{q}}^{+}\Big|\frac{L}{L-\omega+i\eta}\rho_{\mathbf{q}}^{+}\Big) = -\text{Im}\Big(\rho_{\mathbf{q}}\Big|\frac{L}{L+\omega+i\eta}\rho_{\mathbf{q}}\Big) \tag{6.7}$$

the acoustic phonon emission rate can be expressed by the imaginary part of the dynamic susceptibility of the interacting low-dimensional electron system

$$P = \frac{2}{N_{\text{el}}} \sum_{\mathbf{q},\lambda} \omega_{\mathbf{q},\lambda}\, |h_{\mathbf{q},\lambda}|^2 \left(N_{\mathbf{q},\lambda}^{T_{\text{el}}} - N_{\mathbf{q},\lambda}^{T_{\text{c}}}\right) \text{Im}\bigg\{\Big(\rho_{\mathbf{q}}\Big|\frac{L}{L+\omega_{\mathbf{q},\lambda}+i\eta}\rho_{\mathbf{q}}\Big)\Big|_{\eta\to 0}\bigg\}\,. \tag{6.8}$$

The function $N_{\mathbf{q},\lambda}^{T} = [\exp(\hbar\omega_{\mathbf{q},\lambda}/k_{\text{B}}T) - 1]^{-1}$ is the Bose factor at temperature T and $T_{\text{c}} < T_{\text{el}}$ is the (substrate) lattice temperature. Here it is assumed that the lattice is in equilibrium with a heat reservoir so that the emitted acoustic phonons do not raise the lattice temperature.

In the general expression (6.8) all effects of electron confinement on electron-phonon coupling and screening are contained in the dynamic susceptibility $\Big(\rho_{\mathbf{q}}\Big|\frac{L}{L+\omega+i\eta}\rho_{\mathbf{q}}\Big)$ which depends on the dimensionality of the electron system and on the corresponding overlap integrals and form factors (see Appendices B and C). For the case of a quasi-2D electron gas in a modulation-doped heterojunction or quantum well it follows from (6.8) and (B.31)

$$\begin{aligned} P = -\,\frac{2}{N_{\text{el}}} \sum_{\mathbf{q},\lambda} \omega_{\mathbf{q},\lambda} \left(N_{\mathbf{q},\lambda}^{T_{\text{el}}} - N_{\mathbf{q},\lambda}^{T_{\text{c}}}\right) |h_{\mathbf{q},\lambda}|^2\, |G_{11}(q_\perp)|^2 \\ \times\ \text{Im}\bigg\{\frac{\chi_{11}^{T_{\text{el}}}(q_\parallel,\omega_{\mathbf{q},\lambda})}{1 - v(q_\parallel) g_{11}^{11}(q_\parallel) \chi_{11}^{T_{\text{el}}}(q_\parallel,\omega_{\mathbf{q},\lambda})}\bigg\}\,. \end{aligned} \tag{6.9}$$

In calculating this expression it was assumed that only the lowest electron subband is occupied, which holds true in GaAs/$\text{Al}_{\text{x}}\text{Ga}_{1-\text{x}}$As systems as long as the electron densities are not too high, and that the nonparabolicity of the electronic subband can be neglected. The dynamical screening of the electron-phonon coupling by the electron-electron interaction was considered in the RPA, thus $\chi_{11}^{T_{\rm el}}$ is the polarizability function for a noninteracting 2D electron gas at temperature $T_{\rm el}$ as defined in Eq. (B.30). The function $v(q_\parallel)$ is the 2D Fourier transform of the Coulomb potential and is given by Eq. (B.10). The overlap integral $G_{11}(q_\perp)$ and the form factor $g_{11}^{11}(q_\parallel)$ (see Appendix C) arise from the finite extension of the component of the electron wavefunction along the axis normal to the plane of the electron system and depend strongly on the chosen form of the confinement potential. Changing in (6.9) the summation over $\mathbf{q}$ into integration in the spherical coordinates and integrating over all phonon frequencies, we obtain the emitted power per unit angle in the wavevector space (in direction $\hat{\mathbf{q}}$) for a given polarization λ

$$P_{\hat{\mathbf{q}},\lambda} = \frac{2V_{\rm c}}{N_{\rm el}(2\pi)^3}\frac{1}{c_{\hat{\mathbf{q}},\lambda}^3}\int {\rm d}\omega\,\omega^3(N_\omega^{T_{\rm c}} - N_\omega^{T_{\rm el}})\frac{|h_{\mathbf{q},\lambda}|^2}{|\varepsilon_{11}^{11}(q_\parallel,\omega)|^2}\,|G_{11}(q_\perp)|^2\,{\rm Im}\chi_{11}^{T_{\rm el}}(q_\parallel,\omega)\;. \tag{6.10}$$

Here we have made use of the fact that in the relevant frequency range the long-wave approximation for the phase velocities $c_{\mathbf{q},\lambda} = c_{\hat{\mathbf{q}},\lambda}$ is valid and we have introduced the dielectric function $\varepsilon_{11}^{11}(q_\parallel,\omega)$. According to the results in Appendix B (see Eqs. (B.21), (B.32) and (B.33)) the function $|\varepsilon_{11}^{11}(q_\parallel,\omega)|^2$ reads for a 2D electron gas as

$$\begin{aligned}\left|\varepsilon_{11}^{11}(q_\parallel,\omega)\right|^2 = \;& \Big[1+\frac{q_{\rm S}(q_\parallel)}{q_\parallel}\,\frac{k_{\rm F}}{q_\parallel}\,\mathcal{P}\Big(\frac{q_\parallel}{k_{\rm F}},\frac{\hbar\omega}{E_{\rm F}},\frac{k_{\rm B}T_{\rm el}}{E_{\rm F}}\Big)\Big]^2 \\ & + \Big[\frac{q_{\rm S}(q_\parallel)}{q_\parallel}\,\frac{k_{\rm F}}{q_\parallel}\mathcal{L}\Big(\frac{q_\parallel}{k_{\rm F}},\frac{\hbar\omega}{E_{\rm F}},\frac{k_{\rm B}T_{\rm el}}{E_{\rm F}}\Big)\Big]^2\end{aligned} \tag{6.11}$$

with $\mathcal{P}$ and $\mathcal{L}$ defined in (B.34) and (B.35), respectively, and with $k_{\rm F}$ and $E_{\rm F}$ as Fermi wavevector and Fermi energy of the electron system. Additionally, we have used in (6.11) the so called screening wavevector $q_{\rm S}(q_\parallel) = 2g_{11}^{11}(q_\parallel)/a_0^*$ for a (quasi) 2D system (see Appendix B.1.2), where $a_0^* = 4\pi\varepsilon_0\varepsilon_{\rm r}\hbar^2/e^2m^*$ is the effective Bohr radius.[4] Attention should be paid to the $q_\parallel$-dependence of $|\varepsilon_{11}^{11}(q_\parallel,\omega)|^2$ leading to a strong dependence of the emission on screening for emission close to the normal of the 2D electron system. We will later discuss this effect in detail.

Having in mind the different frequency dependence of the electron-phonon interaction potentials it is convenient for discussion to rewrite formula (6.10) for the emission via deformation potential coupling and piezoelectric coupling separately. Replacing on the r.h.s. of (6.10) the variables $q_\parallel$ and $q_\perp$ by their angular parts $\hat{q}_\parallel$ and $\hat{q}_\perp$, respectively, with $q_{\parallel,\perp} = \hat{q}_{\parallel,\perp}q = \hat{q}_{\parallel,\perp}\omega/c_{\hat{\mathbf{q}},\lambda}$ and introducing the dimensionless integration variable $\eta = \hbar\omega/k_{\rm B}T_{\rm el}$ we obtain with (B.33,B.35) and (4.53) for the deformation potential contribution to the phonon emission per unit angle in direction $\hat{\mathbf{q}}$

---

[4] For a strictly 2D system the screening wavevector $q_{\rm S}$ is equal to $2/a_0^*$ since $g_{11}^{11}(q_\parallel) = 1$.

$$\begin{aligned}
P^{(\mathrm{DP})}_{\hat{\mathbf{q}},\lambda} = {} & \frac{m^*\,\Theta_\mathrm{d}^2}{4\pi^3\hbar^5\rho\,k_\mathrm{F}}\left(\frac{k_\mathrm{B}T_\mathrm{el}}{c_{\hat{\mathbf{q}},\lambda}}\right)^4\frac{(\mathbf{e}_{\hat{\mathbf{q}},\lambda}\cdot\hat{\mathbf{q}})^2}{\hat{q}_\parallel} \\
& \times\int_0^\infty\mathrm{d}\eta\left(\frac{\eta^3}{e^\eta-1}-\frac{\eta^3}{e^{\eta\,T_\mathrm{el}/T_\mathrm{c}}-1}\right)\frac{\left|G_{11}\big(\frac{k_\mathrm{B}T_\mathrm{el}\hat{q}_\perp}{\hbar c_{\hat{\mathbf{q}},\lambda}}\,\eta\big)\right|^2}{\left|\varepsilon\big(\frac{k_\mathrm{B}T_\mathrm{el}\hat{q}_\parallel}{\hbar c_{\hat{\mathbf{q}},\lambda}}\,\eta\,,\,\frac{k_\mathrm{B}T_\mathrm{el}}{\hbar}\,\eta\big)\right|^2} \\
& \times\int_{-E_\mathrm{F}/k_\mathrm{B}T_\mathrm{el}}^\infty\mathrm{d}\zeta\frac{e^\zeta}{(e^\zeta+1)^2}\,\mathrm{Re}\left\{\sqrt{1+\frac{k_\mathrm{B}T_\mathrm{el}}{E_\mathrm{F}}\,\zeta-\left(\frac{k_\mathrm{B}T_\mathrm{el}\hat{q}_\parallel}{2\hbar k_\mathrm{F}c_{\hat{\mathbf{q}},\lambda}}\,\eta-\frac{m^*c_{\hat{\mathbf{q}},\lambda}}{\hbar k_\mathrm{F}\hat{q}_\parallel}\right)^2}\right. \\
& \left.\qquad-\sqrt{1+\frac{k_\mathrm{B}T_\mathrm{el}}{E_\mathrm{F}}\,\zeta-\left(\frac{k_\mathrm{B}T_\mathrm{el}\hat{q}_\parallel}{2\hbar k_\mathrm{F}c_{\hat{\mathbf{q}},\lambda}}\,\eta+\frac{m^*c_{\hat{\mathbf{q}},\lambda}}{\hbar k_\mathrm{F}\hat{q}_\parallel}\right)^2}\right\}
\end{aligned} \tag{6.12}$$

and with (4.60) for the piezoelectric contribution

$$\begin{aligned}
P^{(\mathrm{PE})}_{\hat{\mathbf{q}},\lambda} = {} & \frac{m^*\,(2|e|h_{14})^2}{4\pi^3\hbar^3\rho\,k_\mathrm{F}}\left(\frac{k_\mathrm{B}T_\mathrm{el}}{c_{\hat{\mathbf{q}},\lambda}}\right)^2\frac{\big(\hat{q}_x\hat{q}_y(\mathbf{e}_{\hat{\mathbf{q}},\lambda})_z+\hat{q}_y\hat{q}_z(\mathbf{e}_{\hat{\mathbf{q}},\lambda})_x+\hat{q}_x\hat{q}_z(\mathbf{e}_{\hat{\mathbf{q}},\lambda})_y\big)^2}{\hat{q}_\parallel} \\
& \times\int_0^\infty\mathrm{d}\eta\left(\frac{\eta}{e^\eta-1}-\frac{\eta}{e^{\eta\,T_\mathrm{el}/T_\mathrm{c}}-1}\right)\frac{\left|G_{11}\big(\frac{k_\mathrm{B}T_\mathrm{el}\hat{q}_\perp}{\hbar c_{\hat{\mathbf{q}},\lambda}}\,\eta\big)\right|^2}{\left|\varepsilon\big(\frac{k_\mathrm{B}T_\mathrm{el}\hat{q}_\parallel}{\hbar c_{\hat{\mathbf{q}},\lambda}}\,\eta\,,\,\frac{k_\mathrm{B}T_\mathrm{el}}{\hbar}\,\eta\big)\right|^2} \\
& \times\int_{-E_\mathrm{F}/k_\mathrm{B}T_\mathrm{el}}^\infty\mathrm{d}\zeta\frac{e^\zeta}{(e^\zeta+1)^2}\,\mathrm{Re}\left\{\sqrt{1+\frac{k_\mathrm{B}T_\mathrm{el}}{E_\mathrm{F}}\,\zeta-\left(\frac{k_\mathrm{B}T_\mathrm{el}\hat{q}_\parallel}{2\hbar k_\mathrm{F}c_{\hat{\mathbf{q}},\lambda}}\,\eta-\frac{m^*c_{\hat{\mathbf{q}},\lambda}}{\hbar k_\mathrm{F}\hat{q}_\parallel}\right)^2}\right. \\
& \left.\qquad-\sqrt{1+\frac{k_\mathrm{B}T_\mathrm{el}}{E_\mathrm{F}}\,\zeta-\left(\frac{k_\mathrm{B}T_\mathrm{el}\hat{q}_\parallel}{2\hbar k_\mathrm{F}c_{\hat{\mathbf{q}},\lambda}}\,\eta+\frac{m^*c_{\hat{\mathbf{q}},\lambda}}{\hbar k_\mathrm{F}\hat{q}_\parallel}\right)^2}\right\}\,.
\end{aligned} \tag{6.13}$$

Here Θ_d and h_{14} are the deformation potential and the piezoelectric constant, respectively. Eqs. (6.12) and (6.13) generalize relations for the angle-dependent phonon emission which were derived by Jasiukiewicz and Karpus (1996) in the limit of zero-temperature electron response functions. A further advantage of our expressions is that they allow a correct treatment of phonon emission close to the normal of the 2D system.

At low electron temperatures, $k_\mathrm{B}T_\mathrm{el} \ll k_\mathrm{B}T_\mathrm{BG} = \hbar c_{\hat{\mathbf{q}},\lambda}k_\mathrm{F}$, phonon emission with $q \sim k_\mathrm{F}$ becomes exponentially suppressed by temperature and only low-angle scattering of the electrons with $q_\parallel \ll k_\mathrm{F}$ prevails. In this temperature limit, the so called Bloch-Grüneisen (BG) regime, our relations for the phonon emission rate reproduce the known T_el^5 and T_el^3 power law dependence for the total energy relaxation rate due to deformation potential and piezoelectric coupling respectively (Karpus, 1986, 1988). In this case the ζ-integral in (6.12) and (6.13) is equal to $\eta\frac{k_\mathrm{B}T_\mathrm{el}}{2E_\mathrm{F}}$ and $|G_{11}(q_\perp)|^2 \approx 1$ since $q_\perp$ is much smaller than the inverse of the confinement length. Thus the phonon power emitted in all directions is

$$\begin{aligned} P^{(\mathrm{DP})} \xrightarrow{\mathrm{BG}} \; & \frac{m^{*2}\,\Theta_\mathrm{d}^2}{\pi^2\hbar^7\rho\,k_\mathrm{F}^3}\Big(k_\mathrm{B}T_\mathrm{el}\Big)^5 \sum_\lambda \frac{1}{4\pi}\int \mathrm{d}\Omega_\mathbf{q}\,\frac{(\mathbf{e}_{\hat{\mathbf{q}},\lambda}\cdot\hat{\mathbf{q}})^2}{\hat{q}_\parallel c^4_{\hat{\mathbf{q}},\lambda}} \\ & \times \int_0^\infty \mathrm{d}\eta\,\Big(\frac{\eta^4}{e^\eta-1} - \frac{\eta^4}{e^{\eta\,T_\mathrm{el}/T_\mathrm{c}}-1}\Big)\,\frac{1}{\big|\varepsilon\big(\frac{k_\mathrm{B}T_\mathrm{el}\hat{q}_\parallel}{\hbar c_{\hat{\mathbf{q}},\lambda}}\,\eta\,,\,\frac{k_\mathrm{B}T_\mathrm{el}}{\hbar}\,\eta\big)\big|^2} \end{aligned} \tag{6.14}$$

for deformation potential and

$$\begin{aligned} P^{(\mathrm{PE})} \xrightarrow{\mathrm{BG}} \; & \frac{m^{*2}\,(2|e|h_{14})^2}{\pi^2\hbar^5\rho\,k_\mathrm{F}^3}\Big(k_\mathrm{B}T_\mathrm{el}\Big)^3 \\ & \times \sum_\lambda \frac{1}{4\pi}\int \mathrm{d}\Omega_\mathbf{q}\,\frac{(\hat{q}_x\hat{q}_y(\mathbf{e}_{\hat{\mathbf{q}},\lambda})_z + \hat{q}_y\hat{q}_z(\mathbf{e}_{\hat{\mathbf{q}},\lambda})_x + \hat{q}_x\hat{q}_z(\mathbf{e}_{\hat{\mathbf{q}},\lambda})_y)^2}{\hat{q}_\parallel c^2_{\hat{\mathbf{q}},\lambda}} \\ & \times \int_0^\infty \mathrm{d}\eta\,\Big(\frac{\eta^2}{e^\eta-1} - \frac{\eta^2}{e^{\eta\,T_\mathrm{el}/T_\mathrm{c}}-1}\Big)\,\frac{1}{\big|\varepsilon\big(\frac{k_\mathrm{B}T_\mathrm{el}\hat{q}_\parallel}{\hbar c_{\hat{\mathbf{q}},\lambda}}\,\eta\,,\,\frac{k_\mathrm{B}T_\mathrm{el}}{\hbar}\,\eta\big)\big|^2}\,. \end{aligned} \tag{6.15}$$

for piezoelectric coupling. As long as the relevant contributions to the above integrals over η and $\Omega_\mathbf{q}$ are from phonons with $q_\parallel$ not much smaller than $2/a_0^*$, the inverse of the screening length, the influence of screening by the factor $|\varepsilon(q_\parallel,\omega)|^{-2}$ is small and can be ignored in a first approximation. The result is $P^{(\mathrm{DP})} \sim (T_\mathrm{el}^5 - T_\mathrm{c}^5)$ and $P^{(\mathrm{PE})} \sim (T_\mathrm{el}^3 - T_\mathrm{c}^3)$ respectively.

For (very) low electron temperatures $k_\mathrm{B}T_\mathrm{el} \ll 2\hbar c_{\hat{\mathbf{q}},\lambda}/a_0^*$, known as the screening regime, it holds $q_\parallel \ll 2/a_0^* < k_\mathrm{F}$ and with it $|\varepsilon(q_\parallel,\omega)|^{-2} \sim (q_\parallel a_0^*)^2$. The latter relation can be easily derived from (B.38) and the fact that the form factor $g_{11}^{11}(q_\parallel) \to 1$ for $q_\parallel \to 0$ as seen from Eq. (C.14) or Eq. (C.18) in Appendix C.1. As a consequence, this leads to T_el^7 (deformation potential) and T_el^5 (piezoelectric coupling) power laws for the electron energy relaxation rate in the screening regime of 2D systems (Price, 1982).

In contrast, in the high-temperature or equipartition range, where $k_\mathrm{B}T_\mathrm{el} \gg k_\mathrm{B}T_\mathrm{BG}$ but still much less then E_F, the electrons lose their energy in portions much smaller than $k_\mathrm{B}T_\mathrm{el}$. This is due to the $2k_\mathrm{F}$ cutoff for the in-plane component $q_\parallel$ of the phonon wavevector and the restrictions for $q_\perp$ by the overlap integral. In this case, the phonon equilibrium distribution $1/(e^{\hbar\omega/k_\mathrm{B}T_\mathrm{el}} - 1)$ can be replaced by its asymptotic value $k_\mathrm{B}T_\mathrm{el}/\hbar\omega$ giving in a crude approximation a linear temperature dependence of the energy relaxation rate both for deformation potential and piezoelectric coupling (Price, 1982; Jasiukiewicz and Karpus, 1996). In deriving the linear dependence the zero-temperature limit of the response function $\mathrm{Im}\chi_{11}^{T_\mathrm{el}}(q_\parallel,\omega)$ has to be used and screening is assumed to be small. Furthermore, for quasi-2D systems the additional condition $k_\mathrm{F} \gtrsim 1/\Delta z$ must be fulfilled, where Δz is a characteristic length for the electron confinement perpendicular to the 2D plane.

To test our formulas and the corresponding numerical procedures we have calculated the phonon emission in all directions as a function of the electron temperature T_{el} for a modulation-doped GaAs/Al$_{\mathrm{x}}$Ga$_{1-\mathrm{x}}$As heterojunction and compared the results with corresponding experimental data of the electron energy loss rate. The latter were obtained from the temperature dependence of the mobility of a 2D electron gas in a GaAs/Al$_{\mathrm{x}}$Ga$_{1-\mathrm{x}}$As heterojunction (Ouali *et al.*, 1999). Unlike for angle-resolved emission it is possible to measure relatively exact absolute values for the total emitted power. Fig. 6.2 shows the emitted acoustic phonon power per electron, $P^{(\mathrm{DP})}_{\hat{\mathbf{q}},\lambda} + P^{(\mathrm{PE})}_{\hat{\mathbf{q}},\lambda}$, summed over all phonon modes λ and integrated over all directions $\hat{\mathbf{q}}$ for electron temperatures T_{el} close to the Bloch-Grüneisen temperature T_{BG}.[5] The lattice temperature is $T_{\mathrm{c}} = 1.2\,\mathrm{K}$ and the areal density of the quasi-2D electrons is $n_{2\mathrm{D}} = 2.85 \cdot 10^{15}\,\mathrm{m}^{-2}$. The displayed temperature range is of interest since both coupling mechanisms, deformation potential and piezoelectric interaction, give significant contributions to the energy loss rate. At higher

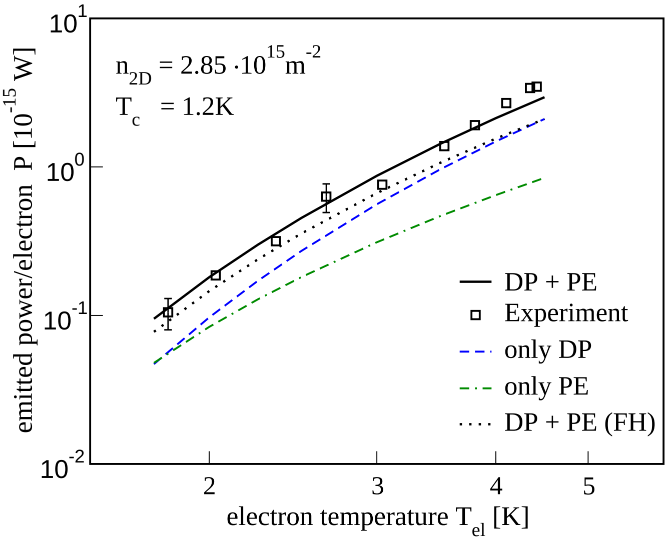

Figure 6.2: Calculated and measured energy loss rate per electron for a 2D electron gas as a function of the electron temperature. The numerical results (solid line) are calculated from the sum over all directions and all phonon polarizations of Eqs. (6.12) and (6.13). The corresponding experimental values displayed by squares are obtained from transport measurements (Ouali, 1998). Theoretical results of energy relaxation due to the individual scattering mechanisms are also plotted in the figure: acoustic phonon scattering via deformation potential coupling (DP) and via piezoelectric interaction (PE). The dotted line shows a calculation where the overlap integral and the form factor are approximated with the help of a variational envelope wavefunction.

---

[5] For the given parameters T_{BG} is about 5 K for LA phonons and 3 K for TA phonons.

temperatures theory (see Fig. 6.15) as well as experiment (see, e.g. Hirakawa *et al.*, 1993) suggest a clear dominance of the deformation potential coupled LA phonons until the energy loss by polar optical phonons or coupled plasmon-phonon modes becomes effective. The numerical calculations were performed with self-consistently determined electron envelope functions (see Eq. 4.25) and included a full dynamic screening of the electron-phonon interaction in RPA. In the given temperature range we have found a temperature dependence of the total energy relaxation rate $\sim (T_{\mathrm{el}}^n - T_{\mathrm{c}}^n)$ with $n = 3.3$, compared to $n = 3.2$ in the experiment. Calculating the power loss we have used the most probable values for the coupling constants (see Section 4.2), namely $|\Theta_{\mathrm{d}}| = 9\,\mathrm{eV}$ for the deformation potential and $eh_{14} = 1.4 \cdot 10^9\,\mathrm{eV/m}$ for the piezoelectric interaction. Bearing in mind that no other fit parameters are used in our calculations the qualitative agreement (power law of the electron energy relaxation rate) and, most notably, the quantitative agreement with the experimental values are very good.

The dotted line in Fig. 6.2 marks the result of a calculation using a Fang-Howard variational wavefunction (see Eq. 4.27) for the electron envelope function, all other parameters are the same. In this case we would obtain an agreement with the experimental values, at least at the lower temperatures, by increasing the value of $|\Theta_{\mathrm{d}}|$ from $9\,\mathrm{eV}$ to $11\,\mathrm{eV}$. This increased value of $|\Theta_{\mathrm{d}}|$ would correspond to the enhanced values of the deformation potential coupling constants found by some authors in GaAs/$\mathrm{Al_xGa_{1-x}As}$ heterojunctions (Kawamura and Das Sarma, 1992; Gorczyca *et al.*, 1992, and references therein). Here, however, the difficulty in determining the correct value for the deformation potential constant in low-dimensional structures becomes apparent. In order to deduce the deformation potential constant one always has to compare the experimental values to model calculations. However, in almost all theoretical models the most simple approximation for the overlap integral, based on (Fang-Howard) variational functions, is applied and sometimes also screening of the electron-phonon interaction is considered inadequately or neglected. The former can lead to an overestimation of the deformation potential constant, as we will show in our discussion about the influence of the electron envelope function on phonon emission in Section 6.3.3. On the other hand, the non-consideration of screening results in an underestimation of the deformation potential constant since the calculated values of power loss are artificially enhanced (see Fig. 6.3). An additional problem appears in all calculations using the isotropic approximation for the electron-phonon matrix elements (Eq. 4.68). At low electron temperatures, $T_{\mathrm{el}} \lesssim T_{\mathrm{BG}}$, this also leads to an overestimation of the deformation potential constant (Jasiukiewicz and Karpus, 1996).

With the help of the relations (6.12) and (6.13) we are able to calculate the acoustic phonon emission into an arbitrary solid angle of wavevector space over a wide temperature range. However, in order to compare our results with heat pulse experiments we need the acoustic phonon power emitted in selected directions $\hat{\mathbf{r}} = \mathbf{r}/|\mathbf{r}|$ of real space. As discussed in Chapter 3, in real space the phonons are propagating in the direction of the group velocity $\mathbf{v}_{\mathbf{q},\lambda}$ which, in general, is not parallel to $\mathbf{q}$. This feature strongly influences the angular distribution of the emitted power in the substrate. So the emitted power of mode λ in the unit solid angle around $\hat{\mathbf{r}}$ has to be expressed by the product of $P^{(\mathrm{DP})}_{\hat{\mathbf{q}},\lambda}$ or $P^{(\mathrm{PE})}_{\hat{\mathbf{q}},\lambda}$ with the corresponding focusing factor $\mathcal{A}_{\hat{\mathbf{q}},\lambda}$ defined in Section 3.2

$$P^{(\mathrm{DP,PE})}_{\hat{\mathbf{r}},\lambda} = \sum_{i=1}^{n_{\hat{\mathbf{q}},\lambda}} \mathcal{A}_{\hat{\mathbf{q}}_i\lambda} \hat{P}^{(\mathrm{DP,PE})}_{\hat{\mathbf{q}}_i,\lambda} \tag{6.16}$$

(Lehmann *et al.*, 1998; Jasiukiewicz, 1998). The phonon wavevector directions $\hat{\mathbf{q}}_i$ $(i = 1, ..., n_{\hat{\mathbf{q}},\lambda})$ contributing to the sum in (6.16) are the solutions of the equation $\hat{\mathbf{v}}_{\hat{\mathbf{q}},\lambda} = \hat{\mathbf{r}}$. For comparison with real experiment the right hand side of Eq. (6.16) has to be calculated taking into account the finite extension of the corresponding detector and source areas.

At the end of this section we want to return once more to the question of screening of the electron-phonon interaction and its influence on the phonon emission. As already mentioned in Section 6.1, it is widely thought that screening is really

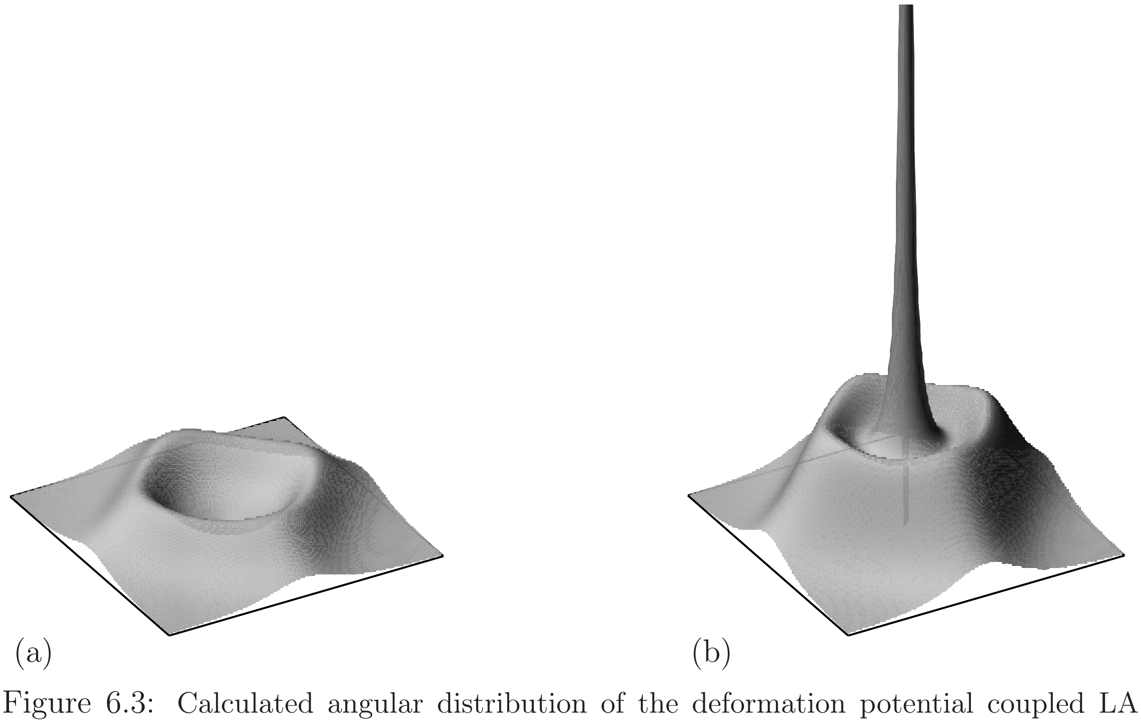

Figure 6.3: Calculated angular distribution of the deformation potential coupled LA phonon emission by 2D electrons in a GaAs/Al$_x$Ga$_{1-x}$As heterojunction (electron temperature $T_{\mathrm{el}} = 25\,\mathrm{K}$, electron density $n_{2\mathrm{D}} = 2.8 \cdot 10^{15}\,\mathrm{m}^{-2}$) including screening (**a**) and without screening (**b**). The phonon intensities are represented as a function of detector position. The images are centered on the [001] propagation direction, and span an angle of approximately ±50°.

only important for acoustic phonon emission of 2D electron systems at low electron temperatures, in the noted screening temperature range where piezoelectric coupling is dominant. However, this general statement is wrong, particularly, in angular-resolved phonon spectroscopy. To demonstrate this fact we have calculated the power of the deformation potential coupled LA phonon emission, $P^{(\mathrm{DP})}_{\hat{\mathbf{r}},\lambda=\mathrm{LA}}$, as a function of the detector direction $\hat{\mathbf{r}}$ for electron temperatures T_{el} much above the screening regime. The results are presented in Fig. 6.3 for 2D electrons in a heterojunction at an electron temperature of 25 K. In (a) the emission is calculated with full wavevector- and temperature-dependent dynamic screening of the electron-phonon interaction in the RPA and in (b) screening is neglected. We observe a general attenuation of the electron-phonon coupling due to the inclusion of electron-electron interaction resulting in slower relaxation rates of the hot carriers. However, most remarkable of all is that the large peak for phonon emission close to the normal to the 2D system, which is present in the unscreened model, completely disappears in the case of screening. The reason is that though for a typical 2D electron gas at $T_{\mathrm{el}} = 25\,\mathrm{K}$ the relation $q > q_{\mathrm{S}}$ holds for the relevant phonon wavevectors, for the emission close to the normal the component $q_{\parallel}$ is very small and so, in respect of Eq. (B.38), the deformation potential interaction is effectively screened.

6.3 Angular and mode dependence of acoustic phonon emission

6.3.1 Results and comparison with experiment

Based on our theoretical model we have performed numerical calculation of the angle-resolved acoustic phonon emission for 1D and 2D electron systems at electron temperatures in the range of 2-50 K. In the discussion that follows we present results for quasi-2D electrons in modulation-doped heterojunctions and quantum wells in GaAs/Al$_{\mathrm{x}}$Ga$_{1-\mathrm{x}}$As structures for $T_{\mathrm{el}} = 20\,\mathrm{K}$ and 25 K.

In Fig. 6.4 the angular dependence of the acoustic phonon emission by 2D electrons in a 5.1 nm quantum well is shown. The contributions of the different phonon modes and coupling mechanisms are depicted separately. The calculations assume a point source, a detector size of $25\times25\,\mu\mathrm{m}^2$, a substrate thickness of $330\,\mu$m and an electron density of $1.8\cdot10^{15}\,\mathrm{m}^{-2}$. The emission is clearly very anisotropic for all phonon modes and coupling mechanisms. At very small angles (relative to the normal to the 2D plane), i.e. at very small in-plane components $q_{\parallel}$ of the phonon wavevector, the emission falls sharply to zero due to the restrictions by the electron response function $\chi^{T_{\mathrm{el}}}_{11}(q_{\parallel},\omega)$ in Eq. (6.10). For electron temperatures $k_{\mathrm{B}}T_{\mathrm{el}} \ll E_{\mathrm{F}}$ the imaginary part of $\chi^{T_{\mathrm{el}}}_{11}(q_{\parallel},\omega)$ is only different from zero if, according to (B.33)

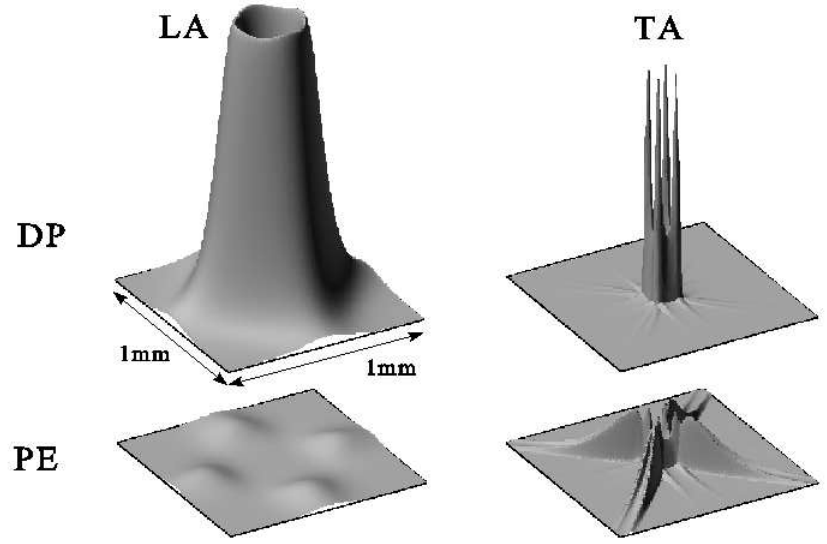

Figure 6.4: Calculated angular distribution of the phonon emission by a 5.1 nm quantum well ($T_{\rm el} = 25\,{\rm K}$). The intensities are represented as a function of the detector position (substrate thickness 330 μm) and the contributions of the different modes (LA and TA = STA + FTA) and coupling mechanisms (deformation potential and piezoelectric interaction) are shown separately. (From Lehmann *et al.*, 2002a.)

and (B.37), the condition

$$\left| \frac{q_\parallel}{2k_{\rm F}} - \frac{m^*\omega}{\hbar k_{\rm F} q_\parallel} \right| < 1 \tag{6.17}$$

holds. Thus $q_\parallel/q \gtrsim m^* c_{\mathbf{q},\lambda}/\hbar k_{\rm F}$ is a necessary condition for emission. Conservation of energy and in-plane momentum account for relation (6.17), which causes also the suppression of phonon emission at large angles, the so-called $2k_{\rm F}$ cutoff for $q_\parallel$. Additionally, at large angles the emission intensity is according to Section 3.3.2, Eq. (3.35), reduced by the geometry factor $\cos\vartheta_{\mathbf{r}}/r^2$, where r is the distance between phonon source and detector and $\vartheta_{\mathbf{r}}$ is the angle between the source-detector direction and the normal to the 2D plane. On the other hand, at small angles with $q_\parallel/q > m^* c_{\mathbf{q},\lambda}/\hbar k_{\rm F}$ but with $q_\parallel \lessapprox q_{\rm S}$ emission is drastically reduced by screening as discussed at the end of Section 6.2. Beyond these effects, caused by the reduced dimensionality of the electron system, source-detector geometry and screening, interesting features, which have their origin in the acoustic anisotropy of GaAs, can be observed in Fig. 6.4. In the case of the TA patterns, peculiarities associated with focusing of the slow and fast TA phonons (see Fig. 3.8(a)) are clearly visible. A further significant result is the surprisingly strong emission of deformation potential coupled slow TA phonons in a direction close to the normal to the 2D electrons. This contribution would be totally absent in calculations using the isotropic approx-

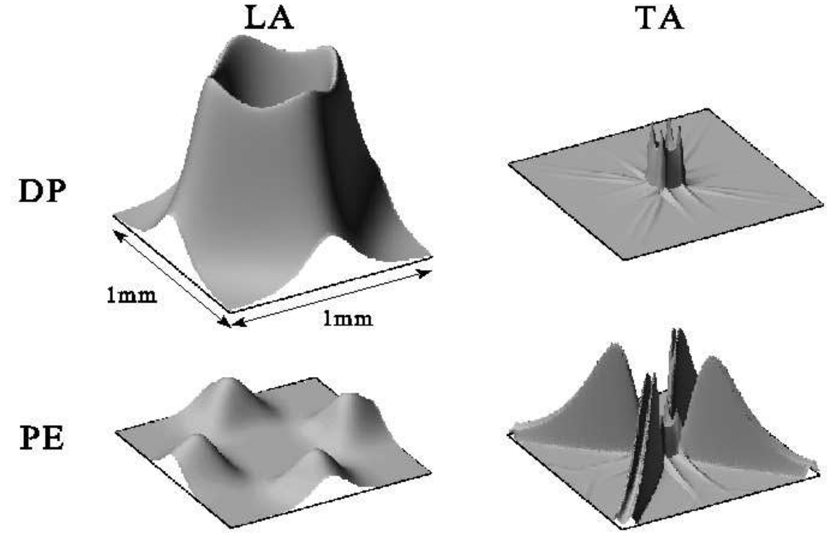

Figure 6.5: As Fig. 6.4 but for a 15 nm quantum well. All phonon intensities have been multiplied by a factor 5 to compensate for the lower total emitted power. (From Lehmann *et al.*, 2002a.)

imation of the electron-phonon coupling coefficients. If we superpose in Fig. 6.4 the contributions of all modes and coupling mechanisms, the essential characteristics of the experimental image (Fig. 2.8(a) in Chapter 2) for the phonon energy flux emitted by hot 2D electrons will be reproduced.

Compared to Fig. 6.4 the results presented in Fig. 6.5 are for a well width of 15 nm instead of 5.1 nm. We notice that, for all modes and coupling mechanisms, the angular distribution of the emitted acoustic phonons is narrower (i.e. closer to the normal to the 2D electrons) in the case of the 5.1 nm well. In addition the phonon power is larger. In Fig. 6.5 the phonon intensities have been multiplied by a factor 5 compared to Fig. 6.4 to compensate for the lower total emitted power from the 15 nm well (see also Figs. 6.16 and 6.15 in Section 6.3.3). The stronger confinement of the electrons in the narrower well, which opens up more momentum space for electron-phonon scattering, is a reason for this effect. This is accounted for by the squared overlap integral $|G_{11}(q_\perp)|^2$ appearing in the equations for the emitted power. The corresponding dependence of the overlap integral on the well width is explicitly given in the formulae (C.16) and (C.17) of Appendix C.1.2.

Next we compare our theoretical results to heat pulse measurements performed by Kent and coworkers. The quasi-2D electron devices were grown on (001) GaAs wafers about 0.4 mm thick. The active region (area of the phonon source) was $120 \times 50\,\mu\mathrm{m}^2$ in size. On the back face of the substrate three $100 \times 10\,\mu\mathrm{m}^2$ aluminium superconducting bolometers were arranged as phonon detectors as shown in Fig. 6.6. For details of the experimental method see Lehmann *et al.* (2002a). The sample parameters for the quantum wells are given in Table 6.1, the heterojunction sample had an electron density of $2.8 \cdot 10^{15}\,\mathrm{m}^{-2}$.

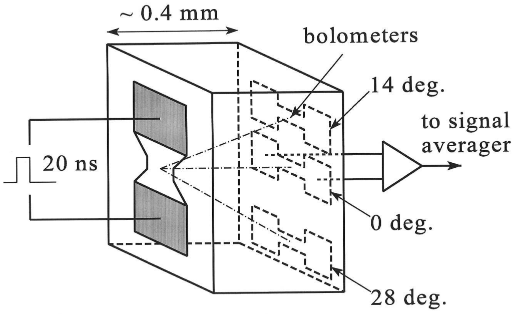

Figure 6.6: Experimental geometry for the experiments described. (From Lehmann *et al.*, 2002a.)

Table 6.1: Parameters of the quantum well samples.

Well width [nm]	3	5.1	6.8	12	15
2D electron density [$10^{15}\,\mathrm{m}^{-2}$]	1.8	1.8	2.0	3.7	3.6

Typical heat pulse signals for the 5.1 nm and 15 nm well with the phonon detector placed directly opposite the device are shown in Fig. 6.7. For both quantum wells the total dissipated power per electron was ≈ 1 pW. The LA and TA phonons are resolved owing to their different times of flight as described in Section 2.2.1. It is eye-catching that for the 15 nm well the intensity is weaker and that the LA signal has almost disappeared. Both facts are clearly supported by our numerical results in Figs. 6.4 and 6.5.

Results similar to those of the 15 nm well could be found for the heterojunction on a (001) substrate (Fig.6.8). Here no LA phonon pulse, which is expected to start at 80 ns, was observed at all for emission close to the normal to the 2D electrons. Taking account of the noise on the signal, one can put an upper bound of 0.05 on the ratio of intensities LA:TA (Lehmann *et al.*, 1998). This result was in contradiction to all previous theories predicting a dominance of the deformation potential coupled LA modes, even with a simultaneous consideration of the strong focusing of TA modes in normal direction. For example, in the given experimental geometry, a ratio of 3.5 would be obtained using the conventional theory that ignores the effect of screening of deformation potential coupling and the effect of acoustic anisotropy when calculating the electron-phonon coupling (see e.g. Challis *et al.*, 1987; Xu and

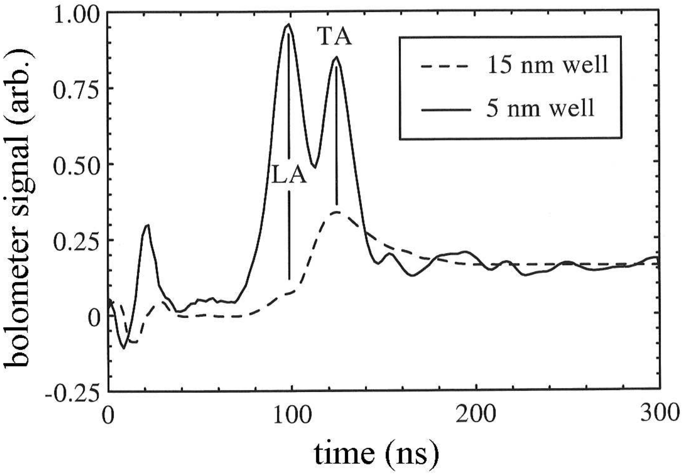

Figure 6.7: Time-resolved bolometer traces (heat pulse signal) for 5.1 nm and 15 nm quantum wells using a bolometer located directly opposite the device. The signal within the first 40 ns after the start of the excitation pulse at time $t = 0$ is due to electromagnetic breakthrough of the pulse. For the 5.1 nm well the LA phonons arrive at about 75 ns followed by the TA phonons at 110 ns. (From Lehmann *et al.*, 2002a.)

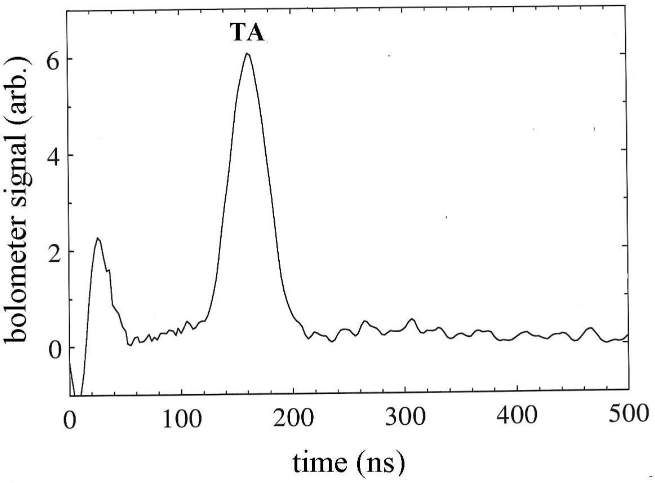

Figure 6.8: Heat pulse signal emitted by hot 2D electrons in a modulation-doped heterojunction. The phonon detector is directly opposite the device. (From Lehmann *et al.*, 1998.)

Table 6.2: Comparison of theory with experiment for a phonon detector directly opposite the device and a power dissipation of approximately 0.1 pW/electron (Lehmann *et al.*, 2002a).

Well width	3 nm	5.1 nm	6.8 nm	12 nm	15 nm	Hetero-junction
LA/TA (experiment)	0.7	0.9	1.1	0.5	0.1	0.05
LA/TA (conv. theory)	255	144	94	29	18	3.5
LA/TA (theory incl. ac. anisotr.+ screening)	0.83	0.84	0.53	0.19	0.16	0.1

Mahanty, 1994; Vasko and Mitin, 1995; Kent *et al.*, 1997c) but does take account of phonon focusing in the GaAs substrate.

Table 6.2 shows the ratio of the LA:TA pulse amplitudes at the phonon detector directly opposite the device obtained from experiment, from the conventional theory, and from our model. One should note that at the low dissipated powers some of the experimental phonon signals are quite noisy and so a maximum uncertainty in LA:TA of (+100/-50)% should be allowed for when comparing the experimental results with theory. The theoretical results were obtained by integrating $P^{(\mathrm{DP})}_{\hat{\mathbf{r}},\lambda} + P^{(\mathrm{PE})}_{\hat{\mathbf{r}},\lambda}$ over all angles corresponding to the given size and shape of device and detector. We can state that the agreement between our theory and the experimental data is quite good (within a factor of about 2) across the range of samples measured. In the calculations we have included isotope scattering of the phonons as they traverse the substrate, see Eqs. (3.16) and (3.38) of Section 3.3. This attenuates the higher frequency ($> 500\,\mathrm{GHz}$) phonons in the emitted spectrum and leads to a reduction of the LA:TA ratio at a very small well width and for the heterojunction device (Lehmann and Jasiukiewicz, 2002). We have also taken into account the penetration of the electrons into the barrier material by using finite potential steps at the interface. Nevertheless, it should be pointed out that the confinement potential used, although an improvement of the conventional theory, is still approximate and could account for some of the deviations between experiment and theory, especially for narrow wells. For very narrow wells (3 nm) effects by the conduction band nonparabolicity, see Section 4.1.3, may also be a source of error.

The conventional theory is shown to be totally inadequate to explain the experimental data for all samples. The LA:TA ratios obtained this way are much too large even though, as in the case of the results in Table 6.2, it includes the screening of the deformation potential interaction in the static approximation. The main reason for the large differences between our theory and the conventional theory is the absence of any deformation potential coupled TA phonons in the conventional model. Also for a (311) device, where the effect of phonon focusing would be much

Table 6.3: Comparison of theory with experiment for the 6.8 nm well at a power dissipation of approximately 0.1 pW/electron. At 28° the TA signal cannot be resolved from the noise, this sets a lower bound on the value of LA:TA (Lehmann *et al.*, 2002a).

Detector	0°	14°	28°
LA/TA (experiment)	1.1	3.8	> 30
LA/TA (theory incl. ac. anisotropy + screening)	0.53	6.9	97

different from that of a (001) device, we have compared the results of the standard theory (including only focusing and the device-detector geometry) with our theory (including also the acoustic anisotropy in the matrix elements) and with experimental results (Lehmann *et al.*, 1998). Also in this case the inclusion of the acoustic anisotropy in the electron-phonon coupling gives results that are much closer to the measurements than the standard theory.

To test our theoretical predictions concerning the angular dependence of the acoustic phonon emission we have compared the LA:TA ratio for nonzero detector angles with corresponding experimental results in Table 6.3. The ratio increases on moving to larger angles because the deformation potential coupled TA phonons that are strongly focused close to the [001] direction (see Figs. 6.4 and 6.5) do not hit on the detector. Although the agreement between theory and experiment is not perfect at the larger angles, the results are much better than for the conventional theories without full screening and acoustic anisotropy, giving LA:TA $\gg 100$ for both the 14° and 28° detector. For a 5 nm quantum well Vasko and Mitin (1995) have shown that at not too small emission angles TA phonon contributions due to macroscopic deformation (ripple) interaction, see Section 4.2.3, are possible. However, their calculation restricted to temperatures below 10 K and based on a very simple isotropic phonon model does not allow any quantitative estimates of the resulting effect on LA:TA ratios.

6.3.2 The effect of acoustic anisotropy

As shown in the previous section, acoustic anisotropy has a decisive influence on the results of angle-resolved phonon emission, and its impact is multifaceted. Therefore, in the following we will illustrate how the emission results are affected by different aspects of acoustic anisotropy. Two effects are dominating: on the one hand the influence on the phonon propagation of the emitted phonons, i.e. the effect by phonon focusing (cf. Sections 3.2 and 3.4), and on the other hand the influence on the angle dependence of acoustic phonon emission itself, i.e. the effect by the anisotropic nature of the electron-phonon coupling (see Section 4.2.4).

In Figs. 6.9–6.12 we compare the 'exact' theoretical angular distribution of the phonon flux emitted from a (001) $\mathrm{GaAs/Al_xGa_{1-x}As}$ heterojunction with a calculation (b) using the isotropic approximation for the electron-phonon matrix elements (Eqs. (4.66)–(4.68)) and with a calculation (c), where the phonon focusing in the substrate is ignored. The results are separately displayed for deformation potential coupled LA phonons (Fig. 6.9), deformation potential coupled TA phonons (Fig. 6.10), piezoelectric coupled LA phonons (Fig. 6.11) and piezoelectric coupled TA phonons (Fig. 6.12). Large deviations in the angular distribution for the patterns without focusing for all modes and coupling mechanisms and the already mentioned significant contribution from the deformation potential coupled TA phonons (Fig. 6.10(a)) are evident. As visualized in Fig. 6.10(b) the latter contribution is completely missing in the model using the isotropic approximation for the interaction matrix elements. This will have considerable consequences for angle-resolved phonon emission with detectors directly opposite the 2D electrons. Whereas, for total emission the importance will be only secondary, since the phonon signal in Fig. 6.10(a) is only in a small angle range around the normal to the 2D system significantly different from zero. This conclusion will also be quantitatively confirmed by our calculations for hot electrons in quantum well structures, see Figs. 6.15 and 6.16 in the next section.

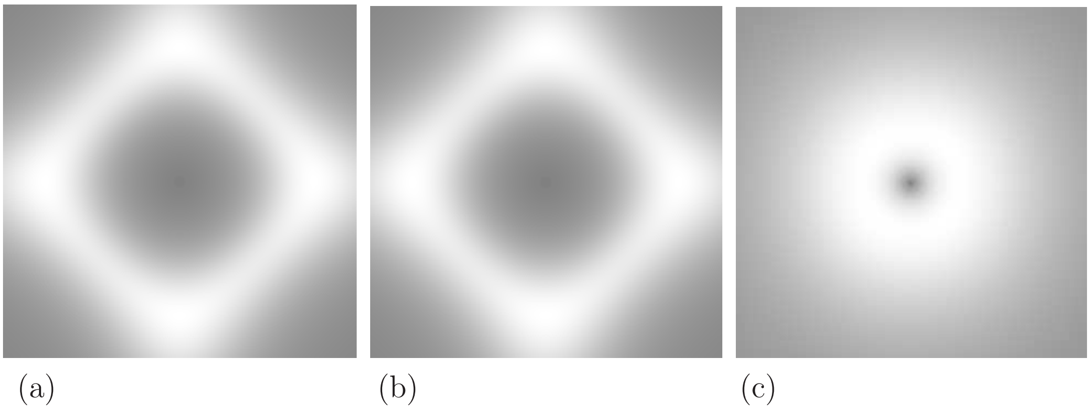

(a) (b) (c)

Figure 6.9: Patterns of the angular dependence of LA phonon emission by deformation potential coupling. Each point of the patterns corresponds to a detector position, whereas the hot 2D electron gas ($T_{\mathrm{el}} = 20\,\mathrm{K}$, $n_{\mathrm{2D}} = 2.8 \cdot 10^{15}\,\mathrm{m}^{-2}$) is at the center on the opposite side of the substrate. A gray tones scale is used, where black means zero phonon flux in this direction and white corresponds to the maximum value of phonon signal. The patterns are centered on the [001] direction, and span an angle of ±56° left to right (in [110] direction). Pattern (**a**) is the result of exact calculations, (**b**) is the result of the isotropic approximation for the electron-phonon matrix elements and (**c**) is without phonon focusing in the substrate. (From Lehmann and Jasiukiewicz, 1999.)

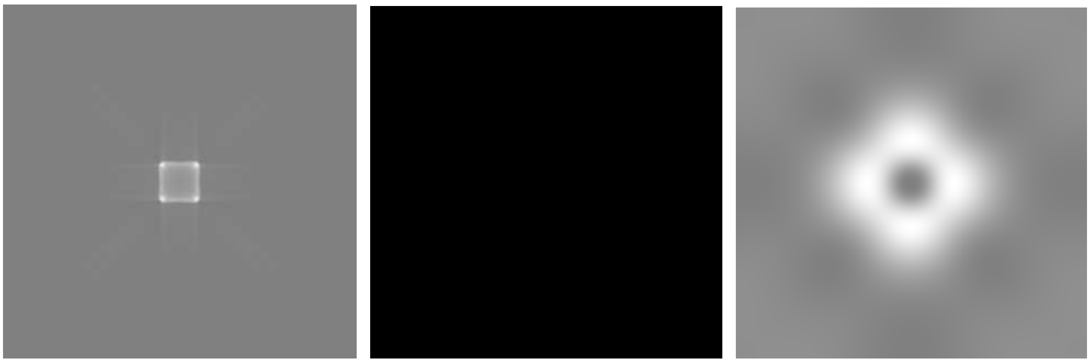

(a) (b) (c)

Figure 6.10: Angular dependence of TA phonon emission by deformation potential coupling. For details see Fig. 6.9.

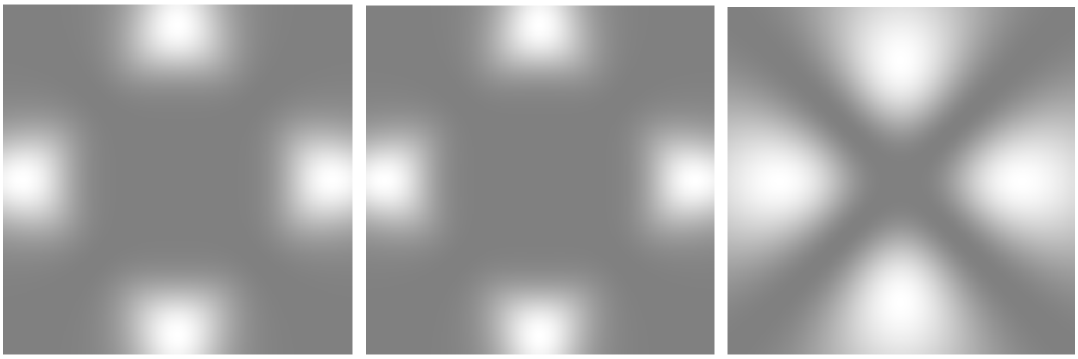

(a) (b) (c)

Figure 6.11: Angular dependence of LA phonon emission by piezoelectric coupling. For details see Fig. 6.9.

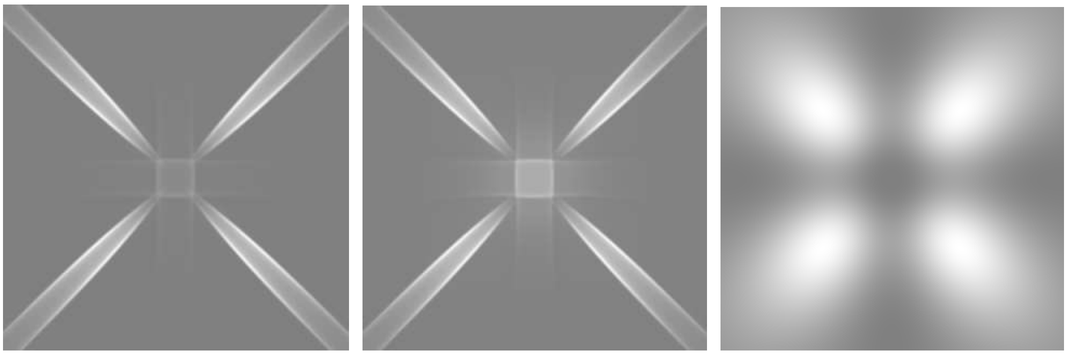

(a) (b) (c)

Figure 6.12: Angular dependence of TA phonon emission by piezoelectric coupling. For details see Fig. 6.9.

Altogether, the results for the different approximations clearly demonstrate that only a complete theory that takes proper account of the full acoustic anisotropy allows a satisfactory description of the phonon emission by hot 2D electrons. Even considering the emission process by itself, i.e. abstracting from focusing of the emitted phonons, it is wrong to say that the angle dependence is entirely due to momentum and energy conservation, as stated for a GaAs based 2D electron gas by Xu and Mahanty (1994). The simplest proof is the comparison of the patterns (a) and (b) in Figs. 6.10 and 6.12.

Further details about the impact of acoustic anisotropy on the acoustic phonon emission by hot 2D and 3D electrons in III-V and II-VI types of cubic semiconductors can be found in the papers of Jasiukiewicz and Karpus (1996), Jasiukiewicz (1998), and Lehmann and Jasiukiewicz (1999).

6.3.3 The effect of carrier confinement

Complying with the results of Section 6.3.1, the confinement of the low-dimensional electrons, in addition to the acoustic anisotropy, accounts for the peculiarities in the phonon emission. According to Eq. (6.10) the phonon emission is strongly influenced by the overlap integral $G_{11}(q_\perp)$ defined in Eq. (4.74) and depends therefore, as shown in Chapter 4, via the electron envelope wavefunctions on the confinement potential of the carriers. We will illustrate this effect in more detail by means of two characteristic examples.

First we consider the question, how sensitive the theoretical results of angle-resolved phonon emission are to the used electron envelope wavefunctions. For these purposes we have calculated the angular dependence and the mode distribution of the emitted phonon signal for a modulation-doped GaAs/$\mathrm{Al_xGa_{1-x}As}$ heterojunction by means of the widely used variational envelope functions of Fang-Howard type (4.27, 4.28) and have compared the results to a model, where we have applied the exact Airy function solution (4.25) for the approximately triangular electron confinement potential. For typical parameters of a modulation-doped heterojunction, an electron density of $n_{\mathrm{2D}} = 2.8 \cdot 10^{15}\,\mathrm{m}^{-2}$ and a depletion charge density of $N_{\mathrm{dep}} = 0.46 \cdot 10^{15}\,\mathrm{m}^{-2}$, Fig. 6.13 shows the angular distribution of the emitted LA and TA phonons for the model with the Fang-Howard envelope function and the model with the Airy function. In both cases the electron envelope wavefunctions were obtained for the same confining potential, where an infinite conduction band discontinuity at the interface was assumed. For almost all emission angles we observe an underestimation of the phonon signal in case of the Fang-Howard envelope function, which is an agreement with our result for the overall energy loss rates in Fig. 6.2. Particularly large deviations occur for phonons at angles close to the normal to the 2D electrons. The main reason for this behaviour can be found in the wavevector dependence of the squared overlap integral $|G_{11}(q_\perp)|^2$

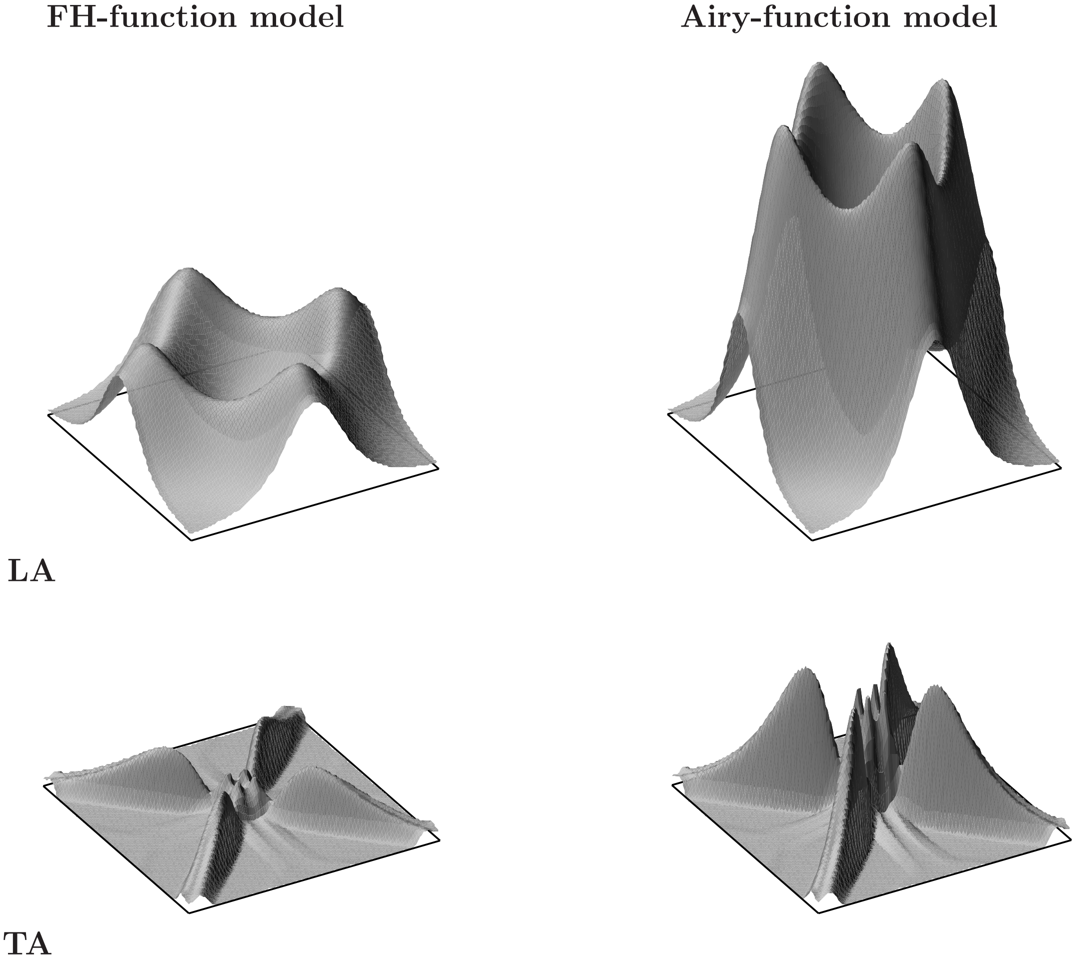

FH-function model

Airy-function model

LA

TA

Figure 6.13: Intensity of phonon signal for LA phonon emission (upper plots) and TA phonon emission (lower plots) as a function of detector position. The intensities are calculated for a hot 2D electron gas at $T_{\mathrm{el}} = 25\,\mathrm{K}$ using two electron envelope wavefunctions of different shape: left figures with the variational Fang-Howard wavefunction, right figures with the self-consistent Airy solution. All other parameters are the same. The images are centered on the [001] propagation direction, and span an angle of approximately ±55°.

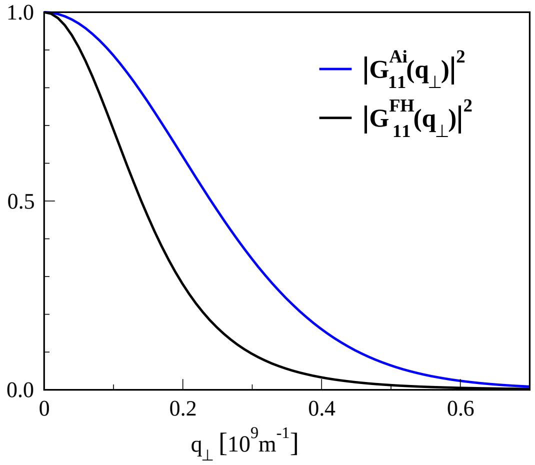

Figure 6.14: Wavevector dependence of the squared overlap integral for the Airy function solution (Ai) and for the Fang-Howard function solution (FH).

shown in Fig. 6.14. The much faster drop of $|G_{11}^{\mathrm{FH}}(q_\perp)|^2$ with the increasing perpendicular component of the phonon wavevector is evident, which suppresses emission in normal direction. This is the result of the slower decline of the Fang-Howard wavefunction if we increase the distance to the interface (see Fig. 4.4 on page 57). To demonstrate the effect on the phonon emission more quantitatively we have compared the results of a calculation using the Airy function solution with the results of the Fang-Howard model for three different electron densities both for the total emission rate and for phonon emission close to the normal to the 2D electrons (Table 6.4). For the directly opposite detector the differences between the two models are not only much more pronounced, up to a factor of 3.6 for the considered electron densities, in contrast to the total phonon emission rate we also find larger changes for the TA phonon modes. This fact leads to a remarkable reduction of the LA:TA ratio, for details see Lehmann and Jasiukiewicz (2002). Both characteristics of the Airy function model, the reduced LA:TA ratio for emission perpendicular to the 2D electrons as well as the higher overall emission rates, are in good agreement with the experimental observations. Further improvements are possible taking into account a finite conduction band discontinuity at the interface, i.e. allowing a penetration of the electron wavefunction into the $\mathrm{Al_xGa_{1-x}As}$ barrier as shown in Fig. 4.4. These adjustments have been borne in mind in our calculations of angle-resolved phonon emission of Section 6.3.1.

Summarizing the given arguments one can state that phonon emission rates are very sensitive to the correct shape of the electron envelope function and that models with simple variational wavefunctions, like the Fang-Howard functions, result in a deficient description. Recently Kent and Wigmore (2003) have qualitatively studied the effect on phonon emission by the application of improved variational wavefunctions as given in Eq. (4.29). These functions show an asymptotic behaviour

Table 6.4: Changes in phonon emission rates for hot 2D electrons ($T_{\mathrm{e}} = 25\,\mathrm{K}$) in GaAs/AlGaAs heterojunctions due to different envelope wavefunctions. For different electron densities the total emission rate (P^{Ai}) and the emission rate ($P_{\perp}^{\mathrm{Ai}}$) into directions close to the normal to the 2D system (ϑ between 0° and 15°) are calculated with the exact ground state solution (Airy function) for the given confinement potential and compared to results (P^{FH}, $P_{\perp}^{\mathrm{FH}}$) obtained with the variational solution (Fang-Howard function).

electron density $[10^{15}\mathrm{m}^{-2}]$	$(P^{\mathrm{Ai}} - P^{\mathrm{FH}})/P^{\mathrm{FH}}$		$(P_{\perp}^{\mathrm{Ai}} - P_{\perp}^{\mathrm{FH}})/P_{\perp}^{\mathrm{FH}}$	
	only LA	only TA	only LA	only TA
1.0	+56%	+34%	+53%	+136%
2.8	+70%	+43%	+140%	+218%
5.0	+75%	+48%	+201%	+262%

which is compared to the Fang-Howard functions much closer to the self-consistent Airy solutions. However, as already mentioned in Section 4.1.3, the price is that the overlap integral and the form factor can no longer be obtained analytically. Therefore the practical advantage over the direct use of numerical self-consistent solutions is small.

Now, as a second example for the influence of electron confinement on the emission rates, we study the emitted acoustic phonon power for GaAs/Al$_{\mathrm{x}}$Ga$_{1-\mathrm{x}}$As quantum wells as a function of the well width. At first, we show the dependence of the total emitted power per electron (Fig. 6.15) at an electron temperature of 25 K for different phonon modes and coupling mechanisms. As expected, the total emission is dominated by the deformation potential coupled LA phonons for all well widths. All other contributions are at least ten times weaker. The deformation potential coupled TA phonon emission is negligible, which accounts, among others, for the relative success of the isotropic approximation for calculations of total energy and momentum relaxation of 2D electrons in GaAs structures. Increasing the well width, the emission rates per electron due to the deformation potential coupled LA and TA phonons decrease while the piezoelectric coupled emission remains fairly constant. The increase in the acoustic deformation potential scattering for narrower quantum wells was already observed in time-resolved luminescence measurements many years ago (Leo *et al.*, 1988), but the effect was attributed to an increase in the deformation potential coupling constant Θ_{d} or to changes of the in-plane effective mass m^* of the electrons. However, from formula (6.12) it follows that the well width dependence of the squared overlap integral, $|\,G_{11}(q_{\perp})|^2 \sim \big[\frac{\sin(q_{\perp}L_{\mathrm{A}}/2)}{1-(q_{\perp}L_{\mathrm{A}}/2\pi)^2}\big]^2/(q_{\perp}L_{\mathrm{A}})^2$ (see Appendix C.1.2), is the main reason, since it suppresses the emission of high-q deformation potential coupled

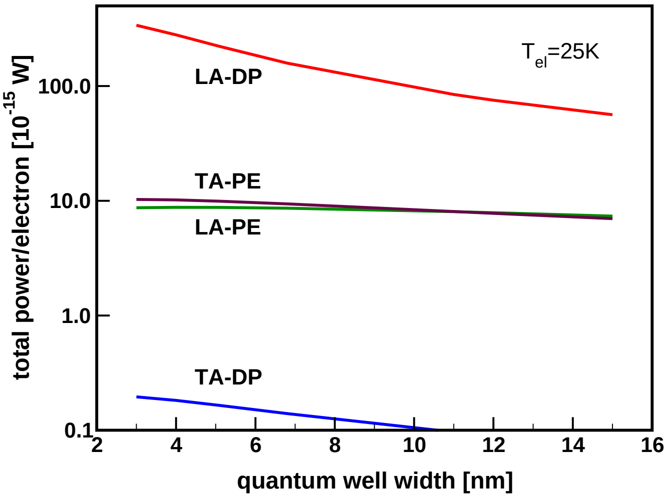

Figure 6.15: Contribution of the different phonon modes and coupling mechanisms to the total energy loss rate of 2D electrons by acoustic phonon emission at $T_{\mathrm{el}} = 25\,\mathrm{K}$ as a function of the quantum well width. The calculations are performed for an electron density of $1.8 \cdot 10^{15}\,\mathrm{m}^{-2}$ within a model including the full acoustic anisotropy, dynamic screening in RPA and finite potential well barriers.

phonons in the wider wells.

A totally different behaviour than in Fig. 6.15 is observed in Fig. 6.16, where the results for the emission into a restricted range of angles corresponding to the experimental geometry of a bolometer directly opposite the device is displayed. For well widths $\leq 7\,\mathrm{nm}$, the deformation potential coupled LA phonons give the largest contribution to the phonon flux at the bolometer. However, for well widths $> 7\,\mathrm{nm}$ the TA mode becomes dominant. This is due to two factors: the weaker confinement for the electrons which leads to the suppression of the high q phonons and, as shown at the end of Section 6.2, screening. If the screening of the deformation potential coupled LA phonons is ignored, as it is sometimes the case in theories for acoustic phonon emission, the emission of deformation potential coupled LA phonons would always dominate in the direction normal to the 2D electron system. It is worth noting that for this geometry no significant contribution from the piezoelectric coupled LA phonons may be evidenced. On the other hand, the surprising dominance of the deformation potential coupled TA phonons for weakly confined electrons (large well widths) can be proved also for higher electron temperatures close to the onset of optical phonon emission (Lehmann *et al.*, 2002a).

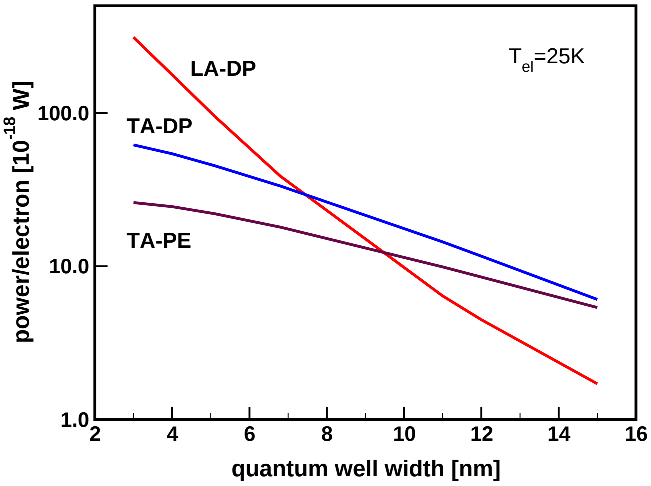

Figure 6.16: Calculated well width dependence of the fraction of the total emitted phonon power, which falls on a detector located directly opposite the device. The source and the detector dimensions are the same as in the experiment described in Section 6.3.1. The contributions of the different modes and coupling constants are shown separately.

6.4 Open problems and outlook

In spite of large progress achieved in the theoretical understanding of electron relaxation in 2D systems some questions are still unanswered or not solved satisfactorily.

A central point is the role of coupled modes and two-phonon processes and their influence on the results of phonon pulse measurements. Calculations are necessary that not only simultaneously include all different relaxation channels but also allow for the full acoustic anisotropy of the interaction matrix elements, the realistic envelope wavefunction and screening. Since only the decay products of coupled modes and two-phonon emission reach the detector and since these decay products are the result of a whole sequence of anharmonic down-conversion processes, corresponding theoretical models for time- and angle-resolved phonon emission should include anharmonic decay and scattering processes for the phonon propagation in the substrate. However, the situation is complicated and highly complex. The present knowledge about the primary decay process of the coupled modes leaves many question open. In addition, not only for the ballistic propagation but also for the quasi-diffusion the temporal and angular distributions of the phonon intensity differ for anisotropic media from the isotropic case (Tamura and Harada, 1985; Msall *et al.*, 1993; Gańcza *et al.*, 2001). Thus the acoustic anisotropy has to be included not only in phonon propagation, but also in scattering and down-conversion.

The remaining discrepancies between experimental and theoretical results in the LA:TA ratios of the angle-resolved phonon emission for narrow quantum wells are another open challenge. Here, the inclusion of the ripple mechanism and the consideration of electron interaction with confined modes seem to be promising refinements if they will combined with realistic anisotropic phonon models.

Compared to both preceding points a further open problem, the detailed angular distribution of acoustic phonon emission if intersubband transitions are allowed, is easier to solve. All theoretical and experimental results presented in the foregoing sections of this chapter were restricted to electron systems in which only the lowest subband is occupied. However, there are practical electronic devices, for example high electron mobility transistors (HEMTs), working at higher densities where higher subbands can be occupied and this at electron temperatures, where acoustic phonon emission is dominant. In this case electron relaxation within higher subbands and between different subbands has to be included. The theoretical treatment is very similar to what has been discussed in Section 6.2. The overlap integral $G_{11}(q_\perp)$ and the dielectric matrix $\varepsilon_{11}^{11}(q_\parallel, \omega)$ in Eq. (6.10) only have to be replaced by $G_{ll'}(q_\perp)$ (see Eq. (B.5)) and the modified dielectric matrix $\varepsilon_{ll'}(\mathbf{q}, \omega)$ (see Eq. (B.24)), respectively, and the sum over all possible interband and intraband transitions l, l' has to be performed. Xu and Mahanty (1994) have calculated the angle dependence of acoustic phonon emission by 2D electrons in case of two occupied electron subbands and found a more marked angle dependence and larger emission rates for intersubband emission processes than for intrasubband processes. However, in their calculations all effects by acoustic anisotropy have been neglected making a quantitative comparison to corresponding phonon emission experiments (Rothenfusser *et al.*, 1986; Hawker *et al.*, 1995) almost impossible. Realistic numerical calculations for 2D electron systems with higher subband occupancy, which include acoustic anisotropy in the matrix elements and in the phonon propagation, can, in combination with detailed angle-resolved phonon measurements, give supplementary information about the electron-phonon coupling and the electron confinement.

A large field of activity both from the practical and the theoretical point of view, but beyond the scope of this chapter, is also the phonon-emission spectroscopy of quantum wires and quantum dots.

Chapter 7

Summary and Conclusions

The generation and propagation of pulses of nonequilibrium acoustic phonons and their interaction with semiconductor nanostructures have been investigated. Such studies can give unique information about the properties of low-dimensional electron systems, but in order to interpret the experiments and to understand the underlying physics, a comparison with theoretical models is absolutely necessary.

A central point of this work is therefore a universal theoretical approach allowing the simulation and the analysis of phonon spectroscopy measurements on low-dimensional semiconductor structures. It has been developed in the past years in conjunction with Cz. Jasiukiewicz and T. Paszkiewicz and has been applied to various problems such as phonon imaging of semiconductor substrates, ballistic phonon absorption by low-dimensional electrons, phonon induced drag in 2D and 1D electron and hole gases, phonon drag in epilayers, phonoconductivity of quantum wires or energy relaxation by hot 2D electrons. The model and the accompanying numerical programs take into account the characteristic properties of the considered systems. These properties are the elastic anisotropy of the substrate material leading to focusing effects and highly anisotropic phonon propagation, the anisotropic nature of the different electron-phonon coupling mechanisms, which depend manifestly on phonon wavevector direction and polarization vector, and the sensitivity to the confinement parameters of the low-dimensional electron systems. We have proved that screening of the electron-phonon interaction (both for piezoelectric *and* deformation potential coupling) can have a much stronger influence on the results of angle-resolved phonon spectroscopy than expected from transport measurements. Since we compare theoretical simulations with real experiments, the geometrical arrangement and the spatial extension of phonon source and detector are also included in the approach enabling a quantitative analysis of the data this way. The numerical results so obtained show a very good agreement with corresponding measurements demonstrating thus the strength of the model in accurately describing the experimental situation.

In the present work, special attention has been given to the effects of acoustic anisotropy and carrier confinement. In earlier theoretical studies the acoustic anisotropy has usually been treated incompletely considering only the focusing in the substrate material and even that often insufficiently. The reason is the complex structure of the phonon slowness surface for crystalline materials usually only allowing simple solutions for the phonon group velocity or the phonon polarization vector for phonon wavevectors directed along the symmetry axes of the crystals. However, in order to calculate the propagation of phonon pulses or the angle dependence of the electron-phonon matrix elements, the phonon group and phase velocity as well as the exact polarization vectors are needed for all wavevector directions and all modes. In theories describing electron transport or thermopower this angle dependence is naturally not so important because these methods average or integrate over all phonon directions and phonon modes. In phonon spectroscopy the situation is totally different since here we are interested in detailed information about the interaction of electrons with phonons of a given wavevector and polarization. Therefore, the complete involvement of acoustic anisotropy is absolutely essential.
Also the theoretical description of carrier confinement demands special care in the case of phonon spectroscopy on low-dimensional electrons. We have demonstrated that approximations as the variational envelope wavefunctions of Fang-Howard type, widely used to model the electron confinement in modulation-doped heterojunctions, can fail in the case of quantitative studies. This is caused by the strong dependence of angle-resolved phonon emission and absorption on the accurate form and width of the electron envelope functions.

To illustrate the influence of acoustic anisotropy and carrier confinement on the results of phonon spectroscopy in detail we have analysed two different applications in the present work and compared our theoretical results to corresponding measurements by A. J. Kent and coworkers. In one case the low-dimensional electron system acts as the phonon detector and the phonon induced drag current is measured. In the other case the low-dimensional electron system is the phonon pulse source and the energy relaxation of the low-dimensional electrons is investigated. Furthermore, in the former case the results are superposed by the quasimomentum focusing image of the phonons in the substrate and in the latter case by the energy focusing image.

We have developed a theoretical model which enables us to calculate the electric current induced in low-dimensional electron systems by pulses of (ballistic) nonequilibrium phonons and which includes the effects of electron confinement, of anisotropic phonon propagation and interaction as well as of the detailed detector-source geometry of real experiments. The low-dimensional carriers here serve as phonon ‘anemometers’ since the drag current is caused by the quasimomentum transfer from the nonequilibrium phonon flux to the low-dimensional electrons or holes. The resulting drag patterns are therefore related to the quasimomentum focusing images of the substrate material. In the case of 2D electrons as detectors these focusing images of phonon quasimomentum flux can be clearly observed for low phonon frequencies and not too small electron densities. For higher phonon frequencies the focusing images are destroyed severely by the (observable) $2k_{\mathrm{F}}$ cutoff of the in-plane component of the phonon wavevector due to energy conservation and in-plane momentum conservation and by the restrictions of phonon absorption due to the electron confinement. Our theoretical patterns reproduce the main features of the experimental images very well taking into account that there are no real free parameters in the calculations. The characteristic 'rotation' and attenuation of the drag patterns in the case of an applied magnetic field can be explained. The sensitivity of phonon-drag patterns to variations of the confining potential of quasi-2D and quasi-1D electrons has been demonstrated. This provides the opportunity to use phonon-drag imaging as unique experimental tool for determining the confinement lengths of low-dimensional electron systems, for example for measuring the confinement width of quasi-2D electrons in modulation-doped heterojunctions. By comparing the experimental and theoretical images it is also possible to estimate the relative strength of the different electron-phonon coupling mechanisms.

In the second application we have studied the angle and mode dependence of the acoustic phonon emission by hot 2D electrons. The results exhibit strong variations in the phonon signal as a function of the detector position and depend markedly on the coupling mechanism, the phonon polarization and the electron confinement width. It has been shown that the ratio of the strengths of the emitted LA and TA phonon modes is predicted correctly only by a theoretical model that properly includes the effects of acoustic anisotropy on the electron-phonon matrix elements, the screening, and the form of the confining potential. As a result, we have been able to explain the 'mystery of the missing longitudinal mode' in heat-pulse experiments with hot 2D electrons in $\mathrm{GaAs/Al_xGa_{1-x}As}$ heterojunctions. For 2D electrons in quantum wells we have proved a remarkable increase of the LA:TA ratio with decreasing well width for emission close to the normal to the 2D electrons, which is also observed in the experiments. The main differences between our results and all foregoing models are that screening prevents a strong peak in the phonon emission of deformation potential coupled LA phonons in a direction nearly normal to the 2D electron system and that deformation potential coupled TA phonons give a significant contribution to the phonon signal in certain emission directions. This deformation potential coupling of TA phonons is particularly interesting since the mechanism is forbidden in all isotropic phonon models. However, our calculations have demonstrated that in experiments of angle-resolved acoustic phonon emission with a phonon detector directly opposite the 2D electrons this contribution may be even the dominating one.

Summarizing, we can state that angle- and time-resolved phonon spectroscopy provides new insight into carrier confinement and the process of electron-phonon coupling of low-dimensional electron systems. In contrast to other techniques, direct information concerning the phonon wavevector and polarization dependence of the electron-phonon interaction and not only information averaged over all phonon modes and directions is available. To analyse the results, a careful treatment of acoustic anisotropy and carrier confinement is necessary. A simple adoption of widely used theoretical assumptions, like the isotropic approximation for the phonons in the electron-phonon matrix elements or the use of simple variational envelope wavefunctions for the carrier confinement, can corrupt or even falsify theoretical predictions.

These conclusions would be incomplete without a comment about the perspectives of phonon spectroscopy on low-dimensional electron systems. The application of phonon spectroscopy is by no means restricted to the classes of electron systems discussed in the previous chapters. Novel types of electronic and optoelectronic nanostructures, like quantum dots, quantum wires based on nanotubes and 2D dilute nitride systems, show fascinating new properties. They are also a challenge for new phonon spectroscopy experiments as well as for further theoretical work on this topic.

Appendix A

Generation and Detection of Nonequilibrium Phonons

A.1 Sources of nonequilibrium phonons

Metal-film radiators

A common way to generate nonequilibrium phonons is to electrically or optically excite the electrons in the crystal. A high electron density is therefore favourable. As, on the other hand, the propagation of phonon pulses is preferentially studied in nonmetallic crystals with low density of free electrons, a metallic material will be deposited on the surface of the crystal under consideration. This metal film can be heated by an electrical current as in the pioneering heat pulse experiment of von Gutfeld and Nethercot (1964) or by laser absorption as first demonstrated by Hensel and Dynes (1977). The latter method additionally allows a continuous shifting of the phonon source position. This is simply realized by scanning the laser beam to focus onto different points on the surface, which, again, is the essential basis for the phonon imaging technique described in Section 2.2.2. However, all heat pulse methods have a disadvantage: the broad thermal distribution of the phonons. Usually it is assumed that there exists a complete thermalization between electrons and phonons in the heater and that the time necessary to establish the common effective temperature is much shorter than the typical excitation pulse length of 10^{-9} to 10^{-7} s. Under these conditions a balance is established between the excitation power and the power radiated as phonons from the heater. According to the acoustic mismatch theory (Little, 1959) the frequency spectrum of the emitted phonons corresponds to a Planckian distribution and the power follows the Stefan-Boltzmann T^4 law. However, the electron-phonon interaction in the source depends on the type and duration of excitation, and many complicated processes are involved both in the heater and at the heater/crystal interface like phonon frequency down-conversion, elastic scattering or formation of hot spots (Hensel and Dynes, 1977; Kazakovtsev and Levinson, 1987). Therefore a precise knowledge of the frequency distribution of the emitted phonons is almost impossible and approximations should be used (see Appendix A.3).

Optical excitation in the bulk crystal

Far infrared photons can be directly converted into phonons via absorption in the vibrational bands of the crystal. However, usually the absorption of light is linked to electronic excitations. The principle is the following (for details see, e.g. the review by Renk, 1985): an electron will be photoexcited from the valence band to a higher unoccupied level in the conduction band leaving simultaneously a hole in the valence band. This nonequilibrium excitation then will decay into secondary excitations and can eventually return to the ground state through electron-hole recombination. One possible way is that the excited electron quickly de-excites towards the bottom of the conduction band by emission of longitudinal optical (LO) or acoustic phonons. After this the electron at the bottom of the conduction band can recombine radiatively by photon emission (such as luminescence) or nonradiatively, e.g. by emitting recombination phonons. Nonradiative recombination often takes place at impurity or crystal defect levels. The emitted LO phonons decay into two acoustic phonons in times less than a picosecond and the high frequency acoustic phonons also split rapidly by anharmonic decay, which scales like the fifth power of the frequency (Klemens, 1955), into lower frequency acoustic phonons. According to the complex processes involved the exact frequency and spatial distribution of the generated nonequilibrium phonons is difficult to designate and depends radically on the optical excitation level (Msall and Wolfe, 2002).

The advantage of the optical technique is that the phonons are generated completely within the sample. Therefore no influence of surface imperfections or interfaces is encountered. Additionally, it allows an access to a wide range of phonon frequencies up to many THz.

Excitation by electron beams

Here, the highly focused electron beam of a scanning electron microscope acts as the phonon generator. By locally heating a small crystal region near the surface nonequilibrium phonons will be emitted (for a review see Huebener, 1984). The advantage of the electron beam technique is that electrons are absorbed near the surface of any crystal, whereas in the case of optical excitation transparent crystals have to be covered with an optically absorbing film.

Tunnel junctions and pumped superconducting films

A generation of quasi-monochromatic acoustic phonons was achieved by Eisenmenger and Dayem (1967) by the use of superconducting tunnel junctions. Applying a bias voltage $V_0 \gtrsim 2\Delta/|e|$ phonons of frequency $\omega = 2\Delta/\hbar$ are emitted by the recombination of pairs of excited quasiparticles, where 2Δ is the width of the energy gap of the superconductors. At $V_0 \geq 2\Delta/|e|$ it becomes possible for Cooper pairs to break into two single particles (quasiparticles) with the result of the creation of one quasiparticle in an unoccupied single particle state on each side of the barrier. While the excited single particles which have tunnelled are not in thermal equilibrium they will quickly decay back into a Cooper state. Firstly, they will relax by the emission of 'relaxation' phonons (with phonon energies between 0 and $|e|V_0 - 2\Delta$) to the upper edge of the gap and, secondly, the relaxed single particles will recombine (see Fig. A.1). The consequence is a broad spectrum of 'relaxation' phonons plus a narrower spectrum of 'recombination' phonons.

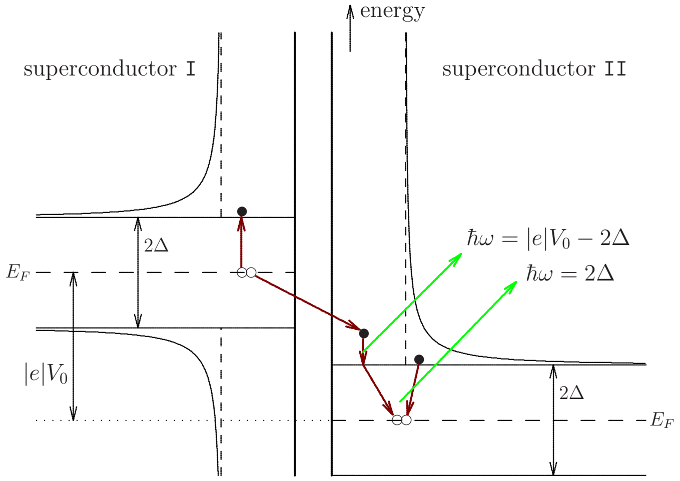

Figure A.1: Schematic view of the possible processes of phonon generation in a superconducting tunnel junction. Cooper pairs are represented by ∞, single quasiparticles by •. (Adapted from Buckel, 1990.)

An analogue quasi-monochromatic phonon spectrum can be obtained by using a superconducting film pumped by a heat pulse (Narayanamurti and Dynes, 1971). Here the excitation of the quasiparticles in the generator film takes place by the high energy phonons of the heater instead of single particle tunnelling. These phonons rapidly break Cooper pairs, thus creating quasiparticle excitations above the energy gap. Again, as result of the following down-conversion process at least two phonons are emitted, one necessarily of energy 2Δ. A technique introduced by Karl *et al.* (1988) works on the same principle. By replacing the heater by a laser focused onto a small area of the superconducting film a movable quasi-monochromatic phonon source became available.

A disadvantage of all phonon sources based on the recombination radiation is their fixed frequency. Small parallel magnetic fields can be applied to adjust the superconducting energy gap and therefore to tune the frequency of the phonons (Narayanamurti and Dynes, 1971). In practice, however, this causes a reduction and broadening of the 2Δ peak of the spectrum. Truly tunable phonon sources have been realized by using the sharp edge of the phonon relaxation spectrum of superconducting tunnel junctions (Kinder, 1972) or by applying ac-Josephson junctions (Berberich *et al.*, 1982). In the first case the phonon 'bremsstrahlung' generated by the relaxation of the excited fast quasiparticles before recombination is exploited. By modulation of the bias voltage V_0 quasi-monochromatic phonons with frequencies $\omega = (|e|V_0 - 2\Delta)/\hbar$ are obtained. In ac-Josephson junctions (tunnelling of Cooper pairs instead of single particles) phonons with a sharp monochromatic peak are excited by the electromagnetic waves in the junction. Thus the phonon peak is coincident with the Josephson frequency $2|e|V/\hbar$ and is tunable by the voltage V.

The advantages of tunable superconducting tunnel junctions are the large frequency range and the narrow bandwidth of the monochromatic component ($\approx 10\,\mu$eV). Disadvantages are the large background of phonons having a broad spectral distribution and primarily, that they cannot be applied for measurements in magnetic fields above the critical field of the used superconductors. As a possible alternative normal state metallic tunnel junctions have been studied (Cooper *et al.*, 1994). However, there exist large practical problems due to the rather low monochromatic phonon power output and the poor resolution (≈ 1 meV at 1.5 K) caused by the thermal broadening of the excited electron population.

Semiconductor nanostructures

Not only the response of semiconductor nanostructures to nonequilibrium phonons is in the focus of attention, such systems also attract interest as generators of well defined nonequilibrium acoustic phonons. In contrast to a heated metal film, the phonon spectrum generated, e.g. by a heated (quasi) 2D electron gas in a quantum well or a heterojunction is very nonthermal. As described in Chapter 6 both the frequency and the angular distribution of the emitted phonons are very different from the 3D case. Chin *et al.* (1984) were the first who used 2D electrons in semiconductor nanostructures as an acoustic phonon source. Since then the phonon generation by 1D and 2D semiconductors has attracted considerable interest both experimentally and theoretically (see, e.g. Roshko *et al.*, 1998; Totland *et al.*, 1999, and references therein). The attempts to use cyclotron phonon emission from a heated magnetically quantized 2D electron gas as a monochromatic phonon source (Toombs *et al.*, 1987; Kent *et al.*, 1988b; Cooper *et al.*, 1995) are an example. However, in this case as well the monochromatic component is only a small signal superimposed on a large phonon background.

In recent years there have been new approaches for the electrical and optical excitation of coherent monochromatic acoustic phonons in semiconductor superlattice structures. One attempt is the generation of high frequency acoustic phonons in an electrically biased weakly coupled doped superlattice (Glavin *et al.*, 1999, 2002; Cavill *et al.*, 2002). In the hopping regime, perpendicular electron transport in such superlattices can give rise to a population inversion with respect to the states involved in phonon-assisted interwell electron transitions which comes along with phonon emission and absorption. However, up to now a practical phonon source based on this method is still missing. To date, the ultra fast optical excitation of semiconductor superlattices described in the next subsection seems to be the more promising way in the search for a usable source of (coherent) monochromatic acoustic phonons.

New sources of monochromatic acoustic phonons by ultra fast optical excitation of metallic and semiconductor layered structures

Since the beginning of phonon spectroscopy, there has been a continuous interest in the search for tunable sources of monochromatic acoustic phonon beams of usable intensity. The reason is the limited spectral information in phonon spectroscopy experiments using broadband, e.g. Planckian, phonon sources. A truly monochromatic (and coherent) phonon source would revolutionize the field of phonon spectroscopy and would enable ‘phonon optics’. New hope of a practical realization of such a phonon source exists since the application of ultra fast optical excitation techniques has become possible.

One approach is the laser-induced thermomodulation of thin metallic transducers evaporated onto the sample (Damen *et al.*, 1995, 2001). By the use of two interfering single frequency lasers operating at slightly different frequencies a periodic heating of the surface of the transducer is produced which is converted into strain via thermal expansion synchronous with the optical difference frequency. The resulting strain wave is injected into the crystal as a longitudinally polarized acoustic wave. Frequency tuning of the phonon beam is possible by varying the optical difference frequency, but so far the generation was limited to acoustic phonons in the gigahertz range.

Another approach is the emission of coherent acoustic phonons due to the ultra fast excitation of electrons and holes in GaAs/$\mathrm{Al_xGa_{1-x}As}$ quantum wells (Baumberg *et al.*, 1997) and superlattices (Yamamoto *et al.*, 1994). Baumberg *et al.* have shown that for ultra fast (femtosecond) optical pulses a longitudinal acoustic (LA) phonon pulse is generated in a single quantum well through a coherent deformation potential mechanism at the earliest stages of optical excitation (within the first 100 fs). Because it is expected that the injected stress and with it also the phonon wave packet follow to first order the confined electron density, the frequency of the phonon pulse is tunable by changing the confinement potential. However, the acoustic phonon generation mechanism seems to be not yet fully clarified and more detailed theoretical and experimental work is required.

Less vaguely is the situation in the case of superlattices. Here the periodicity in the acoustic impedance along the growth direction leads to a mini Brillouin zone into which the acoustic phonon dispersion is folded (Tamura *et al.*, 1988). This permits the coupling of light with high frequency acoustic phonons in the 100 GHz to THz range having very low phonon wavevectors. Under resonant photoexcitation (Brillouin scattering) coherent acoustic phonons are generated in the superlattice with a fundamental frequency corresponding to the first Brillouin center mode and $q \approx 0$. The coherent superlattice phonons modes have been detected by time-resolved reflectivity (Yamamoto *et al.*, 1994; Bartels *et al.*, 1999). Hawker *et al.* (2000) and Kent *et al.* (2002, 2004) have shown that the superlattice phonons leak out of the superlattice into propagating monochromatic LA and TA phonons which can be detected in the substrate at distances up to 1 mm. In a recent paper (Stanton *et al.*, 2003b) we have given an upper bound on the bandwidth of the monochromatic phonon beam and have also determined the relative proportions of the longitudinal phonon signal that are due to monochromatic phonons and broadband phonons from carrier relaxation. This is possible by using a second superlattice between the generator superlattice and the phonon detector which acts as a notch filter.

A.2 Phonon detectors

The criteria for an ideal phonon detector are: small size, high temporal and spectral resolution and sufficient sensitivity and dynamic range. Due to the significant progress made in the past, thin film superconducting detectors (bolometers and tunnel junctions) fulfil the above attributes, with exception of the required spectral resolution. The time response of the devices is in the range of nanoseconds (allowing time-of-flight studies) and the detector dimensions are in the micrometer range (required for a good angular resolution in phonon imaging experiments). A handicap is that no external magnetic field can be applied.

The simplest superconducting bolometer (and the most common type of phonon detector) is an evaporated metal film cooled to its superconducting transition temperature (von Gutfeld and Nethercot, 1964). Therefore a small change in temperature provoked by the absorption of phonons induces a large change in resistivity. Usually it is assumed that all incident phonons are absorbed. Consequently, the response signal is proportional to the total incident phonon energy.[1]

For operation in magnetic fields and over a wider temperature range semiconductor bolometers are applied as well.

In contrast to bolometers, superconducting tunnel junction detectors have some crude spectral selectivity. Their functioning is based on the inverse of the recombination process (Eisenmenger and Dayem, 1967). Incident phonons with energy $\hbar\omega > 2\Delta$ are able to break Cooper pairs and thus increase the steady state quasiparticle density. This leads to an enhancement in the tunnelling current at bias voltages $V_0 < 2\Delta/|e|$. Since phonons with energy $\leq 2\Delta$ are not absorbed at sufficiently low temperature, the junction detector has a frequency threshold of $2\Delta/\hbar$. Combined with the high frequency limit in the ballistic phonon propagation caused by the strong frequency dependence of phonon-isotope scattering in the crystal (scattering rate $\sim \omega^4$) the onset frequency of tunnel junctions enables at least some frequency selectivity in phonon detection (Dietsche *et al.*, 1982). The use of heterogeneous tunnel junctions (tunnel junctions consisting of two superconductors with different energy gaps) can enhance the frequency selectivity (Dietsche, 1978). Here the frequency threshold is voltage tunable.

---

[1] By careful analysis of the bolometer characteristics it is possible to deconvolve the bolometer signal to obtain information about the incident phonon flux with enhanced temporal resolution (Edwards *et al.*, 1989; Danilchenko *et al.*, 2004).

Better spectral resolution, but only at fixed frequencies, can be achieved by probing the excited states of selectively absorbing impurities by optical techniques (see the reviews by Renk, 1985; Wybourne and Wigmore, 1988, and references therein). A prominent example is the so called ruby phonon spectrometer (Renk and Deisenhofer, 1971). Here the relative luminescence of two nearby excited electronic states of Cr^{3+} ions in sapphire (Al_2O_3) is used to measure the temporal and spatial distribution of 870 GHz phonons. Another possibility is to exploit the vibronic sidebands appearing in optical absorption and emission spectra due to lattice vibrations to investigate the frequency distribution of nonequilibrium phonons (for a review see Bron, 1980). A disadvantage of all these kinds of spectrometers is that they require special bulk materials which cannot be applied for all phonon studies of interest.

An interesting class of phonon detectors is represented by low-dimensional electron devices operating both as the object of study as well as a pure detector instrument. One kind of application is based on the phonoconductivity technique in which the change in the resistance of the device caused by the nonequilibrium phonons is detected. For this purpose 2D electron and hole gases in GaAs heterojunctions (Eisenstein *et al.*, 1986; Kent *et al.*, 1996), 2D electron gases in Si MOSFETs (Kent *et al.*, 1988a), in δ-doped GaAs (Poplavsky *et al.*, 2000) and GaAs HEMTs (Wigmore *et al.*, 1991) or 1D electron systems in nonballistic and short ballistic quantum wires (Kent *et al.*, 1997b, 2000) have been used. A new type of information, namely about the quasimomentum of the propagating nonequilibrium phonons, is supplied by a detector technique which takes advantage of the phonon-drag effect. Here the electrical current induced in 2D or 1D electron systems by nonequilibrium phonon pulses is measured (see Chapter 5 for details).

Another aim of the work on semiconductor nanostructures is to produce phonon detectors that have spectral resolution. For this reason the inelastic phonon assisted tunnelling caused by pulses of nonequilibrium acoustic phonons has been investigated in tunnel devices. The effect could be demonstrated both in GaAs/$Al_xGa_{1-x}As$ double barrier structures (Ouali *et al.*, 1995) and in GaAs/AlAs superlattices (Cavill *et al.*, 2002). A different approach was tried with so called quantum well based phonon detectors which make use of the properties of a weakly confined 2D electron gas (Bai *et al.*, 2002). By appropriate design of the quantum well, the energy spacing between the electronic levels of the confinement potential can be tailored to absorb THz LA phonons with a sharp angular and energy response function.

A further approach for a time- and space-resolved phonon detector is to use the effect of exciton luminescence both in bulk and 2D (quantum well) semiconductor structures (Ramsbey *et al.*, 1994; Akimov *et al.*, 1994, 1997). Using a sharply focused probe laser a local population of excitons is created and the changes in the exciton luminescence induced by the nonequilibrium phonons are observed.

A.3 Wavevector and frequency dependence of a phonon radiator

The study of the kinetics of phonon pulses in crystals requires as input information the correct momentum and frequency dependence of the source term in the Boltzmann equation (3.16) for (as much as possible) realistic models of phonon sources. In the following we will consider the problem using the example of a heated metal film as the phonon source. For this reason we will adapt a formalism that was developed by O. Weis et al. (Weis, 1969; Rösch and Weis, 1977, 1978) for thermal phonon radiation and transmission to our approach of ballistic heat pulse propagation described in Section 3.3. Under conditions in which the phonon distribution in the source contains primarily phonons of frequency less than 1 THz (low heater power), this formalism should quite adequately describe the experimental situation.

Two assumptions are made for the phonon source (radiator): Firstly, the polycristalline metal film is approximated by an elastically isotropic medium. Secondly, the phonons created by heating such a film undergo frequent collisions with the electrons. As a consequence the phonons inside the radiator possess a complete equilibrium distribution and we deal with a perfect diffuse phonon field. Under these conditions the spectral phonon energy density $u_\lambda^{\mathrm{s}}(\omega)$ for a given polarization λ with a frequency between ω and $\omega + \mathrm{d}\omega$ is given by

$$u_\lambda^{\mathrm{s}}(\omega)\mathrm{d}\omega = \hbar\omega D_{\mathrm{s}}(\omega) N_\omega^{T_{\mathrm{s}}} \frac{1}{V_{\mathrm{s}}}\, \mathrm{d}\omega \;, \tag{A.1}$$

where $D_{\mathrm{s}}(\omega) = \frac{V_{\mathrm{s}}\omega^2}{2\pi^2 (c_\lambda^{\mathrm{s}})^3}$ is the density of phonon states, V_{s} is the volume of the radiator material and $N_\omega^{T_{\mathrm{s}}} = \frac{1}{e^{\hbar\omega/k_B T_{\mathrm{s}}}-1}$ is the Planckian distribution function determined by the phonon source temperature T_{s}. From the phonon energy density the energy flux per unit frequency, $\hat{\mathbf{q}}\, c_\lambda^{\mathrm{s}}\, u_\lambda^{\mathrm{s}}(\omega)\, \frac{\mathrm{d}\Omega_{\mathbf{q}}}{4\pi}$, propagating within a solid angle $\mathrm{d}\Omega_{\mathbf{q}}$ about the direction $\hat{\mathbf{q}}$ follows. Here we have used the fact that for isotropic media in the long-wavelength limit the phonon group velocity $\mathbf{v}_{\mathbf{q},\lambda}^{\mathrm{s}}$ can be substituted by the phase velocity c_λ^{s} by $\mathbf{v}_{\mathbf{q},\lambda}^{\mathrm{s}} = \mathbf{v}_{\hat{\mathbf{q}},\lambda}^{\mathrm{s}} = c_\lambda^{\mathrm{s}}\, \hat{\mathbf{q}}$. The spectral phonon power of mode λ (coming from the solid angle $\mathrm{d}\Omega_{\mathbf{q}}$ and falling onto an interface area A_{s}

with normal direction $\hat{\mathbf{n}}$) is therefore

$$\mathrm{d}P_{\mathrm{s}}^{\lambda}(\hat{\mathbf{q}},\omega) = u_{\lambda}^{\mathrm{s}}(\omega)\, c_{\lambda}^{\mathrm{s}}\, \hat{\mathbf{q}}\cdot\hat{\mathbf{n}}\, A_{\mathrm{s}}\, \frac{\mathrm{d}\Omega_{\mathbf{q}}}{4\pi} = A_{\mathrm{s}}\, \frac{\hbar\omega^3 N_{\omega}^{T_{\mathrm{s}}}}{2\pi^2 (c_{\lambda}^{\mathrm{s}})^2}\, \hat{\mathbf{q}}\cdot\hat{\mathbf{n}}\, \frac{\mathrm{d}\Omega_{\mathbf{q}}}{4\pi}\,. \tag{A.2}$$

By angle integration over the half-space we find the whole spectral phonon power of polarization λ coming from inside the radiator and falling onto the interface

$$P_{\mathrm{s}}^{\lambda}(\omega) = \frac{1}{2}\int_0^{\pi/2} \mathrm{d}\vartheta_{\mathbf{q}}\, \sin\vartheta_{\mathbf{q}}\, \frac{A_{\mathrm{s}}\hbar\omega^3 N_{\omega}^{T_{\mathrm{s}}}\cos\vartheta_{\mathbf{q}}}{2\pi^2 (c_{\lambda}^{\mathrm{s}})^2} = \frac{A_{\mathrm{s}}\hbar\omega^3 N_{\omega}^{T_{\mathrm{s}}}\cos\vartheta_{\mathbf{q}}}{8\pi^2 (c_{\lambda}^{\mathrm{s}})^2}\,, \tag{A.3}$$

where $\vartheta_{\mathbf{q}}$ is the angle between the normal direction $\hat{\mathbf{n}}$ and the wavevector $\mathbf{q}$. Finally we calculate the whole phonon power P_{s} coming from inside the radiator and falling onto the interface of area A_{s}

$$P_{\mathrm{s}} = \sum_{\lambda}\int \mathrm{d}\omega P_{\mathrm{s}}^{\lambda}(\omega) = \sum_{\lambda} A_{\mathrm{s}} \frac{\pi^2 (k_{\mathrm{B}}T_{\mathrm{s}})^4}{120\hbar^3 (c_{\lambda}^{\mathrm{s}})^2} = A_{\mathrm{s}} \frac{\pi^2 (k_{\mathrm{B}}T_{\mathrm{s}})^4}{120\hbar^3}\left(\frac{1}{(c_{\mathrm{LA}}^{\mathrm{s}})^2} + \frac{2}{(c_{\mathrm{TA}}^{\mathrm{s}})^2}\right)\,, \tag{A.4}$$

where we have applied the relation $\int \mathrm{d}\omega\omega^3/(e^{\hbar\omega/k_{\mathrm{B}}T_{\mathrm{s}}} - 1) = (k_{\mathrm{B}}T_{\mathrm{s}}\pi/\hbar)^4/15$. Assuming that there are no losses (no radiation into vacuum), P_{s} should be equal to the electrical or laser power P supplied to the heater. Therefore, one is able to calculate the source (radiator) temperature for a given input laser power P

$$T_{\mathrm{s}} = \frac{1}{k_{\mathrm{B}}}\left\{\frac{120\hbar^3}{A_{\mathrm{s}}\pi^2}\left(\frac{1}{(c_{\mathrm{LA}}^{\mathrm{s}})^2} + \frac{2}{(c_{\mathrm{TA}}^{\mathrm{s}})^2}\right)^{-1}\right\}^{1/4} P^{1/4}\,. \tag{A.5}$$

At the source/crystal interface the emitted spectral phonon power within the angle $\mathrm{d}\Omega_{\mathbf{q}}$ into the crystal is linked with the incident spectral power of the source by the power transmission factors $t_{\nu\lambda}^{\mathrm{s-c}}(\vartheta_{\mathbf{q},\nu\lambda}^{\mathrm{s}}, \varphi_{\mathbf{q},\nu\lambda}^{\mathrm{s}})$ of continuum acoustics

$$\begin{aligned}\mathrm{d}P_{\mathrm{c}}^{\lambda}(\hat{\mathbf{q}},\omega) &= \sum_{\nu} t_{\nu\lambda}^{\mathrm{s-c}}(\vartheta_{\mathbf{q},\nu\lambda}^{\mathrm{s}}, \varphi_{\mathbf{q},\nu\lambda}^{\mathrm{s}})\, \mathrm{d}P_{\mathrm{s}}^{\nu}(\hat{\mathbf{q}}_{\mathrm{s}},\omega) \\ &= \sum_{\nu} t_{\nu\lambda}^{\mathrm{s-c}}(\vartheta_{\mathbf{q},\nu\lambda}^{\mathrm{s}}, \varphi_{\mathbf{q},\nu\lambda}^{\mathrm{s}})\cos\vartheta_{\mathbf{q},\nu\lambda}^{\mathrm{s}}\, \frac{A_{\mathrm{s}}\hbar\omega^3 N_{\omega}^{T_{\mathrm{s}}}}{8\pi^3 (c_{\nu}^{\mathrm{s}})^2}\, \mathrm{d}\Omega_{\mathbf{q},\nu\lambda}^{\mathrm{s}}\,,\end{aligned} \tag{A.6}$$

where the sum over ν runs over all phonon polarizations (ν = LA, FTA, STA). The factor $t_{\nu\lambda}^{\mathrm{s-c}}(\vartheta_{\mathbf{q},\nu\lambda}^{\mathrm{s}}, \varphi_{\mathbf{q},\nu\lambda}^{\mathrm{s}})$ corresponds to the probability that an incident phonon of polarization ν and with a wavevector in $(\vartheta_{\mathbf{q},\nu\lambda}^{\mathrm{s}}, \varphi_{\mathbf{q},\nu\lambda}^{\mathrm{s}})$-direction will be transmitted across the interface into a phonon of polarization λ and with a wavevector in $(\vartheta_{\mathbf{q}}, \varphi_{\mathbf{q}})$-direction. The ratio of the solid angles $\mathrm{d}\Omega_{\mathbf{q},\nu\lambda}^{\mathrm{s}}/\mathrm{d}\Omega_{\mathbf{q}}$ can be expressed with the help of Snell's law

$$\frac{\sin\vartheta_{\mathbf{q}}}{c_{\mathbf{q}}^{\mathrm{c}}} = \frac{\sin\vartheta_{\mathbf{q}}^{\mathrm{s}}}{c^{\mathrm{s}}} \tag{A.7}$$

and the differential form of Snell's law

$$\left(\frac{\cos\vartheta^{\mathrm{s}}_{\mathbf{q}}}{c^{\mathrm{s}}} - \frac{\sin\vartheta^{\mathrm{s}}_{\mathbf{q}}}{(c^{\mathrm{s}})^2}\frac{\partial c^{\mathrm{s}}}{\partial\vartheta^{\mathrm{s}}_{\mathbf{q}}}\right)\mathrm{d}\vartheta^{\mathrm{s}}_{\mathbf{q}} = \left(\frac{\cos\vartheta_{\mathbf{q}}}{c^{\mathrm{c}}_{\mathbf{q}}} - \frac{\sin\vartheta_{\mathbf{q}}}{(c^{\mathrm{c}}_{\mathbf{q}})^2}\frac{\partial c^{\mathrm{c}}_{\mathbf{q}}}{\partial\vartheta_{\mathbf{q}}}\right)\mathrm{d}\vartheta_{\mathbf{q}} \tag{A.8}$$

by

$$\begin{aligned}\frac{\mathrm{d}\Omega^{\mathrm{s}}_{\mathbf{q},\nu\lambda}}{\mathrm{d}\Omega_{\mathbf{q}}} &= \frac{\sin\vartheta^{\mathrm{s}}_{\mathbf{q},\nu\lambda}\,\mathrm{d}\vartheta^{\mathrm{s}}_{\mathbf{q},\nu\lambda}\mathrm{d}\varphi^{\mathrm{s}}_{\mathbf{q},\nu\lambda}}{\sin\vartheta_{\mathbf{q}}\,\mathrm{d}\vartheta_{\mathbf{q}}\,\mathrm{d}\varphi_{\mathbf{q}}} = \frac{c^{\mathrm{s}}_{\nu}}{c^{\mathrm{c}}_{\hat{\mathbf{q}}\lambda}}\frac{\mathrm{d}\vartheta^{\mathrm{s}}_{\mathbf{q},\nu\lambda}}{\mathrm{d}\vartheta_{\mathbf{q}}} \\ &= \left(\frac{c^{\mathrm{s}}_{\nu}}{c^{\mathrm{c}}_{\hat{\mathbf{q}},\lambda}}\right)^2 \frac{\cos\vartheta_{\mathbf{q}} - \frac{\sin\vartheta_{\mathbf{q}}}{c^{\mathrm{c}}_{\hat{\mathbf{q}},\lambda}}\frac{\partial c^{\mathrm{c}}_{\hat{\mathbf{q}},\lambda}}{\partial\vartheta_{\mathbf{q}}}}{\cos\vartheta^{\mathrm{s}}_{\mathbf{q},\nu\lambda}} = \frac{v^{\mathrm{c}}_{\hat{\mathbf{q}},\lambda}\cos\vartheta_{\mathbf{v}^{\mathrm{c}}_{\hat{\mathbf{q}},\lambda}}/(c^{\mathrm{c}}_{\hat{\mathbf{q}},\lambda})^3}{\cos\vartheta^{\mathrm{s}}_{\mathbf{q},\nu\lambda}/(c^{\mathrm{s}}_{\nu})^2}\,.\end{aligned} \tag{A.9}$$

In the last step of (A.9) we benefit from Eq. (3.9) and from the fact that for long-wavelength phonons the phase velocities depend only on the direction of the wavevector. Thus we derive for the spectral phonon power into the crystal (coming from area A_{s} and falling into $\hat{\mathbf{q}}$-direction)

$$\mathrm{d}P^{\lambda}_{\mathrm{c}}(\hat{\mathbf{q}},\omega) = \frac{A_{\mathrm{s}}\hbar\omega^3 N^{T_{\mathrm{s}}}_{\omega}}{8\pi^3}\frac{v^{\mathrm{c}}_{\hat{\mathbf{q}},\lambda}}{(c^{\mathrm{c}}_{\hat{\mathbf{q}},\lambda})^3}\cos\vartheta_{\mathbf{v}^{\mathrm{c}}_{\hat{\mathbf{q}},\lambda}}\sum_{\nu} t^{\nu\lambda}_{\mathrm{s-c}}(\vartheta^{\mathrm{s}}_{\mathbf{q},\nu\lambda},\varphi^{\mathrm{s}}_{\mathbf{q},\nu\lambda})\,\mathrm{d}\Omega_{\mathbf{q}}\,. \tag{A.10}$$

This equation shows clearly that for emission into the same solid angle the ratio of emitted LA phonons to emitted TA phonons is in a first approximation inversely proportional to the square of the phonon phase velocities in the crystal (the size of the contributing solid angles in the heater is different for different modes). In contrast, the ratio of the total number of LA phonons to the total number of TA phonons emitted into the crystal depends from the phonon phase velocities in the heater material. This is due to the fact that the critical angles for phonon emission into the crystal $\vartheta^{\mathrm{crit}}_{\mathbf{q},\nu\lambda} = \arcsin(c^{\mathrm{c}}_{\hat{\mathbf{q}},\lambda}/c^{\mathrm{s}}_{\nu})$ are mode dependent.

If the surface between the metal film heater and the crystal is rough on a scale larger than the phonon wavelength, specular transmission may still apply, but the distributions of surface normals will tend to average out the anisotropy. However, it is known from optics that a rough surface generally exhibits a cosine-like angular dependence (Lambert's law). Therefore it seems that the cosine factor in the transmitted **q**-space flux may appear for both specular and diffuse scattering.

For real calculations one needs the transmission coefficients $t^{\mathrm{s-c}}_{\nu\lambda}$ for each angle and mode including all reflection and mode conversion processes. This is a practical impossibility without approximations and in any case very time consuming. Therefore, to simplify the calculations we have neglected all mode conversion processes at the heater/crystal interface. Furthermore, the probability for transmission is assumed to be one for all angles smaller than the critical one. In this case the spectral phonon power of mode λ into the crystal is

$$\mathrm{d}P^{\lambda}_{\mathrm{c}}(\hat{\mathbf{q}},\omega) = \frac{A_{\mathrm{s}}\hbar\omega^3 N^{T_{\mathrm{s}}}_{\omega}}{8\pi^3}\frac{v^{\mathrm{c}}_{\hat{\mathbf{q}},\lambda}}{(c^{\mathrm{c}}_{\hat{\mathbf{q}},\lambda})^3}\cos\vartheta_{\mathbf{v}^{\mathrm{c}}_{\hat{\mathbf{q}},\lambda}}\,\Theta\Big(\frac{c^{\mathrm{c}}_{\hat{\mathbf{q}},\lambda}}{c^{\mathrm{s}}_{\lambda}} - \sin\vartheta_{\mathbf{q}}\Big)\,\mathrm{d}\Omega_{\mathbf{q}}\,. \tag{A.11}$$

It remains the question of the relation between the above derived spectral phonon power $\mathrm{d}P_{\lambda}^{\mathrm{c}}(\hat{\mathbf{q}},\omega)$ and the source term $Z(\mathbf{q},\lambda,\mathbf{r},t)$ of the Boltzmann-Peierls kinetic equation (3.16) describing the phonon pulse propagation. From the total balance of transmitted phonons for a heater with temperature T_{s} located at $z=0$ with surface area A_{s} and pulse duration Δt

$$\int \mathrm{d}\omega \int \mathrm{d}P_{\mathrm{c}}^{\lambda}(\hat{\mathbf{q}},\omega)\,\Theta(t)\Theta(\Delta t - t) = \sum_{\mathbf{q}} \int \mathrm{d}^3 r\, \hbar\omega_{\hat{\mathbf{q}},\lambda} Z(\mathbf{q},\lambda,\mathbf{r},t) \tag{A.12}$$

the phonon distribution in the source term follows immediately with (3.17) and (A.11)

$$\gimel_{\mathrm{s}}(\hat{\mathbf{q}},\omega_{\hat{\mathbf{q}},\lambda},\mathbf{e}_{\hat{\mathbf{q}},\lambda}) = \Delta t\,\frac{A_{\mathrm{s}}}{V_{\mathrm{c}}}\,\frac{1}{e^{\hbar\omega_{\hat{\mathbf{q}},\lambda}/k_{\mathrm{B}}T_{\mathrm{s}}}-1}\,v_{\hat{\mathbf{q}},\lambda}^{\mathrm{c}}\cos\vartheta_{\mathbf{v}_{\hat{\mathbf{q}},\lambda}^{\mathrm{c}}}\,\Theta\Big(\frac{c_{\hat{\mathbf{q}},\lambda}^{\mathrm{c}}}{c_{\lambda}^{\mathrm{s}}} - \sin\vartheta_{\mathbf{q}}\Big)\,. \tag{A.13}$$

Appendix B

Dynamic Susceptibility of Quasi Low-Dimensional Electron Gases

B.1 Quasi two-dimensional systems

B.1.1 The magnetic field case

We consider a quasi-2D electron gas in the xy-plane under the influence of a magnetic field directed along the z-axis. In this case the magnetic field does not influence the motion in z-direction which is governed exclusively by the confinement potential $V(z)$. Thus the corresponding wavefunctions $\varphi_l(z)$ given in Section 4.1.3 remain unchanged. Assuming the vector potential in Landau gauge, $\mathbf{A} = Bx\mathbf{e}_y$, the normalized electron wavefunctions are

$$\psi_{lnk}(\mathbf{r}) = \varphi_l(z) L_y^{-1/2} e^{iky} \phi_n(x + l_B^2 k) \ , \tag{B.1}$$

where $n = 1, 2, \ldots$ and k is taking the discrete values $k = 2\pi\kappa/L_y$ with $\kappa = 0, \pm 1, \ldots, \pm\frac{1}{2}\frac{L_x L_y}{2\pi l_B^2}$. L_x, L_y are the normalization lengths of the xy-plane and $l_B = \sqrt{\hbar/|e|B}$ is the magnetic length. The functions

$$\phi_n(x) = \sqrt{\frac{1}{\pi^{1/2}(n-1)!\, 2^{n-1}\, l_B}}\; e^{-x^2/2l_B^2}\ \mathrm{H}_{n-1}(x/l_B) \tag{B.2}$$

are the eigenfunctions of a simple harmonic oscillator, where $\mathrm{H}_n(x)$ denotes the Hermite polynomials

$$\mathrm{H}_n(x) = (-1)^n e^{x^2} \frac{\mathrm{d}^n}{\mathrm{d}x^n} e^{-x^2} \ . \tag{B.3}$$

As a consequence of Eq. (B.1) the Fourier transform of the electron density operator becomes

$$\rho_{\mathbf{q}}^{+} = \rho_{-\mathbf{q}} = \sum_{l,l'} G_{ll'}(-q_z) \rho^{ll'}(-\mathbf{q}_{\parallel}) \tag{B.4}$$

with the overlap integral

$$G_{ll'}(q_z) = \int \mathrm{d}z\, \varphi_l^*(z) e^{-iq_z z} \varphi_{l'}(z) \tag{B.5}$$

and the in-plane component of the density operator

$$\rho^{ll'}(\mathbf{q}_\parallel) = \sum_{n,n'} \sum_k \rho_{nn'}^{ll'}(k, \mathbf{q}_\parallel) = \sum_{n,n'} \sum_k I_{nn'}(-q_x, k - q_y, k)\, c_{lnk-q_y}^+ c_{l'n'k}\ . \tag{B.6}$$

The function $I_{nn'}(q_x, k, k')$ is defined by

$$I_{nn'}(q_x, k, k') = \int \mathrm{d}x\, \phi_n^*(x + l_B^2 k) e^{iq_x x} \phi_{n'}(x + l_B^2 k') \tag{B.7}$$

and the operators c_{lnk}^+ and c_{lnk} create and annihilate an electron in the state $\{lnk\}$, respectively. Working out the commutator of $\rho_{nn'}^{ll'}(k, \mathbf{q}_\parallel)$ with the unperturbed electron part of the Hamilton operator (i.e. without the electron-phonon coupling, but including the electron-electron interaction)

$$\begin{aligned} H_{\mathrm{el}} &= \sum_{l,n} \sum_k E_{ln} c_{lnk}^+ c_{lnk} \qquad\qquad (\mathrm{B.8}) \\ &\quad + \sum_{\mathbf{q}_\parallel \neq 0} v(q_\parallel) \left(\sum_{l_1,l_2,l_3,l_4} g_{l_3 l_4}^{l_1 l_2}(q_\parallel)\, \rho^{l_1 l_3}(-\mathbf{q}_\parallel) \rho^{l_4 l_2}(\mathbf{q}_\parallel) - \sum_{l,n} \sum_k c_{lnk}^+ c_{lnk} \right) \end{aligned}$$

we derive the equation

$$\begin{aligned} [H_{\mathrm{el}}, \rho_{nn'}^{ll'}(k, \mathbf{q}_\parallel)] &= (E_{ln} - E_{l'n'})\, \rho_{nn'}^{ll'}(k, \mathbf{q}_\parallel) + \frac{1}{2} \sum_{\mathbf{q}'_\parallel \neq 0} v(q_\parallel{}') \sum_{l_1,l_2} \sum_{\tilde{l},\tilde{n}} \Bigg\{ \\ &\quad g_{l_1 l_2}^{\tilde{l} l}(q_\parallel{}') I_{\tilde{n} n}(+q'_x, k + q'_y - q_y, k - q_y) I_{nn'}(-q_x, k - q_y, k) \\ &\qquad\qquad \times [c_{\tilde{l}\tilde{n}k+q'_y-q_y}^+ c_{l'n'k}\, , \rho^{l_1 l_2}(\mathbf{q}'_\parallel)]_+ \\ &\quad - g_{l_1 l_2}^{l' \tilde{l}}(q_\parallel{}') I_{n' \tilde{n}}(q'_x, k, k - q'_y) I_{nn'}(-q_x, k - q_y, k) \\ &\qquad\qquad \times [c_{lnk-q_y}^+ c_{\tilde{l}\tilde{n}k-q'_y}\, , \rho^{l_1 l_2}(\mathbf{q}'_\parallel)]_+ \Bigg\}\ . \end{aligned} \tag{B.9}$$

In (B.9) we have introduced the notations $E_{ln} = E_{lnk}$ for the subband energies, $v(q_\parallel)$ for the Fourier transform of the 2D Coulomb interaction

$$v(q_\parallel) = \frac{e^2}{2\varepsilon_0 \varepsilon_\mathrm{r} q_\parallel L_x L_y} \tag{B.10}$$

and $g_{l_3 l_4}^{l_1 l_2}(q_\parallel)$ for the form factor

$$g_{l_3 l_4}^{l_1 l_2}(q_\parallel) = \iint \mathrm{d}z \mathrm{d}z'\, \varphi_{l_1}^*(z) \varphi_{l_2}(z) \varphi_{l_3}^*(z') \varphi_{l_4}(z') e^{-q_\parallel |z - z'|} = g_{l_1 l_2}^{l_3 l_4}(q_\parallel)\ . \tag{B.11}$$

Using the RPA, i.e. keeping only the term ${\mathbf{q}_\parallel}' = \mathbf{q}_\parallel$ and replacing the operator $c^+_{lnk} c_{\tilde{l}\tilde{n}k}$ by its expectation value, (B.9) reduces to a set of coupled linear equations

$$\begin{aligned}[H_{\rm el}, \rho^{ll'}_{nn'}(k,\mathbf{q}_\parallel)] &= (E_{ln} - E_{l'n'})\, \rho^{ll'}_{nn'}(k,\mathbf{q}_\parallel) - v(q_\parallel) I_{nn'}(-q_x, k-q_y, k) \\ &\times I_{n'n}(q_x, k, k-q_y)(f_{ln} - f_{l'n'}) \sum_{l_1,l_2} g^{l'l}_{l_1 l_2}(q_\parallel)\, \rho^{l_1 l_2}(\mathbf{q}_\parallel) \end{aligned} \tag{B.12}$$

with $f_{ln} = \langle c^+_{lnk} c_{lnk} \rangle$ as the Fermi distribution function.

In the following we will apply these equations to determine the matrix of the dynamic susceptibility

$$\left(\rho_\mathbf{q} | \frac{L}{L+\omega+i\eta} \rho_\mathbf{q}\right)\Big|_{\eta\to 0} , \tag{B.13}$$

where we have used the formulation by the Liouville operator L and the Mori operator product as introduced in Section 5.2. We start with the operator identity

$$z\frac{L}{L+z} + \frac{L}{L+z} L = L \tag{B.14}$$

and set $z = \omega + i\eta$. That way we obtain in RPA

$$\begin{aligned}&\left\{z + \frac{1}{\hbar}(E_{ln} - E_{l'n'})\right\} \left(\rho_\mathbf{q} | \frac{L}{L+z} \rho^{ll'}_{nn'}(k,\mathbf{q}_\parallel)\right) \;-\; v(q_\parallel) I_{nn'}(-q_x, k-q_y, k) \\ &\qquad\times\; I_{n'n}(q_x, k, k-q_y)\big\{f_{ln} - f_{l'n'}\big\} \sum_{l_1,l_2} g^{l'l}_{l_1 l_2}(q_\parallel) \left(\rho_\mathbf{q} | \frac{L}{L+z} \rho^{l_1 l_2}(\mathbf{q}_\parallel)\right) \\ &= \left(\rho_\mathbf{q} | L \rho^{ll'}_{nn'}(k,\mathbf{q}_\parallel)\right) . \end{aligned} \tag{B.15}$$

For the r.h.s. of Eq. (B.15) we use the Kubo identity and find

$$\begin{aligned}\left(\rho_\mathbf{q} | L \rho^{ll'}_{nn'}(k,\mathbf{q}_\parallel)\right) &= \frac{1}{\hbar} \left\langle [\rho^+_\mathbf{q}, \rho^{ll'}_{nn'}(k,\mathbf{q}_\parallel)] \right\rangle_{\hat{\rho}^\beta_{\rm el}} \\ = \big\{f_{l'n'} - f_{ln}\big\} G_{l'l}(-q_z) I_{nn'}&(-q_x, k-q_y, k) I_{n'n}(q_x, k, k-q_y) . \end{aligned} \tag{B.16}$$

Dividing Eq. (B.15) by $\left\{z + \frac{1}{\hbar}(E_{ln} - E_{l'n'})\right\}$ and summing over n, n' and k, we derive a set of equations

$$\begin{aligned}&\sum_{l_1,l_2} \left\{\delta_{l,l_1}\delta_{l',l_2} - v(q_\parallel) g^{l'l}_{l_1 l_2}(q_\parallel) \chi^{(B)}_{ll'}(\mathbf{q}_\parallel,\omega)\right\} \left(\rho_\mathbf{q} | \frac{L}{L+\omega+i\eta} \rho^{l_1 l_2}(\mathbf{q}_\parallel)\right) \\ &\quad = -\, G_{l'l}(-q_z) \chi^{(B)}_{ll'}(q_\parallel,\omega) , \end{aligned} \tag{B.17}$$

where

$$\chi^{(B)}_{ll'}(q_\parallel,\omega) = \frac{1}{\hbar} \sum_{n,n'} C_{nn'}(q_\parallel) \frac{f_{l'n'} - f_{ln}}{(E_{l'n'} - E_{ln})/\hbar - \omega - i\eta} \tag{B.18}$$

and

$$\begin{aligned} C_{nn'}(q_\parallel) &= \sum_k I_{nn'}(q_x, k+q_y, k) I_{n'n}(-q_x, k, k+q_y) \\ &= \frac{L_x L_y}{\pi l_B^2} \frac{(n_1-1)!}{(n_2-1)!} \Big(\frac{q_\parallel^2 l_B^2}{2} \Big)^{n_2-n_1} e^{-\frac{q_\parallel^2 l_B^2}{2}} \left[L_{n_1-1}^{n_2-n_1}(\frac{q_\parallel^2 l_B^2}{2}) \right]^2 \end{aligned} \qquad \text{(B.19)}$$

(see Ting *et al.*, 1977). Here $n_2 = \max(n, n')$, $n_1 = \min(n, n')$ and the $L_n^m(x)$ are the associated Laguerre polynomials

$$L_n^m(x) = \sum_{r=0}^{n} (-1)^r \frac{(n+m)!}{(m+r)!\,(n-r)!\,r!}\, x^r\ . \qquad \text{(B.20)}$$

The quantity $\chi_{ll'}^{(B)}(q_\parallel, \omega)$ corresponds to the dynamic susceptibility of a quasi-2D *non*interacting electron system in a perpendicular magnetic field B. Introducing the dielectric matrix

$$\varepsilon_{l_1 l_2}^{ll'}(q_\parallel, \omega) = \delta_{l,l_1}\delta_{l',l_2} - v(q_\parallel) g_{l_1 l_2}^{l'l}(q_\parallel) \chi_{ll'}^{(B)}(q_\parallel, \omega) \qquad \text{(B.21)}$$

we obtain from Eq. (B.17)

$$\Big(\rho_{\mathbf{q}} | \frac{L}{L+\omega+i\eta} \rho^{l_1 l_2}(\mathbf{q}_\parallel) \Big) = -\sum_{l,l'} \left(\varepsilon^{-1}(q_\parallel, \omega) \right)_{ll'}^{l_1 l_2} G_{ll'}^*(q_z) \chi_{ll'}^{(B)}(q_\parallel, \omega) \qquad \text{(B.22)}$$

and finally

$$\Big(\rho_{\mathbf{q}} | \frac{L}{L+\omega+i\eta} \rho_{\mathbf{q}} \Big) = -\sum_{l_1, l_2} \sum_{l,l'} G_{l_1 l_2}(q_z) \left(\varepsilon^{-1}(q_\parallel, \omega) \right)_{ll'}^{l_1 l_2} G_{ll'}^*(q_z) \chi_{ll'}^{(B)}(q_\parallel, \omega)\ . \qquad \text{(B.23)}$$

From (B.23) follows that a straightforward screening factor cannot be defined without matrix inversion in quasi low-dimensional systems. The use of a modified dielectric matrix in the form of

$$\varepsilon_{ll'}(\mathbf{q}, \omega) = \frac{G_{ll'}(q_z)}{\sum_{l_1, l_2} G_{l_1 l_2}(q_z) \left(\varepsilon^{-1}(q_\parallel, \omega) \right)_{ll'}^{l_1 l_2}} \qquad \text{(B.24)}$$

leads to an equation of the dynamic susceptibility that is at least formally simpler:

$$\Big(\rho_{\mathbf{q}} | \frac{L}{L+\omega+i\eta} \rho_{\mathbf{q}} \Big) = -\sum_{l,l'} \frac{|G_{ll'}(q_z)|^2 \chi_{ll'}^{(B)}(q_\parallel, \omega)}{\varepsilon_{ll'}(\mathbf{q}, \omega)}\ . \qquad \text{(B.25)}$$

Fortunately, there are cases where the treatment of screening is less expensive. For quasi-2D systems in semiconductor heterostructures it is a common situation that the energy spacing between the substates with different l is sufficiently large.

Therefore, at low temperatures only the lowest substate with $l = 1$ is occupied. On these terms Eq. (B.25) simplifies substantially and we obtain in a reasonable approximation

$$\Big(\rho_{\mathbf{q}}|\frac{L}{L+\omega+i\eta}\rho_{\mathbf{q}}\Big) = -\frac{|G_{11}(q_z)|^2\chi_{11}^{(B)}(q_\parallel,\omega)}{1-v(q_\parallel)g_{11}^{11}(q_\parallel)\chi_{11}^{(B)}(q_\parallel,\omega)} \quad . \tag{B.26}$$

B.1.2 The zero field case

In this case the electrons move freely in the xy-plane and are confined in z-direction. According to (4.13) the electron wavefunctions are

$$\psi_{l\mathbf{k}_\parallel}(\mathbf{r}) = \varphi_l(z)\,\frac{1}{(L_xL_y)^{1/2}}\,e^{ik_xx}e^{ik_yy} \ . \tag{B.27}$$

Thus the Fourier transform of the electron density operator reads

$$\rho_{\mathbf{q}}^+ = \rho_{-\mathbf{q}} = \sum_{l,l'} G_{ll'}(-q_z)\sum_{\mathbf{k}_\parallel,\sigma} c^+_{l\mathbf{k}_\parallel+\mathbf{q}_\parallel\sigma}c_{l'\mathbf{k}_\parallel\sigma} \tag{B.28}$$

with the overlap integral $G_{ll'}(q_z)$ given in (B.5). The dynamic susceptibility can be determined similar to the magnetic case and we obtain

$$\Big(\rho_{\mathbf{q}}|\frac{L}{L+\omega+i\eta}\rho_{\mathbf{q}}\Big) = -\sum_{l,l'}\frac{|G_{ll'}(q_z)|^2\chi_{ll'}^{(0)}(\mathbf{q}_\parallel,\omega)}{\varepsilon_{ll'}(\mathbf{q},\omega)} \tag{B.29}$$

with

$$\chi_{ll'}^{(0)}(\mathbf{q}_\parallel,\omega) = \chi_{ll'}^{(0)}(q_\parallel,\omega) = \frac{1}{\hbar}\sum_{\mathbf{k}_\parallel,\sigma}\frac{f_{l'\mathbf{k}_\parallel+\mathbf{q}_\parallel}-f_{l\mathbf{k}_\parallel}}{(E_{l'\mathbf{k}_\parallel+\mathbf{q}_\parallel}-E_{l\mathbf{k}_\parallel})/\hbar-\omega-i\eta} \ . \tag{B.30}$$

The modified dielectric matrix $\varepsilon_{ll'}(\mathbf{q},\omega)$ in Eq. (B.29) is defined analogously to (B.24). In the special case that only the lowest substate is occupied ($l = l' = 1$) Eq. (B.29) reduces to intrasubband transitions

$$\Big(\rho_{\mathbf{q}}|\frac{L}{L+\omega+i\eta}\rho_{\mathbf{q}}\Big) = -\frac{|G_{11}(q_z)|^2\chi_{11}^{(0)}(q_\parallel,\omega)}{1-v(q_\parallel)g_{11}^{11}(q_\parallel)\chi_{11}^{(0)}(q_\parallel,\omega)} \ . \tag{B.31}$$

For an electron gas at a temperature $T_{\rm el}$ well below the Fermi temperature the real and imaginary part of the function $\chi_{11}^{(0)}(q_\parallel,\omega)$ can be calculated as following,

$$\mathrm{Re}\chi_{11}^{(0)}(q_\parallel,\omega) \;=\; -\frac{L_xL_ym^*k_{\rm F}}{\pi\hbar^2q_\parallel}\,\mathcal{P}(\frac{q_\parallel}{k_{\rm F}},\frac{\hbar\omega}{E_{\rm F}},\frac{k_{\rm B}T_{\rm el}}{E_{\rm F}}) \tag{B.32}$$

$$\mathrm{Im}\chi_{11}^{(0)}(q_\parallel,\omega) \;=\; -\frac{L_xL_ym^*k_{\rm F}}{\pi\hbar^2q_\parallel}\,\mathcal{L}(\frac{q_\parallel}{k_{\rm F}},\frac{\hbar\omega}{E_{\rm F}},\frac{k_{\rm B}T_{\rm el}}{E_{\rm F}}) \ , \tag{B.33}$$

where k_{F} and E_{F} are the Fermi wavevector and the Fermi energy of the 2D electron gas, respectively, and

$$\begin{aligned}\mathcal{P}(\alpha,\beta,\gamma) = \frac{\alpha}{e^{-1/\gamma}+1} - \int\limits_{-1/\gamma}^{\infty} \frac{\mathrm{d}\zeta\; e^{\zeta}}{(e^{\zeta}+1)^2}\, \mathrm{Re}\Bigg\{ & \sqrt{\frac{1}{4}\Big(\alpha+\frac{\beta}{\alpha}\Big)^2 - 1 - \gamma\zeta} \\ & + \operatorname{sgn}\Big(\alpha-\frac{\beta}{\alpha}\Big)\sqrt{\frac{1}{4}\Big(\alpha-\frac{\beta}{\alpha}\Big)^2 - 1 - \gamma\zeta}\Bigg\}\,,\end{aligned} \tag{B.34}$$

$$\begin{aligned}\mathcal{L}(\alpha,\beta,\gamma) = \int\limits_{-1/\gamma}^{\infty} \frac{\mathrm{d}\zeta\; e^{\zeta}}{(e^{\zeta}+1)^2}\, \mathrm{Re}\Bigg\{ & \sqrt{1+\gamma\zeta-\frac{1}{4}\Big(\alpha-\frac{\beta}{\alpha}\Big)^2} \\ & - \sqrt{1+\gamma\zeta-\frac{1}{4}\Big(\alpha+\frac{\beta}{\alpha}\Big)^2}\Bigg\}\,.\end{aligned} \tag{B.35}$$

Deriving (B.34) and (B.35) we have neglected the temperature dependence of the chemical potential.

At zero temperature ($T_{\mathrm{el}} = 0$) the function $\chi_{11}^{(0)}(q_{\|},\omega)$ simplifies to the well known 2D analogue of the Lindhard function (Stern, 1967) with

$$\mathcal{P}(\alpha,\beta,0) = \alpha - \mathrm{Re}\Bigg\{\sqrt{\frac{1}{4}\Big(\alpha+\frac{\beta}{\alpha}\Big)^2 - 1} + \operatorname{sgn}\Big(\alpha-\frac{\beta}{\alpha}\Big)\sqrt{\frac{1}{4}\Big(\alpha-\frac{\beta}{\alpha}\Big)^2 - 1}\Bigg\} \tag{B.36}$$

and

$$\mathcal{L}(\alpha,\beta,0) = \mathrm{Re}\Bigg\{\sqrt{1-\frac{1}{4}\Big(\alpha-\frac{\beta}{\alpha}\Big)^2} - \sqrt{1-\frac{1}{4}\Big(\alpha+\frac{\beta}{\alpha}\Big)^2}\Bigg\}\,. \tag{B.37}$$

From Eq. (B.21) (now for $B = 0$) and the relations (B.32–B.37) we are able to obtain the dielectric function $\varepsilon_{11}^{11}(q_{\|},\omega)$ for finite and zero electron temperature numerically. In the static limit and for $T_{\mathrm{el}} = 0$ the result is simple (Ando *et al.*, 1982), namely

$$\varepsilon_{11}^{11}(q_{\|},0) = \begin{cases} 1+\frac{q_{\mathrm{S}}}{q_{\|}} & \text{if} \quad q_{\|} \le 2k_{\mathrm{F}} \\ 1+\frac{q_{\mathrm{S}}}{q_{\|}}\big[1-\sqrt{1-(2k_{\mathrm{F}}/q_{\|})^2}\big] & \text{else}\end{cases}\,. \tag{B.38}$$

In contradiction to the strictly 2D case the screening wavevector $q_{\mathrm{S}} = \frac{e^2 m^*}{2\pi\varepsilon_0\varepsilon_{\mathrm{r}}\hbar^2} g_{11}^{11}(q_{\|})$ is here still a function of $q_{\|}$ and depends by the form factor on the given confinement potential in z-direction.

B.2 Quasi one-dimensional systems

In this case electrons move freely only in one direction (here in y-direction) and are confined in the other two. As pointed out in Section 4.1.3 the electron wavefunction can be written in the form

$$\psi_{lnk}(\mathbf{r}) = \varphi_l(z)\,\phi_n(x)\frac{1}{L_y^{1/2}}\,e^{iky}\ . \tag{B.39}$$

The functions $\varphi_l(z)$ and $\phi_n(x)$ are determined by the confinement in z- and x-direction. Thus the Fourier transform of the electron density operator is equal to

$$\rho_{\mathbf{q}}^{+} = \rho_{-\mathbf{q}} = \sum_{l,l'}\sum_{n,n'} G_{nn'}^{ll'}(-q_z,-q_x)\sum_{k,\sigma} c_{lnk+q_y\sigma}^{+}c_{l'n'k\sigma}\ , \tag{B.40}$$

where the overlap integral $G_{nn'}^{ll'}(q_z,q_x)$ is now a 2D one and is defined by

$$G_{nn'}^{ll'}(q_z,q_x) = \iint \mathrm{d}z\mathrm{d}x\,\varphi_l^*(z)e^{-iq_z z}\varphi_{l'}(z)\,\phi_n^*(x)e^{-iq_x x}\phi_{n'}(x)\ . \tag{B.41}$$

To reduce the number of indices we will consider below only the case that from the subbands regarding the confinement in z-direction exclusively the lowest one is occupied ($l = l' = 1$). This is an adequate restriction for the systems we are interested in where the confinement length in growth direction is small, typically much smaller than the (additional) lateral confinement in the plane. The dynamical susceptibility can be obtained similar to the 2D case, i.e.

$$\Big(\rho_{\mathbf{q}}|\frac{L}{L+\omega+i\eta}\rho_{\mathbf{q}}\Big) = -\sum_{n,n'}\frac{|G_{nn'}^{11}(q_z,q_x)|^2\chi_{nn'}^{1\mathrm{D}}(q_y,\omega)}{\varepsilon_{nn'}(\mathbf{q},\omega)} \tag{B.42}$$

with

$$\chi_{nn'}^{1\mathrm{D}}(q,\omega) = \frac{1}{\hbar}\sum_{k,\sigma}\frac{f_{1n'k+q}-f_{1nk}}{(E_{1n'k+q}-E_{1nk})/\hbar-\omega-i\eta} \tag{B.43}$$

and

$$\varepsilon_{nn'}(\mathbf{q},\omega) = \frac{G_{nn'}^{11}(q_z,q_x)}{\sum_{n_1,n_2} G_{n_1n_2}^{11}(q_z,q_x)\,(\varepsilon^{-1}(q_y,\omega))_{nn'}^{n_1n_2}}\ . \tag{B.44}$$

The dielectric matrix is equal to

$$\varepsilon_{n_1n_2}^{nn'}(q,\omega) = \delta_{n,n_1}\delta_{n',n_2} - \frac{e^2}{2\pi\varepsilon_0\varepsilon_{\mathrm{r}}L_y}\hat{g}_{n_1n_2}^{n'n}(q)\chi_{nn'}^{1\mathrm{D}}(q,\omega) \tag{B.45}$$

with $\frac{e^2}{2\pi\varepsilon_0\varepsilon_{\mathrm{r}}L_y}$ as the Fourier transform of the 1D Coulomb interaction. The function $\hat{g}_{n_1n_2}^{n'n}(q)$ is the quasi-1D analogue of the form factor and is given by

$$\begin{aligned}\hat{g}_{n_1n_2}^{n'n}(q) \quad &= \quad \iiiint \mathrm{d}z\mathrm{d}z'\mathrm{d}x\mathrm{d}x'\,|\varphi_1(z)|^2|\varphi_1(z')|^2\phi_{n'}^*(x)\phi_n(x)\phi_{n_1}^*(x')\phi_{n_2}(x') \\ &\times \quad \mathrm{K}_0\left(q\sqrt{(z-z')^2+(x-x')^2}\right)\ ,\end{aligned} \tag{B.46}$$

where $\mathrm{K}_0(x) = \int_0^\infty \frac{\mathrm{d}t\cos(xt)}{\sqrt{t^2+1}}$ is a modified Bessel function of the second kind.

In the zero temperature limit the summation on the r.h.s. of (B.43) can be performed explicitly and we get for the response function

$$\chi^{\mathrm{1D}}_{nn'}(q,\omega) = K_{nn'}(q,\omega) + K^*_{n'n}(-q,-\omega)\ . \tag{B.47}$$

The real and imaginary part of $K_{nn'}$ are given by

$$\begin{aligned}\mathrm{Re}K_{nn'}(q,\omega) &= \frac{L_y m^*}{\pi\hbar^2 q}\ln\left|\frac{2k_{\mathrm{F}}^{(n)} - q + 2\tilde{k}_{nn'}(q,\omega)}{2k_{\mathrm{F}}^{(n)} + q - 2\tilde{k}_{nn'}(q,\omega)}\right|\ , && \text{(B.48)}\\ \mathrm{Im}K_{nn'}(q,\omega) &= -\frac{L_y m^*}{\hbar^2|q|}\,\Theta\left(2k_{\mathrm{F}}^{(n)} - |q - 2\tilde{k}_{nn'}(q,\omega)|\right)\ . && \text{(B.49)}\end{aligned}$$

Here, we have introduced the abbreviations $\tilde{k}_{nn'}(q,\omega) = \frac{m^*}{\hbar^2 q}(E_{1n0} - E_{1n'0} + \hbar\omega)$ and $k_{\mathrm{F}}^{(n)} = \sqrt{\frac{2m^*}{\hbar^2}(E_{\mathrm{F}} - E_{1n0})}$. The variable $k_{\mathrm{F}}^{(n)}$ is something like the Fermi wavevector of the n-th subband. It describes the relative position of the Fermi energy E_{F} to the respective subband minima E_{1n0}.

If we neglect screening, then only the imaginary part of the response function (B.43) is of interest for the electron-phonon interaction. This part can be worked out analytically for finite electron temperatures T_{el}, even in the case of a quantum wire with multi-populated subbands. It is

$$\mathrm{Im}\,\chi^{\mathrm{1D}}_{nn'}(q,\omega) = -\frac{L_y m^*}{\hbar^2|q|}\,\frac{\sinh(\beta\hbar\omega/2)}{\cosh(\beta\hbar\omega/2) + \cosh(\beta R_{nn'}(q,\omega))} \tag{B.50}$$

(Hu and O'Connell, 1991), where

$$R_{nn'}(q,\omega) = \frac{\hbar^2 q^2}{8m^*} + \frac{E_{1n'0} + E_{1n0}}{2} + \frac{\hbar^2}{2m^*}\,\tilde{k}^2_{nn'}(q,\omega) - \mu \tag{B.51}$$

and μ denotes the chemical potential. Since we are mainly concerned with low T_{el}, we use the approximation $\mu \approx E_{\mathrm{F}}$.

Appendix C

Overlap Integrals and Form Factors

C.1 Quasi two-dimensional systems

C.1.1 Modulation-doped heterojunctions

To obtain the matrix elements of the electron-phonon and the electron-electron interaction we need to know the wavevector dependence of the squared overlap integral (B.5)

$$|G_{ll'}(q_z)|^2 = \Big| \int \mathrm{d}z \, \varphi_l^*(z) e^{-iq_z z} \varphi_{l'}(z) \Big|^2 \tag{C.1}$$

and the form factor (B.11)

$$g_{l_3 l_4}^{l_1 l_2}(q_\parallel) = \iint \mathrm{d}z \mathrm{d}z' \, \varphi_{l_1}^*(z) \varphi_{l_2}(z) \varphi_{l_3}^*(z') \varphi_{l_4}(z') \, e^{-q_\parallel |z-z'|} \, , \tag{C.2}$$

where in most cases we can restrict ourself to the electrons in the ground substate ($l = 1$).

According to (4.25) the z-component of the envelope function is

$$\varphi_{(\mathrm{c})_1}^{\mathrm{Ai}}(z) = \begin{cases} B_\mathrm{h} \exp\left(\sqrt{\frac{2m_\mathrm{B}^* V_{(\mathrm{c})}}{\hbar^2} - \frac{m_\mathrm{B}^* \tilde{k}^2}{m_\mathrm{A}^*}} \, z \right) & \text{for } z < 0 \\ A_\mathrm{h} \, \mathrm{Ai}(z/\bar{\gamma} - \tilde{k}^2 \bar{\gamma}^2) & \text{for } z > 0 \end{cases} \tag{C.3}$$

with $\bar{\gamma}$ given by $\bar{\gamma} = (\hbar^2/2m_\mathrm{A}^*\gamma)^{1/3}$ and Eq. (4.23). The value of $\tilde{k}^2$ is equal to the ground state solution of equation

$$\frac{m_\mathrm{B}^*}{m_\mathrm{A}^*} \frac{\mathrm{d} \ln \mathrm{Ai}(z)}{\mathrm{d}z} \Big|_{z=-\tilde{k}^2\bar{\gamma}^2} = \frac{\bar{\kappa}_{(\mathrm{c})} \bar{\gamma}}{2} \, . \tag{C.4}$$

The latter relation follows from the matching conditions for the wavefunction and the electron flux at $z = 0$. Because the barrier height $V_{(\mathrm{c})}$ is usually large compared to the ground substate energy we have made use of the approximation $(\frac{2m_{\mathrm{B}}^{*}V_{(\mathrm{c})}}{\hbar^2}-\frac{m_{\mathrm{B}}^{*}\tilde{k}^2}{m_{\mathrm{A}}^{*}})^{1/2}\approx(\frac{2m_{\mathrm{B}}^{*}V_{(\mathrm{c})}}{\hbar^2})^{1/2}\equiv\frac{\bar{\kappa}_{(\mathrm{c})}}{2}$. Substituting (C.3) into (C.1) and using again the continuity of the wavefunction at $z=0$ we obtain for the form factor

$$|G_{11}^{\mathrm{Ai}}(q_z)|^2=\left|\frac{\bar{G}_{11}^{\mathrm{Ai}}(q_z)}{\bar{G}_{11}^{\mathrm{Ai}}(0)}\right|^2 \tag{C.5}$$

with

$$\bar{G}_{11}^{\mathrm{Ai}}(q)=\frac{\mathrm{Ai}^2(-\tilde{k}^2\bar{\gamma}^2)}{\bar{\kappa}_{(\mathrm{c})}-iq}+\int\limits_0^\infty \mathrm{d}z\,\mathrm{Ai}^2\big(\frac{z}{\bar{\gamma}}-\tilde{k}^2\bar{\gamma}^2\big)e^{-iqz}\ . \tag{C.6}$$

The function $\bar{G}_{11}^{\mathrm{Ai}}(q)$ has to be evaluated numerically for each $q=q_z$. The corresponding equation for the form factor is

$$g_{11}^{11\,\mathrm{Ai}}(q_\parallel)=\frac{\bar{g}_{11}^{11\,\mathrm{Ai}}(q_\parallel)}{\bar{g}_{11}^{11\,\mathrm{Ai}}(0)}\ , \tag{C.7}$$

where after some transformation

$$\begin{aligned}\bar{g}_{11}^{11\,\mathrm{Ai}}(q)=&\frac{\mathrm{Ai}^4\big(-\tilde{k}^2\bar{\gamma}^2\big)}{\bar{\kappa}_{(\mathrm{c})}(\bar{\kappa}_{(\mathrm{c})}+q)}+\frac{2\mathrm{Ai}^2\big(-\tilde{k}^2\bar{\gamma}^2\big)}{\bar{\kappa}_{(\mathrm{c})}+q}\int\limits_0^\infty \mathrm{d}z\,\mathrm{Ai}^2\big(\frac{z}{\bar{\gamma}}-\tilde{k}^2\bar{\gamma}^2\big)e^{-qz}\\ &+2\int\limits_0^{\pi/4}\mathrm{d}\alpha\int\limits_0^\infty \mathrm{d}z z\,\mathrm{Ai}^2\big(\frac{z}{\bar{\gamma}}\cos\alpha-\tilde{k}^2\bar{\gamma}^2\big)\mathrm{Ai}^2\big(\frac{z}{\bar{\gamma}}\sin\alpha-\tilde{k}^2\bar{\gamma}^2\big)e^{-qz(\cos\alpha-\sin\alpha)}\ .\end{aligned} \tag{C.8}$$

Above equations simplify with the assumption of an infinite barrier. Now $\tilde{k}^2$ is determined by the condition that the Airy function vanishes at $z=0$, i.e. $\mathrm{Ai}(-\tilde{k}^2\bar{\gamma}^2)=0$. Thus $\bar{G}_{11}^{\mathrm{Ai}}(q)$ and $\bar{g}_{11}^{11\,\mathrm{Ai}}(q)$ reduce to

$$\bar{G}_{11}^{\mathrm{Ai}}(q)=\int\limits_0^\infty \mathrm{d}z\,\mathrm{Ai}^2\big(\frac{z}{\bar{\gamma}}-\tilde{k}^2\bar{\gamma}^2\big)e^{-iqz} \tag{C.9}$$

and

$$\bar{g}_{11}^{11\,\mathrm{Ai}}(q)=2\int\limits_0^{\pi/4}\mathrm{d}\alpha\int\limits_0^\infty \mathrm{d}z z\,\mathrm{Ai}^2\big(\frac{z}{\bar{\gamma}}\cos\alpha-\tilde{k}^2\bar{\gamma}^2\big)\mathrm{Ai}^2\big(\frac{z}{\bar{\gamma}}\sin\alpha-\tilde{k}^2\bar{\gamma}^2\big)e^{-qz(\cos\alpha-\sin\alpha)}\ . \tag{C.10}$$

The use of Fang-Howard or modified Fang-Howard trial functions is an easier alternative and sufficient for some applications. It has the advantage of analytic expressions for the overlap integral and the form factor. With the result of (4.28)

$$\varphi^{\mathrm{FH}}_{(\mathrm{c})_1}(z) = \left\{ \begin{array}{ll} B'_{\mathrm{h}} e^{\bar{\kappa}_{(\mathrm{c})} z/2} & \text{for } z < 0 \\ A'_{\mathrm{h}} (z - z_0) e^{-z/2b} & \text{for } z \geq 0 \end{array} \right. \tag{C.11}$$

the calculation for the squared overlap integral yields

$$\begin{aligned} |G^{\mathrm{FH}}_{11}(q_z)|^2 = & \frac{1}{\left(1+(q_z b)^2\right)^3} \, \frac{1}{1+\left(\frac{q_z}{\bar{\kappa}_{(\mathrm{c})}}\right)^2} \cdot \\ & \left\{ \left(1 + \frac{(q_z b)^2 b\bar{\kappa}_{(\mathrm{c})} (\frac{m^*_{\mathrm{A}}}{m^*_{\mathrm{B}}} - 1)}{1 + 2b\bar{\kappa}_{(\mathrm{c})} + \frac{m^*_{\mathrm{A}}}{m^*_{\mathrm{B}}} b^2 \bar{\kappa}^2_{(\mathrm{c})} + \frac{b\bar{\kappa}_{(\mathrm{c})}}{2} (1 + \frac{m^*_{\mathrm{A}}}{m^*_{\mathrm{B}}} b\bar{\kappa}_{(\mathrm{c})})^2} \right)^2 \right. \\ & \left. + (q_z b)^2 \left(1 - \frac{b\bar{\kappa}_{(\mathrm{c})} (\frac{m^*_{\mathrm{A}}}{m^*_{\mathrm{B}}} - 1) + \frac{1}{2}(1 + b\bar{\kappa}_{(\mathrm{c})})(1 + \frac{m^*_{\mathrm{A}}}{m^*_{\mathrm{B}}} b\bar{\kappa}_{(\mathrm{c})})^2}{1 + 2b\bar{\kappa}_{(\mathrm{c})} + \frac{m^*_{\mathrm{A}}}{m^*_{\mathrm{B}}} b^2 \bar{\kappa}^2_{(\mathrm{c})} + \frac{b\bar{\kappa}_{(\mathrm{c})}}{2} (1 + \frac{m^*_{\mathrm{A}}}{m^*_{\mathrm{B}}} b\bar{\kappa}_{(\mathrm{c})})^2} \right)^2 \right\} . \end{aligned} \tag{C.12}$$

The trial parameter b has to be determined by the minimum condition of the ground state energy.

In the infinite barrier case ($\bar{\kappa}_{(\mathrm{c})} \to \infty$) the term inside the curly braces is equal to 1 and we reproduce the known formula of the overlap integral for a heterojunction with infinitely high barrier

$$|G^{\mathrm{FH}}_{11}(q_z)|^2 = \frac{1}{\left[1+(q_z b)^2\right]^3} . \tag{C.13}$$

The corresponding result for the form factor is

$$g^{11\,\mathrm{FH}}_{11}(q_\parallel) = \frac{1}{\left(1+q_\parallel b\right)^3} \left\{ 1 + \frac{3}{8} q_\parallel b \, (3 + q_\parallel b) \right\} . \tag{C.14}$$

C.1.2 Quantum wells

In a quantum well of width L_{A} the z-component of the envelope function for the electron ground substate is according to (4.34) equal to

$$\varphi_{(\mathrm{c})}(z) = \left\{ \begin{array}{lll} A \cos(k_{\mathrm{A}} z) & \text{if} & |z| < L_{\mathrm{A}}/2 \\ B e^{-\kappa_{(\mathrm{c})}(|z| - L_{\mathrm{A}}/2)} & \text{if} & |z| \geq L_{\mathrm{A}}/2 \end{array} \right. . \tag{C.15}$$

Substitution of this wavefunction into (C.1) and integration over z lead to the overlap integral for a finite potential well

$$|\,G_{11}(q_z)|^2 = \left\{ \frac{\sin(k_\mathrm{A}L_\mathrm{A})\cos\frac{q_zL_\mathrm{A}}{2} + \big(\frac{2k_\mathrm{A}}{q_z} - \frac{q_z}{k_\mathrm{A}}\cos^2\frac{k_\mathrm{A}L_\mathrm{A}}{2}\big)\sin\frac{q_zL_\mathrm{A}}{2}}{\big[k_\mathrm{A}L_\mathrm{A} + \frac{k_\mathrm{A}}{\kappa_{(\mathrm{c})}} + \sin(k_\mathrm{A}L_\mathrm{A}) + \frac{k_\mathrm{A}}{\kappa_{(\mathrm{c})}}\cos(k_\mathrm{A}L_\mathrm{A})\big]\big[1-(\frac{q_z}{2k_\mathrm{A}})^2\big]} + \frac{\frac{k_\mathrm{A}}{\kappa_{(\mathrm{c})}}\cos^2\frac{k_\mathrm{A}L_\mathrm{A}}{2}\big(2\cos\frac{q_zL_\mathrm{A}}{2} - \frac{q_z}{\kappa_{(\mathrm{c})}}\sin\frac{q_zL_\mathrm{A}}{2}\big)}{\big[k_\mathrm{A}L_\mathrm{A} + \frac{k_\mathrm{A}}{\kappa_{(\mathrm{c})}} + \sin(k_\mathrm{A}L_\mathrm{A}) + \frac{k_\mathrm{A}}{\kappa_{(\mathrm{c})}}\cos(k_\mathrm{A}L_\mathrm{A})\big]\big[1+(\frac{q_z}{2\kappa_{(\mathrm{c})}})^2\big]} \right\}^2, \tag{C.16}$$

where k_A follows from condition (4.37).

For an infinite potential well it is $k_\mathrm{A} = \pi/L_\mathrm{A}$ and $\kappa_{(\mathrm{c})} \to \infty$. The expressions become simpler and we obtain for the squared overlap integral

$$|\,G_{11}(q_z)|^2 = \left[\frac{\pi^2}{\pi^2 - (\frac{q_zL_\mathrm{A}}{2})^2}\right]^2 \cdot \left[\frac{\sin\frac{q_zL_\mathrm{A}}{2}}{\frac{q_zL_\mathrm{A}}{2}}\right]^2 \tag{C.17}$$

and for the form factor

$$g_{11}^{11}(q_\|) = \left(\frac{\pi^2}{\pi^2 + (\frac{q_\|L_\mathrm{A}}{2})^2}\right)^2 \left\{\frac{2(e^{-q_\|L_\mathrm{A}}-1)}{(q_\|L_\mathrm{A})^2} + \frac{2}{q_\|L_\mathrm{A}} + \frac{q_\|L_\mathrm{A}}{4\pi^2}\left(5+3\frac{(q_\|L_\mathrm{A})^2}{4\pi^2}\right)\right\} \tag{C.18}$$

(cf. also Ridley, 1997). We note that $|G_{11}(q_z)|^2$ and $g_{11}^{11}(q_\|)$ go to unity as L_A goes to zero. Thus both functions are unity for a strictly 2D system.

C.2 Quasi one-dimensional systems

Finally, we want to determine the wavevector dependence of the squared overlap integral (B.41)

$$\begin{aligned} |\,G_{nn'}^{11}(q_z,q_x)|^2 &= \left|\iint \mathrm{d}z\mathrm{d}x\,\varphi_1^*(z)e^{-iq_zz}\varphi_1(z)\,\phi_n^*(x)e^{-iq_xx}\phi_{n'}(x)\right|^2 \\ &= |\,G_{11}(q_z)|^2 \cdot |\,I_{nn'}(q_x)|^2 \end{aligned} \tag{C.19}$$

and the form factor (B.46)

$$\begin{aligned} \hat{g}_{n_1n_2}^{n'n}(q) &= \iiiint \mathrm{d}z\mathrm{d}z'\mathrm{d}x\mathrm{d}x'\,|\varphi_1(z)|^2|\varphi_1(z')|^2\phi_{n'}^*(x)\phi_n(x)\phi_{n_1}^*(x')\phi_{n_2}(x') \\ &\times\ \mathrm{K}_0\left(q\sqrt{(z-z')^2+(x-x')^2}\right) \end{aligned} \tag{C.20}$$

for a quasi-1D electron system with multi-populated subbands. Due to the different confinement in growth and lateral direction, we have introduced the notation

$$I_{nn'}(q_x) = \int_{-\infty}^{\infty} \mathrm{d}x\,\phi_n^*(x)e^{-iq_xx}\phi_{n'}(x) \tag{C.21}$$

in (C.19) to distinguish this overlap integral from the overlap integral in z-direction (note, $I_{nn'}(q_x)$ is identical to the function $I_{nn'}(q_x,0,0)$ defined in Appendix B.1.1). With the help of the transformation for the modified Bessel function

$$K_0(a\sqrt{x^2+z^2}) = \frac{1}{2\pi}\int\limits_{-\infty}^{\infty}\mathrm{d}q_x\int\limits_{-\infty}^{\infty}\mathrm{d}q_z\frac{e^{i(q_x x+q_z z)}}{a^2+q_x^2+q_z^2} = \frac{1}{2}\int\limits_{-\infty}^{\infty}\mathrm{d}q_x\frac{e^{iq_x x}e^{-\sqrt{a^2+q_x^2}|z|}}{\sqrt{a^2+q_x^2}} \tag{C.22}$$

and the definition (C.2) for the form factor g_{11}^{11} of a quasi-2D system we derive a new expression for the form factor $\hat{g}_{n_1n_2}^{n'n}$ of a quasi-1D electron system

$$\hat{g}_{n_1n_2}^{n'n}(q) = \frac{1}{2}\int\limits_{-\infty}^{\infty}\mathrm{d}q_x\frac{I_{nn'}(q_x)I_{n_1n_2}(-q_x)}{\sqrt{q^2+q_x^2}}\;g_{11}^{11}(\sqrt{q^2+q_x^2})\;. \tag{C.23}$$

In the previous section, see Eqs. (C.14) and (C.18), we have already determined the functional dependence of $g_{11}^{11}(q)$ for common confinement potentials. Thus expression (C.23) allows a very effective calculation of form factors with different subband indices.

In the case that a single heterojunction with infinitely high barrier serves as the 2D basis of our quasi-1D system we find for the overlap integral

$$|\,G_{nn'}^{11}(q_z,q_x)|^2 = \frac{|\,I_{nn'}(q_x)|^2}{\left(1+(q_zb)^2\right)^3} \tag{C.24}$$

and for the form factor

$$\hat{g}_{n_1n_2}^{n'n}(q) = \frac{1}{2}\int\limits_{-\infty}^{\infty}\frac{\mathrm{d}q_x\;I_{nn'}(q_x)I_{n_1n_2}(-q_x)}{\sqrt{q_x^2+q^2}\left(1+b\sqrt{q_x^2+q^2}\right)^3}\left\{1+\frac{3}{8}b\sqrt{q_x^2+q^2}\left(3+b\sqrt{q_x^2+q^2}\;\right)\right\}. \tag{C.25}$$

For the lateral confinement of the quantum wire we first consider a parabolic potential, namely $V(x)=\frac{\hbar^2}{2m^*}\frac{x^2}{w^4}$. Then the functions $\phi_n(x)$ are eigenfunctions of a harmonic oscillator (see Eq. (4.46)). Thus the integral $I_{nn'}(q_x)$ is equal to

$$I_{nn'}(q_x) = \sqrt{\frac{(s'-1)!}{(s-1)!}}\left(\frac{wq_x}{i\sqrt{2}}\right)^{s-s'}e^{-(\frac{wq_x}{2})^2}\;L_{s'-1}^{s-s'}(\frac{w^2q_x^2}{2}) \tag{C.26}$$

with $s=\max(n,n')$, $s'=\min(n,n')$ and $L_{s'}^{s}(x)$ as associated Laguerre polynomial (see Eq. (B.20)). Substituting (C.26) into (C.24) we obtain the following analytic expression for the squared overlap integral

$$|G_{nn'}^{11}(q_z,q_x)|^2 = \left(\frac{1}{1+(q_zb)^2}\right)^3\frac{(s'-1)!}{(s-1)!}\left(\frac{q_x^2w^2}{2}\right)^{s-s'}e^{-\frac{q_x^2w^2}{2}}\left[L_{s'-1}^{s-s'}(\frac{q_x^2w^2}{2})\right]^2, \tag{C.27}$$

where $G^{11}_{nn'}(q_z, q_x) = G^{11}_{n'n}(q_z, q_x)$ holds. Explicitly we get for the lowest subbands

$$\begin{aligned}
|\,G^{11}_{11}(q_z,q_x)|^2 &= \frac{e^{-q_x^2 w^2/2}}{\big(1+(q_z b)^2\big)^3}\,, \quad |\,G^{11}_{22}(q_z,q_x)|^2 = \frac{\big(1-\frac{q_x^2 w^2}{2}\big)^2 e^{-q_x^2 w^2/2}}{\big(1+(q_z b)^2\big)^3}\,, \\
|\,G^{11}_{21}(q_z,q_x)|^2 &= \frac{\frac{q_x^2 w^2}{2}\; e^{-q_x^2 w^2/2}}{\big(1+(q_z b)^2\big)^3}\,, \quad |\,G^{11}_{31}(q_z,q_x)|^2 = \frac{\big(\frac{q_x^2 w^2}{2}\big)^2\; e^{-q_x^2 w^2/2}}{2\big(1+(q_z b)^2\big)^3}\,, \\
|\,G^{11}_{32}(q_z,q_x)|^2 &= \frac{\frac{q_x^2 w^2}{2}\,\big(2-\frac{q_x^2 w^2}{2}\big)^2\; e^{-q_x^2 w^2/2}}{2\big(1+(q_z b)^2\big)^3}\,.
\end{aligned} \tag{C.28}$$

For the form factor one has to perform the numerical integration of

$$\hat{g}^{n'n}_{n_1 n_2}(q) = \int_0^\infty \mathrm{d}q_x \frac{1+\frac{3}{8}\,b\sqrt{q_x^2+q^2}\,\big(3+b\sqrt{q_x^2+q^2}\,\big)}{\sqrt{q_x^2+q^2}\,\big(1+b\sqrt{q_x^2+q^2}\,\big)^3}\; A^{n'n}_{n_1 n_2}\Big(\frac{q_x^2 w^2}{2}\Big) \tag{C.29}$$

with

$$\begin{array}{lll}
A^{11}_{11}(t) = e^{-t}\,, & A^{22}_{11}(t) = (1-t)e^{-t}\,, & A^{13}_{11}(t) = -\frac{1}{\sqrt{2}}\,te^{-t}\,, \\
A^{12}_{12}(t) = te^{-t}\,, & A^{23}_{12}(t) = -\frac{1}{\sqrt{2}}\,t(2-t)e^{-t}\,, & A^{13}_{13}(t) = \frac{1}{2}t^2 e^{-t}\,, \\
A^{22}_{13}(t) = -\frac{1}{\sqrt{2}}\,t(1-t)e^{-t}\,, & A^{22}_{22}(t) = (1-t)^2 e^{-t}\,, & A^{23}_{23}(t) = \frac{1}{2}\,t(2-t)^2 e^{-t}\,, \\
\ldots & &
\end{array} \tag{C.30}$$

The form factor $\hat{g}^{n'n}_{n_1 n_2}(q)$ vanishes if $n_1 + n_2 + n + n'$ is odd. From symmetry arguments it follows $\hat{g}^{n'n}_{n_1 n_2}(q) = \hat{g}^{n'n}_{n_2 n_1}(q) = \hat{g}^{n_1 n_2}_{n'n}(q)$.

As a second model for the lateral confinement of a quantum wire we have discussed in Section 4.1.3 the rectangular well potential. In this case the functions $\phi_n(x)$ are harmonic waves restricted to a region of width $2w$ (see Eq. (4.45)). This yields

$$I_{nn'}(q_x) = \frac{i\pi^2 nn'\, q_x w\,[1 \mp e^{-i2q_x w}]/2}{[(q_x w)^2 - (\frac{\pi(n+n')}{2})^2][(q_x w)^2 - (\frac{\pi(n-n')}{2})^2]}\,, \tag{C.31}$$

where the upper (lower) sign is valid for $n + n' =$ even (odd). Therefore the corresponding result for the squared overlap integral is

$$|G^{11}_{nn'}(q_z, q_x)|^2 = \left(\frac{1}{1+(q_z b)^2}\right)^3 \left(\frac{\pi^2 nn'(q_x w)\sin(wq_x + \frac{\pi}{2}(n+n'))}{[(q_x w)^2 - (\frac{\pi(n+n')}{2})^2][(q_x w)^2 - (\frac{\pi(n-n')}{2})^2]}\right)^2 . \tag{C.32}$$

Bibliography

Abramowitz, M., and I. A. Stegun (eds.), 1972, *Handbook of Mathematical Functions* (U. S. GPO).

Adachi, S., 1994, *GaAs and Related Materials* (World Scientific).

Akimov, A. V., S. A. Basun, A. A. Kaplyanskii, V. A. Rachin, and R. A. Titov, 1977, JETP Lett. **25**(10), 461.

Akimov, A. V., L. J. Challis, and C. J. Mellor, 1991, Physica B **169**(1–4), 563.

Akimov, A. V., A. A. Kaplyaanskii, and E. S. Moskalenko, 1994, in *Die Kunst of Phonons*, edited by T. Paszkiewicz and K. Rapcewicz (Plenum Press, New York), pp. 113–128.

Akimov, A. V., A. V. Scherbakov, A. L. Zhmodikov, V. P. Kochereshko, D. R. Yakovlev, W. Ossau, and G. Landwehr, 1997, Phys. Rev. B **56**(19), 12100.

Al Jawhari, H., A. G. Kozorezov, M. Sahraoui-Tahar, J. K. Wigmore, and C. D. W. Wilkinson, 1999, Physica B **263–264**, 211.

Alcalde, A. M., G. E. Marques, G. Weber, and T. L. Reinecke, 2000, Solid State Commun. **116**(5), 247.

Altarelli, M., 1983, Phys. Rev. B **28**(2), 842.

Ando, T., A. B. Fowler, and F. Stern, 1982, Reviews of Modern Physics **54**(2), 437.

Ando, T., and Y. Uemura, 1974, J Phys. Soc. Japan **36**, 959.

Apalkov, V. M., and M. E. Portnoi, 2002, Phys. Rev. B **66**, 121303(R).

Asche, M., R. Hey, H. Kostial, B. Danilchenko, A. Klimashov, and S. Roshko, 1995, Phys. Rev. B **51**(12), 7966.

Askerov, B. M., 1994, *Electron Transport Phenomena in Semiconductors* (World Scientific).

Auld, B. A., 1973, *Acoustic Waves and Fields in Solids,* Vol. 1 (Wiley, New York).

Bai, X., C. Kurdak, S. Krishna, and P. Bhattacharya, 2002, Physica B **316–317**, 362.

Balkan, N. (ed.), 1998, *Hot Electrons in Semiconductors – Physics and Devices* (Clarendon Press, Oxford).

Balkan, N., H. Çelik, A. J. Vickers, and M. Cankurtaran, 1995, Phys. Rev. B **52**(24), 17210.

Bardeen, J., and W. Shockley, 1950, Phys. Rev. **80**(1), 72.

Bartels, A., T. Dekorsy, H. Kurz, and K. Köhler, 1999, Phys. Rev. Lett. **82**(5), 1044.

Bastard, G., 1981, Phys. Rev. B **24**(10), 5693.

Bastard, G., 1992, *Wave Mechanics Applied to Semiconductor Heterostructures* (Les Ed. de Physique, Les Ulis).

Bastard, G., J. Brum, and R. Ferreira, 1991, *Solid State Physics: Advances in Research and Applications,* Vol. 44 (Academic, Boston), p. 229.

Baumberg, J. J., D. A. Williams, and K. Köhler, 1997, Phys. Rev. Lett. **78**(17), 3358.

BenDaniel, D. J., and C. B. Duke, 1966, Phys. Rev. **152**(2), 683.

Benedict, K. A., 1991, J. Phys.: Condens. Matter **3**(10), 1279.

Benedict, K. A., and R. K. Hills, 2001, Phys. Rev. B **63**, 235304.

Benedict, K. A., R. K. Hills, and C. J. Mellor, 1999, Phys. Rev. B **60**(15), 10984.

Berberich, P., R. Buemann, and H. Kinder, 1982, Phys. Rev. Lett. **49**(20), 1500.

Bir, G. L., and G. E. Pikus, 1960, Fiz. Tverd. Tela **2**, 2287.

Bir, G. L., and G. E. Pikus, 1972, *Simmetrija i deformacionnye effekty v poluprovodnikach* (Nauka, Moskva).

Blakemore, J. S., 1982, J. Appl. Phys. **53**(10), R123.

Blencowe, M., and A. Shik, 1996, Phys. Rev. B **54**(19), 13899.

Blencowe, M., and A. Shik, 1999, Physica B **263–264**, 504.

Broido, D. A., and L. J. Sham, 1985, Phys. Rev. B **31**(2), 888.

Bron, W. E., 1980, Rep. Prog. Phys. **43**(3), 301.

Bron, W. E., Y. B. Levinson, and J. M. O'Connor, 1982, Phys. Rev. Lett. **49**(3), 209.

Buckel, W., 1990, *Supraleitung* (VCH, Weinheim), 4th edition.

Burt, M. G., 1988a, Semicond. Sci. Technol. **3**(8), 739.

Burt, M. G., 1988b, Semicond. Sci. Technol. **3**(12), 1224.

Butcher, P., 1993, in *Physics of Low–Dimensional Semiconductor Structures*, edited by P. Butcher, N. H. March, and M. P. Tosi (Plenum Press), pp. 95–176.

Cai, W., M. C. Marchetti, and M. Lax, 1987, Phys. Rev. B **35**(3), 1369.

Cavill, S. A., L. J. Challis, A. J. Kent, F. F. Ouali, A. V. Akimov, and M. Henini, 2002, Phys. Rev. B **66**, 235320.

Çelik, H., M. Cankurtaran, N. Balkan, and A. Bayrakli, 2002, Semicond. Sci. Technol. **17**(1), 18.

Challis, L. (ed.), 2003, *Electron-Phonon Interactions in Low-Dimensional Structures* (Oxford University Press).

Challis, L. J., and A. J. Kent, 1994, in *Die Kunst of Phonons*, edited by T. Paszkiewicz and K. Rapcewicz (Plenum Press, New York), pp. 159–187.

Challis, L. J., A. J. Kent, and V. W. Rampton, 1990, Semicond. Sci. Technol. **5**(12), 1179.

Challis, L. J., G. A. Toombs, and F. W. Sheard, 1987, in *Physics of Phonons*, edited by T. Paszkiewicz (Springer, Berlin), Lecture Notes in Physics, Vol. 285, pp. 348–374.

Chin, M. A., V. Narayanamurti, H. L. Störmer, and A. C. Gossard, 1985, in *Proc. 17th Int. Conf. on Physics of Semiconductors*, edited by J. D. Chadi and W. A. Harrison (Springer, Berlin), pp. 333–336.

Chin, M. A., V. Narayanamurti, H. L. Störmer, and J. C. M. Hwang, 1984, in *Phonon Scattering in Condensed Matter*, edited by W. Eisenmenger, K. Lassman, and S. Döttinger (Springer, Berlin), Springer Series in Solid-State Sciences, Vol. 51, p. 328.

Conwell, E. M., 1967, *High Field Transport in Semiconductors* (Academic Press, New York).

Cooper, J., F. F. Quali, L. J. Challis, and C. J. Mellor, 1995, Phys. Rev. B **51**(11), 7085.

Cooper, J., S. Roshko, W. Dietsche, Y. Kershaw, and U. Wenschuh, 1994, Phys. Rev. Lett. **50**(12), 8352.

Cottam, R. I., and G. A. Saunders, 1973, J. Phys. C: Solid State Phys. **6**(13), 2105.

Cross, A. J., 2001, *Electron-Phonon Interaction in GaAs/AlGaAs Quantum Wells*, Ph.D. thesis, University of Nottingham.

Cross, A. J., A. J. Kent, P. Hawker, D. Lehmann, C. Jasiukiewicz, and M. Henini, 1999, Physica B **263–264**, 526.

Damen, E. P. N., A. F. M. Arts, and H. W. de Wijn, 1995, Phys. Rev. Lett. **74**(21), 4249.

Damen, E. P. N., D. J. Dieleman, A. F. M. Arts, and H. W. de Wijn, 2001, Phys. Rev. B **64**(17), 174303.

Danilchenko, B., D. Kazakovtsev, and I. Obukhov, 1994a, Zh. Eksp. Teor. Fiz. **106**(5), 1439.

Danilchenko, B., A. Klimashov, S. Roshko, and M. Asche, 1994b, Phys. Rev. B **50**(8), 5725.

Danilchenko, B., A. Klimashov, S. Roshko, M. Asche, R. Hey, and H. Kostial, 1994c, J. Phys.: Condens. Matter **6**(39), 7955.

Danilchenko, B. A., W. M. Gancza, C. Jasiukiewicz, and T. Paszkiewicz, 1999, Phys. Rev. B **60**(8), 6113.

Danilchenko, B. A., C. Jasiukiewicz, T. Paszkiewicz, and S. Wolski, 2004, Eur. Phys. J.-Appl. Phys. **26**(3), 151.

Das Sarma, S., V. B. Campos, M. A. Stroscio, and K. W. Kim, 1992, Semicond. Sci. Technol. **7**(3B), B60.

Das Sarma, S., J. K. Jain, and R. Jalabert, 1988a, Phys. Rev. B **37**(9), 4560.

Das Sarma, S., J. K. Jain, and R. Jalabert, 1988b, Phys. Rev. B **37**(3), 1228.

Das Sarma, S., J. K. Jain, and R. Jalabert, 1988c, Phys. Rev. B **37**(11), 6290.

Das Sarma, S., J. K. Jain, and R. Jalabert, 1990, Phys. Rev. B **41**(6), 3561.

Devitt, A. M., S. H. Roshko, A. J. Kent, K. A. Benedict, C. J. Mellor, and M. Henini, 2002, Physica B **316–317**, 101.

Devitt, A. M., S. H. Roshko, U. Zeitler, C. J. Mellor, A. J. Kent, K. A. Benedict, T. Cheng, and M. Henini, 2000, Physica E **6**(1–4), 47.

Dietsche, W., 1978, Phys. Rev. Lett. **40**(12), 786.

Dietsche, W., S. J. Kirch, and J. P. Wolfe, 1982, Phys. Rev. B **26**(2), 780.

Dietsche, W., G. A. Northrop, and J. P. Wolfe, 1981, Phys. Rev. Lett. **47**(9), 660.

Dietzel, F., W. Dietsche, and K. Ploog, 1993, Phys. Rev. B **48**(7), 4713.

Dietzel, F., U. Klass, W. Dietsche, and K. Ploog, 1994, in *Die Kunst of Phonons*, edited by T. Paszkiewicz and K. Rapcewicz (Plenum Press, New York), pp. 189–200.

Dingle, R., H. L. Störmer, A. C. Gossard, and W. Wiegmann, 1978, Appl. Phys. Lett. **33**, 665.

Edwards, S. C., Hamid bin Rani, and J. K. Wigmore, 1989, J. Phys. E: Scientific Instruments **22**, 582.

Eichele, R., R. P. Hübener, and H. Seifert, 1982, Z. Phys. B – Condensed Matter **48**, 89.

Eisenmenger, W., 1980, in *Proc. 3rd Int. Conf. on Phonon Physics in Condensed Matter*, edited by H. J. Marris (Plenum Press, New York), p. 303.

Eisenmenger, W., and A. H. Dayem, 1967, Phys. Rev. Lett. **18**(4), 125.

Eisenstein, J. P., V. Narayanamurti, H. L. Störmer, A. Y. Cho, and J. C. M. Hwang, 1986, in *Phonon Scattering in Condensed Matter*, edited by A. C. Anderson and J. P. Wolfe (Springer, Berlin), pp. 401–403.

Eisenstein, J. P., H. L. Störmer, V. Narayanamurti, A. C. Gossard, and W. Wiegmann, 1984, Phys. Rev. Lett. **53**(27), 2579.

Ekenberg, U., 1989, Phys. Rev. B **40**(11), 7714.

Ekenberg, U., and M. Altarelli, 1984, Phys. Rev. B **30**(6), 3569.

Esaki, L., and R. Tsu, 1970, IBM J. Dev. **14**, 61.

Every, A. G., 1980, Phys. Rev. B **22**(4), 1746.

Every, A. G., 1981, Phys. Rev. B **24**(6), 3456.

Every, A. G., K. Y. Kim, and W. Sachse, 1994, in *Die Kunst of Phonons*, edited by T. Paszkiewicz and K. Rapcewicz (Plenum Press, New York), pp. 73–85.

Every, A. G., G. L. Koos, and J. P. Wolfe, 1984, Phys. Rev. B **29**(4), 2190.

Every, A. G., and A. K. McCurdy, 1987, Phys. Rev. B **36**(3), 1432.

Every, A. G., and A. J. Stoddart, 1985, Phys. Rev. B **32**(2), 1319.

Falko, V. I., and L. J. Challis, 1993, J. Phys.: Condens. Matter **5**, 3945.

Falko, V. I., and S. V. Iordanskii, 1992, J. Phys.: Condens. Matter **4**, 9201.

Fang, F. F., and W. E. Howard, 1966, Phys. Rev. Lett. **16**, 797.

Fick, E., and G. Sauermann, 1990, *The Quantum Statistics of Dynamic Processes*, Springer Series in Solid-State Sciences (Springer, Berlin).

Fletcher, R., M. D'Iorio, A. S. Sachrajda, R. Stoner, C. T. Foxon, and J. J. Harris, 1988, Phys. Rev. B **37**, 3137.

Fröhlich, H., 1937, Proc. Roy. Soc A **160**, 230.

Gańcza, W. M., C. Jasiukiewicz, A. J. Kent, D. Lehmann, T. Paszkiewicz, K. R. Strickland, and R. E. Strickland, 1996, Semicond. Sci. Technol. **11**, 1030.

Gańcza, W. M., I. A. Obukhov, T. Paszkiewicz, and B. A. Danilchenko, 2001, Comp. Meth. Sci. Technol. **7**(2), 7.

Gańcza, W. M., and T. Paszkiewicz, 1995, Comput. Phys. Commun. **85**(3), 423.

George, R. E., K. R. Strickland, and A. J. Kent, 1995, in *Proceedings of the 22nd International Conference on the Physics of Semiconductors*, edited by D. J. Lockwood (World Scientific, Singapore), pp. 899–902.

Giltrow, M., A. Kozorezov, M. Sahraoui-Tahar, J. K. Wigmore, J. H. Davies, C. R. Stanley, B. Vogel, and C. D. W. Wilkinson, 1995, Phys. Rev. Lett. **75**(9), 1827.

Glavin, B. A., V. A. Kochelap, and T. L. Linnik, 1999, Appl. Phys. Lett. **74**(23), 3525.

Glavin, B. A., V. A. Kochelap, T. L. Linnik, K. W. Kim, and M. A. Stroscio, 2002, Phys. Rev. B **65**, 085303.

Gorczyca, I., T. Suski, E. Litwin-Staszewska, L. Dmowski, J. Krupski, and B. Etienne, 1992, Phys. Rev. B **46**(7), 4328.

Greipel, K., and U. Rössler, 1992, Semicond. Sci. Technol. **7**(4), 487.

Gösele, U., Y. Bluhm, G. Kästner, P. Kopperschmidt, G. Kräuter, R. Scholz, A. Schumacher, S. Senz, Q.-Y. Tong, L.-J. Huang, Y.-L. Chao, and T. H. Lee, 1999, J. Vac. Sci. Technol. A **17**(4), 1145.

Gurevich, L. E., 1946, Zh. Eksp. Teor. Fiz. **16**, 193.

Gurevich, Y. G., and O. L. Mashkevich, 1989, Physics Reports **181**(6), 327.

Hauser, M. R., R. Gaitskell, and J. P. Wolfe, 1999, Phys. Rev. B **60**(5), 3072.

Hawker, P., A. J. Kent, L. J. Challis, A. Bartels, T. Dekorsy, H. Kurz, and K. Köhler, 2000, Appl. Phys. Lett. **77**(20), 3209.

Hawker, P., A. J. Kent, N. Hauser, and C. Jagadish, 1995, Semicond. Sci. Technol. **10**(5), 601.

Hawker, P., A. J. Kent, O. H. Hughes, and L. J. Challis, 1992, Semicond. Sci. Technol. **7**(B3), B29.

Hayden, R. K., L. Eaves, M. Henini, E. C. Valadares, O. Kühn, D. K. Maude, J. C. Portal, T. Takamasu, N. Miura, and U. Ekenberg, 1994, Semicond. Sci. Technol. **9**, 298.

Hebboul, S. E., and J. P. Wolfe, 1989, Z. Phys. B – Condensed Matter **73**, 437.

Held, E., W. Klein, and R. P. Hübener, 1989a, Z. Phys. B – Condensed Matter **75**, 17.

Held, E., W. Klein, and R. P. Hübener, 1989b, Z. Phys. B – Condensed Matter **75**, 223.

Hensel, J. C., and R. Dynes, 1977, Phys. Rev. Lett. **39**(15), 969.

Hensel, J. C., R. Dynes, and D. C. Tsui, 1981, J. Phys. (Paris) Colloq. **42**(C6), 308.

Hensel, J. C., R. Dynes, and D. C. Tsui, 1983a, Phys. Rev. B **28**(2), 1124.

Hensel, J. C., B. I. Halperin, and R. Dynes, 1983b, Phys. Rev. Lett. **51**(25), 2302.

Hirakawa, K., M. Grayson, D. C. Tsui, and Ç. Kurdak, 1993, Phys. Rev. B **47**(24), 16651.

Hirakawa, K., and H. Sakaki, 1986, Appl. Phys. Lett. **49**(14), 869.

Höpfel, R. A., and G. Weimann, 1985, Appl. Phys. Lett. **46**(3), 291.

Höss, C., J. P. Wolfe, and H. Kinder, 1990, Phys. Rev. Lett. **64**(10), 1134.

Houng, M.-P., Y.-C. Chang, and W. I. Wang, 1988, J. Appl. Phys. **64**(9), 4609.

Hu, G. Y., and R. F. O'Connell, 1987, Phys. Rev. B **36**(11), 5798.

Hu, G. Y., and R. F. O'Connell, 1991, J. Phys.: Condens. Matter **3**, 4633.

Huebener, R. P., 1984, Rep. Prog. Phys. **47**(2), 175.

Hurley, D. C., S. Tamura, J. P. Wolfe, and H. Morkoç, 1987, Phys. Rev. B **58**(23), 2446.

Hurley, D. C., S. Tamura, J. P. Wolfe, K. Ploog, and J. Nagle, 1988, Phys. Rev. B **37**(15), 8829.

Hutson, A. R., 1961, J. Appl. Phys. **32**, 2287.

Jasiukiewicz, C., 1998, Semicond. Sci. Technol. **13**(6), 537.

Jasiukiewicz, C., and V. Karpus, 1996, Semicond. Sci. Technol. **11**(12), 1777.

Jasiukiewicz, C., D. Lehmann, A. J. Kent, A. J. Cross, and P. Hawker, 1999, Physica B **263-264**, 183.

Jasiukiewicz, C., D. Lehmann, and T. Paszkiewicz, 1991, Z. Phys. B – Condensed Matter **84**, 73.

Jasiukiewicz, C., D. Lehmann, and T. Paszkiewicz, 1992, Z. Phys. B – Condensed Matter **86**, 225.

Jasiukiewicz, C., D. Lehmann, and T. Paszkiewicz, 1996, Acta Physica Polonica **90**(4), 829.

Jasiukiewicz, C., T. Paszkiewicz, and D. Lehmann, 1994, Z. Phys. B – Condensed Matter **96**, 213.

Karl, H., W. Dietsche, A. Fischer, and K. Ploog, 1988, Phys. Rev. Lett. **61**(20), 2360.

Karpus, V., 1986, Sov. Phys.-Semicond. **20**, 6.

Karpus, V., 1988, Sov. Phys.-Semicond. **22**, 268.

Kawamura, T., and S. Das Sarma, 1992, Phys. Rev. B **45**(7), 3612.

Kawamura, T., S. Das Sarma, R. Jalabert, and J. K. Jain, 1990, Phys. Rev. B **42**(8), 5407.

Kazakovtsev, D. V., and I. V. Levinson, 1978, Pis'ma Zh. Eksp. Teor. Fiz. **27**(3), 194.

Kazakovtsev, D. V., and I. V. Levinson, 1987, in *Physics of Phonons*, edited by T. Paszkiewicz (Springer, Berlin), Lecture Notes in Physics 285, pp. 276–289.

Kelly, M. J., 1995, *Low-Dimensional Semiconductors*, Series on Semiconductor Science and Technology, Vol. 3 (Oxford University Press).

Kelsall, R. W., R. I. Taylor, A. C. G. Wood, and R. A. Abram, 1990, Semicond. Sci. Technol. **5**, 877.

Kent, A. J., A. J. Cross, P. Hawker, and M. Henini, 1997a, phys. stat. sol.(b) **204**(1), 230.

Kent, A. J., G. A. Hardy, P. Hawker, and D. C. Hurley, 1990, in *3rd Int. Conf. on Phonon Physics*, edited by S. Hunklinger, W. Ludwig, and G. Weiss (World Scientific, Singapore).

Kent, A. J., G. A. Hardy, P. Hawker, V. W. Rampton, M. I. Newton, P. A. Russell, and L. J. Challis, 1988a, Phys. Rev. Lett. **61**(2), 180.

Kent, A. J., A. J. Naylor, P. Hawker, and M. Henini, 2000, Phys. Rev. B **61**(24), R16311.

Kent, A. J., A. J. Naylor, P. Hawker, M. Henini, and B. Bracher, 1997b, Phys. Rev. B **55**(15), 9775.

Kent, A. J., V. W. Rampton, M. I. Newton, P. J. A. Carter, G. A. Hardy, P. Hawker, P. A. Russell, and L. J. Challis, 1988b, Surf. Sci. **196**(1–3), 410.

Kent, A. J., N. M. Stanton, L. J. Challis, and M. Henini, 2002, Appl. Phys. Lett. **81**(18), 3497.

Kent, A. J., N. M. Stanton, R. N. Kini, and M. Henini, 2004, in *Ultrafast Phenomena in Semiconductors and Nanostructure Materials VIII*, edited by K.-T. Tsen, J.-J. Song, and H. Jiang, Proceedings of SPIE, Vol. 5352, pp. 231–238.

Kent, A. J., K. R. Strickland, and R. E. Strickland, 1995, Meas. Sci. Technol. **6**(12), 1679.

Kent, A. J., R. E. Strickland, K. R. Strickland, A. J. Cross, P. Hawker, and M. Henini, 1997c, Semicond. Sci. Technol. **12**(7), 849.

Kent, A. J., R. E. Strickland, K. R. Strickland, and M. Henini, 1996, Phys. Rev. B **54**(3), 2019.

Kent, A. J., and J. K. Wigmore, 2003, in *Electron-Phonon Interactions in Low-Dimensional Structures*, edited by L. Challis (Oxford University Press), pp. 5–58.

Kershaw, Y. M., S. J. Bending, W. Dietsche, and K. Eberl, 1996, Semicond. Sci. Technol. **11**(7), 1036.

Kinder, H., 1972, Phys. Rev. Lett. **28**(24), 1564.

Klemens, P. G., 1955, Proc. Phys. Soc. London **A 68**(12), 1113.

Knipp, P. A., and T. L. Reinecke, 1995a, Phys. Rev. B **52**(8), 5923.

Knipp, P. A., and T. L. Reinecke, 1995b, in *22nd International Conference on the Physics of Semiconductors*, edited by D. J. Lockwood (World Scientific), pp. 1927–1930.

Kolomenskii, A. A., and A. A. Maznev, 1993, Phys. Rev. B **48**(19), 14502.

Kozorezov, A. G., J. K. Wigmore, and M. Giltrow, 1997, J. Phys.: Condens. Matter **9**(23), 4863.

Kubakaddi, S. S., K. Suresha, and B. G. Mulimani, 2002, Semicond. Sci. Technol. **17**, 557.

Kwok, P. C., 1968, Phys. Rev. **175**(3), 1208.

Lai, W. Y., and S. Das Sarma, 1986, Phys. Rev. B **33**(12), 8874.

Laux, S. E., D. J. Frank, and F. Stern, 1988, Surf. Sci. **196**, 101.

Lawaetz, P., 1968, Phys. Rev. **174**(3), 867.

Lax, M., and V. Narayanamurti, 1980, Phys. Rev. B **22**(10), 4876.

Leburton, J. P., J. Pascual, and C. M. Sotomayor Torres (eds.), 1993, *Phonons in Semiconductor Nanostructures*, NATO ASI Series E, Vol. 236 (Kluwer Academic Publishers).

Lega, A., H. Karl, W. Dietsche, A. Fischer, and K. Ploog, 1990, Surf. Sci. **229**, 116.

Lehmann, D., 1994, in *Die Kunst of Phonons*, edited by T. Paszkiewicz and K. Rapcewicz (Plenum Press, New York), pp. 211–217.

Lehmann, D., and C. Jasiukiewicz, 1999, Tr. J. of Physics **23**(4), 583.

Lehmann, D., and C. Jasiukiewicz, 2002, Physica B **316-317**, 226.

Lehmann, D., C. Jasiukiewicz, and A. J. Kent, 1998, Physica B **249-251**, 718.

Lehmann, D., C. Jasiukiewicz, and A. J. Kent, 2000, Physica E **6**, 538.

Lehmann, D., C. Jasiukiewicz, and T. Paszkiewicz, 1997a, Acta Physica Polonica A **92**(5), 891.

Lehmann, D., C. Jasiukiewicz, R. E. Strickland, K. R. Strickland, A. J. Kent, and T. Paszkiewicz, 1996, Physica B **219-220**, 25.

Lehmann, D., A. J. Kent, C. Jasiukiewicz, A. J. Cross, P. Hawker, and M. Henini, 2002a, Phys. Rev. B **65**(8), 085320.

Lehmann, D., A. J. Kent, N. M. Stanton, A. V. Akimov, S. A. Cavill, C. Jasiukiewicz, T. S. Cheng, and C. T. Foxon, 2002b, Physica B **316-317**, 110.

Lehmann, D., A. J. Kent, R. E. Strickland, K. R. Strickland, M. Henini, C. Jasiukiewicz, and T. Paszkiewicz, 1997b, in *High Magnetic Fields in the Physics of Semiconductors II*, edited by G. Landwehr and W. Ossau (World Scientific, Singapore), pp. 379–382.

Leo, K., W. W. Rühle, and K. Ploog, 1988, Phys. Rev. B **38**(3), 1947.

Little, W. A., 1959, Can. J. Phys. **37**, 334.

Luttinger, J. M., and W. Kohn, 1955, Phys. Rev. **97**(4), 869.

Ma, Y., R. Fletcher, E. Zaremba, M. D'Iorio, C. T. Foxon, and J. J. Harris, 1991, Phys. Rev. B **43**(11), 9033.

Maris, H. J., 1971, J. Acoust. Soc. Am. **50**(pt.2, 3), 812.

Maris, H. J., 1990, Phys. Rev. B **41**(14), 9736.

Martin, T., R. Bruinsma, and P. M. Platzman, 1988, Phys. Rev. B **38**(4), 2257.

Marvin, A. M., V. Bortolani, and F. Nizzoli, 1980, J. Phys. C: Solid State Phys. **13**(2), 299.

Mayer, H., and U. Rössler, 1991, Phys. Rev. B **44**(16), 9048.

McKitterick, D. J., A. Shik, A. J. Kent, M. Henini, and H. Kinder, 1994, Phys. Rev. B **49**(4), 2585.

Meijer, H. J. G., and D. Polder, 1953, Physica **19**, 255.

Mellor, C. J., R. H. Eyles, J. E. Digby, A. J. Kent, K. A. Benedict, L. J. Challis, M. Henini, C. T. Foxon, and J. J. Harris, 1995, Phys. Rev. Lett. **74**(12), 2339.

Mellor, C. J., U. Zeitler, A. M. Devitt, S. H. Roshko, A. J. Kent, K. A. Benedict, T. Cheng, and M. Henini, 1999, Physica B **263-264**, 196.

Mendez, E. E., 1986, Surf. Sci. **170**(1–2), 561.

Meney, A. T., 1992, Superlatt. Microstruct. **11**(1), 31.

Mooradian, A., and G. B. Wright, 1966, Phys. Rev. Lett. **16**(22), 999.

Msall, M., W. Dietsche, K.-J. Friedland, and Q.-Y. Tong, 2000, Phys. Rev. Lett. **85**(3), 598.

Msall, M., and J. P. Wolfe, 2002, Phys. Rev. B **65**, 195205.

Msall, M. E., A. Klimashov, S. Kronmüller, H. Kostial, W. Dietsche, and K. Friedland, 1999, Appl. Phys. Lett. **74**(6), 821.

Msall, M. E., S. Tamura, S. E. Esipov, and J. P. Wolfe, 1993, Phys. Rev. Lett. **70**(22), 3463.

Msall, M. E., and J. P. Wolfe, 1997, Phys. Rev. B **56**(15), 9557.

Narayanamurti, V., and R. C. Dynes, 1971, Phys. Rev. Lett. **27**(7), 410.

Naylor, A. J., K. R. Strickland, A. J. Kent, and M. Henini, 1996, Surf. Sci. **362**$(1-3)$, 660.

Nishiguchi, N., 1994, Phys. Rev. B **50**(15), 10970.

Nishiguchi, N., 1995, Phys. Rev. B **52**(7), 5279.

Nishiguchi, N., 2002, Physica E **13**(1), 1.

Northrop, G. A., 1982, Phys. Rev. B **26**(2), 903.

Northrop, G. A., and J. P. Wolfe, 1979, Phys. Rev. Lett. **43**(19), 1424.

Northrop, G. A., and J. P. Wolfe, 1980, Phys. Rev. B **22**(12), 6196.

Northrop, G. A., and J. P. Wolfe, 1984, Phys. Rev. Lett. **52**(24), 2156.

Obata, H., Y. Tanaka, and S. Tamura, 2001, Phys. Rev. B **64**(11), 115430.

Oh, I.-K., and J. Singh, 2001, J. Phys.: Condens. Matter **13**, 10851.

Ouali, F., N. Zinovev, L. Challis, F. Sheard, M. Henini, D. Steenson, and K. Strickland, 1995, Phys. Rev. Lett. **75**(2), 308.

Ouali, F. F., 1998, private communication, the experimental technique is described in Ouali *et al.* (1999).

Ouali, F. F., H. R. Francis, and H. C. Rhodes, 1999, Physica B **263–264**, 239.

Paszkiewicz, T., and M. Pruchnik, 1996, Physica A **232**, 747.

Paszkiewicz, T., and M. Pruchnik, 2001, Eur. Phys. J. B **24**(1), 91.

Paszkiewicz, T., and M. Wilczynski, 1995, in *Dynamical Properties of Solids,* Vol. 7, edited by G. K. Horton and A. A. Maradudin (North-Holland).

Payne, M. C., R. A. Davies, J. C. Inkson, and M. Pepper, 1983, J. Phys. C: Solid State Phys. **16**, L291.

Petroff, P. M., A. C. Gossard, R. A. Logan, and W. Wiegmann, 1982, Appl. Phys. Lett. **41**(7), 635.

Poplavsky, D., B. Danilchenko, and H. Kostial, 2000, Phys. Rev. B **61**(16), 10941.

Price, P. J., 1982, J. Appl. Phys. **53**(10), 6863.

Ramsbey, M. T., I. Szafranek, G. Stillman, and J. P. Wolfe, 1994, Phys. Rev. B **49**(23), 16427.

Ramsbey, M. T., S. Tamura, and J. P. Wolfe, 1992, Phys. Rev. B **46**(3), 1358.

Renk, K. F., 1985, in *Non-Equilibrium Phonon Dynamics*, edited by W. E. Bron (Plenum Press), p. 59.

Renk, K. F., and J. Deisenhofer, 1971, Phys. Rev. Lett. **26**(13), 764.

Ridley, B. K., 1991, Rep. Prog. Phys. **54**(2), 169.

Ridley, B. K., 1997, *Electrons and Phonons in Semiconductor Multilayers*, Cambridge Studies in Semiconductor Physics and Microelectronic Engineering (Cambridge University Press).

Roshko, S., W. Dietsche, and L. J. Challis, 1998, Phys. Rev. Lett. **80**(17), 3835.

Roshko, S., W. Dietsche, and L. J. Challis, 1999, Physica B **263-264**, 187.

Rothenfusser, M., L. Köster, and W. Dietsche, 1986, Phys. Rev. B **34**(8), 5518.

Rösch, F., and O. Weis, 1977, Z. Phys. B – Condensed Matter **27**, 33.

Rösch, F., and O. Weis, 1978, Z. Phys. B – Condensed Matter **29**, 71.

Rössler, U., and R. Winkler, 1997, private communication.

Ruf, C., H. Obloh, B. Junge, E. Gmelin, and K. Ploog, 1988, Phys. Rev. B **37**(11), 6377.

Sakaki, H., 1980, Jpn. J. Appl. Phys. **19**(12), L735.

Schreyer, H., W. Dietsche, and H. Kinder, 1984, in *Proc. of the 17th Int. Conf. on Low Temp. Phys.*, edited by U. Eckern, A. Schmid, W. Weber, and H. Wuhl (North Holland, Amsterdam), p. 665.

Schulze-Wischeler, F., U. Zeitler, M. Monka, F. Hohls, R. J. Haug, and K. Eberl, 2001, Physica B **298**(1–4), 164.

Senna, J. R., and S. Das Sarma, 1993, Phys. Rev. Lett. **70**(17), 2593.

Shah, J. (ed.), 1992, *Hot Carriers in Semiconductor Nanostructures* (Academic Press, New York).

Shah, J., 1999, *Ultrafast Spectroscopy of Semiconductors and Semiconductor Nanostructures*, Springer Series in Solid-State Sciences, Vol. 115 (Springer, Berlin).

Shah, J., R. C. C. Leite, and J. F. Scott, 1970, Sol. State Commun. **8**(14), 1089.

Shah, J., A. Pinczuk, A. C. Gossard, and W. Wiegmann, 1985, Phys. Rev. Lett. **54**(18), 2045.

Shields, J. A., M. E. Msall, M. S. Carroll, and J. P. Wolfe, 1993, Phys. Rev. B **47**(19), 12510.

Shields, J. A., J. P. Wolfe, and S. Tamura, 1989, Z. Phys. B – Condensed Matter **76**, 295.

Shik, A. Y., and L. J. Challis, 1993, Phys. Rev. B **47**(4), 2082.

Short, J. D., and J. P. Wolfe, 2000, Phys. Rev. Lett. **85**(24), 5198.

Smith, D. L., and C. Mailhiot, 1990, Rev. Mod. Phys. **62**(1), 173.

Smith, M. J., and P. N. Butcher, 1990, J. Phys.: Condens. Matter **2**, 2375.

Stanton, N. M., A. V. Akimov, A. J. Kent, S. A. Cavill, T. S. Cheng, and C. T. Foxon, 2000, Appl. Phys. Lett. **77**, 3403.

Stanton, N. M., A. J. Kent, and D. Lehmann, 2003a, Semicond. Sci. Technol. **18**, L4.

Stanton, N. M., R. N. Kini, A. J. Kent, M. Henini, and D. Lehmann, 2003b, Phys. Rev. B **68**(11), 113302.

Stern, F., 1967, Phys. Rev. Lett. **18**, 546.

Stern, F., 1972, Phys. Rev. B. **5**(12), 4891.

Stern, F., and S. Das Sarma, 1984, Phys. Rev. B. **30**(2), 840.

Stroscio, M. A., and M. Dutta, 2001, *Phonons in Nanostructures* (Cambridge University Press).

Sugawara, Y., O. B. Wright, O. Matsuda, M. Takigahira, Y. Tanaka, S. Tamura, and V. E. Gusev, 2002, Phys. Rev. Lett. **88**(18), 185504.

Sugaya, T., J. P. Bird, D. K. Ferry, A. Sergeev, V. Mitin, K.-Y. Jang, M. Ogura, and Y. Sugiyama, 2002, Appl. Phys. Lett. **81**(4), 727.

Takada, Y., and Y. Uemura, 1977, J. Phys. Soc. Japan **43**(1), 139.

Tamura, S., 1984, Phys. Rev. B **30**(2), 849.

Tamura, S., 1993, Phys. Rev. B **48**(18), 13502.

Tamura, S., and T. Harada, 1985, Phys. Rev. B **32**(8), 5245.

Tamura, S., D. C. Hurley, and J. P. Wolfe, 1988, Phys. Rev. B **38**(12), 1427.

Tamura, S., and H. Kitagawa, 1989, Phys. Rev. B **40**(12), 8485.

Tanaka, Y., M. Narita, and S. Tamura, 1998, J. Phys.: Condens. Matter **10**, 8787.

Taylor, B., H. J. Maris, and C. Elbaum, 1969, Phys. Rev. Lett. **23**(8), 416.

Ting, C. S., and T. W. Nee, 1986, Phys. Rev. B **33**(10), 7056.

Ting, C. S., S. C. Ying, and J. J. Quinn, 1977, Phys. Rev. B **16**(12), 5394.

Toombs, G. A., F. W. Sheard, D. Neilson, and L. J. Challis, 1987, Sol. State Commun. **64**(4), 577.

Totland, H., Y. M. Galperin, and V. L. Gurevich, 1999, Phys. Rev. B **59**(4), 2833.

Valadares, E. C., 1992, Phys. Rev. B **46**(7), 3935.

Vasko, F. T., O. G. Balev, and P. Vasilopoulos, 1993, Phys. Rev. B **47**(24), 16433.

Vasko, F. T., and V. V. Mitin, 1995, Phys. Rev. B **52**(3), 1500.

Vass, E., 1987, Sol. State Commun. **61**(2), 127.

Vines, R. E., M. R. Hauser, and J. P. Wolfe, 1995a, Z. Phys. B – Condensed Matter **98**, 255.

Vines, R. E., S. Tamura, and J. P. Wolfe, 1995b, Phys. Rev. Lett. **74**(14), 2729.

von Gutfeld, R. J., and A. H. Nethercot, 1964, Phys. Rev. Lett. **12**(23), 641.

Weilert, M. A., M. E. Msall, A. C. Anderson, and J. P. Wolfe, 1993, Phys. Rev. Lett. **71**(5), 735.

Weis, O., 1969, Angew. Phys. **26**(5), 325.

Wendler, L., and V. G. Grigoryan, 1988, Surf. Sci. **206**(1-2), 203.

Wheeler, R. G., K. K. Choi, A. Goel, R. Wisnieff, and D. E. Prober, 1982, Phys. Rev. Lett. **49**(22), 1674.

White, S. R., and L. J. Sham, 1981, Phys. Rev. Lett. **47**(12), 879.

Wichard, R., and W. Dietsche, 1992, Phys. Rev. B **45**(17), 9705.

Wigmore, J. K., H. A. Al Jawhari, A. G. Kozorezov, and M. Sahraoui-Tahar, 2001, in *Proc. 25th Int. Conf. on Physics of Semiconductors*, edited by N. Miura and T. Ando (Springer, Berlin), p. 881.

Wigmore, J. K., M. Erol, M. Sahraoui-Tahar, M. Ari, C. D. W. Wilkinson, J. H. Davies, M. Holland, and C. Stanley, 1993, Semicond. Sci. Technol. **8**(3), 322.

Wigmore, J. K., M. Erol, M. Sahraoui-Tahar, C. D. W. Wilkinson, J. H. Davies, and C. Stanley, 1991, Semicond. Sci. Technol. **6**(9), 837.

Williams, R., 1977, J. Vac. Sci. Technol. **14**(5), 1106.

Winkler, R., and U. Rössler, 1993, Phys. Rev. B **48**(12), 8918.

Wolfe, J. P., 1989, in *Festkörperprobleme (Advances in Solid State Physics),* Vol. 29, edited by U. Rössler (Vieweg, Braunschweig), pp. 75–105.

Wolfe, J. P., 1998, *Imaging Phonons* (Cambridge University Press).

Wright, O. B., Y. Sugawara, O. Matsuda, M. Takigahira, Y. Tanaka, S. Tamura, and V. E. Gusev, 2002, Physica B **316-317**, 29.

Wybourne, M. N., and J. K. Wigmore, 1988, Rep. Prog. Phys. **51**(7), 923.

Xu, W., 1996, Phys. Rev. B **54**(4), 2775.

Xu, W., and J. Mahanty, 1994, J. Phys.: Condens. Matter **6**(31), 6265.

Xu, W., and C. Zhang, 1996, J. Phys.: Condens. Matter **8**(50), 11111.

Yamamoto, A., T. Mishina, and Y. Masumoto, 1994, Phys. Rev. Lett. **73**(5), 740.

Yang, C. H., J. M. Carlson-Swindle, S. A. Lyon, and J. M. Worlock, 1985, Phys. Rev. Lett. **55**(21), 2359.

Yokota, I., 1961, J. Phys. Soc. Jpn. **16**, 2075.

Zachau, M., F. Koch, G. Weimann, and W. Schlapp, 1986, Phys. Rev. B **33**(12), 8564.

Zeitler, U., A. M. Devitt, J. E. Digby, C. J. Mellor, A. J. Kent, K. A. Benedict, and T. Cheng, 1999, Phys. Rev. Lett. **82**(26), 5333.

Zelakiewicz, S., and T. J. Gramila, 2002, Phys. Rev. Lett. **88**(14), 149702.

Zelakiewicz, S., H. Noh, T. J. Gramila, L. N. Pfeiffer, and K. W. West, 2000, Phys. Rev. Lett. **85**(9), 1942.

Zheng Yisong, Lu Tianquan, Wang Yiding, Wu Xuhong, Zhang Chengxiang, and Su Wenhui, 1997, Semicond. Sci. Technol. **12**(3), 296.

Zook, J. D., 1964, Phys. Rev. **136**(3A), A869.

Acknowledgement

First of all, I am indebted to Prof. Tadeusz Paszkiewicz for introducing me to the fascinating field of phonon propagation and interaction, for his continuous encouragement and for all his help during my first steps in the topic.

Similarly, I am truly grateful to Prof. Czesław Jasiukiewicz. During all the years he was always an open-minded discussion partner and, by his intense work on the numerical programs for our calculations, he also contributed much to the success of this work.

I have benefitted enormously from interaction with collaborators and colleagues. I am very grateful to Prof. Lawrence Challis, Prof. Boris Danilchenko, Dr Vitautas Karpus, Dr Seiji Mizuno, Prof. Keith Wigmore and many others for their advice and stimulating discussions.

In particular, I would like to thank Prof. Werner Dietsche and Dr Anthony Kent and the members of their experimental groups for the intense collaboration, for their support and for many, many fruitful discussions and ideas.

Prof. Klaus Becker, as the head of the Solid State Theory Group in the Dresden University of Technology, continuously supported my work and I am very grateful for this. He always had an open ear for questions and problems.

My thanks also go to all the past and present members of the Institute of Theoretical Physics in Dresden for the warm atmosphere, for the discussions and for all their help during and outside working ours.

Special thank is given to Nora Ritschel for the improvements of the English in the manuscript. I also thank Dr Jörg Bergmann for the help with the graphics.

Last but not least I would like to thank my family and my friends for all their support, encouragement and patience, particularly at the time of finishing this work.